

Statistical Modeling of Radiometric Error Propagation in
Support of Hyperspectral Imaging Inversion and Optimized
Ground Sensor Network Design

by

Scott Klempner

B. S. United States Air Force Academy, 1998

M. Eng. University of Colorado, 1999

A dissertation submitted in partial fulfillment of the
requirements for the degree of Doctor of Philosophy
in the Chester F. Carlson Center for Imaging Science

Rochester Institute of Technology

4 September 2008

Signature of the Author _____

Accepted by _____
Coordinator, Ph.D. Degree Program _____ Date _____

Report Documentation Page			Form Approved OMB No. 0704-0188	
<p>Public reporting burden for the collection of information is estimated to average 1 hour per response, including the time for reviewing instructions, searching existing data sources, gathering and maintaining the data needed, and completing and reviewing the collection of information. Send comments regarding this burden estimate or any other aspect of this collection of information, including suggestions for reducing this burden, to Washington Headquarters Services, Directorate for Information Operations and Reports, 1215 Jefferson Davis Highway, Suite 1204, Arlington VA 22202-4302. Respondents should be aware that notwithstanding any other provision of law, no person shall be subject to a penalty for failing to comply with a collection of information if it does not display a currently valid OMB control number.</p>				
1. REPORT DATE 01 OCT 2008	2. REPORT TYPE N/A	3. DATES COVERED -		
4. TITLE AND SUBTITLE Statistical Modeling of Radiometric Error Propagation in Support of Hyperspectral Imaging Inversion and Optimized Ground Sensor Network Design			5a. CONTRACT NUMBER	
			5b. GRANT NUMBER	
			5c. PROGRAM ELEMENT NUMBER	
6. AUTHOR(S)			5d. PROJECT NUMBER	
			5e. TASK NUMBER	
			5f. WORK UNIT NUMBER	
7. PERFORMING ORGANIZATION NAME(S) AND ADDRESS(ES) Rochester Institute Of Technology Rochester, New York			8. PERFORMING ORGANIZATION REPORT NUMBER	
9. SPONSORING/MONITORING AGENCY NAME(S) AND ADDRESS(ES) AFIT Wright-Patterson AFB, OH 45433-7221			10. SPONSOR/MONITOR'S ACRONYM(S)	
			11. SPONSOR/MONITOR'S REPORT NUMBER(S) CI09-0034	
12. DISTRIBUTION/AVAILABILITY STATEMENT Approved for public release, distribution unlimited				
13. SUPPLEMENTARY NOTES The original document contains color images.				
14. ABSTRACT				
15. SUBJECT TERMS				
16. SECURITY CLASSIFICATION OF:			17. LIMITATION OF ABSTRACT UU	18. NUMBER OF PAGES 325
a. REPORT unclassified	b. ABSTRACT unclassified	c. THIS PAGE unclassified		

Disclaimer

The views expressed in this dissertation are those of the author and do not reflect the official policy or position of the Department of Defense or the United States Government.

CHESTER F. CARLSON CENTER FOR IMAGING SCIENCE
ROCHESTER INSTITUTE OF TECHNOLOGY
ROCHESTER, NEW YORK

CERTIFICATE OF APPROVAL

Ph.D. DEGREE DISSERTATION

The Ph.D. Degree Dissertation of Scott Klempner
has been examined and approved by the
dissertation committee as satisfactory for the
dissertation required for the
Ph.D. degree in Imaging Science

Dr. John R. Schott, dissertation Advisor

Dr. John P. Kerekes

Dr. Peter Bajorski

Dr. Steven M. LaLonde

Date

Thesis/Dissertation Author Permission Statement

Title of thesis or dissertation: Statistical Modeling of Radiometric Error Propagation in Support of Hyperspectral Imaging Inversion and Optimized Ground Sensor Network Design

Name of author: Scott Klempner
Degree: Doctor of Philosophy
Program: Imaging Science
College: College of Science

I understand that I must submit a print copy of my thesis or dissertation to the RIT Archives, per current RIT guidelines for the completion of my degree. I hereby grant to the Rochester Institute of Technology and its agents the non-exclusive license to archive and make accessible my thesis or dissertation in whole or in part in all forms of media in perpetuity. I retain all other ownership rights to the copyright of the thesis or dissertation. I also retain the right to use in future works (such as articles or books) all or part of this thesis or dissertation.

Print Reproduction Permission Granted:

I, Scott Klempner, hereby **grant permission** to the Rochester Institute Technology to reproduce my print thesis or dissertation in whole or in part. Any reproduction will not be for commercial use or profit.

Signature of Author: _____ Date: _____

Print Reproduction Permission Denied:

I, _____, hereby **deny permission** to the RIT Library of the Rochester Institute of Technology to reproduce my print thesis or dissertation in whole or in part.

Signature of Author: _____ Date: _____

Inclusion in the RIT Digital Media Library Electronic Thesis & Dissertation (ETD) Archive

I, Scott Klempner, additionally grant to the Rochester Institute of Technology Digital Media Library (RIT DML) the non-exclusive license to archive and provide electronic access to my thesis or dissertation in whole or in part in all forms of media in perpetuity.

I understand that my work, in addition to its bibliographic record and abstract, will be available to the world-wide community of scholars and researchers through the RIT DML. I retain all other ownership rights to the copyright of the thesis or dissertation. I also retain the right to use in future works (such as articles or books) all or part of this thesis or dissertation. I am aware that the Rochester Institute of Technology does not require registration of copyright for ETDs.

I hereby certify that, if appropriate, I have obtained and attached written permission statements from the owners of each third party copyrighted matter to be included in my thesis or dissertation. I certify that the version I submitted is the same as that approved by my committee.

Signature of Author: _____ Date: _____

**Statistical Modeling of Radiometric Error Propagation in
Support of Hyperspectral Imaging Inversion and Optimized
Ground Sensor Network Design**

by

Scott Klempner

Submitted to the
Chester F. Carlson Center for Imaging Science
in partial fulfillment of the requirements
for the Doctor of Philosophy Degree
at the Rochester Institute of Technology

Abstract

A method is presented that attempts to isolate the relative magnitudes of various error sources present in common algorithms for inverting the effects of atmospheric scattering and absorption on solar irradiance and determine in what ways, if any, operational ground truth measurement systems can be employed to reduce the overall error in retrieved reflectance factor. Error modeling and propagation methodology is developed for each link in the imaging chain, and representative values are determined for the purpose of exercising the model and observing the system behavior in response to a wide variety of inputs. Three distinct approaches to model-based atmospheric inversion are compared in a common reflectance error space, where each contributor to the overall error in retrieved reflectance is examined in relation to the others. The modeling framework also allows for performance predictions resulting from the incorporation of operational ground truth measurements. Regimes were identified in which uncertainty in water vapor and aerosols were each found to dominate error contributions to final retrieved reflectance. Cloud cover was also shown to be a significant contributor, while state-of-the-industry hyperspectral sensors were confirmed to not be error drivers. Accordingly, instruments for measuring water vapor, aerosols, and downwelled sky radiance were identified as key to improving reflectance retrieval beyond current performance by current inversion algorithms.

Acknowledgements

I wish to express gratitude toward Dr. Schott and my dissertation committee. Their guidance was invaluable and forbearance necessary as I finished this work from three states and 380 miles away. Likewise, I wish to sincerely thank Cindy Schultz for making this long distance relationship work. Every time I worked with her to get closer to this finish point, it was personally encouraging to me, and there were times it was really needed. I feel if I attempted to capture on printed page all the praise she really deserves, it might double the length of this document.

After leaving Rochester and moving to Virginia, I encountered a whole new group of people who offered continual support and encouragement, especially Eleanor, Tiina, Brett, and the Colonels. I greatly appreciated it.

I would like to especially thank my wife Amy. Not only is she the nicest person I know, she has also endured far more than any spouse should have to, even if it is common in this line of work. She was only expecting three years of school-induced separation, and I handed her five. The two most important phrases in a marriage seem apropos here: I'm sorry, and I love you. Thank you.

I would like to thank my partners Brent Bartlett and Brian Daniel for their special assistance in the field research of operationally deployed atmospheric sounding systems and hydrodynamic power generation.

Finally, thanks to Jake Ward for always taking the outside lane.

For Patrick, Colin, Will, and Sean

Contents

1	Introduction	1
2	Objectives	9
2.1	Main Objectives	9
2.2	Minor Objectives	10
2.3	Scope	11
2.4	Success Criteria	12
3	Background	15
3.1	Radiative transfer model	15
3.2	Inversion algorithm descriptions	19
3.2.1	Empirical algorithm: the Empirical Line Method	21
3.2.2	Model-based algorithm: Green's method	25
3.2.3	Model-based algorithm: Fast Line-of-Sight Atmospheric Analysis of Spectral Hypercubes (FLAASH)	28
4	Approach and Theory	31
4.1	Introduction	31
4.2	Imaging operators	32
4.3	Forward uncertainty model description	33
4.4	Error propagation in analytical functions	36
4.4.1	Total error	36
4.4.2	Random component	38
4.4.3	Bias component	40
4.5	Governing equation	41
4.6	Application of error propagation	44
4.6.1	Main equations	44
4.6.2	Correlation coefficients	45

4.6.3	Partial derivatives	47
4.6.4	Bias terms	48
4.7	Numerically-determined derivatives	50
4.7.1	General equations	51
4.7.2	Error considerations	53
4.8	Slope calculation using MODTRAN	55
4.9	Uncertainty in atmospheric parameters	57
4.9.1	Error sources from climatology	58
4.9.2	Error sources from ground instruments	60
4.9.3	Error sources from inversion algorithms	60
4.10	Total atmospheric error	61
4.11	Physical models	61
4.11.1	Elevation knowledge	62
4.11.2	Exoatmospheric solar irradiance	63
4.12	Sensor error models	65
4.12.1	Radiometric calibration	66
4.12.2	Spectral calibration	67
4.12.3	Ground radiometer	71
4.12.4	Mechanical factors	74
4.13	Environmental error models	75
4.13.1	Target tilt	76
4.13.2	Clouds	79
4.13.3	Background objects	87
4.13.4	Pointing	93
4.14	Scenario setup	97
4.15	Validation	99
5	Results and Discussion	103
5.1	Atmospheric partial derivatives	105
5.1.1	Step size selection	105
5.1.2	Slope determination in MODTRAN functional space . . .	106
5.2	Atmospheric constituent uncertainty	113
5.2.1	Constituents from Climatology	114
5.2.2	Constituents from Instrumentation	115
5.2.3	Constituents from In-scene Algorithms	116
5.2.4	Atmospheric Constituent Scenarios	124
5.3	Error in Modeling Outputs	124
5.4	Sensor Modeling Results	125

5.4.1	Radiometric precision	125
5.4.2	Radiometric accuracy	128
5.4.3	Spectral calibration	128
5.5	Environmental error modeling results	135
5.5.1	Pointing angle modeling results	136
5.5.2	Cloud modeling results	138
5.5.3	Background object modeling results	140
5.5.4	Environmental error scenario summary	141
5.5.5	Combined effects	141
5.6	Total error	142
5.6.1	Scenario 1 – Climatological sources	144
5.6.2	Scenario 2 – Field-quality ground instruments	146
5.6.3	Scenario 3 – Research quality ground instruments	147
5.6.4	Scenarios 4 and 5 – In-scene sources	147
5.6.5	Scenarios 6 through 8 – Off-nadir pointing bias	149
5.6.6	Scenarios 9 and 10: Off-nadir pointing uncertainty	150
5.6.7	Scenario 11: Ground tilt bias	150
5.6.8	Scenarios 12–13: Ground tilt knowledge uncertainty	150
5.6.9	Scenarios 14–17: Bias error due to cloud cover and background objects	151
5.6.10	Scenario 18: Sensor noise	153
5.6.11	Scenario 19: Sensor radiometric calibration bias	153
5.6.12	Scenario 20: Bias error due to spectral misregistration	155
5.6.13	Scenario 21: Spectral jitter uncertainty	156
5.6.14	Final Scenario: Mean squared error for combined effects	157
5.7	Validation	165
5.8	Error sensitivity study	167
5.8.1	Scenario 1	168
5.8.2	Explanation of counterintuitive results	169
5.8.3	Scenarios 2 and 3	172
5.8.4	Scenario 4	173
5.8.5	Scenario 5	173
5.8.6	Direct measurement of τ_1 and L_d	174
5.9	Optimal network design	176
5.10	Summary of results	182

6 Conclusions and Future Work	185
6.1 Modeling Work and System Behavior	185
6.2 Future Work	189
A Full Expressions for Selected Equations	191
A.1 Partial derivatives of reflectance	191
A.2 Correlation and error terms	193
A.3 Consolidated expressions	196
A.4 Digital elevation model altitude error	199
B Climatology Analysis Results	201
C Environmental Effect Modeling Results	207
D Atmospheric Uncertainty Results	217
E Environmental Effect Results	229
F Validation Results	243
G Error Improvement Sensitivity Results	263
H Atmospheric Derivative Functional Spaces	285
I Explanation of Water Vapor Units	293

List of Figures

1.1	Early satellite imagery	2
1.2	LandSAT VII diagram	3
1.3	Unattended sensor network	4
3.1	Indirect radiance sources	18
3.2	Sky fraction naming convention	20
3.3	The linear relationship of the empirical line method	22
3.4	ELM uncertainty	23
3.5	ELM linear regression	24
3.6	760 nm oxygen feature variation with sensor altitude	26
3.7	Water vapor absorption features by total column amount	27
4.1	Imaging operator block diagram	33
4.2	Target/image space model	34
4.3	Forward uncertainty chain	35
4.4	Three-level uncertainty chain block diagram	36
4.5	Antecedent sources in the modeling chain	44
4.6	Chebyshev curve fit slope error	53
4.7	A comparison of systematic and functional error	54
4.8	Construction of total error in each model output	61
4.9	DEM interpolation visualization	62
4.10	DEM altitude error using SRTM values and flat terrain	63
4.11	Illustration of spectral calibration errors and their effects on the imaging chain	68
4.12	Percent error in radiance as a function of band center shift	70
4.13	Reflectance curves used to simulate spectral cal errors	71
4.14	Radiance curves used to simulate spectral cal errors	72
4.15	Ground reflectometer in dual-input configuration	73

4.16 Tilted target relative to the local horizon	76
4.17 Elevation measurement scenario	77
4.18 DEM interpolation error in elevation	78
4.19 DEM interpolation error in direct solar term	78
4.20 Cloud concepts	81
4.21 Clear-sky radiance results for 72 and 1224 quads	83
4.22 Radiance sources for a background object	88
4.23 Background radiance, measured vs predicted	90
4.24 Quad integration approach for background objects	91
4.25 Azimuthal variation in simulated background objects	92
4.26 Nadir and off-nadir pointing terms	94
4.27 Upwelled radiance by azimuth and nadir angle	95
4.28 Variation in L_u and τ_2 by pointing angle, relative to nadir	96
5.1 Map of Component Results	104
5.2 Water vapor slope step size sensitivity	107
5.3 Altitude slope step size sensitivity	108
5.4 Aerosol/Visibility slope step size sensitivity	109
5.5 Derived slopes for τ_1	111
5.6 Derived slopes for τ_2	111
5.7 Derived slopes for L_d	112
5.8 Derived slopes for L_u	112
5.9 Relationship between aerosol optical depth and visibility	113
5.10 CIBR and APDA validation results	121
5.11 Sample results for error in modeling outputs	126
5.12 Instrument radiometric calibration noise models	129
5.13 Reflectance retrieval from Hyperion imagery	130
5.14 AVIRIS radiometric calibration bias	131
5.15 Hyperion radiometric calibration bias	132
5.16 Radiance bias error due to spectral misregistration	133
5.17 Standard deviation in percent radiance error	134
5.18 Uncertainty in radiance due to 0.5 nm spectral jitter	136
5.19 Relationships between cloud quads and sky fraction	139
5.20 Correlation between background quads and sky fraction	141
5.21 Total reflectance uncertainty summary for basic scenarios 1-5	145
5.22 940 nm absorption feature	156
5.23 Bias in retrieved CIBR water vapor	157
5.24 Cloud reflectance bias for final scenario	158

5.25	Background reflectance bias for final scenario	159
5.26	Total reflectance bias error for final scenario	159
5.27	Final scenario mean squared error	160
5.28	Square root of mean squared error for the final scenario (with geo-metric variability for clouds and background objects)	162
5.29	Final scenario variant mean squared error	163
5.30	Square root of mean squared error for the final scenario (with geo-metric variability for clouds and background objects)	164
5.31	Reflectance uncertainty sensitivity	171
5.32	Instrument Tradeoff Matrix	179
B.1	GPS-based climate model for water vapor	201
B.2	Radiosonde-based climate model for water vapor	202
B.3	MODIS-based climate model for water vapor	202
B.4	Airport observation-based climate model for density altitude	203
B.5	GPS-based climate model for density altitude	203
B.6	Radiosonde-based climate model for density altitude	204
B.7	MODIS-based climate model for aerosols	204
B.8	Airport observation-based climate model for visibility	205
B.9	Airport observation-based visibility histogram	205
C.1	Off-nadir pointing effects, sensor at 792 m	208
C.2	Off-nadir pointing effects, sensor at 4 km	209
C.3	Off-nadir pointing effects, sensor at 11 km	210
C.4	Off-nadir pointing effects, sensor at 100 km	211
C.5	Multiple scattering algorithm effect on off-nadir pointing	212
C.6	Cumulus cloud modeling results	213
C.7	Cloud type comparison	214
C.8	Background modeling results	215
D.1	Legend for reflectance results	218
D.2	Legend for correlation results	218
D.3	Scenario 1 – reflectance error	219
D.4	Scenario 1 – correlations	220
D.5	Scenario 2 – reflectance error	221
D.6	Scenario 2 – correlations	222
D.7	Scenario 3 – reflectance error	223
D.8	Scenario 3 – correlations	224
D.9	Scenario 4 – reflectance error	225

D.10 Scenario 4 – correlations	226
D.11 Scenario 5 – reflectance error	227
D.12 Scenario 5 – correlations	228
E.1 Scenarios 6-8, off-nadir pointing bias error, 100% reflector	230
E.2 Scenarios 6-8, off-nadir pointing bias error, 20% reflector	231
E.3 Scenarios 9-10, off-nadir pointing random error	232
E.4 Scenario 11, ground tilt bias error	233
E.5 Scenarios 12-13, ground tilt random error, 100% reflector	234
E.6 Scenarios 14-15, cloud bias error, 100% reflector	235
E.7 Scenarios 14-15, cloud bias error, 20% reflector	236
E.8 Scenarios 16-17, background object bias error, 100% reflector	237
E.9 Scenarios 16-17, background object bias error, 20% reflector	238
E.10 Scenario 18, sensor noise random error	239
E.11 Scenario 19, sensor radiometric calibration bias error	240
E.12 Scenario 20, retrieved reflectance bias error due to spectral misregistration	241
E.13 Scenario 21, uncertainty in retrieved reflectance due to 0.5 nm spectral jitter	242
F.1 Validation scenario 1 – 100% reflector	244
F.2 Validation scenario 1 – 20% reflector	245
F.3 Validation scenario 2 – 100% reflector	246
F.4 Validation scenario 2 – 20% reflector	247
F.5 Validation scenario 3 – 100% reflector	248
F.6 Validation scenario 3 – 20% reflector	249
F.7 Validation scenario 4 – 100% reflector	250
F.8 Validation scenario 4 – 20% reflector	251
F.9 Validation scenario 5 – 100% reflector	252
F.10 Validation scenario 5 – 20% reflector	253
F.11 Validation scenario 6 – 100% reflector	254
F.12 Validation scenario 6 – 20% reflector	255
F.13 Validation scenario 7 – 100% reflector	256
F.14 Validation scenario 7 – 20% reflector	257
F.15 Validation scenario 8 – 100% reflector	258
F.16 Validation scenario 8 – 20% reflector	259
F.17 Validation scenario 9 – 100% reflector	260
F.18 Validation scenario 9 – 20% reflector	261

G.1	Legend for error sensitivity results	263
G.2	Scenario 1 – <i>a priori</i> knowledge climatology inputs	264
G.3	Scenario 1 – multiple reflectance comparison	265
G.4	Scenario 1 – aerosol individual results	266
G.5	Scenario 1 – water vapor individual results	267
G.6	Scenario 2 – inputs from commercial quality instrumentation	268
G.7	Scenario 2 – multiple reflectance comparison	269
G.8	Scenario 2 – aerosol individual results	270
G.9	Scenario 2 – water vapor individual results	271
G.10	Scenario 3 – inputs from ARM-grade instrumentation	272
G.11	Scenario 3 – multiple reflectance comparison	273
G.12	Scenario 3 – aerosol individual results	274
G.13	Scenario 3 – water vapor individual results	275
G.14	Scenario 4 – <i>a priori</i> knowledge climatology inputs	276
G.15	Scenario 4 – multiple reflectance comparison	277
G.16	Scenario 4 – aerosol individual results	278
G.17	Scenario 4 – water vapor individual results	279
G.18	Scenario 5 – <i>a priori</i> knowledge climatology inputs	280
G.19	Scenario 5 – multiple reflectance comparison	281
G.20	Scenario 5 – aerosol individual results	282
G.21	Scenario 5 – water vapor individual results	283
H.1	Derivative $\partial\tau_1/\partial alt$	286
H.2	Derivative $\partial\tau_1/\partial vis$	286
H.3	Derivative $\partial\tau_1/\partial H_2O$	287
H.4	Derivative $\partial\tau_2/\partial vis$	287
H.5	Derivative $\partial\tau_2/\partial alt$	288
H.6	Derivative $\partial\tau_2/\partial H_2O$	288
H.7	Derivative $\partial L_d/\partial vis$	289
H.8	Derivative $\partial L_d/\partial H_2O$	289
H.9	Derivative $\partial L_d/\partial alt$	290
H.10	Derivative $\partial L_u/\partial vis$	290
H.11	Derivative $\partial L_u/\partial alt$	291
H.12	Derivative $\partial L_u/\partial H_2O$	291

List of Tables

4.1	Baseline Scenario Geometry	98
4.2	Baseline Sensor Parameters	98
4.3	Baseline MODTRAN Atmospheric Parameters	98
4.4	Other Selectable Parameters	99
4.5	Validation scenario summary	102
5.1	Partial Derivative Settings Summary	105
5.2	Climatology Results Summary (Month 5)	115
5.3	Temperature	116
5.4	Pressure	117
5.5	Aerosol Optical Depth	117
5.6	Water Vapor	121
5.7	Inversion algorithm constituent determination summary	124
5.8	Atmospheric Uncertainty Scenario Settings	125
5.9	Environmental Error Scenario Settings	142
5.10	Combined Effect Scenario Settings	143
5.11	Validation scenario summary	165
5.12	Instrument improvement analysis (averaged over visible bands) . .	178

Chapter 1

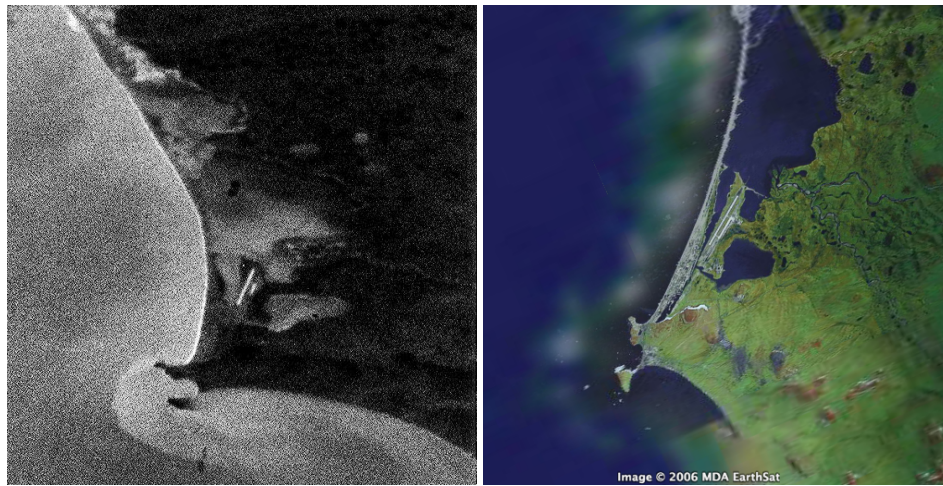
Introduction

The story of remote sensing has been one of steady technological innovation, evolving image processing and data extraction techniques, and branching applications. Each new generation of technology builds on needs that have emerged from the previous generation's remote sensing applications and data processing methods and, in turn, prompts new application branches and new data extraction capabilities. Taking photographs from a balloon, first documented in 1858, predates the US Civil War, and this capability led to the employment of battlefield surveillance techniques during the war. The invention of the first modern camera in 1888 (including flexible rolled film and standardized chemical processing) and powered flight shortly thereafter enabled the first true aerial photography, employed in World War I and II. The invention of color infrared film not only had applications in detecting camouflage but also vegetation health. This discovery in the mid-1950's established the utility of remote sensing in agricultural research (Campbell, 1987).

The spiral evolution of remote sensing has continued with satellite photography, digital imaging, multispectral, multitemporal, and most recently hyperspectral imaging. The Corona project, the existence of which was made public in 1995, marked the first time remote sensing was conducted from space - the result of which is shown in figure 1.1. This excerpt from a 1960 memorandum to the US Intelligence Board illustrates the relationship between needs, technology, applications, and exploitation:

For six years the U. S. intelligence agencies have had extensive experience with the larger scale photography from overflight held in the [redacted] and TALENT Systems. New equipment bearing upon the art of photographic interpretation has clearly expanded the quantity

and quality of information derived from that photography. We have seen the extensive uses to which the material and the information derived therefrom can be put for strategic intelligence purposes, emergency war planning, intelligence purpose related to the responsibility of theater commanders, research and development requirements of the Department of Defense, and operational purposes of the military as well as intelligence operations (Ruffner, 1995).



(a) **First satellite photo ever taken (Corona project, August 18, 1960)** (b) **Modern satellite image of the same subject**

Figure 1.1: Soviet Airstrip at $68^{\circ}53'N$ $179^{\circ}24'W$

Near the end of the Corona satellite program, the National Photographic Interpretation Center (NPIC) expressed an opinion that color photography from a satellite platform could be useful for non-military uses. The 1971 report provided strong evidence that global land observation for geological classification, mapping, and other purposes would be extremely useful and highly beneficial. The section entitled “The Value of Color Cannot Be Overstated” hints at the later-discovered uses of multispectral and hyperspectral imagery (Ruffner, 1995). The LandSAT program, the product of a decade’s research by NASA and the National Academy of Sciences, was initiated the very next year as a systematic and repeatable earth observation program. The space vehicles and their data products, shown in figure 1.2, revolutionized many fields, including ground mapping, geology, forestry,

agriculture and soil quality, and land use (Campbell, 1987). Later developments in digital imagery, imaging spectroscopy, and automated data processing continued the trends traced thus far in the history of remote sensing.

The inherent strengths of remote sensing—the potential to operate on large geographic areas at one time, access to otherwise inaccessible or denied areas, and standoff distance—point to what may be thought of as proper or improper applications of the discipline. However, as has been shown so far, new application areas can be opened up as a result of novel uses of technology and processing. It has long been taken for granted that the proper role of ground truth in remote sensing is strictly limited to support roles: instrument calibration, basic phenomenology research, and algorithm development/validation. Ground truth takes many forms, including measurement of ground material properties, radiometric quantities in the sky, and atmospheric constituency, and all are generally deemed to be too expensive and too burdensome to routinely measure as part of an operational remote sensing activity. After all, if it were viable to simply “sense,” there would be no need to “remotely sense.”

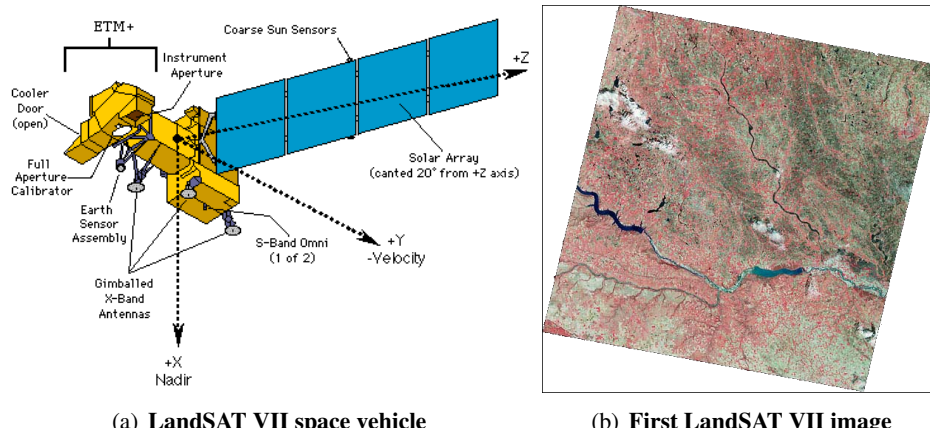
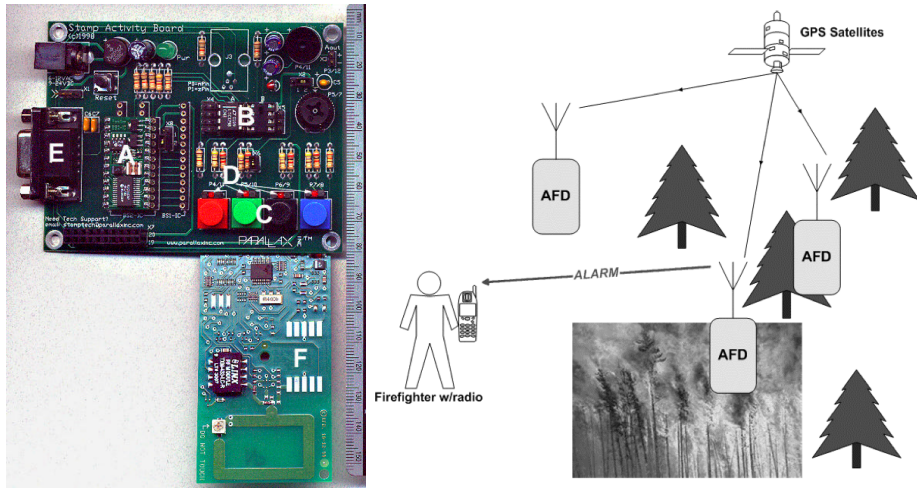


Figure 1.2: Launched in 1999, the LandSAT VII platform continues the 34-year-old Earth observing program.

However, enabling technology has recently developed such that networks of ground truth sensors deployed in conjunction with remote sensing image data collection deserve reconsideration. These technologies are inexpensive wireless communication and computer chips. The products are sensors that can be manufactured cheaply, ruggedized or be made disposable, left unattended, and remotely commu-

nicated with. These sensors, in effect, can become remote sensors. Networking these sensors produces a remote sensing system – not one that collects imagery data, but one that collects data in one of several different modes.

While novel, systems of this type are not unheard of. Such a multi-modal system is notionally depicted in figure 1.3, in which inexpensive autonomous wild-fire detection and monitoring sensors constructed from common commercially-available components are arrayed throughout a wide geographic area. Overhead multispectral imagery provides an uncalibrated heat release map over the entire area while the ground sensors provide necessary calibration information. Together, the fused imaging and non-imaging data allow an estimate of fuel consumption and other burn characteristics of scientific and practical interest (Kremens et al., 2005).



(a) **Photograph of a prototype autonomous fire detector** (b) **Autonomous fire detection network concept illustration**

Figure 1.3: Example of an inexpensive, arrayed, unattended sensor system (Kremens et al., 2003).

It is hypothesized that proper application of this concept to other remote sensing research areas can produce significant performance gains for the application and poses the potential to stimulate the upward spiral of remote sensing application development through the operational use of multi-modal sensing. Finding ways to combine non-imaging data from a sensor network with imaging data results in a system of systems geared to provide novel capabilities that serve both research and operational interests. Ideally, the design of the system would be focused on the

final information product rather than on the modality chosen, though there may be limits to the usefulness of such a high level of abstraction.

At the practical level, atmospheric inversion is one of the most active areas, indeed a primary motivation, of remote sensing research. Removing the effects of the atmosphere on photons coming from a known source and reflecting off an unknown target allows the identification of the ground material's reflectance spectrum, which is, in essence, one type of fingerprint of the material's nature. The reflectance spectrum is an intermediate remote sensing data product that is used to find many derivative data products and acts as a gateway to a host of applications, including land classification, land or water quality, anomaly and target detection, and others. It is also widely accepted that reducing imaging data to reflectance spectra provides a time-stable common foundation for working with imaging data and is an inherently valuable task.

Boardman (1990) describes the components the inversion process: the observed data and the modeling of physical operators can be combined to predict the original controlling parameters that produced the original observations. To this process he adds ancillary data and error models. It is common to introduce ancillary data to enhance, enable, or validate the radiance-to-reflectance inversion. Not only does ground truth spectra or other ground measurement unlock certain types of inversion models, fusing ground truth into image processing algorithms can result in an overall increase in precision in the data product.

The inclusion of error models in the inversion process is somewhat curious. Considering the random side of error, it is impossible to predict with an error model the exact value of the noise perturbation for any particular link in the imaging chain at any given time. Time averaging is used to reduce random error, but even if it were not made problematic by the constantly-changing remote sensing environment, it renders moot the need for error models. Use of ancillary measurements precise enough to determine controlling parameters below the noise threshold of the remote sensing instrument has the same effect. Error models are therefore not used to produce the inversion results.

On the other hand, use of error models to predict uncertainty in retrieved reflectance is both possible and necessary. Despite the explicit inclusion of error models in this foundational description of what hyperspectral inversion is and how it should be carried out, this step is not accomplished. In literature on the subject there are perhaps three trends. Often the author explains why the assumptions used are minor enough such that the error will be negligible; it is then ignored. Alternately, authors take a ground truth measurement, compare it to one or more retrieved spectra, and assume the discrepancy to be typical and repeatable. The

final category is the not uncommon sensitivity study, where changes in one parameter are observed to have a corresponding change in the final result. Griffin and Burke (2003) performed a fairly detailed study of this sort, comparing the performance of two hyperspectral inversion algorithms in response to changes in water vapor determination method, aerosol model, aerosol quantity, atmospheric model type, and solar zenith angle. In each case, a variation in a parameter is related to a resulting error in the retrieved surface reflectance, which varied from $\pm 1\text{-}10\%$. While useful and important, it is difficult to translate sensitivity studies like into a framework that demonstrates how the entire system of variables functions as a whole. This type of “direct pass-through” study does not use the statistical language of errors, nor does it place the input perturbations into a meaningful context. It is argued here that none of these approaches employs error modeling in a manner that attaches uncertainty to the “estimates of controlling parameters of interest” (Boardman, 1990).

A different approach was taken by Kerekes (1998) to describe, quantify, and analyze sources of error using statistical language. By analyzing hyperspectral imagery containing large calibration panels, the author was able to use multiple pixels accompanied by ground truth to create a data set subject to statistical analysis. Two methods of obtaining the surface properties were exercised, resulting in an estimate of both random error, expressed as the standard deviation of a probability distribution (on the order of 1-2%), and any bias present in the system (found for one of the methods to be on the order of 1-4%). There was a desire expressed to understand how each of several sources of error, including water vapor estimation error and sensor effects, contributed to uncertainty in the final result. However, without a way to link error in precursor sources to the final product, there are some limitations on how well these sensitivities can be studied and expressed. As a foundational work, this is an excellent starting point. It is precisely the goal here to express the retrieval of surface properties in the same statistical language and accurately model the contributions of individual sources. Extending this work involves the introduction of a method of modeling error in each source, propagating it through the non-linear imaging system, and expressing it in terms common with all the other sources.

The purpose of this investigation is to explore the process of using error modeling to rigorously predict uncertainty in the retrieved reflectance, expressed as an error model. Additionally, this process will be used to determine what types of ancillary data would be most effective in improving radiometric inversion, quantify the expected benefit of collecting ancillary data, and prescribe optimal methods for the use of ancillary data to enhance multi- and hyperspectral reflectance extraction.

The scope and detailed objectives of this work are presented in chapter 2. Inversion methods and ground truth usage will be examined in chapter 3 to provide a basic foundation of work already performed in this area.

A method is presented in chapter 4 that uses basic error propagation theory to isolate the relative magnitudes of various error sources present in common atmospheric inversion algorithms and determine in what ways, if any, operational ground truth measurement systems can be employed to reduce the overall error in retrieved reflectance factor. Several types of common ground truth measurements are examined, including calibration panel reflectance factor, radiometric quantities that can be directly measured such as downwelled radiance, and atmospheric parameters such as water vapor content. The end result of this process is a configurable error propagation model in which each type of measurement is cast into a common uncertainty framework. The error model is built to accept uncertainty inputs from a variety of sources and features a pluggable architecture, where specific instrument noise models, inversion techniques, and sensing scenarios can be added or changed to tailor the model's predictions.

The model is exercised for a family of example scenarios, the results of which are presented in chapter 5. A combination of error sources are used to create the model's components, including published noise models for several imaging spectrometers, commercially available weather sensing instruments, historical climate data for the region and time-of-year used, and typical inversion algorithm performance in determining the various atmospheric variables required. These serve as default values to two ends. First, they are placeholders for actual parameters that may be used to predict uncertainty performance in applications of future interest. More importantly, this scenario's results are also used to expose the inner workings of a non-linear system. The results provide insight into how each part of the imaging chain affects the final outputs, and because the inputs are representative of current remote sensing practices, these results will be relevant to the family of scenarios standard within the community today.

While this space is frequently investigated, normally changes in the reflectance spectra are compared as a function of changes to the inversion process or inputs. This dissertation takes a different approach, conducting the entire analysis in error space instead of reflectance space. Error space reflectance, while expressed in the same units as actual retrieved reflectance, is a non-literal quantity that does not attempt to predict the absolute value of a retrieved spectrum, rather, it predicts the amount of uncertainty present in each retrieved band. Casting results in error space allows the use of a statistical language to describe the aforementioned changes in reflectance spectra observed elsewhere. The use of retrieved reflectance

offers a non-intuitive metric, useful only when compared to a reference spectrum. In contrast, terms expressed in error space provide an immediate insight into the processes at work.

Chapter 2

Objectives

The main objective of this research is to determine a method for optimally reducing the error in retrieved reflectance factors through the use of ancillary data (of which ground truth is a subset). It closely matches the goals of NASA's Integrated Sensing Systems Initiative (ISSI) program, which seeks to enhance remote sensing products through ground-truth augmentation. This primary goal will be attained by completing the major and minor objectives listed below. Completion of the major objectives is required to sufficiently investigate the hypothesis. The completion of the minor objectives adds value to the overall degree of comprehensiveness of the work, but it is not absolutely required that these be completed. Thus, the minor objectives will be accomplished pending completion of the main objectives and in the context of the available time and resources. A list of success criteria is provided by which work towards meeting the major objectives can be measured. Finally, the scope of the work is listed. Defining a scope makes it clear what areas of inquiry will not be answered by this proposed research.

2.1 Main Objectives

Top level goal: Prescribe an optimal ancillary data measurement framework, including type and number of ancillary data measurement devices. Optimal is defined in relation to the precision of retrieved reflectance and accounts for the amount of precision gain, network cost, and instrument complexity.

1. Characterize the forward error chain
 - Review or establish the processes by which error is introduced to the forward remote sensing chain

- Determine the amount of inherent uncertainty in each process, specifically with regards to the use of available *a priori* ancillary data
 - Create a statistical model for each error-introducing process for each element in the forward remote sensing chain
 - Determine the sensitivity of the at-sensor radiance to incremental changes in each physical-world atmospheric input parameter
 - Determine the sensitivity of the at-sensor radiance to incremental changes in the following non-atmospheric input parameters: sky fraction; cloud fraction; spectral band widths, bias, and centers; look geometry; and ground target tilt
2. Characterize the reverse uncertainty chain
 - Perform an uncertainty analysis of several major inversion algorithms
 - Determine the sensitivity of the retrieved spectral reflectance to incremental reductions of uncertainty in each parameter considered by each inversion algorithm
 - Predict for each inversion algorithm what quantity should be measured for the greatest reduction of uncertainty of retrieved spectral reflectance
 - Compare instrument-induced errors to algorithm-induced errors (due to uncertainty in atmospheric parameters or inherent assumptions)
 3. Analyze the scene-wide effectiveness of different types of uncertainty-reduction schemes
 - Determine how ancillary data measurements improve retrieved spectral reflectance as a function of measurement type, precision, and frequency
 4. Validate these predictions with experimental data
 - Design and conduct an experiment using synthetic image modeling
 - Design and conduct an experiment using real-world aerial and/or satellite imagery and simultaneous ancillary data measurements

2.2 Minor Objectives

- Demonstrate the usefulness of improved spectral reflectance factor precision and accuracy in deriving remote sensing products

- Connect the reduction of error in retrieved spectral reflectance to improvements in common remote sensing applications
- Consider the effects of errors inherent in MODTRAN on the sensitivity analysis

2.3 Scope

Limiting the scope of the investigation serves to focus the work towards a specific and definable hypothesis. Expanding the limits of the scope is a subject for any future work.

- The wavelength range is limited to the non-thermally emissive portion of the electromagnetic spectrum, VIS/NIR/SWIR ($0.4 \mu m - 2.5 \mu m$). A wide variety of instruments is used in this research, and many have a limited spectral range. Thus, practicality further limits this spectral range to just the VIS/NIR ranges (approx $0.4 \mu m - 1.1 \mu m$) in the context of experimental validation of predictions.
- Whereas a near-infinite set of atmospheric parameters is available for study, a limited set of atmospheric parameters is studied. Parameter selection was decided from preliminary literary research and investigation and designed to have the broadest impact and predictive value possible
- The atmospheric constituents studied—water vapor, aerosols, and well-mixed gas molecules—are assumed to behave as statistically independent random variables, which allows an assumption that the parameters are also uncorrelated.
 - The caveat only applies to correlations between the atmospheric constituents themselves, not radiometric observables (radiance and transmittance). It is noted that functions of the constituents are known to be highly correlated to one another in practice, and the analysis results used in the governing equations constructed for the model bear this out.
 - The mathematical apparatus to accommodate non-independence of these input parameters is fully developed and made available for use in the error propagation model.
 - Determining the degree of independence and correlation between atmospheric constituents is a study in meteorology left beyond the scope of this investigation.

- No temporal variation in atmospheric conditions is analyzed. This is to say that the atmosphere is assumed to be the same during image collection as it is during ground truth collection unless explicitly stated.
- Sensor noise is assumed to be a stationary random variable. No temporal variation (calibration drift) in instrument capabilities is studied. As a practical matter, sensitivity of the results to sensor drift could be a significant concern and requires further investigation.
- To improve the tractability of an analysis of this type, a truncated set of inversion algorithms is studied. The algorithms studied are the empirical line method (ELM) and the fast line-of-sight atmospheric analysis of spectral hypercubes algorithm (FLAASH), and are taken to be representative members of a family of inversion algorithms. This assumption allows results from similar algorithms (like ATREM) to be used without a loss in validity in the conclusions made.
- The model-based inversion algorithms are treated as “black boxes” in that their inner workings are beyond the scope. Inputs, outputs, and reported error results are accepted at face value. A rigorous treatment of the internal mechanisms responsible for FLAASH’s results and errors would be an extremely interesting but ultimately off-topic direction for this investigation to take.

2.4 Success Criteria

To declare this research a success, two simple criteria must be met.

- With regards to uncertainty in retrieved reflectance, the antecedent sources of uncertainty in each atmospheric parameter or modeling output must be clearly traced, quantified, and ranked by relative magnitude, spectrally if necessary.
- An optimal strategy for using information about error source strength, if one exists, must be provided. In other words, an answer will be provided to the question, “Do I purchase a field reflectometer, a sun photometer, or a better instrument?”

Sub-objectives of results validation and a description of value-added to remote sensing activities are extremely important, but they support these two fundamental

criteria. It may also be the case that an optimal strategy does not exist, and if this is the case the optimal strategy of “don’t waste resources collecting ground truth because...” will be accepted. A bottom-line goal of 66% reduction in reflectance uncertainty is set. For an uncertainty of 3-5 reflectance units, the desired result is a reduction to 1-1.5 reflectance units or better.

Chapter 3

Background

Atmospheric inversion with the intent of obtaining ground reflectance spectra has long been a staple of multi- and hyperspectral image processing. The spectral content of remote sensing products allows the extension of lab spectrographic classification of materials to the world at large with the added value of high spatial coverage and access. What differs from lab spectroscopy, however, is the presence of the atmosphere; molecules in the atmosphere scatter, absorb, and emit radiation that obscure the true spectral signature of objects on the ground. During the past several decades many approaches have been devised to model, compensate for, predict, or circumvent the effect of the atmosphere on photons passing through it. The historical development of atmospheric compensation methods will provide the context in which this research is meaningful.

3.1 Radiative transfer model

The physics based model used to describe radiative transfer is detailed first. Each model accounts for the sources and processes operating on photons as they traverse the atmosphere. There are two major flavors in terms of terminology used, but each one, as well as the many variants, essentially models the same phenomena. The model used here is based on the one derived by Schott (1997), with the other common terminology convention originating with the FLAASH crowd (Berk et al., 2002). The model will be described briefly, primarily to provide a common terminology base as well as to highlight differences from the literature required to accommodate the extended modeling framework introduced herein.

There is a great deal of detail that can go into a radiative transfer model, but limiting the scope of the effects the model attempts to encompass allows a formidable

task – the accounting for every photon to enter a sensor – to be reduced into a manageable one. Any time light interacts with matter, it can either be reflected, absorbed, or transmitted. Light that reflects off the ground back at an airborne or spaceborne sensor subsequently contains the material’s unique spectral signature (color), which in turn is the sole source of reflectance signature information for remote sensing applications. Because of its intended usage, the model is focused on target reflectance. Reflectance, also known as bidirectional reflectance, describes how light is scattered in a particular direction and is a function of the incoming radiation angle and the outgoing radiation angle in relation to some material reference angle. Reflectance factor, r , is a directionless and unit-less quantity that gives the ratio of radiation reflected in a direction to the amount of radiation that would be reflected by a Lambertian (perfectly diffuse) material illuminated in a similar fashion. Light reaching a sensor, then, contains both photons encoded with the reflectance information of interest and photons that do not contain this information. Separation of photons into target-reflected and non-target-reflected groups allows a conceptually simple universal radiance model as the starting point, equation 3.1. The terms are divided into these two categories and replaced with two coefficients: c_1 and c_2 .

$$L_{SR} = c_1 r + c_2 \quad (3.1)$$

Radiance terms will continue to appear with various subscripts; these will always be denoted by L . The sensor output is an integer number of digital counts, which will always be denoted by DC . All terms are implicitly spectral where appropriate, including irradiance, radiance, digital counts, reflectance, and transmittance. Recasting the expression in terms of sensor output, and assuming a linear relationship between incident radiance and output digital counts gives a fundamentally identical expression, although the coefficients have been marked with primes to indicate a difference with those in equation 3.1 (the application of the linear radiance-to-counts calibration). This expression is equation 3.2.

$$DC = c'_1 r + c'_2 \quad (3.2)$$

The simplified coefficients will now be expanded to reflect the physics-based model commonly developed elsewhere (Schott, 1997). The basic radiative transfer expression, in which sensor reaching radiance L_{SR} is described in terms of the applicable atmospheric, geometrical, and material parameters involved, is given as equation 3.3:

$$L_{SR} = \left(\frac{E_s}{\pi} \cos \sigma_{s'} \tau_1 + L_d \right) \tau_2 r + L_u \quad (3.3)$$

For the sake of future reference, these terms are easily rearranged in equation 3.4 to isolate reflectance.

$$r = \frac{L_{SR} - L_u}{\left(\frac{E_s}{\pi} \cos \sigma_{s'} \tau_1 + L_d \right) \tau_2} \quad (3.4)$$

Electromagnetic radiation from the sun is expressed as exoatmospheric solar irradiance, a measure of the power of incident photons per unit area. It is assumed to be constant leaving the sun and varies seasonally due to changes in the earth-sun distance. This term is denoted as E_s . The water vapor, well-mixed gases, and suspended particles in the atmosphere scatter and absorb the light as it travels from the top of the atmosphere to the ground. The ratio of light that makes it to the ground without interacting with atmospheric molecules to the total light incident on the atmosphere is known as the atmospheric transmittance of the downward path or solar path transmissivity. It will be denoted as τ_1 . Just as light passing through the atmosphere can be scattered out of the downward path, light is also scattered from all points in the atmospheric dome down to the ground. This irradiance is known as sky light or downwelled irradiance and is reflected off the ground according to its surface properties. If the reflector is perfectly diffuse, the irradiance is converted to radiance by dividing by π .

There are other sources of radiation illuminating the ground. Two major sources are background objects and clouds. These can be thought of as fixed in the sky dome in unknown locations and proportions and either reduce or increase the amount of radiance depending on their specific albedos. Either type of object can be brighter, darker, or a different color relative to the sky radiance it supplants. A final source is self-emitted thermal photons, which are negligible in the visible part of the spectrum. In aggregate, radiance coming from the sky, clouds, and background objects are known as downwelled radiance, L_d .

Another factor that affects how the radiation is reflected is the relative orientation of the surface to the earth's local horizontal plane. Due to projected area effects, the zenith angle to the sun will reduce the amount of direct solar irradiance hitting the ground; the angle $\sigma_{s'}$ is the zenith angle corrected for any deviation between the target's normal plane and the earth's local horizontal plane.

Light on its way from the ground to the sensor encounters the same scattering and absorption effects that it did on the way down. The ratio of light passing through the atmosphere to total light leaving the ground is denoted as τ_2 and is

a transmittance factor just like τ_1 , except it is for the ground-to-sensor path. The final term in the equation, L_u , is known as upwelled radiance and accounts for the addition of light that was never reflected off the target ground spot.

The upwelled and downwelled radiance terms will be expanded into constituents. In strict usage, upwelled radiance technically refers to photons scattered in the atmosphere up towards the sensor. It was forced to collect all categories of light that enter the sensor's field of view without first reflecting off the target (instead reflecting off non-target ground objects one or more times and scattered into the sensor's field of view) because it is sometimes convenient to collect these two terms into a single variable as was originally done in equation 3.3 so as to resemble equation 3.1. All photons covered by the term are functionally identical: they do not contain the target spectral signature. However, from a modeling standpoint it is necessary to account for the various types of photons separately. A second term, L_{adj} , is added to account for these adjacent non-target ground object photons and the original term, L_u , is recast into its strict definition.

Likewise, the downwelled radiance term is a collection of several very important terms. Functionally the sub-terms all share the character of indirect solar radiation that has reflected off the target into the sensor's view. However, there are three diverse sources contributing to this. The first is the strictly downwelled solar radiance, which is scattered by the atmosphere directly onto the target. The second is radiance reflected off of terrestrial background objects, and third is radiance coming from clouds. These three sources of radiance are shown in figure 3.1.

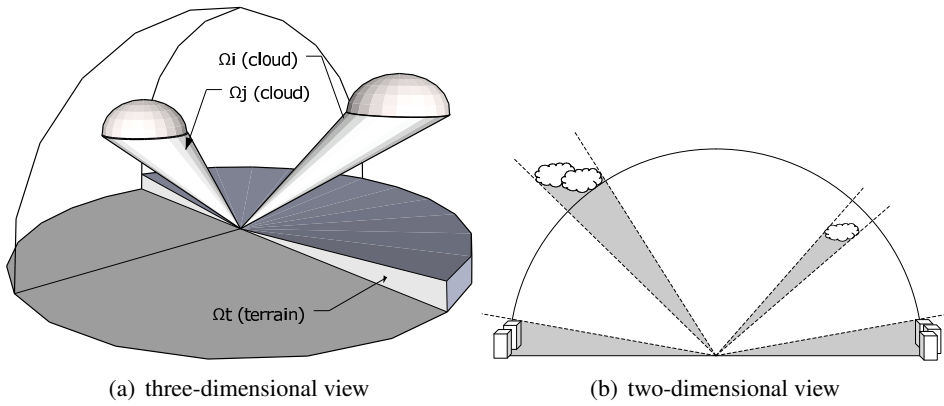


Figure 3.1: Indirect radiance sources

In figure 3.1, background radiance geometry is modeled as a terrain mask an-

gle, which is a compromise between the rigorous modeling of terrain features advocated elsewhere and the traditional custom of ignoring background radiance completely. Everything below the mask angle is assumed to be background radiance and everything above it is sky and cloud. Background radiance and cloud radiance are equally volatile sources: it is not possible to mathematically predict their effects because their antecedent sources – human activity, weather patterns, terrain, and vegetation – are unpredictable without prior knowledge of the area and/or time history. Rigorously modeling both the terrain features and their contributions to the radiance incident on a target is a task for physics-based scene generation algorithms. The use of such algorithms may well be necessary for the accurate computation of the background radiance, but for the purposes of this investigation it is not absolutely required.

In a slight departure from other treatments, diffuse radiance is modeled with a three-part mixing model and two sky fraction coefficients rather than a two-part mixing model and a single sky fraction coefficient. The fraction F_1 is used to represent all clear sky unobstructed by clouds or background objects or terrain. The other coefficient, F_2 , accounts for all sky not masked by background objects or terrain. The difference between F_1 and F_2 represents the portion of the sky occupied by clouds. Both terms are depicted visually in figure 3.2. These additions result in a slightly longer form of equation 3.3, which has been rewritten as equation 3.5. This is the form that will be analyzed using the error propagation techniques to be outlined in chapter 4.

$$\begin{aligned} L_{SR} &= \frac{E_s}{\pi} \cos \sigma_s' \tau_1 \tau_2 r \\ &+ (F_2 (F_1 L_d + (1 - F_1) L_{cld}) + (1 - F_2) L_{bkg}) \tau_2 r \\ &+ L_u + L_{adj} \end{aligned} \quad (3.5)$$

3.2 Inversion algorithm descriptions

Several handfuls of methods exist to invert equation 3.5 and isolate the reflectance term. The main difficulty is obtaining accurate values for each of the component terms, although a subset of the problem is to just separate the terms with a multiplicative relationship to reflectance from those with an additive relationship.

With respect to multi- or hyperspectral imagery in the visible spectral region, inversion algorithms can be divided into several roughly-defined groups. One family of algorithms aggregates equation terms into multiplicative or additive factors in

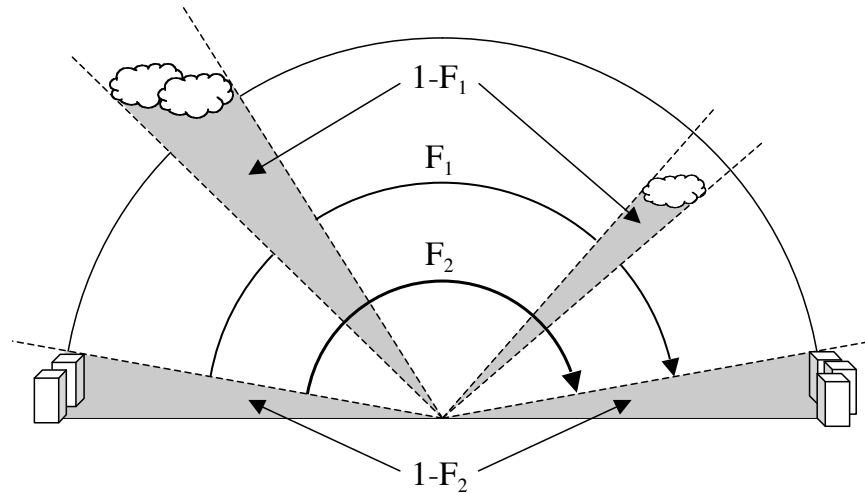


Figure 3.2: Sky fraction naming convention

order to isolate reflectance. There are several diverse strategies for estimating one or both of these factors without needing to determine each component term, but these algorithms are united in their disinterest in the individual terms of equation 3.5. As the empirical line method is today the flagship algorithm for this group, and because observation, measurement, or experience enable their underlying assumptions, perhaps it would be appropriate to refer to these as empirical algorithms.

The other family of algorithms, in contrast, uses atmospheric modeling with the admirable yet difficult goal of approximating the absolute value of each of the component terms of the radiative transfer equation 3.5. A physics-based model is seeded with the appropriate conditions, and by simulating atmospheric scattering and absorption effects, the algorithm estimates, via a pre-built lookup table, the correct mix of atmospheric constituents using various cues available in the pixel spectra. The radiative transfer components are then determined by the software, isolating pixel reflectance spectra as the algorithm output. These model-based algorithms use computer code that simulates the atmosphere's scattering and absorption through numerical integration of the applicable governing equations. Two such atmospheric modeling programs are MODTRAN (Berk et al., 1989) and 6S (the Second Simulation of the Satellite Signal in the Solar Spectrum) (Vermote et al., May 1997). MODTRAN 4 (Berk et al., 1999) was used in this work.

The primary benefit of the modeling approach is that it can be done using solely in-scene spectral radiance data with no external ground truth information. An-

other significant benefit is the possibility of an individual solution for each pixel as opposed to a single scene-wide transformation whose validity is known only at the point in the scene at which ground truth was taken and is in question everywhere else. Drawbacks to model-based algorithms are their complexity and reliance on assumptions inherent both in the algorithm and the simulation software. This makes their results sensitive to inaccuracies in underlying models or failure to account for differences between real-world conditions and those assumed. Because these differences are rarely catastrophic, model-based algorithms tend to produce acceptable output, although there are regimes in which model-based algorithms are thought to be weak (for example, humid environments), as well as instances of when various models fail to agree with each other. After reviewing the basic methods, a quick survey of results will attempt to bound the performance of these algorithms, to include the anomalies mentioned.

3.2.1 Empirical algorithm: the Empirical Line Method

The empirical line method (ELM) is one of the simplest and most time-worn atmospheric inversion algorithm in the imaging scientist's toolbox. Its persistence is an indicator of its usefulness, which is due to the fact that it takes advantage of uncalibrated radiance, requires a minimum of external information, is mathematically simple, and generally produces decent results.

Smith and Milton (1999) provide a brief overview of the method in the context of their larger discussion of calibration target selection. The atmosphere is assumed to be a linear operator with respect to ground-leaving radiance, following the form in equation 3.2. Although equation 3.3 shows there is much complexity in predicting the equations constants from a bottom-up approach, the empirical line method by-passes it, instead focusing on the single reflectance term. If two or more radiance spectra are collected on known-reflectance targets, a linear plot similar to that shown in figure 3.3 can be constructed. Ostensibly, one is done at this point, having determined the slope and intercept, which are equivalent to the terms c'_1 and c'_2 from equation 3.2. Any digital count in the image can be converted to reflectance simply applying c'_1 and c'_2 to equation 3.6.

$$r = \frac{DC - c'_2}{c'_1} \quad (3.6)$$

The need to apply prudent precautions when using this method in the field is often mentioned. The primary consideration is the error in ground truth reflectance measurements can create significant error. To mitigate the sensitivity of the results

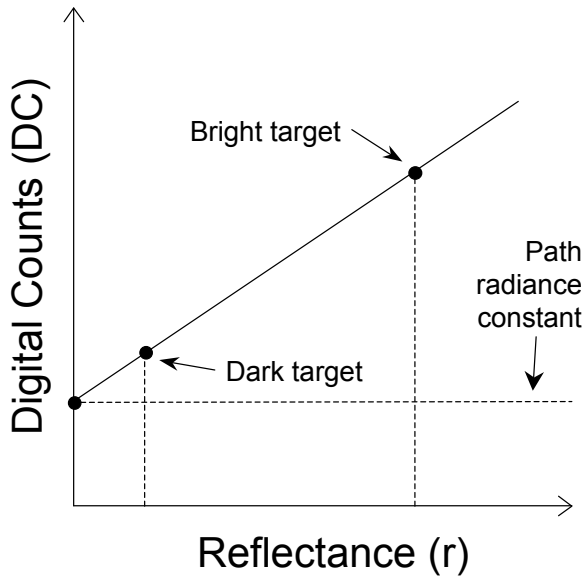


Figure 3.3: The linear relationship of the empirical line method

to measurement error, the reflectance targets used to calibrate the model must encompass the widest possible dynamic range. Second, a high number of reflectance targets is preferable so that a linear regression solution may be used to reduce the overall impact of sensor noise. Smith and Milton (1999) and Karpouzli and Malthus (2003) both take these steps, with the former demonstrating the disastrous effects of using reflectance targets closely grouped in brightness. A notional illustration of this effect is shown in figure 3.4, in which ground measurement error is added as horizontal bars. The boundaries indicate the limit of erroneous reflectance retrievals based on the ground truth error. When the targets are closer together, the larger error region shows the potential extrapolation error grows considerably.

The benefits of using multiple calibration targets are shown in figure 3.5. The least-squares solution drives down error to its minimum point, after which further improvement is possible only by adding much more data or by reducing error in the ground truth measurement. Besides target spread and use of many targets, two other major considerations are frequently discussed. First is atmospheric variability across the image. This is important because the model constants reflect actual atmospheric conditions, and they are only valid if the atmosphere they describe actually exists in the line of sight to each pixel. Most literature claims the small

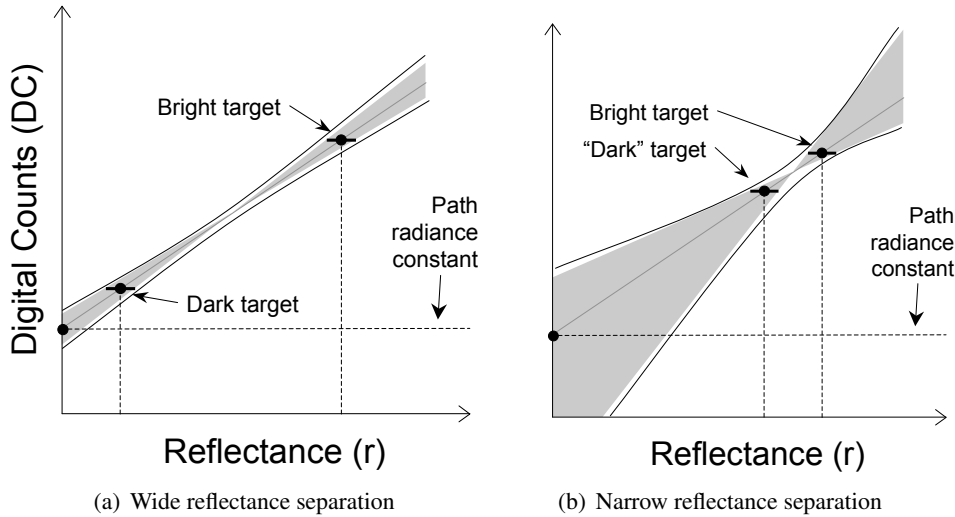
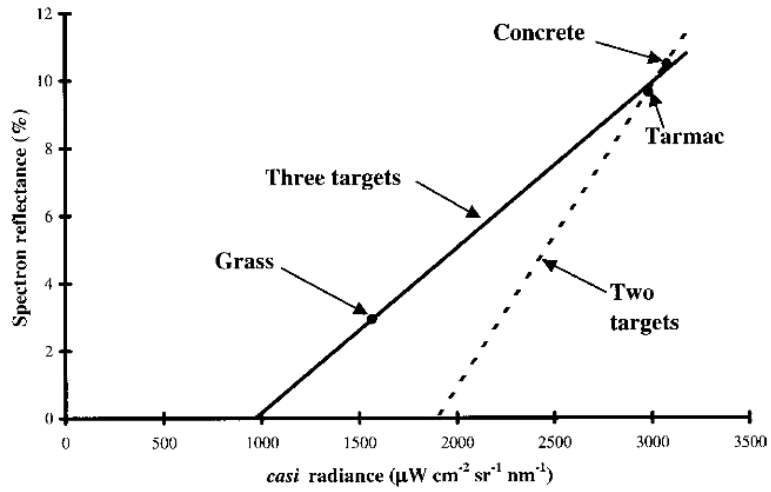


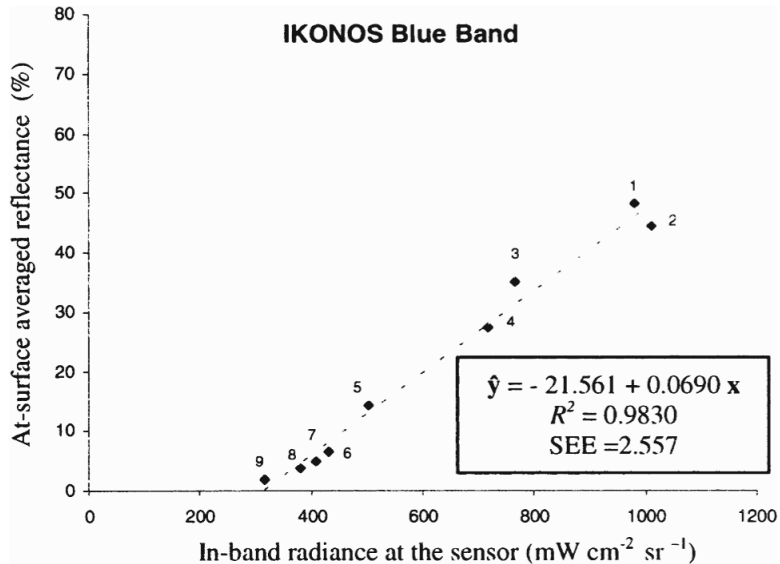
Figure 3.4: ELM error exacerbated by poor cal target selection

image swath justifies ignoring this problem as a source of error, but this intuitive judgment is not supported with data. The second consideration is related to the first. Whereas spatial atmospheric variation is beyond control (and usually beyond measurement), temporal variation is carefully avoided. Cloud cover and its effect on illumination is the primary cause of temporal variation in atmospheric conditions. Again, a qualitative judgment is usually the technique employed to ignore the impact of this effect. The problem is that even when clouds are not visible to the human eye, illumination is changing in ways perceptible by the ground truth instrument, over time periods as low as 30-60 seconds (Smith, 2004). It is important to understand these sources of error in the empirical line method because the method is so commonly used and is considered reliable in a wide variety of situations.

Companion algorithms to the empirical line method employ similar approaches without requiring supplemental ground truth measurements. Different techniques exist to determine one or both of the required coefficients for performing the linear inversion method described above.



(a) CASI ELM results (Smith and Milton, 1999)



(b) IKONOS ELM results (Karpouzli and Malthus, 2003)

Figure 3.5: ELM results improved by linear regression from multiple targets

3.2.2 Model-based algorithm: Green's method

Robert Green described a method of estimating atmospheric parameters from in-scene spectra to aid in the processing of AVIRIS data. AVIRIS is the Airborne Visible/Infrared Imaging Spectrometer, a hyperspectral VNIR instrument built by NASA (Vane, 1987). Aerosol optical depth, atmospheric water vapor, and surface pressure were the parameters selected to fully account for the scattering and absorbing species in the space between source, target, and sensor. This parameter selection is seminal with respect to derivative algorithms as well as the modeling presented in this work, which have adopted them as the standard variables for spanning the atmospheric variability space (Green et al., 1993). Variations on these parameters are possible, for example, using horizontal visibility as a proxy parameter for optical depth or molecular number density instead of a scale height. Green's parameters possess advantages for the modeling process described in this work, so they will be used here, albeit with a minor modification described later on.

Under some conditions, aerosol optical depth can be a primary driver for the amount of backscattered radiance reaching the sensor, dominant over other constituents in the visible blue-green region. Optical depth refers to an extinction exponent that models transmission decay of light through a non-vacuum medium. In equation 3.7, the optical depth δ_α is shown to be related to an absorption coefficient β_α and the distance into the medium over which absorption takes place, x . A process described as non-linear least square spectral fitting (NLLSSF) was iteratively used to determine what optical depth setting at 500 nm produces the closest match with the observed AVIRIS spectra over the visible region between 400-600 nm. The use of a pre-generated lookup table allows the algorithm to efficiently search through a series of optical depths until the best parameter fit is obtained. The fit method was found to achieve results comparable with other methods, such as the Regression Intersection Method for Aerosol Correction (Crippen, 1986; Webber et al., 2001).

Spatial variability in the parameters was a key finding of Green's initial results with this method. Aerosol optical depth was found to vary up to 200% from one edge of an 11 km × 10 km AVIRIS scene to the other.

$$\tau = e^{-\beta_\alpha x} = e^{-\delta_\alpha} \quad (3.7)$$

Green used an oxygen absorption feature at 760 nm to estimate the amount of gas in the air column. The gases are said to be well-mixed, meaning their ratios are treated as globally uniform. Therefore, the quantities of all other gases can be determined from any single one, and by using a NLLSSF procedure similar to

the one used for aerosols, an optimal value for surface pressure height can be determined. Surface pressure height correlates to well-mixed gas because the model atmosphere used in MODTRAN follows a standard profile in which the aggregate gas column decreases with increasing altitude. This effect is shown for sample MODTRAN spectra in figure 3.6.

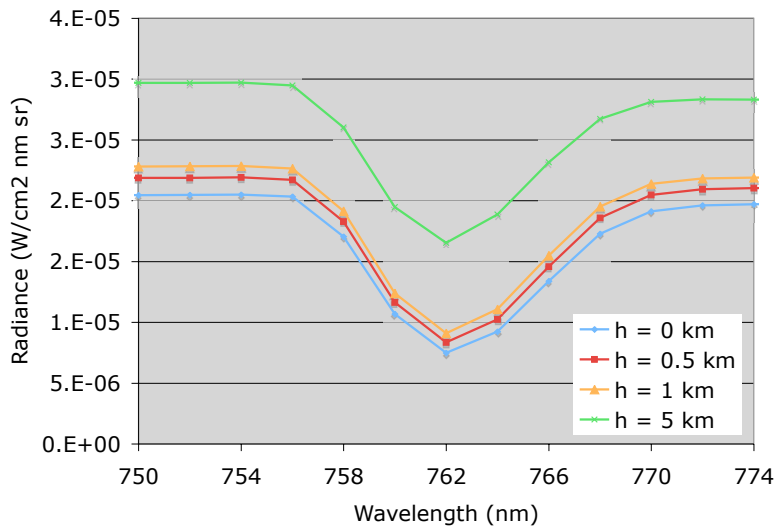


Figure 3.6: 760 nm oxygen feature variation with sensor altitude

The ratios of feature shoulder to feature bottom are 0.37, 0.38, 0.40, and 0.56 for altitudes of 0, 0.5, 1, and 5 km respectively. It was found that this method produced values more or less matching the terrain features of the image used, though it is not known on how fine a scale this was true or if differences were observed, which would suggest a non-standard day during the collection of the reference image.

Water vapor is acknowledged as having one of the strongest effects on reflectance spectra. The effects are confined to the numerous absorption bands, but the bands widen as gaseous water vapor increases to the point where there are few regions not affected in some way. To determine column water vapor, Green uses another band retrieval method, this time at 940 nm. Figure 3.7 shows how the spectral feature varies with increasing water vapor content in the absorption column. Water content on the ground, specifically in green vegetation, can distort the retrieval results in the 940 nm feature, so Green adds a requirement to compensate for that additional absorption using a sample leaf reflectance spectrum when

calculating the ratio. Later studies also found that surface water greatly distorts water vapor retrieval (Felde et al., 2004). It is noted that water vapor was observed to have varied as much as 20% across scenes, although results certainly exist that exceed that amount by an order of magnitude or more.

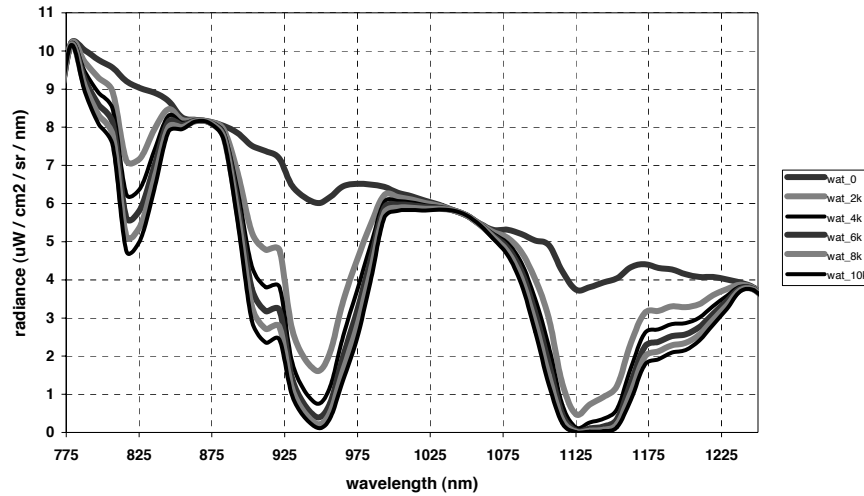


Figure 3.7: Water vapor absorption features by total column amount. Figure taken from Felde et al. (2004). Legend indicates water vapor content in $\times 1000 \text{ atm-cm}$. 1 atm-cm is equivalent to approximately $8.04 \times 10^4 \text{ gm/cm}^2$.

Green's final inversion equations, shown below as equations 3.8 and 3.9 (Green et al., 1993), are basically identical to equations 3.3 and 3.4. L_t is the total radiance, ρ is the target spectral reflectance, F is the exoatmospheric solar irradiance, T_{du} is the combined down/up transmission, and L_p is the path radiance. These terms are all directly available from a MODTRAN run properly configured with the retrieved atmospheric parameters.

$$L_t = (F * T_{du} * \rho) / \pi + L_p \quad (3.8)$$

$$\rho = (L_t - L_p) / (F / \pi * T_{du}) \quad (3.9)$$

Green mentions some important areas for further investigation, namely sensor calibration, field measurements, temporal effects, and choice of aerosol model – presumably to account for the shape of the scattering spectrum as described by the

angstrom exponent and the phase function/particle size distribution. Since then, the general method has undergone countless refinements and examinations for its effectiveness in various regimes, looking at different types of sensors, humidity, and implementations, to name a few. This method is described because it most closely matches the modeling technique used in this investigation. Other inversion methods have been developed in parallel, such as Gao and Goetz' ATREM (Gao et al., 1993), Carrere and Conel's CIBR technique for obtaining constituents from in-scene band ratios (Carrere and Conel, 1993), and several others that are variations on the same general idea. The algorithm has been improved in several ways, for example adding other absorption features in the case of ATREM and its successor HATCH (Qu et al., 2003) and the modeling of adjacency as is the case with FLAASH (Berk et al., 2002). FLAASH will be examined in a bit more detail because it is designed to be more of an operational implementation of the basic inversion algorithm.

3.2.3 Model-based algorithm: Fast Line-of-Sight Atmospheric Analysis of Spectral Hypercubes (FLAASH)

Fast Line-of-Sight Atmospheric Analysis of Spectral Hypercubes (Berk et al., 2002) is one of a handful of algorithms and variants available to perform model-based inversion. It was developed by AFRL and Spectral Sciences Inc. specifically to take advantage of the MODTRAN4 radiative transfer code. The approach used in the algorithm builds on methods described by Gao and Goetz (1990a), Green et al. (1993), and several others. The governing equation is reproduced here as equation 3.10 (Cooley et al., 2002). It follows the general form of equation 3.1, in which radiance is assumed to be linearly related to reflectance, but the specific form was derived from the physical theory underlying the 6S code (Vermote et al., 1994), in particular the method by which multiple scattering events are modeled.

$$L^* = \frac{A\rho}{1 - \rho_e S} + \frac{B\rho_e}{1 - \rho_e S} + L_a^* \quad (3.10)$$

In equation 3.10, L^* is again used to denote radiance. The terms ρ and ρ_e are, respectively, the spectral reflectance of the pixel in question and an averaged spectral reflectance of the area immediately surrounding the pixel in question. S is the spherical albedo of the atmosphere, effectively treating the dome as a reflector for the purpose of calculating multiple scattering. L_a^* is upwelled path radiance, and coefficients A and B represent multiplicative terms seen in equation 3.3 obtained from MODTRAN4. It is noted that the entire "B" side of the equation accounts for photons directly locally adjacent to the target pixel scattered into the sensor's

field of view, whereas the effects of multiple scattering in the denominator of both sides manifest over a larger general area. Thus, the ρ_e terms in the numerator and denominator are technically different terms, although in practice the difference is small.

FLAASH is fed the same basic metadata that Green's method would need: collection geometry, time, location, and sensor band model (FLAASH has built-in support for AVIRIS and HYDICE, the Hyperspectral Digital Imagery Collection Experiment (Mitchell, 1995)). The code first prepares a lookup table (LUT) by varying water vapor over a range of values. As with the previous algorithm, the band ratio between the shoulder of an absorption feature and the bottom of the feature is used to index the water vapor amount. FLAASH also accounts for changes to the absolute radiance value of the feature.

Once the water vapor lookup table is available, FLAASH can then use the associated MODTRAN outputs A , B , L_a^* , and S to construct radiance results for every reflectance unit between 0 and 100 (or between 0.0 and 1.0 in 0.01 increments). This new LUT is re-gridded so that the algorithm can index it according to water vapor band ratio and radiance, and a water vapor column value is retrieved.

The baseline FLAASH algorithm retrieves aerosols using a general scene-wide estimate based on empirical work by the MODIS team (Kaufman et al., 1997). The ratio between the $0.66 \mu\text{m}$ and $2.1 \mu\text{m}$ bands is expected to be constant over dark vegetation. This observation can be exploited to back out spectral differences between the two bands caused by aerosols, which largely affect visible bands. Surface pressure altitude is also retrieved.

The adjacency correction is implemented by performing spatial convolution with a decaying exponential kernel over the scene. The correction is required both for the final reflectance calculation as well as the aerosol retrieval. MODTRAN selects the size of the kernel by accounting for factors such as sensing altitude and presumed settings for aerosol scale height and phase function.

A cloud mask is required. Cloud determination relies on an algorithms developed by the MODIS group and others, which detects both opaque clouds and partially transparent cirrus clouds. Opaque clouds must be excluded from the spatially averaged reflectance convolution operation as well as the reflectance inversion. Pixels under the cloud mask are replaced with average scene radiance.

FLAASH performs a very straightforward implementation of the generalized model-based algorithm. Input parameters are determined in a computationally efficient manner, and the MODTRAN outputs are used to solve equation 3.10.

For the remainder of this investigation, FLAASH is essentially treated as a black box. Parameter determination is not explicitly studied. However, parame-

ter determination is used as a virtual injection point – one can imagine stopping FLAASH once it has determined the water vapor column, for example, and swapping that value with a measured value. That measurement may be better or worse, but the point is that the relative effects can be studied. It is not currently possible to literally swap out FLAASH’s decisions with different values midstream, but this thought experiment style of approach enables the evaluation of the value of ground truth sensor networks in a standardized environment. In instances when FLAASH cannot be performed, such as with sensors lacking the requisite bands, it might even be possible to evaluate the trade between adding a network of ground sensors or adding bands to the remote sensing instrument.

Chapter 4

Approach and Theory

4.1 Introduction

During the course of introducing a radiometric inversion bias correction technique at the seventh JPL Airborne Earth Science Workshop in 1998, Dr. Joseph Boardman of AIG provided the perfect framing and motivation for the problem at hand. The AVIRIS instrument was designed to be a highly precise instrument, subject to continuous improvement over time, but it could not by itself rise above the limitations of the rest of the imaging chain of which it was a part. This became apparent when inversion results did not improve along with improvements to AVIRIS' calibration accuracy, noise sources, and stability, pointing to an obvious root cause:

The reason for this is the limited accuracy of the combined chain of absolute standards, calibrations, models and measurements that connect the high precision raw DN to the final output of relatively low accuracy apparent surface reflectance. Sources of error including: errors in the NIST standard bulbs; spectral and radiometric calibration uncertainty; in-flight system changes; solar irradiance model errors, inaccuracy in atmospheric parameter estimation; and radiative transfer code errors combine to limit the accuracy of the final apparent reflectance data to no better than several percent (Boardman, 1998).

“Boardman’s lament” concludes in apparent vexation:

Filtered by this relatively inaccurate signal processing chain, the very high precision (1 part in thousands) of the new AVIRIS data is under-utilized. It is like a very high quality rifle in the hands of a near-sighted marksman, lots of precision but limited accuracy (Boardman, 1998).

The basic concern of one who attempts to retrieve a reflectance spectrum is this: “How close to truth is my solution and why?” As countless parameters interact in obtaining any radiometric inversion, uncertainty is generated, accumulates, and multiplies. Understanding the “why” part of the question requires that the error in the final result be picked apart and traced back to its sources. Understanding the behavior of error in the system involves thorough knowledge of the system itself and how uncertainty in the various parts of the chain interact to produce an error-laden result.

This chapter develops a method for accounting for the primary sources of error in an imaging chain, provides baseline models for each source, and shows how errors can be propagated through a non-linear system into a common framework, namely reflectance units. The propagation of statistical error provides a statistical result, the main value of which is to show the relative magnitudes and sensitivities of each source. The following approach is developed and proposed to answer the question, “How can error in retrieved reflectance be most effectively reduced, and how much reduction can be achieved?”

4.2 Imaging operators

Imaging is the act by which the three-dimensional physical world is somehow recorded in a spatially-indexed array of data. In the context of this research, photons originate from a source, propagate through space, are operated on by the physical world, and cause a measurable effect in a detector instrument, namely the creation of an electric charge. The electric charge is then operated on further by the instrument until it is stored as digital data. As the photon is operated on in a predictable, physics-based manner, the real world is given a representation as an image.

The act of imaging, therefore, is a transformation operation, such as that shown in general form in equation 4.1. The function g is the spectral vector for each spatial point x', y' in the image. The function f depends on the three-dimensional spatial position of an object, its spectral properties, how it changes over time, and a host of other physical qualities of the object being imaged. The operator, \mathcal{O} , is comprised of several sub-operations: photon propagation, reflection, scattering, absorption, transduction to an electrical charge, operation on the charge, and quantization. This chain of operators is depicted conceptually in figure 4.1.

$$g(x', y') = \mathcal{O} \{ f(x, y, z, \lambda, t, \dots) \} \quad (4.1)$$

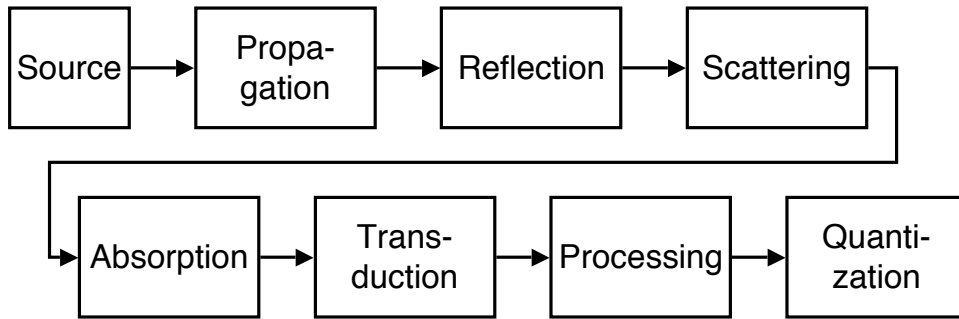


Figure 4.1: Imaging operator block diagram

This research is concerned with operator inversion. Remote sensing applications act within either the target (i.e. real-world) domain or the image domain (and some can act in both). Even reflectance-type applications such as band ratio products, scene equalization, and phenomenology regression can use an image-space representation. However, determining a physical quantity such as the absolute magnitude of an object's reflectance factor, which most closely corresponds to the notional function f in equation 4.1, necessarily involves working exclusively in target space. The conceptual relationship between the two spaces is depicted in figure 4.2. It will be necessary to fully understand both the transformation operations (forward direction) and inversion operations (reverse direction) to characterize the uncertainty present in each step.

4.3 Forward uncertainty model description

Imaging with the intention of obtaining a spectral radiance signature for the objects in the scene is a bi-directional process. The forward direction tracks the propagation of solar and self-emitted thermal photons as they are scattered, absorbed, or transmitted through the atmosphere, reflect off the target and various non-target objects, travel through the atmosphere again, and enter the sensor. Once inside the sensor, these photons interact with the instrument's optical and dispersion elements and are ultimately absorbed by a photoactive material. The resulting electrical signal is processed, quantized, and converted to an integer number stored digitally in a computer. The forward direction also typically includes a button-hook in which the final sensor product is commonly converted to sensor-reaching radiance through the sensor-calibration process. The button-hook metaphor highlights reverse travel

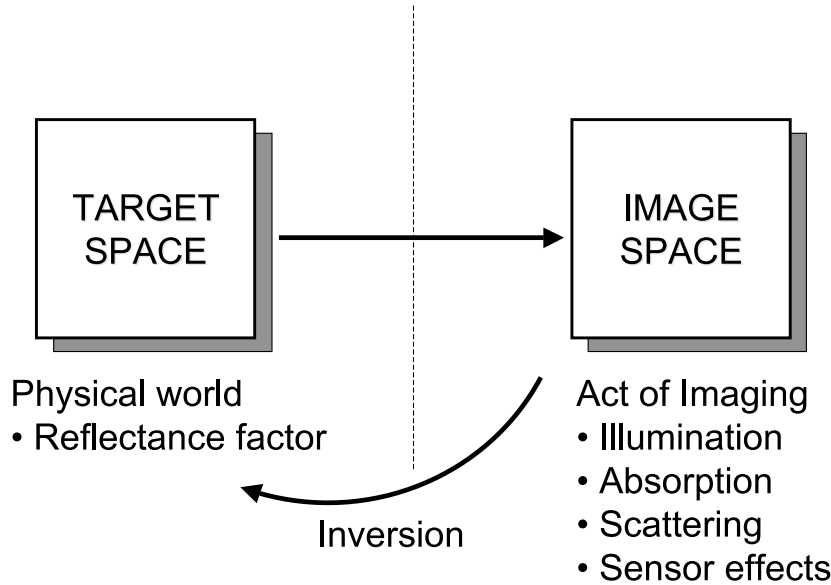


Figure 4.2: Target/image space model

along the chain back through the sensor to the physical quantity, usually a vital step in reflectance retrieval.

The mathematical model of radiation transfer is presented as a deterministic process that attempts to categorize and account for every photon, yet the ability of an observer to accurately predict and measure the actual events that occur at each point in the radiation chain is an elusive thing. The forward radiation chain can be abstracted into a series of processes: source photon arrival at earth, scattering, absorption, and reflection, depicted conceptually in figure 4.3, where each term in the figure corresponds to the terms in equation 3.3. Each process cannot be perfectly modeled due to varying degrees of inherent uncertainty. For the sun-earth transport, the instantaneous solar exitance is not fully known. For scattering and absorption, the exact quantity of scattering and absorbing species is not fully known. Neither are the exact orientation of the ground target, the material properties of tall background objects, etc. Some of these may be guessed at, and others may be modeled or measured very precisely, but ultimately each process has an inherent amount of uncertainty remaining after all ordinary methods to pin down these quantities have been exhausted.

In the forward uncertainty model, a three level uncertainty chain, shown in fig-

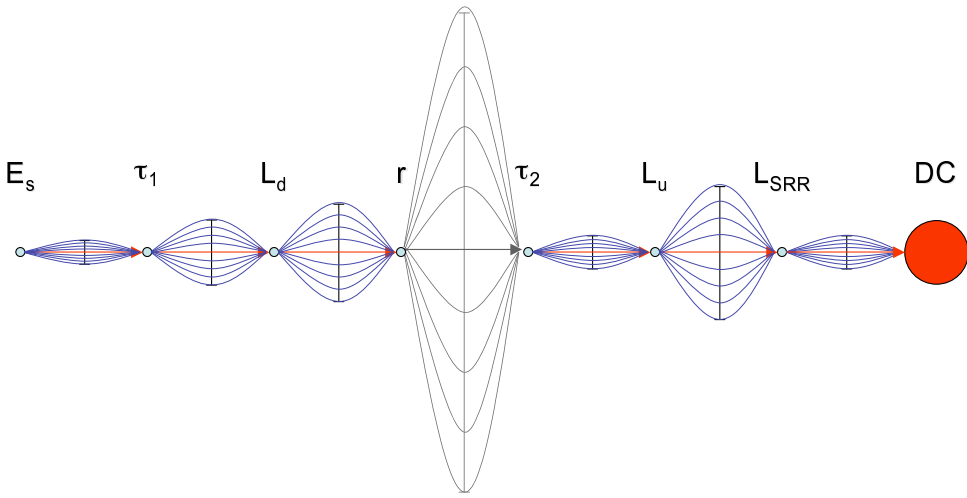


Figure 4.3: Forward uncertainty chain block diagram

ure 4.4, will be established. The first level is in the atmospheric and geometric parameters. These include water vapor profile, size and quantity of non-molecular particles (aerosols), type and quantity of well-mixed molecular gases, temperature profile, and pressure profile. Clouds are a special case of atmospheric parameter that will be treated very gingerly by this research. As highly absorbing and scattering bodies, clouds introduce magnitude discontinuities that make it difficult to use the statistical and spatial methods that will be presented. The first level also includes the geometric parameters that, along with the atmospheric parameters, make up the physical world in which radiation transfer and detection take place. The main geometric parameters of interest are the sky fraction and target orientation. The sky is masked by surrounding terrain, which means a fraction of the albedo assuming to be coming from the sky is actually reflected off of nearby objects such as trees and buildings. This additional reflection changes both the magnitude and spectral character of the light reflecting off the target. Together, clouds and background constitute a poorly-modeled perturbation to the traditional sky dome model. The target orientation is a geometric parameter that, when inadequately measured, modeled, or guessed at will also change the character of the reflected light, sometimes drastically so.

The second part of the uncertainty chain is the functional abstraction of the parameters, namely the terms in equation 4.18. As these terms are the product of the

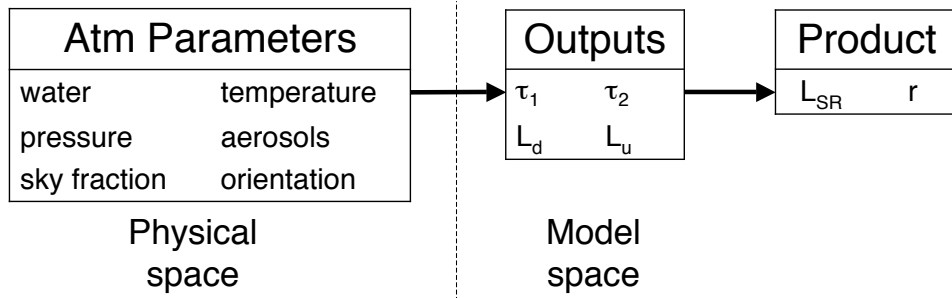


Figure 4.4: Three-level uncertainty chain block diagram

physical world acting on the source photons, they all have a physical dependence on the state of the atmospheric and geometric parameters. However, they can also be called model outputs since radiative transfer modeling attempts to provide the same terms. This abstraction level also includes the key geometric terms that are unrelated to measurement of the atmosphere. These include ground target tilt, look angle, sun zenith and azimuth angles, and sky fraction.

The final part of the forward chain is the final product, which is either sensor-reaching radiance or digital count value depending on the application. The final product's relationship with the model outputs is deterministically defined by the radiative transfer equation, so both the value and its error are relatively easy to calculate provided the intermediate stage of figure 4.4 is sufficiently well characterized. Consideration of digital counts instead of sensor-reaching radiance requires an error model for the sensor, while a chain that stops with sensor-reaching radiance is dependent on the physical world only, hence is portable to any sensor system. It is not implied here that the sensor can be ignored; indeed, the instrument can be a source of spectacular error and is treated separately.

4.4 Error propagation in analytical functions

4.4.1 Total error

Since the main objective of the research is to determine the relative effects of uncertainty reduction techniques in atmospheric inversion, it is necessary to mathematically describe the effects of random processes. A random process is an ensemble of signals or outcomes, the parameters of which are randomly selected and governed

by some probability distribution. A specific outcome produced when the random process is accessed is a realization of the process (Peebles, 2001). In this field of study, the atmospheric parameters can be modeled as random processes, as can random noise in each measurement.

In a statistically rigorous treatment, population statistics and sample statistics are never used interchangeably. Population statistics are estimated from sample statistics, and even measurement of an entire "population" cannot guarantee the reliability of descriptive statistics regarding the likelihood of a certain behavior or characteristic in a marginal addition to the population. One can use metrics such as sample size to gage this reliability, but there is no way to truly know how closely the measured statistics match the population statistics. Although special effort will not be spent on distinguishing population statistics from sample statistics, terminology traditionally used for sample standard deviation, S , will be used to indicate the standard deviation of a variable. It will be assumed that statistics calculated from the sample are believed to be sufficiently close to the population statistic for the purposes required by this investigation.

A generic function y of multiple variables, x_1 and x_2 , is shown in equation 4.2. The variable \hat{y} is an estimator of that function, which is expressed as the true value y plus a random error variable, ε , as shown in equation 4.3.

$$y = f(x_1, x_2) \quad (4.2)$$

$$\hat{y} = y + \varepsilon \quad (4.3)$$

Expressed in these terms, the purpose of this research is to determine the statistical properties of ε as applied to the imaging science application of reflectance retrieval in hyperspectral imagery. The properties of interest are the bias of \hat{y} , which corresponds to the expected value of ε , and the variability of \hat{y} , which will be indicated by assuming a normal distribution for ε and using its variance. Although it is not possible to fully describe a probability distribution with a single number – the shape and symmetry are unknown without further description – the variance or its square root, the standard deviation, is still the best way to describe the precision of a measurement (Barford, 1967). The estimator bias is developed according to equation 4.4 and expressed in equation 4.5. The variance of \hat{y} follows the traditional definition, as shown in equation 4.6. Because y is defined as the true value of $f(x)$, its expected value is always the value itself with a variance of zero. Therefore, the variability of the estimator \hat{y} is equal to the variability of the error term ε .

$$\begin{aligned}
E[\hat{y}] &= E[y + \varepsilon] \\
&= E[y] + E[\varepsilon] \\
&= y + E[\varepsilon]
\end{aligned} \tag{4.4}$$

$$bias(\hat{y}) = E[E[\varepsilon]] = E[E[\hat{y}] - y] \tag{4.5}$$

$$Var(\hat{y}) = E[\hat{y} - E[\hat{y}]]^2 = E[\varepsilon - E[\varepsilon]]^2 \tag{4.6}$$

The bias is defined as the expected value of ε . However, total error in ε is the true goal here. The random deviations in ε are centered on the mean value of ε , so they sum to zero unless the sign is removed by taking the absolute value or squaring the term. The expected value of the squared error is known as the mean squared error and is one of the most common methods for describing variability in a random variable. It is developed according to equation 4.7 (Montgomery and Runger, 1998).

$$\begin{aligned}
E[\varepsilon^2] &= E[\hat{y} - y]^2 \\
&= E[(\hat{y} - E[\hat{y}]) + (E[\hat{y}] - y)]^2 \\
&= E[(\hat{y} - E[\hat{y}])^2 + 2(\hat{y} - E[\hat{y}])(E[\hat{y}] - y) + (E[\hat{y}] - y)^2] \\
&= E[\hat{y} - E[\hat{y}]]^2 + 2(E[\hat{y}] - E[\hat{y}])(E[\hat{y}] - E[y]) + E[E[\hat{y}] - y]^2 \\
&= E[\hat{y} - E[\hat{y}]]^2 + 0 + E[E[\hat{y}] - y]^2 \\
&= Var(\hat{y}) + bias(\hat{y})^2
\end{aligned} \tag{4.7}$$

4.4.2 Random component

Given a group of measurements or data points, the sample variance of ε is computed in the traditional manner, as shown in equation 4.8. It would not be completely correct to equate S^2 to the expected value expression in equation 4.6, but this is how that expected value expression is estimated. From this point forward, S_y will indicate the random component of the error in a generic variable y .

$$S_y^2 = \frac{\sum_{i=1}^N (y_i - \bar{y})^2}{N - 1} \tag{4.8}$$

Beers (1957) describes a method of building upon equation 4.8 to derive a method of propagating random error in a function's component variables to random error in the function itself. The formulation starts with the same generic function of two variables from equation 4.2, shown in expanded form using a Taylor series in equation 4.9, which is then squared in equation 4.10. The Taylor series is truncated to the first order.

$$y_i - \bar{y} = (x_{1i} - \bar{x}_1) \frac{\partial y}{\partial x_1} + (x_{2i} - \bar{x}_2) \frac{\partial y}{\partial x_2} \quad (4.9)$$

$$\begin{aligned} (y_i - \bar{y})^2 &= (x_{1i} - \bar{x}_1)^2 \frac{\partial y}{\partial x_1}^2 + (x_{2i} - \bar{x}_2)^2 \frac{\partial y}{\partial x_2}^2 \\ &\quad + 2(x_{1i} - \bar{x}_1)(x_{2i} - \bar{x}_2) \frac{\partial y}{\partial x_1} \frac{\partial y}{\partial x_2} \end{aligned} \quad (4.10)$$

The equality of form between the left-hand side of equation 4.10 and the right-hand side numerator of equation 4.8 leads to the insertion of both sides of the former into the latter, producing equation 4.11. The definitions of sample variance and covariance are then used to simplify the expressions to produce equation 4.12.

$$S_y^2 = \sum_{i=1}^N \frac{(x_{1i} - \bar{x}_1)^2 \frac{\partial y}{\partial x_1}^2 + (x_{2i} - \bar{x}_2)^2 \frac{\partial y}{\partial x_2}^2 + 2(x_{1i} - \bar{x}_1)(x_{2i} - \bar{x}_2) \frac{\partial y}{\partial x_1} \frac{\partial y}{\partial x_2}}{N - 1} \quad (4.11)$$

$$S_y^2 = S_{x_1}^2 \frac{\partial y}{\partial x_1}^2 + S_{x_2}^2 \frac{\partial y}{\partial x_2}^2 + 2S_{x_1 x_2} \frac{\partial y}{\partial x_1} \frac{\partial y}{\partial x_2} \quad (4.12)$$

The term ρ_{ij} denotes the correlation coefficient for variables x_i and x_j . The expression for estimating the correlation coefficient for two such variables from a series of observations of each is given in equation 4.13. It allows one final substitution, yielding the common expression for error propagation using partial derivatives. There is more than one way to define error and more than one way to propagate it forward through a system, but this expression was chosen for its general versatility and widespread use. It does depend upon an assumption of linearity because of the truncated Taylor series, but since other parts of this investigation apply the same assumption of *local* linearity rather liberally, requiring it here does not in any way degrade the final result.

$$\rho_{(x_1 x_2)} = \frac{E[x_1 x_2]}{S_{x_1} S_{x_2}} = \frac{\sum_{i=1}^N (x_{1i} - \bar{x}_1)(x_{2i} - \bar{x}_2)}{(N - 1) S_{x_1} S_{x_2}} \quad (4.13)$$

The final form of the error propagation equation is presented in equation 4.14. The generic function y is now expanded to be a function of an arbitrary number of variables, x_1 through x_n . When there are more than two variables, all possible combinations of variables produce covariance terms that must be included.

$$\begin{aligned} S_y^2 &= \left(\frac{\partial y}{\partial x_1} S_{x_1} \right)^2 + \left(\frac{\partial y}{\partial x_2} S_{x_2} \right)^2 + \cdots + \left(\frac{\partial y}{\partial x_n} S_{x_n} \right)^2 \\ &+ \sum_{i \neq j} 2\rho_{ij} \frac{\partial y}{\partial x_i} \frac{\partial y}{\partial x_j} S_{x_i} S_{x_j} \end{aligned} \quad (4.14)$$

The expressions presented so far will be revisited to not only produce the specific forms of error propagation functions themselves, but they will also be required to support the construction of other deterministic functions using the random variables considered. Specifically, the expression for retrieved reflectance will be a deterministic function based on functions of random variables.

4.4.3 Bias component

The propagation of random error does not account for all types of possible error in a result. Bias or systematic error also affects final retrieval results. Normally, it is assumed that this type of error is driven as low as possible through the calibration process. In fact, no bias error is propagated across the uncertainty chain abstraction levels shown in figure 4.4. However, bias will be present in the final result due to geometric effects on imaging that are traditionally poorly treated or completely ignored.

Bias error starts with the same basic equation as random error, repeated as equation 4.15. However, instead of estimating the instantaneous derivative of this function, a finite distance will be traveled in x to produce a change in output in y . If x is incorrect due to a systematic error, then the difference in y is the systematic error in the output, as shown in equation 4.16.

$$y = f(x_1, x_2) \quad (4.15)$$

$$\hat{y} = f(x_1 + \Delta x_1, x_2 + \Delta x_2) \quad (4.16)$$

Unlike slope calculated for random error, which is only valid close to the center point, this bias difference only depends on the end points, as shown in equation

4.17. As long as the functional relationship is valid, the bias error is a valid calculation regardless of distance. Unlike random error, bias error is sign dependent, with each effect moving the cumulative bias in one direction or the other.

$$\Delta y_{bias} = \hat{y} - y \quad (4.17)$$

4.5 Governing equation

The vital question to be considered is how retrieved reflectance depends on its input parameters, and, more to the point, how sensitive the retrieved reflectance is to errors in each of these components. The basic expression of this concept is found in equation 4.18. Inverting the model in equation 3.5 produces a straightforward expression of the reflectance factor.

$$r = \frac{L_{SR} - L_u - L_{adj}}{\left(\frac{E_s}{\pi} \cos \sigma_s' \tau_1 + (F_2 (F_1 L_d + (1 - F_1) L_{cld}) + (1 - F_2) L_{bkg}) \right) \tau_2} \quad (4.18)$$

The whole activity of atmospheric compensation is discovery of each term to sufficiently high precision. Inversion algorithms always attempt to provide them using a variety of strategies. Two major classes of strategies that are considered here are ground truth-based methods (mainly the empirical line method) and model-based methods. The empirical line method (ELM) attempts to determine all of the parameters at once in a manner that does not allow explicit separation of individual terms. Model-based methods attempt to predict the state of the actual atmosphere at the time the image was taken and use a radiative transfer routine to numerically determine the outputs required for the inversion. Thus, inverted reflectance may also be considered a function of the physical atmospheric parameters, a concept expressed in equation 4.19, where H_2O represents column water vapor, AOD represents aerosol optical depth, alt represents the density altitude, and F represents the fraction of the sky hemisphere that is either clear or obscured by clouds or background objects.

$$r = f(L_d, L_u, \tau_1, \tau_2, \dots) = f(H_2O, alt, AOD, F_{SKY}, F_{CLOUD}, \dots) \quad (4.19)$$

Parameter selection follows those used by Green et al. (1993) with the exception of pressure elevation. Pressure elevation attempts to account for variation in the molecular number density in the air column above the target site. The amount

of well-mixed gas varies from the “standard day” profile when the air pressure differs from standard pressure. The use of density altitude allows for further variation in the air column, accounting for temperature effects. Density altitude is pressure altitude corrected for variations from standard temperature, which is at least as common as departures from standard pressure (Federal Aviation Administration, 2003). It was felt that accounting for both effects would allow for more accurate modeling and not leave unaddressed a significant source of atmospheric variability. It levied a requirement that pressure and temperature be collected together, which is generally the case anyway. In MODTRAN, the variation of elevation changes the air column using both the pressure and temperature settings, so density altitude is already the *de facto* parameter used in radiative transfer modeling.

The switch from one type of altitude to the other required only the modification of the equations used in the model code, whereas further parameter changes in the name of better model fidelity, namely inversion layer altitude, would have forced major architectural changes in the modeling process and are thought to not add much accuracy to the final results. As long as a single surface parameter accounts for the total quantity of molecules in the air column, as density altitude theoretically does, shifting masses of air vertically should not change the result in the limited cases studied herein. One could imagine the situation in which the positioning of a cloud layer in relation to the inversion altitude could affect illumination slightly, but that should be about the extent of the unmodeled error.

There are an infinite number of variables available for inclusion in equation 4.19, most of which pertain to the type, size, and number density of molecules photons may encounter as they traverse the atmosphere. The remainder pertain to sun-target-observer geometry.

The primary constituents responsible for atmospheric absorption are water vapor (H_2O), carbon dioxide (CO_2), ozone (O_3), nitrous oxide (N_2O), carbon monoxide (CO), methane (CH_4), and gaseous oxygen (O_2) (Gao et al., 1993), whose densities are generally very slowly time-variant and spatially invariant. As a result, these are referred to as *well-mixed* to indicate their homogeneity. In addition to these major contributors, there are trace quantities of various pollutants, including NH_3 , SO_2 , HNO_3 , and several chlorofluorocarbons (CFCs) whose densities are very low and generally not addressed. However, preliminary research showed radiative transport can be highly sensitive to these large molecules. Since pollutants are invariant neither temporally nor spatially, if error analysis ever reaches the point of predicting extreme accuracy, this might be a fertile future study area.

There are seasonal and long term trends in well-mixed gas concentration, but their day-to-day concentration is indexed to temperature and pressure, which jointly

determine the gaseous density of the atmosphere. In addition to molecular gases, there are two other important atmospheric constituents: water vapor and aerosols. Water vapor is technically also a molecular gas, but it is treated separately because of water vapor's unique role in global climatology. As part of the water cycle, water vapor is highly variable in location and concentration over a short period of time in a way not shared by the other gases. Aerosols are particles suspended in the atmosphere ranging in size from sub-micron to millimeter range. These have a variety of sources, including terrestrial dust, water vapor droplets from ocean foam and condensation, and industrial soot products. Aerosols are generated, migrate, and settle, usually over the course of days or weeks. As a result, they are also handled independently of other atmospheric constituents.

The radiative transfer model in MODTRAN handles the details of the function f and its inputs in equation 4.19. For the reasons stated above three parameters are singled out for particular treatment: water vapor content (H_2O), pressure-temperature scale altitude (alt), and aerosol optical depth (AOD). These determine the amount of scattering and absorbing species photons will encounter and hence the values for transmissivity and scattered radiance.

A word of explanation regarding the use of scale altitude is required. Scale altitude is an indirect parameter. It is a single value that indexes two separate parameters, pressure and temperature, to a single value. This is possible because pressure is generally well-behaved in its vertical regression as modified by the temperature. In aeronautical terms this can also be thought of as the density altitude, and this term more precisely describes the concept addressed here. Temperature and pressure together determine the integrated number density of the well-mixed gas molecules in the vertical atmospheric column. When low pressure and/or high temperature exist, the column density is lower such that the integrated number density of the well-mixed gas molecules equals the density of scattering species that would be observed had the ground been located at a higher or lower altitude on a standard atmospheric day. This will create the odd situation that pressure and temperature are measured directly as vertical profiles, which in turn can be fed into the modeling software as literal profiles but whose error models are determined by inputting scale altitude, and whose modeling output is expressed as a molecular number density or optical depth.

Each of these parameters is fed into the modeling code, yet each parameter itself has common antecedent sources: wind patterns and weather fronts. It might be desirable to trace the three parameters back to a common set of independent sources, but the systems are too complex to accurately predict behavior in the context of remote sensing model generation. The relationship is illustrated in figure

4.5. This bears mentioning because the three parameters will be treated as independent random variables although there is undoubtedly a degree of correlation between them. However, given the high complexity and low reliability of climate modeling at this point, the assumption of independence is kept, and a line is drawn here such that parametric characteristics of the antecedent sources are excluded as potential uncertainty-reduction measurement possibilities. The positive side effect is the atmospheric parameters that remain (equation 4.19) constitute the entirety of measurable quantities.

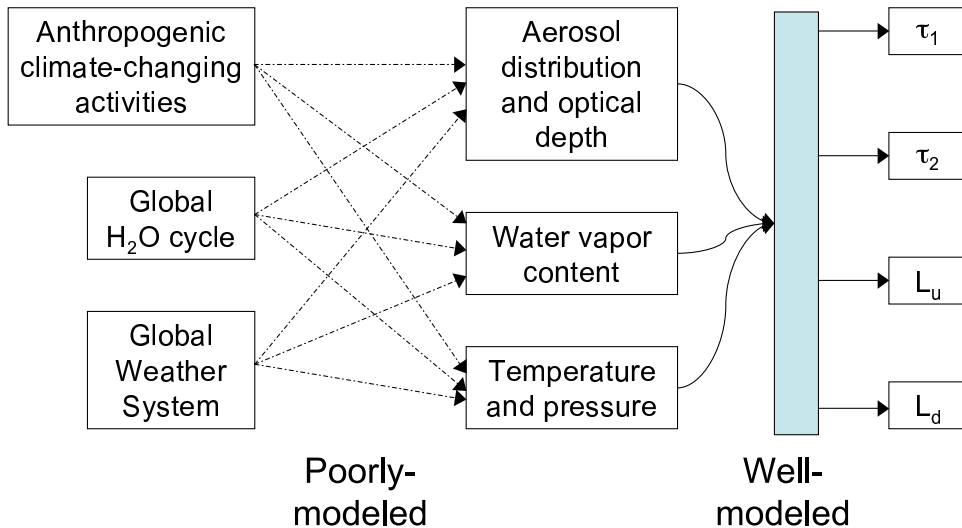


Figure 4.5: Breaks in the modeling chain dictate the choice of independent variables

4.6 Application of error propagation to the governing equations

4.6.1 Main equations

Regardless of how the inversion equation is written, each term contains a degree of inherent error that propagates to the final result. The result of applying the error propagation technique to general inversion equation 4.18 produces the main equations that will be treated by this investigation, included in detailed form for com-

pleteness in appendix A. Equation 4.20 shows the initial expression, and equation A.24 the expanded form. It is condensed slightly in equation A.26.

$$\begin{aligned}
 S_r^2 &= \left(\frac{\partial r}{\partial E_s} S_{E_s} \right)^2 + \left(\frac{\partial r}{\partial \sigma_{s'}} S_{\sigma_{s'}} \right)^2 + \left(\frac{\partial r}{\partial \tau_1} S_{\tau_1} \right)^2 \\
 &+ \left(\frac{\partial r}{\partial \tau_2} S_{\tau_2} \right)^2 + \left(\frac{\partial r}{\partial L_d} S_{L_d} \right)^2 + \left(\frac{\partial r}{\partial L_{cld}} S_{L_{cld}} \right)^2 \\
 &+ \left(\frac{\partial r}{\partial L_{bkg}} S_{L_{bkg}} \right)^2 + \left(\frac{\partial r}{\partial F_2} S_{F_2} \right)^2 + \left(\frac{\partial r}{\partial F_1} S_{F_1} \right)^2 \\
 &+ \left(\frac{\partial r}{\partial L_u} S_{L_u} \right)^2 + \left(\frac{\partial r}{\partial L_{adj}} S_{L_{adj}} \right)^2 + \left(\frac{\partial r}{\partial L_{SR}} S_{L_{SR}} \right)^2 \\
 &+ 2\rho_{(\tau_1, \tau_2)} S_{\tau_1} S_{\tau_2} \frac{\partial r}{\partial \tau_1} \frac{\partial r}{\partial \tau_2} + 2\rho_{(\tau_1, L_d)} S_{\tau_1} S_{L_d} \frac{\partial r}{\partial \tau_1} \frac{\partial r}{\partial L_d} \\
 &+ 2\rho_{(\tau_1, L_u)} S_{\tau_1} S_{L_u} \frac{\partial r}{\partial \tau_1} \frac{\partial r}{\partial L_u} + 2\rho_{(\tau_2, L_d)} S_{\tau_2} S_{L_d} \frac{\partial r}{\partial \tau_2} \frac{\partial r}{\partial L_d} \\
 &+ 2\rho_{(\tau_2, L_u)} S_{\tau_2} S_{L_u} \frac{\partial r}{\partial \tau_2} \frac{\partial r}{\partial L_u} + 2\rho_{(L_d, L_u)} S_{L_d} S_{L_u} \frac{\partial r}{\partial L_d} \frac{\partial r}{\partial L_u} \quad (4.20)
 \end{aligned}$$

4.6.2 Correlation coefficients

Since this is simply an application of the partial derivative method of error propagation and the 4 quantities L_d , L_u , τ_1 , and τ_2 are each functions of the same atmospheric and geometric parameters, the correlations between each pair of parameters must be considered. In this case, the relationship is technically a stochastic interaction between light and matter, but the modeled behavior is effectively a deterministic function (the exact shape of which is determined by the specific software implementation).

When functions of a single random variable are used in the creation of other deterministic functions, the correlation between these functions is unity: a random variable is always perfectly correlated with itself, irrespective of the specific functional forms in which the variable appears (increasing vs. decreasing, linear vs. parabolic vs. exponential, etc.). When two or more random variables are propagated, correlations are also propagated by using substitution. Thus, in order to properly model the known correlations between the radiometric parameters, it is necessary to start mathematically at an earlier point, with the atmospheric constituents, and derive the correlations by analysis.

Equation 4.21 illustrates this for three random variables, u , v , and w , and two functions of the random variables, $x(u, v, w)$ and $y(u, v, w)$. If the functions are linear combinations (a flat n-dimensional plane), or if it is possible to assume the functions are linear within a sufficiently restricted range about the point for which the function is calculated, then functions x and y may be recast in first-order expanded form in equations 4.22 and 4.23.

$$\rho_{xy}\sigma_x\sigma_y = \sigma_{xy}^2 = \frac{1}{N-1} \sum_{i=1}^N (x_i - \bar{x})(y_i - \bar{y}) \quad (4.21)$$

$$x_i - \bar{x} = (u_i - \bar{u}) \frac{\partial x}{\partial u} + (v_i - \bar{v}) \frac{\partial x}{\partial v} + (w_i - \bar{w}) \frac{\partial x}{\partial w} \quad (4.22)$$

$$y_i - \bar{y} = (u_i - \bar{u}) \frac{\partial y}{\partial u} + (v_i - \bar{v}) \frac{\partial y}{\partial v} + (w_i - \bar{w}) \frac{\partial y}{\partial w} \quad (4.23)$$

Substituting these expressions into the covariance formula allows the propagation of correlation terms for the original random variables. This is seen in equations 4.24 and 4.25, where in the latter equation the definitions of the variance and covariance are applied as appropriate for the collection of terms.

$$\begin{aligned} \sigma_{xy}^2 &= \frac{1}{N-1} \sum_{i=1}^N \left((u_i - \bar{u})(u_i - \bar{u}) \frac{\partial x}{\partial u} \frac{\partial y}{\partial u} + (u_i - \bar{u})(v_i - \bar{v}) \frac{\partial x}{\partial u} \frac{\partial y}{\partial v} \right. \\ &\quad + (u_i - \bar{u})(w_i - \bar{w}) \frac{\partial x}{\partial u} \frac{\partial y}{\partial w} + (v_i - \bar{v})(u_i - \bar{u}) \frac{\partial x}{\partial v} \frac{\partial y}{\partial u} \\ &\quad + (v_i - \bar{v})(v_i - \bar{v}) \frac{\partial x}{\partial v} \frac{\partial y}{\partial v} + (v_i - \bar{v})(w_i - \bar{w}) \frac{\partial x}{\partial v} \frac{\partial y}{\partial w} \\ &\quad + (w_i - \bar{w})(u_i - \bar{u}) \frac{\partial x}{\partial w} \frac{\partial y}{\partial u} + (w_i - \bar{w})(v_i - \bar{v}) \frac{\partial x}{\partial w} \frac{\partial y}{\partial v} \\ &\quad \left. + (w_i - \bar{w})(w_i - \bar{w}) \frac{\partial x}{\partial w} \frac{\partial y}{\partial w} \right) \end{aligned} \quad (4.24)$$

$$\begin{aligned} \sigma_{xy}^2 &= \sigma_u^2 \frac{\partial x}{\partial u} \frac{\partial y}{\partial u} + \sigma_v^2 \frac{\partial x}{\partial v} \frac{\partial y}{\partial v} + \sigma_w^2 \frac{\partial x}{\partial w} \frac{\partial y}{\partial w} \\ &\quad + \sigma_{uv}^2 \left(\frac{\partial x}{\partial u} \frac{\partial y}{\partial v} + \frac{\partial x}{\partial v} \frac{\partial y}{\partial u} \right) + \sigma_{uw}^2 \left(\frac{\partial x}{\partial u} \frac{\partial y}{\partial w} + \frac{\partial x}{\partial w} \frac{\partial y}{\partial u} \right) \\ &\quad + \sigma_{vw}^2 \left(\frac{\partial x}{\partial v} \frac{\partial y}{\partial w} + \frac{\partial x}{\partial w} \frac{\partial y}{\partial v} \right) \end{aligned} \quad (4.25)$$

The covariance terms can be set to zero because of the assumption of statistical independence between water vapor column depth, aerosol optical depth, and density altitude. Equation 4.26 shows this simplified expression. Note the code underlying the uncertainty propagation model uses the original form in equation 4.25 to accommodate any future need to model correlations between atmospheric constituents, with the relevant terms simply configured to be zero for the time being.

$$\rho_{xy} S_x S_y = S_u^2 \frac{\partial x}{\partial u} \frac{\partial y}{\partial u} + S_v^2 \frac{\partial x}{\partial v} \frac{\partial y}{\partial v} + S_w^2 \frac{\partial x}{\partial w} \frac{\partial y}{\partial w} \quad (4.26)$$

The final step is to replace the notional variables used so far with actual terms. Three atmospheric parameters directly affect four modeling outputs, producing six correlation pairs, all listed in equation 4.20. Using τ_1 and L_d as examples, the correlation term for these two outputs is given in equation 4.27. The expression is repeated for the other five possible combinations of τ_1 , τ_2 , L_d , and L_u in equations A.14 through A.19 and incorporated into equation A.24 (see appendix A). Note that while radiometric parameters are shown to be cross-correlated, the cross-correlation terms between the *constituents* have dropped out in equation 4.27 as a result of the independence assumption. These terms still exist in the model should reliable nonzero correlation factors become available.

$$\begin{aligned} S_{\tau_1} S_{L_d} \rho_{(\tau_1 L_d)} &= S_{H_2O}^2 \frac{\partial \tau_1}{\partial H_2O} \frac{\partial L_d}{\partial H_2O} + S_{alt}^2 \frac{\partial \tau_1}{\partial alt} \frac{\partial L_d}{\partial alt} \\ &+ S_{AOD}^2 \frac{\partial \tau_1}{\partial AOD} \frac{\partial L_d}{\partial AOD} \end{aligned} \quad (4.27)$$

4.6.3 Partial derivatives

While the partial derivatives of reflectance with respect to each term are analytical functions, finding the values of and error in each term is another matter entirely. The value of each term is a function of the atmospheric parameters and determined by the radiative transfer code. The relationship is described conceptually in equations 4.28 to 4.31. The function is defined by the radiative transfer code. In other words, a single piece of software runs over all the atmospheric parameters simultaneously and tracks several different quantities during the course of its numeric integration, which then become the modeling outputs.

$$\tau_1 = f_1(H_2O, alt, AOD, \dots) \quad (4.28)$$

$$\tau_2 = f_2(H_2O, alt, AOD, \dots) \quad (4.29)$$

$$L_d = f_3(H_2O, alt, AOD, \dots) \quad (4.30)$$

$$L_u = f_4(H_2O, alt, AOD, \dots) \quad (4.31)$$

Because there is no analytical form for the functions defining the modeling outputs, the error in each output is only marginally better defined than the earlier expressions for error in reflectance. However, the good news is that they can be obtained numerically. The reduced forms of the equations are shown in equations 4.32 through 4.35, while the expanded set of relationships are included as equations A.20 through A.23. Here, the behavior of the atmosphere *is* the functional space, and the ability to “reach back” through the nonlinear space to obtain the partial derivatives with respect to each physical atmospheric parameter requires the application of numerical differentiation techniques (as described in section 4.7) to the radiative transfer code. It was a major task of this research to define and quantify the relationships expressed by equations A.20 through A.23, analyze the relative magnitude of each of the terms, and make recommendations for ground truth measurement networks based on the results. Note that the correlation coefficients between the atmospheric parameters are implicitly assumed to be zero due to the assumption of statistical independence stated earlier.

$$S_{\tau_1}^2 = \left(\frac{\partial \tau_1}{\partial H_2O} S_{H_2O} \right)^2 + \left(\frac{\partial \tau_1}{\partial alt} S_{alt} \right)^2 + \left(\frac{\partial \tau_1}{\partial AOD} S_{AOD} \right)^2 \quad (4.32)$$

$$S_{\tau_2}^2 = \left(\frac{\partial \tau_2}{\partial H_2O} S_{H_2O} \right)^2 + \left(\frac{\partial \tau_2}{\partial alt} S_{alt} \right)^2 + \left(\frac{\partial \tau_2}{\partial AOD} S_{AOD} \right)^2 \quad (4.33)$$

$$S_{L_d}^2 = \left(\frac{\partial L_d}{\partial H_2O} S_{H_2O} \right)^2 + \left(\frac{\partial L_d}{\partial alt} S_{alt} \right)^2 + \left(\frac{\partial L_d}{\partial AOD} S_{AOD} \right)^2 \quad (4.34)$$

$$S_{L_u}^2 = \left(\frac{\partial L_u}{\partial H_2O} S_{H_2O} \right)^2 + \left(\frac{\partial L_u}{\partial alt} S_{alt} \right)^2 + \left(\frac{\partial L_u}{\partial AOD} S_{AOD} \right)^2 \quad (4.35)$$

4.6.4 Bias terms

Three effects are modeled that induce bias errors: off-nadir pointing, off-normal ground tilt angle, and the obscuration of clear sky, either by clouds or background objects. The underlying models for deriving each effect (essentially obtaining the term in equation 4.16) are developed in section 4.13. According to equation 4.17, bias error is the difference between the assumed effect and the actual effect. Applying this to the governing equation 4.18, bias terms can be derived.

Off-nadir pointing affects upwelled path radiance, L_u , and target-sensor transmissivity, τ_2 . If the difference between the nadir and off-nadir path lengths is significant, the effect may affect the final reflectance retrieval, with path radiance increasing and transmissivity decreasing. The governing equation 4.18 does not explicitly specify a pointing angle, but nadir is assumed in the radiative transfer process. Therefore, unless it is accounted for somehow (and model-based algorithms do detect pointing effects during atmospheric determination), a bias error would exist. Equation 4.36 shows this relationship, with the off-nadir term considered the truth term and the nadir-pointing term considered the erroneous estimate term because it contains the blind assumption.

The off-nadir term is expressed in equation 4.37. The angle ψ represents off-nadir pointing angle, with 0° corresponding to nadir and 90° corresponding to horizontal. The subscript 0 is used for nadir terms, and ψ is used for terms where the pointing angle is non-zero. There is an azimuthal dependence that is implicitly accounted for in the modeling process. Note that in equation 4.37 the downwelled, cloud, and background terms are condensed into the L_d term, indicating zero sky fractions for clouds or background objects (for now). The difference is expanded in equation 4.38.

$$\Delta r = r_0 - r_\psi \quad (4.36)$$

$$r_\psi = \frac{L_{SR} - L_{u,\psi}}{\left(\frac{E_s}{\pi} \cos \sigma_{s'} \tau_1 + L_d\right) \tau_{2,\psi}} \quad (4.37)$$

$$\Delta r_\psi = \frac{\tau_{2,\psi} (L_{SR} - L_{u,0}) - \tau_{2,0} (L_{SR} - L_{u,\psi})}{\left(\frac{E_s}{\pi} \cos \sigma_{s'} \tau_1 + L_d\right) \tau_{2,\psi} \tau_{2,0}} \quad (4.38)$$

Off-normal ground tilt can be a troublesome effect because no algorithm can adequately distinguish a cosine-induced radiance change from an actual variation in reflectance. The affected cosine term resides in the denominator of equation 4.18, shown in equation 4.39. Normally, $\sigma_{s'}$ has a sun-sensor geometry component and a local normal component, shown in figure 4.16, but the local normal component is normally assumed to be zero unless explicitly measured. The term σ_{tilt} is used to track a term with a non-zero local normal component (the solar geometry component is the same). The bias difference is expanded in equation 4.40.

$$r_{tilt} = \frac{L_{SR,tilt} - L_u}{\left(\frac{E_s}{\pi} \cos \sigma_{tilt} \tau_1 + L_d\right) \tau_2} \quad (4.39)$$

$$\Delta r_{tilt} = \frac{\frac{E_s}{\pi} \tau_1 (L_{SR} - L_u) (\cos \sigma_{tilt} - \cos \sigma_{s'})}{\left(\frac{E_s}{\pi} \cos \sigma_{s'} \tau_1 + L_d \right) \left(\frac{E_s}{\pi} \cos \sigma_{tilt} \tau_1 + L_d \right) \tau_2} \quad (4.40)$$

An unknown bias in the radiometric calibration of a remote sensing instrument can have a dominant effect on the retrieved reflectance. Bias can be dependent on signal level or be a straight increase or decrease in signal independent of scene brightness. The error propagation model is capable of handling either case. The modeling technique is very straightforward. Given a miscalibrated radiance term \hat{L}_{SR} that includes the sensor bias, the expression for reflectance bias as a function of radiometric calibration bias is shown in equation 4.41.

$$\Delta r_{cal} = \frac{\hat{L}_{SR} - L_{SR}}{\left(\frac{E_s}{\pi} \cos \sigma_{s'} \tau_1 + L_d \right) \tau_2} \quad (4.41)$$

The final bias error sources are due to clouds and background objects. These are explicitly assumed to affect only downwelled sky radiance and not either direct path to or from the target. Equation 4.42 shows this, where L_{sky} is used to represent the composite downwelled radiance resulting from non-zero cloud and background sky fractions. The general form is given in equation 4.43, where specificity to either clouds or background objects alone is accomplished by setting the complementary sky fraction term to zero.

$$r_{sky} = \frac{L_{SR} - L_u}{\left(\frac{E_s}{\pi} \cos \sigma_{s'} \tau_1 + L_{sky} \right) \tau_2} \quad (4.42)$$

$$\Delta r_{sky} = \frac{(L_{SR} - L_u)(L_{sky} - L_d)}{\left(\frac{E_s}{\pi} \cos \sigma_{s'} \tau_1 + L_d \right) \left(\frac{E_s}{\pi} \cos \sigma_{s'} \tau_1 + L_{sky} \right) \tau_2} \quad (4.43)$$

4.7 Numerically-determined derivatives

The error analysis requires the numerical computation of partial first derivatives, which are used in equations A.14 through A.19 and A.20 through A.23. The first derivative of a function describes the function's rate of change or instantaneous slope of the function. This quantity tells how much the function changes with respect to a change in an input variable. The function in question is the effect of the atmosphere as modeled by MODTRAN. The independent variables are MODTRAN's input parameters. The components of the gradient will be calculated and

compared to each other. As will be demonstrated, correctly calculating the derivative depends on the magnitude of the function and its derivatives. Functional and machine error in calculating derivatives are “modeling overhead” that cannot be fully avoided but add nothing to the modeling results. Both need to be minimized with sufficient due diligence and attention paid to the fact that a discrete step size either too large or too small will increase one of these error sources. With multiple variables, that additional danger exists that relative differences in these sources between variables could be misinterpreted as a model result. Until the behavior of the function as a function of each input parameter is better understood, there will be an emphasis on error reduction when calculating the first derivative.

4.7.1 General equations

The basic formulation of the derivative of a single variable is given in equation 4.44. When extended to a multivariable function, the partial derivative is defined by equation 4.45. When applied to analytical expressions, the procedure for finding a derivative or partial derivative is essentially the same for each, with the variables for which the partial derivative is not being determined being treated as constants. When the partial derivatives of $f(x_1, x_2, \dots, x_n)$ are grouped together as a vector, the result is termed the gradient, or $\nabla f(x_1, x_2, \dots, x_n)$ (Stewart, 1995). The gradient vector has a three-dimensional physical analogy, which is that it determines the slope of a surface in each of the unit vector directions. The directional derivative is the slope of such a surface in an arbitrary direction, and it is calculated using the gradient.

$$\frac{df(x)}{dx} = \lim_{\Delta x \rightarrow 0} \frac{f(x + \Delta x) - f(x)}{\Delta x} \quad (4.44)$$

$$\frac{\partial f(x_1, x_2)}{\partial x_1} = \lim_{\Delta x_1 \rightarrow 0} \frac{f(x_1 + \Delta x_1, x_2) - f(x_1, x_2)}{\Delta x_1} \quad (4.45)$$

The concept of the slope of a surface does not have a direct physical analogy to the problem under current consideration, but the usage is the same. It is desired to determine which direction has the greatest rate of change. In the physical casting of the problem, each unit vector represents an actual direction. In this problem, each unit vector represents an independent atmospheric parameter, and the functional output is the at-sensor radiance. The function itself is the physics-based numerical radiative transfer code, MODTRAN in this case. The instantaneous rate of change of the at-sensor radiance in response to an infinitesimal change in an input parameter is useful because it characterizes the behavior of the system, which is useful,

in turn, in that inputs can be related to outputs. In non-linear systems, such a relationship can be difficult to determine by other means. This technique is the basic approach used by algorithms that seek to perform nonlinear optimization, though moving through the nonlinear vector space is not of immediate interest (McIntyre, 2004). However, the method of obtaining derivatives is applicable.

When a function has no analytical expression, or if data are collected without direct access to the underlying physical relationship, one must resort to numerical methods of estimating the derivatives. Because no direct analytical expression for “the atmosphere” is available, numerical techniques are thus required. The most common way to do this is described in Dennis and Schnabel (1996) and shown in equation 4.46. The expression is a result of truncating and rearranging the traditional Taylor series expansion of $f(x + \Delta x)$, as explained in Press et al. (1990). The form of the Taylor series is given as equation 4.47, and the rearrangement is shown in equation 4.48, but in univariate form. The higher order terms of the series are then discarded leaving the form in equation 4.46, which has been trivially extended to the multivariate form.

$$\frac{\partial f(x_1, x_2)}{\partial x_1} \approx \frac{f(x_1 + \Delta x_1, x_2) - f(x_1, x_2)}{\Delta x_1} \quad (4.46)$$

$$f(x + \Delta x) = f(x) + \Delta x f'(x) + \frac{\Delta x^2 f''(x)}{2!} + \frac{\Delta x^3 f'''(x)}{3!} + \dots \quad (4.47)$$

$$\frac{f(x + \Delta x) - f(x)}{\Delta x} = f'(x) + \left(\frac{\Delta x f''(x)}{2!} + \frac{\Delta x^2 f'''(x)}{3!} + \dots \right) \quad (4.48)$$

There are other techniques for numerically estimating a first derivative of a function, such as guessing an exponential form and performing a least-squares curve fit or fitting a Chebychev polynomial to the univariate curve and using the analytical derivative (Press et al., 1990). However, because the objective of this portion of the work is to compare the components of the function’s gradient to each other at a small number of selected points rather than compute the derivative at a large number of points, these approaches would be inappropriate. Additionally, the numerical methods discussed are sufficient for the intended use and avoid some of the artifact problems inherent in polynomial curve fitting, such as periodic instability that increases at the edges. This is illustrated in figure 4.6, where a curve fit was attempted on transmission data as a function of visibility.

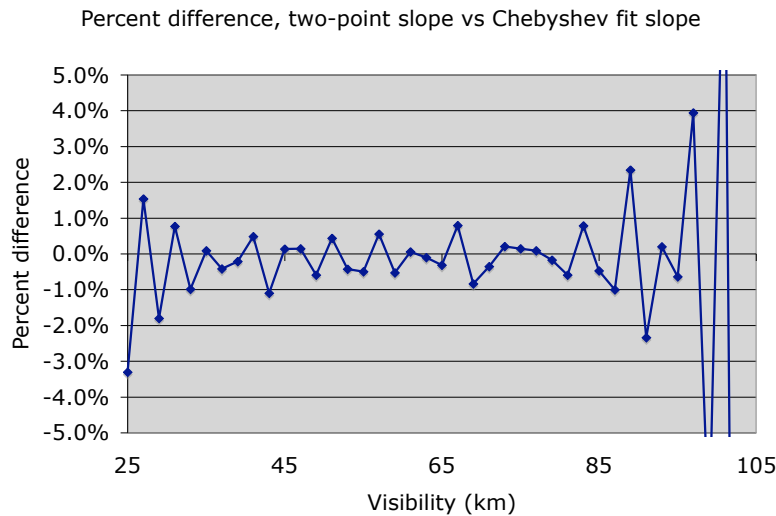


Figure 4.6: Error comparison for Chebyshev curve fit-derived slope

4.7.2 Error considerations

Because of the truncation of equation 4.48 and the non-infinitesimal step size, there is a degree of error inherent in the finite difference method of calculating numerical derivatives. According to Press et al. (1990), in addition to error introduced by the truncation of the higher order terms of equation 4.48, inexact variable storage, machine precision, and errors in the calculation of $f(x, \dots)$ cause significant problems. The combination of these error sources means that an optimal finite step size can be neither very large (for the sake of the truncation errors, which are a failure in assumptions underlying finite difference methods) nor very small (due to the functional/machine noise). This claim is supported by figure 4.7. In the figure, an example function's derivative was numerically computed using equation 4.46. The step size (denominator of equation 4.46), is varied along the x-axis. When the step size is large, systematic error is dominant. As the step size decreases, the derivative's value settles to its best approximation. As step size decreases even further, then machine effects take over creating first small fluctuations in value then large ones. At the smallest step sizes, the value goes completely haywire and is essentially pure noise.

It is important to minimize the error where possible, and it is also useful to have an estimate of the error. There are three steps in Press et al. (1990) that are easily

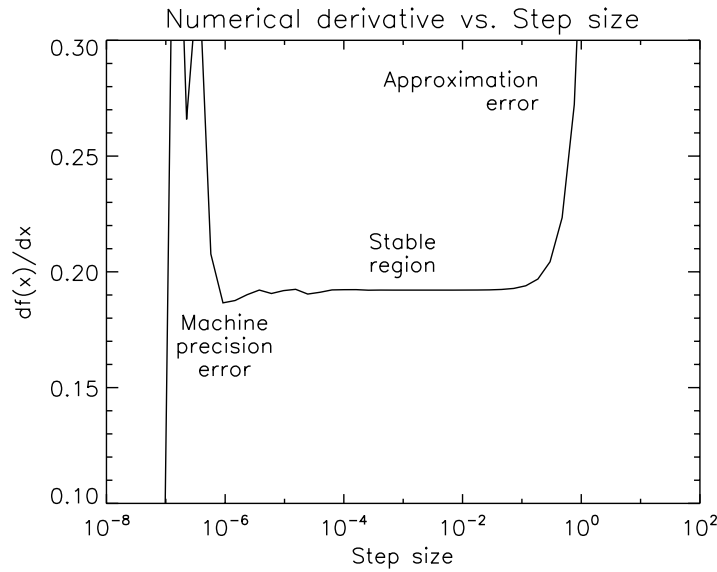


Figure 4.7: A comparison of systematic and functional error sources in functions

taken to reduce errors. The first involves storing and retrieving the step size Δx to/from the computer's memory. This mitigates the effect of machine truncation when translating the number to a specific data type since the actual step size used will be rounded off beforehand and will not change during the computation. This method is not applicable when using MODTRAN as the function because it reads text configuration files, and the user has no control over the machine storage of variables. Pre-truncating the step-size variable used in calculating the derivative will not guarantee the same number is used in both cases.

The second strategy for error reduction is to use a form of 4.46 that is centered on the point of interest rather than using it as an endpoint. The reformulated method is presented as equation 4.49. This technique is highly effective, but it only reduces systematic error and does not affect machine precision error. However, this added leeway is essential in the specific case of using MODTRAN as a functional operator. It permits the step size calculation to err on the high side with greatly reduced effect on the calculated slopes and the avoidance of a very dominant machine precision error regime.

$$\frac{\partial f(x_1, x_2)}{\partial x_1} \approx \frac{f(x_1 + \Delta x_1, x_2) - f(x_1 - \Delta x_1, x_2)}{2\Delta x_1} \quad (4.49)$$

The final step suggested is to select an optimal step size. Figure 4.7 makes the necessity of this recommendation obvious. Optimal step size can deliver accuracy in computing the first derivative on the order of the square root of the machine precision when using equation 4.46 or the squared cube root of the machine precision when using equation 4.49 (Press et al., 1990). It is possible to analytically determine an appropriate order of magnitude for the step size if additional information about the function is available or estimable. Absent that, one can empirically calculate the optimal derivative step size either via brute force or using a numerical method such as Ridders' method (Ridders, 1982), which generally requires less calculations of the function as well as providing an estimate of the error.

The cost of computing valuations of $f(x, \dots)$ is typically a significant factor when determining how to reduce error, but in the case of this investigation the time and computational resources are available to perform detailed calculations for some or all of the variables and input variables used. The current functional speed can range from under 0.5 up to 30 minutes depending on the spectral resolution and multiple scattering settings selected. If this work moves out of the lab and into an operational setting, these considerations will become important, but for the time being the chosen method of implementing the third recommendation is to reproduce figure 4.7 for each atmospheric parameter and determine an optimal "stable" region taking into account all spectral bands. It is the most time-consuming and labor-intensive method of doing it, but it is also the most rigorous and reliable.

4.8 Slope calculation using MODTRAN

There are three simple steps to applying equation 4.49 to solve for the appropriate terms in equations A.20 through A.23. They are determine the appropriate step size, run MODTRAN twice with varied inputs, and calculate the change in spectral output per change in parameter input. Determining the nature of the functional space using multiple MODTRAN runs is not a new idea; in fact, there is at least one commercial product that performs multiple runs automatically (Schläpfer and Nieke, 2005). While it can be useful to map out the entire functional space to provide a double-check on the output's behavior, it is much more practical to get the step size determination correct the first time and enjoy the reduced processing requirements when examining any scenario variations thereafter.

It has been verified in preliminary calculations (as part of section 5.1.1) that functional errors driven by the MODTRAN output precision (rather than internal storage errors) dominate the numerical error considerations, with systematic approximation errors in a distant (but significant) second place. There is a very narrow window where both errors of the type inherent in equation 4.49 and MODTRAN functional error can be avoided. The window only exists because the behaviors involved are smooth and gently varying, so while functional errors prevent the use of any reasonably small step size, Taylor series truncation errors accumulate slowly. This is true for total water vapor column amount, aerosol optical depth, and surface pressure/temperature scale height. As is shown in section 5.1.1, a very large atmospheric parameter step size is needed to find this window in the first place. Step size can be computed in detail, at high computational expense, for one point in the input parameter space and then adapted for use at other points using the approximation as a guide.

Although slope results are not necessarily being presented here, it is appropriate to mention what step sizes were chosen and how. The graphs in section 5.1.1 show several surprising effects. The different plot curves represent a sampling of wavelengths between 400 nm and 2500 nm, roughly 200 nm apart. This was done to show the wide variety of behavior within the spectrum of a single parameter.

Three main effects are observed. First, on the left-hand edge of most curves is the machine noise regime, caused by limitations in storing real numbers as single- or double-precision floating point variables. Even double-precision variables can occasionally be susceptible to errors simply because the magnitude of the numbers involved can be on the order of $10^{\pm 15}$. The other two are on the right-hand side of some of the plots, where there exist both non-periodic variation and periodic variation. The non-periodic variation is the slope approximation error discussed earlier. In some cases it converges quickly, and in others it appears to barely converge at all. The periodic variation, which appears primarily in the calculations for τ_1 , is an effect that has not yet been discussed. It is a form of truncation error similar to the machine precision issue, but it manifests as roundoff in the ASCII text output files. Consider two MODTRAN tape decks run with slightly different parameters: the outputs are identical to two, three, or four places (depending on how many places were reported in the text output) due to roundoff. The two distinct inputs are used as the denominators in equation 4.49. This creates a characteristic sawtooth pattern in the slope, whereas the original output was stair-stepped. Assuming the roundoff follows the common rule, the best estimate for the slope is halfway up the side of a “tooth.”

These characteristics indicate the presence of error in some of the curves. The

amount of error one is willing to live with is a key question because these curves are essentially the main guts of the entire modeling effort. A mitigating factor is that for the majority of the curves, there exists a relatively stable region where it is possible to pick a good step size. In bands where this is not the case, the problems transcend mere step size selection. Colliding error regimes not only make it difficult to choose a step size, but they also have the primary effect of increasing the amount of error observed.

Options exist for reducing the variation and its impact on slope calculation. Although none of these was implemented here, future work may consider them. A permanent fix would be to re-engineer then re-compile the radiative transfer code where possible to carry along the maximum amount of precision available and report answers to a greater precision. Since treating MODTRAN as anything other than a black box is outside the scope of this work, it was not pursued. It would be possible to select different step sizes for each band that best fit each curve's individual behavior. This was not pursued because it was not practical to manually examine some 12,000 curves, and there is no guarantee the results would be transportable to other sensing configurations. Fitting a curve to the data was previously rejected as a slope calculation strategy, and not only because it requires many more MODTRAN runs but also there is the real possibility of having to supervise coefficient selection for many of these 12,000 curves. However, it does have a nice side effect of finding the solution with the least squared error and eliminating much of the random jitter present in the results.

It is believed that the final values chosen represent something akin to a “natural frequency” with respect to the behavior of the real-world systems that would transport well to other sensing scenarios. They are 0.25 cm or 2.5 mm of total precipitable water vapor, 0.1 km or 100 m in density altitude, and 2 km of horizontal visibility. The visibility step size has a nonlinear relationship to vertical and slant-range aerosol optical depth step size that is computed internally each time the model is run. This value is retrieved and used, but because it is a function of the baseline visibility no set number is used across the board.

4.9 Uncertainty in atmospheric parameters

In previous sections the mechanism of error modeling has been developed, and this treatment of error in the atmospheric variables now opens up the model's interface. The ability to specify the amount of error present in each basic term is precisely what allows the model to be exercised in various ways. The primary capabilities are to predict the amount of error in inversion results, test combinations

of algorithms and instruments, and estimate error performance-per-cost (monetary or computational).

The next terms that will be considered are the uncertainty in the water vapor column depth, density altitude, and aerosol optical depth. They have been denoted as S_{H_2O} , S_{alt} , and S_{AOD} . They are treated here as synonymous as the standard deviations of these terms, but this begs the question, “Of what data set are they the standard deviation?” The concept of uncertainty inherent in these parameters somewhat transcends a statistical definition, but as is usually the case, using inherent uncertainty in practice means computing the standard deviation of sample data to estimate it. However, the data for which statistics are calculated depends on the source. There are three main categories of input sources: inherent estimates anchored to a specific location, ground instrument estimates, and in-scene algorithm estimates. Each source of parameters also is a source of parameter estimation uncertainty.

Stripped down to bare bones, model-based algorithms isolate reflectance by estimating every other term in the model. All model-based inversion algorithms all need to somehow provide the parameters currently under consideration. This serves as the common framework from which any such algorithm can be decomposed and analyzed. At this level of abstraction, inputs can be readily substituted, perhaps to trade high uncertainty for lower uncertainty. The baseline circumstances for doing this is augmenting or checking in-scene parameter retrieval algorithms with ground instruments. Most often field instruments are used to validate final results, *i.e.* the retrieved reflectance, because this is considered to be the most effective use of the resource (look to Staenz (2002) and Goetz et al. (2003) for ready examples). Validation of retrieval algorithms is the usual motivation for measuring atmospheric constituents in support of remote sensing (an example is discussed by Kaufman et al. (1997)), but it is also possible to hybridize in-scene inversion algorithms through fusion with ground truth measurements. This technique has been employed in support of Landsat/HyMap (Rochford et al., 2005) and AVIRIS (Clark et al., 1995) and holds the potential to correct less precise instruments and extend the capabilities of instruments that lack or have poorly-selected spectral bands for in-scene constituent retrieval.

4.9.1 Error sources from climatology

When estimating an atmospheric parameter without having made any measurements, inherent uncertainty or inherent error is the error figure automatically attached to the estimate. It is a property of geographic area, and whereas it is common to express average values for an area, it is basically unheard of to report typical

uncertainty in those values. However, to those properly trained, a reported value is nearly meaningless unless its uncertainty is also given, and it is no different in this case. While the concept of inherent uncertainty may be somewhat esoteric, it tends to appear often and almost always without acknowledgment. Whenever a study reports that the “MODTRAN default” values (including the use of the ubiquitous mid-latitude summer atmospheric model) were used to predict expected values or assist in atmospheric inversion, inherent uncertainty drives the output error. The six model atmospheres available in MODTRAN are themselves attempts to report geography-based average values in a way most useful to the modeling code’s many users.

Weather and climate patterns create a natural probability distribution for each of the atmospheric parameters. This implies that with no prior knowledge of actual atmospheric conditions, it is possible to make an approximate guess with a degree of uncertainty dictated by the local area’s climatology. The nature of this distribution is determined solely on the past weather history of the area being studied. This characterization of an area must be accomplished beforehand, since it involves culling archived weather observations and constructing statistical models based on that data. The construction of a statistical model simply involves calculation of the standard deviation of each atmospheric parameter, which is usually a derived result from an operational ground measurement data set.

Once atmospheric observations have been collected, it is generally preferable and straightforward (but tedious) to slice the data along temporal lines, making distinction by time of year and time of day. Indeed, the default MODTRAN atmospheres are themselves split according to summer and winter. Grouping by time of year and by time of day are both useful, provided adequate data are available. In this analysis, data were grouped by month but not by time of day because although *most* data are time-stamped, the date of the observation is more universally available than the time of the observation.

Presenting inherent error is more of a conceptual exercise than a practical tool. Unless someone happens to be curious about an area’s intrinsic climatic variability or is in a circumstance where it is not possible to use either ground instruments or an in-scene inversion algorithm, determining inherent variability in one or more atmospheric parameters is not required under normal conditions. Thus, it does not directly add value to any particular remote sensing activity, but it provides a starting point for this investigation. The results of the atmospheric profiling provide default values for each of the three atmospheric error terms and give an upper bound on reflectance retrieval errors. The process for collecting the required data and calculating the inherent uncertainty will be briefly discussed.

4.9.2 Error sources from ground instruments

The basic premise of this work is that whereas ground instruments were previously regarded as undesirable in operational imaging, recent advances in wireless electronics and miniaturization have made low-cost networks of autonomous, unattended, and remotely placed ground sensors feasible and worth examining.

Using an instrument to measure either an atmospheric parameter or one of the modeling outputs directly produces both an answer and a measurement uncertainty. This estimation of measurement error comes straight from a basic physics class lesson in lab discipline and technique. Each instrument is calibrated and characterized individually, and the uncertainty is generally available on a product data sheet.

Although the actual instruments used for each data source are listed elsewhere, it will be assumed that the reported measurement uncertainty either for that instrument or that class of instruments is what one can reasonably expect to observe when incorporating a ground instrument into a sensing network.

4.9.3 Error sources from inversion algorithms

Each inversion algorithm must, by definition, somehow solve equation 4.18. The two main classes of inversion algorithms, ground truth-based and model-based, each obtain the terms differently. The empirical line method, the prime example of the first type determines the reflectance-to-digital count linear conversion factor, which is an inseparable combination of all of the multiplicative terms. FLAASH, an example of the second type, obtains each of the modeling outputs as described here and uses them to solve for the constants A and B in equation 3.10.

Error in ELM is not considered at this time because its result, the linear conversion factor, is largely incompatible with the error analysis performed in this research. It will be examined later for comparison purposes, but there is no meaningful translation of error in one of the terms to error in the entire combination of terms making up the conversion factor. It is possible to imagine hybridized ELM algorithms that can take advantage of ground methods either in the direct result, a portion of the direct result (numerator or denominator), or in the spatial propagation of the result. However, constructing such algorithms is beyond the scope of this work.

A useful output of FLAASH is the water vapor and aerosol abundance maps it produces. However, these parameter maps are not accompanied by any kind of estimation uncertainty.

4.10 Total error due to atmospheric constituent uncertainty

In the terminology used here, there are four modeling outputs: sun-ground transmissivity, ground-sensor transmissivity, downwelled radiance, and upwelled radiance. Given a set of atmospheric parameters, the radiative transfer code MODTRAN produces these as results, hence the terminology “modeling outputs.” The errors in each of these outputs— S_{τ_1} , S_{τ_2} , S_{L_d} , and S_{L_u} —are key terms in the error propagation model. The construction of these error terms is straightforward, as is illustrated in figure 4.8.

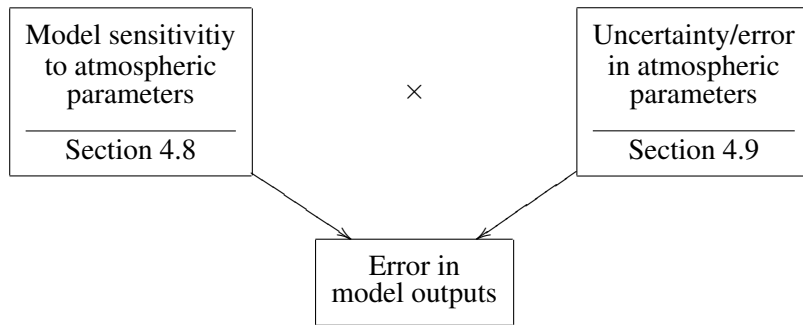


Figure 4.8: Construction of total error in each model output

Each error term is calculated according to equations A.20 through A.23. The partial derivative terms are the MODTRAN slopes described in section 4.8 computed numerically for each imaging scenario. The error in each atmospheric parameter is derived from one of several possible ways, as described in section 4.9. The result of this calculation is a single multiplication producing one value per spectral band that represents the root-sum-square of the uncertainty in each parameter with the sensitivity of each modeling output to a change in parameter value.

4.11 Physical models

While not error models *per se*, these factors are key enablers to the modeling process. Terrain altitude is a required input for radiative transfer modeling, and exoatmospheric solar irradiance is a term found directly in the governing equation. Uncertainty in both will affect the final result, so error modeling methodology for these factors is shown here.

4.11.1 Elevation knowledge

Although density altitude is used to index the atmospheric column density to a single ground-based parameter, terrain elevation knowledge across the image is also required. Geographic survey data are available for the United States, but the resolution may be insufficient to be useful for remote sensing. Local digital elevation models (DEM) may also be available, but a lack of universal availability would invalidate some of the assumptions upon which the overall effort rests. An increasingly common method is through GPS, although care must be given to ensure the result is adjusted to the correct geodesic reference, and high terrain variability reduces the usefulness of a handful of sensors scattered throughout an area. Fortunately there is at least one dataset, the Shuttle Radar Topography Mission (SRTM), that provides global coverage at good resolution with well-understood accuracy (Rodriguez et al., 2005). DEM data can be interpolated to any point in an image, as is shown in figure 4.9.

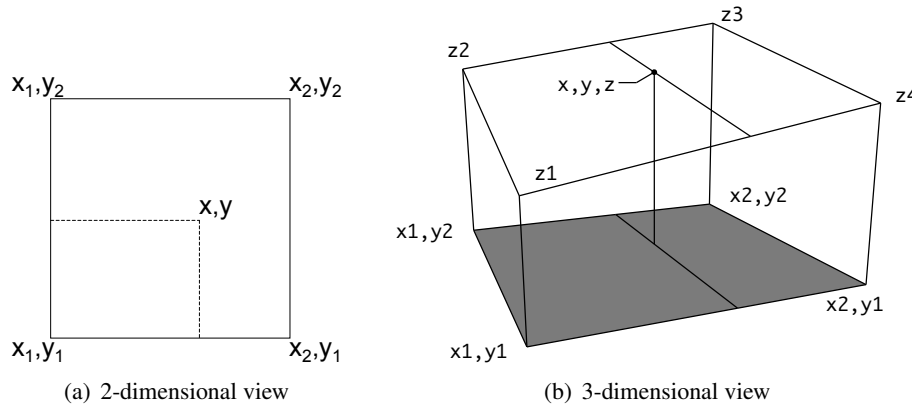


Figure 4.9: DEM interpolation visualization

Given performance inputs for the circular coordinate error (which is evenly decomposed into 2D orthographic coordinate error) and z-height measurement error, it is simple to propagate the error into the interpolated coordinate. The mechanics for doing so are included as equation A.29. The SRTM performance specifications at 90% confidence were 16 meters for z-height error and 20 meters for circular error. Typical performance was closer to 5 meters for z-height error and 15 meters for circular coordinate error (Rodriguez et al., 2005).

Using a scenario concept to establish a performance baseline, the SRTM per-

formance specs were used as worst case values to predict the error in interpolated altitude across the DEM grid. Figure 4.10 shows the resulting error in altitude given flat terrain and the SRTM performance cited above.

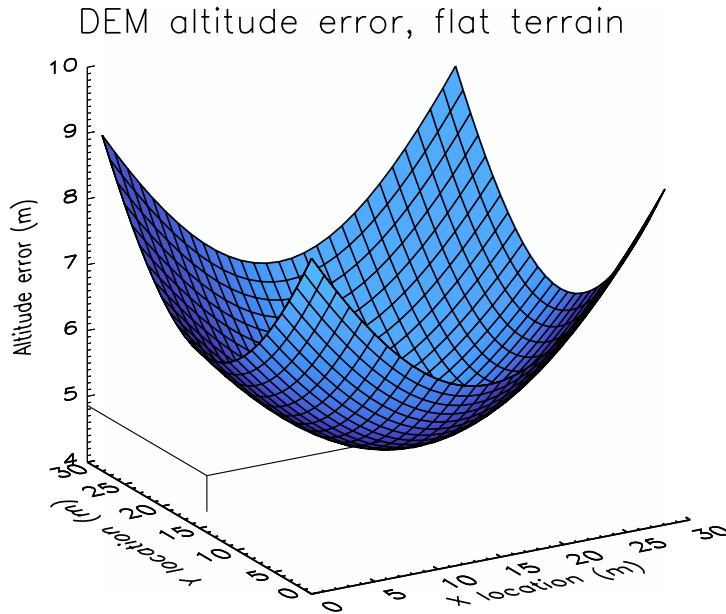


Figure 4.10: DEM altitude error using SRTM values and flat terrain

Because linear interpolation assumes a defined surface of some sort (4 points can lead to a curved surface rather than a flat plane), each DEM point samples the same geometry. The samples are essentially added in quadrature, providing an RSS result that is a minimum when the samples are equidistant (Soukup, 2008). As the point of interest gets closer to any individual sample location, the error increases to a local maximum corresponding to the error for each measurement. Using the values cited above, the altitude uncertainty ranges between 4-9 meters. For non-flat, non-planar surfaces, the error surface is skewed towards the regions of higher slope.

4.11.2 Exoatmospheric solar irradiance

The final term of equation 4.20 to be considered does not fall into any of the previous categories. Exoatmospheric solar irradiance variability will be fully explored,

but the result is so small so as to be called trivial, even in this analysis where errors are not lightly cast aside.

High-precision solar ephemeris data is publicly available (Giorgini et al., 1996). The instantaneous earth-sun distance is mathematically predicted to within 10^{-5} astronomical units (AU), where the mean earth-sun distance is equivalent to 1 AU. The mean exoatmospheric solar irradiance, E_s , is also published. However, the value of the constant, while precise, is anything but constant. During the year, the instantaneous earth-sun distance fluctuates cyclically as the earth revolves around the sun. There is also a long period fluctuation in the mean irradiance due to the sun's 11 year sunspot cycle (as well as a *very* long period fluctuation due to solar fuel depletion and long term sunspot trends). Finally, there is day-to-day and minute-to-minute variability in the solar constant due to sunspots, fluid convection, magnetic effects, and other solar activity (Solanki et al., 2005). Thus, both the mean irradiance and instantaneous earth-sun distance must be updated.

Much work has gone into modeling the cyclic fluctuations of the solar irradiance constant, and the decade-scale periodic fluctuation of the mean solar constant can be accurately modeled (Solanki and Krivova, 2004). A current mean value of $1366.22W/m^2$ with a maximum error of 0.1% was defined as the Space Absolute Radiation Reference (SARR) by the SOLCON project through data reduction of a series of ongoing spaceborne instrument data collections (Crommelynck et al., 1995). This reference value had the secondary effect of providing an instrument cross-calibration that can be propagated to future measurements. The capability exists to measure the fluctuating constant with a 95% confidence interval value of $\pm 0.35W/m^2$ (a normal distribution is assumed). The 95% confidence interval of a normal distribution corresponds to 1.96 standard deviations, so the value of 1 standard deviation can be derived. Assuming a simple adjustment of the form in equation 4.50, the error in the average irradiance is calculated as shown in equation 4.51. The errors in each component are assumed to be independent.

$$E_{s,avg} = ref + adj \quad (4.50)$$

$$\begin{aligned} S_{E_{s,avg}}^2 &= S_{ref}^2 + S_{adj}^2 \\ &= \left(\frac{0.1\% \times 1366.22}{\sqrt{12}} \right)^2 + \left(\frac{0.35}{1.96} \right)^2 \approx (0.43W/m^2)^2 \end{aligned} \quad (4.51)$$

Because instantaneous exoatmospheric solar irradiance follows a well-defined inverse square relationship, it is an easy matter to both determine the irradiance and

calculate its error. The distance correction is shown in equation 4.52 (Schott, 1997). Note that the average earth-sun radius r_{avg} is always 1 if the units are astronomical units, in which case the instantaneous earth-sun distance r is expressed as a fraction of 1 AU. A noise term is added to account for short-period variations in the solar constant. These were measured in one experiment to be as much as $1.5W/m^2$, but it was generally observed to be about a third less than that. A Gaussian model is assumed for these random variations (Crommelynck et al., 1995).

$$E_s = \frac{r^2}{r_{avg}^2} E_{s,avg} + noise \quad (4.52)$$

The error in the exoatmospheric irradiance is obtained by applying the error propagation equation, yielding equation 4.53. In this instance, the actual error value is predicted in equation 4.54 to be on the order of $1.5W/m^2$. The implication is that the system is heavily dominated by solar “noise.” Since there is no possibility of using a less noisy celestial body in the calculation, the only ways to reduce the error are to construct a more complex model that encompasses daily solar activity or measure the solar constant with much greater frequency. Neither of these approaches is feasible in the foreseeable future. The upside of this is that this variation is extremely tiny.

$$S_{E_s}^2 = \left(\frac{\partial E_s}{\partial r} S_r \right)^2 + \left(\frac{\partial E_s}{\partial E_{s,avg}} S_{E_{s,avg}} \right)^2 + S_{noise}^2 \quad (4.53)$$

$$S_{E_s} = \sqrt{(2rE_{s,avg}10^{-5})^2 + (r^20.43)^2 + 1.5^2} \quad (4.54)$$

The modeling approach for determining the variability due to exoatmospheric solar irradiance is to calculate two MODTRAN runs, each using a value for solar constant that varies on the order of the solar irradiance uncertainty. The results would then be compared. However, it was found that the difference in the two inputs were below MODTRAN’s ability to produce distinct output. Using a larger step size and normalizing it down to the required order of magnitude produced a variability that was still exceedingly close to zero.

4.12 Sensor error models

As described in section 4.3, sensor-reaching radiance is treated in a possibly counter-intuitive way. This term describes the radiance after it has suffered all of the atmospheric effects but before it encounters the sensor. However, it is always expressed

as dependent on the sensor's operation. This is because true sensor-reaching radiance is an unknowable quantity. Like all big equation terms, it must be measured with an instrument. The imaging spectrometer is just another one of these "truth" instruments, except it is specialized to take many sequential and/or simultaneous data points registered to spatial locations.

Generally a single number is sufficient to describe the error in ground truth instruments, but these are simpler instruments designed to read out perhaps one or two transducers. With an imaging spectrometer, the instrument's complexity is such that a comprehensive model of the noise inherent in several different components needs to be built before this final result can be produced. The error sources considered are categorized by radiometric calibration accuracy, spectral calibration accuracy, and physical factors such as knowledge of the platform's location and orientation.

4.12.1 Radiometric calibration

The error sources required to consider radiometric calibration accuracy are photon noise, electronic shot noise, thermal noise, dark current, and hardware-induced noise sources such as cross-channel contamination and fixed-pattern noise. Photon noise and electronic shot noise result from the fact that both light and charge are carried by discrete quanta that travel and arrive at independent random rates. Thermal noise results from the thermally-induced Brownian motion of electrons. Dark current is any signal present in the absence of input and has thermal shot noise as its main component. It can also include any intentional bias. Pixel cross-talk results when charge in one detector element influences the output of spatially proximate pixels, either during photon collection or during readout. Some detectors can also have various amounts of hardware-induced noise, many of which types can be designed or calibrated out of the system. Reset noise is one such source, which occurs when there is variability in the reference signal against which the readout is measured. Fixed pattern noise is another common example, where variability in material composition, workmanship, physical dimensions, or electrical properties (among other characteristics) cause differences in output not due to signal (Hewlett-Packard Components Group, 1998).

Producing a credible model of a sensor's ability to measure sensor-reaching radiance is a critical part of an error propagation model. While there are inversion algorithms that do not require sensor-reaching radiance, radiance space is the chosen common framework in which all errors are cast. Whether or not digital counts are converted to radiance in a specific application does not alter the need to express the uncertainty introduced by the detector in radiance units. This permits

the comparison of sensor hardware to the other sources of inversion uncertainty.

Although there are typical sources and magnitudes of hardware noise that affect all instruments, there is no model that can adequately capture the entire range of variability and still be useful to a particular sensor. The chosen approach is to use actual results from one or more instruments that can be considered typical or representative of the state of the industry. The error propagation model will use any sensor noise model expressed in noise equivalent change in radiance ($NE\Delta L$), which is the resulting radiance fluctuation that corresponds to noise fluctuations in any part of the hardware chain: photon flux, charge well electrons, voltage, etc. This output metric is itself a common framework for expressing noise derived from potentially very different hardware configurations.

Signal-to-noise ratio (SNR) can also be used for expressing the noise. Because some noise regimes are tied to signal level, and the model is agnostic as to which noise regime is dominant, it is a general guideline that the SNR or $ne\Delta L$ should be derived from signal levels on the same order of magnitude as those encountered when conducting normal image collection operations. Because this guideline reads like it came from an instruction manual, it is appropriate to recall the proper purpose of the error propagation model. The model is a testbed with which system behaviors can be explored and conclusions can be made regarding the sources and impacts of errors given particular configurations. It is not intended to be an application suitable for users to predict the performance of a particular sensor in a specific sensing configuration. The practical difference can be subtle, but it is the primary reason for ignoring the sensor's spectral convolution model and interpolating the given data to the spectral range and resolution chosen for the model at the top level specification.

For the purposes of running the error propagation model, published sensor radiometric calibration data for typical-of-the-field instruments were used to provide the uncertainty in sensor-reaching radiance. Radiometric bias will be assumed to driven to zero. The spectrometers chosen are AVIRIS (Vane, 1987), HYDICE (Mitchell, 1995), and Hyperion (Browne, 1999).

4.12.2 Spectral calibration

Spectral registration refers to the difference between the spectral band model and the actual band widths and centers. Each sensor's band model consists of a list of band centers, widths, and response curves. When a band is reported to be $\Delta\lambda$ nm wide centered on wavelength λ_0 , a width or centering error introduces an error into the resulting spectrum. The amount of spectral misregistration may or may not be thought of as a random variable, depending on whether it is a fixed

or random difference. Spectral misregistration is normally thought of as a fixed phenomenon, though Nischan et al. (1999) describes random spectral jitter effects in the HYDICE sensor.

Figure 4.11 shows examples for these effects. In figure 4.11(a), a simple bias in band center produces a shift in radiance ΔL_{SR} . The lower radiance assigned to that band would affect band ratios and any spectral products dependent on the retrieved reflectance, such as classification or abundances. The shift in radiance represents a bias that can be propagated forward into reflectance space.

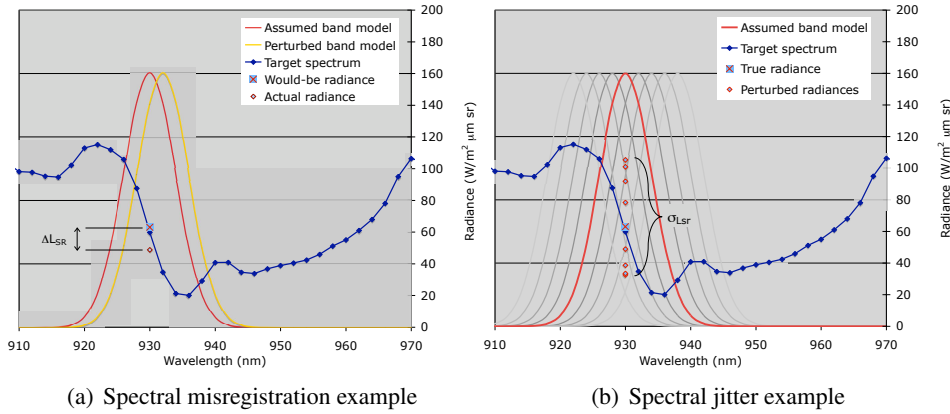


Figure 4.11: Illustration of spectral calibration errors and their effects on the imaging chain

In figure 4.11(b), a baseline band center is subject to random variation. The frequency of each perturbed spectrum is given by a probability distribution governing the amount of spectral jitter. The result of this random variation in band center is to produce a range of radiances assigned to that band. The parameter σ_{Lsr} is intended to denote the standard deviation of the resulting distribution. The expected value of the radiance should more or less match the baseline result, but the variance in the radiance now represents an uncertainty in sensor radiance that can be propagated into reflectance space.

The degree of change in radiance due to a change in any of these parameters is highly context dependent. For a perfectly flat spectrum, a shift in band center would have no effect, whereas an error in the band width would produce a linear increase or decrease in integrated radiance. For a highly variable spectrum, changing the center of the spectrum has a significant effect on the output for that band. A defect in the band widths would show the same increase or decrease in

integrated radiance, though the change amount is not as predictable. The relevant factors are band center, band width, target reflectance, and atmospheric conditions, which produce the absorption bands that tend to dominate the spectral shape.

The governing equation for spectral response function and signal spectrum interaction is shown in equation 4.55. The function $\Phi(\lambda)$ is the spectral flux incident on the detector. The spectral response function for band i of n bands, annotated as $R_i(\lambda)$, is generally modeled as Gaussian, supergaussian (the exponent on the independent variable is an integer greater than 2, yielding a flatter top), rectangular, trapezoidal, or triangular in shape. Gaussian response functions are used for all modeling in this work.

Although the left-hand term in equation 4.55 is traditionally signal (S_i), calibrated sensor radiance for band i (L_i) will be used to avoid terminology confusion. S is used elsewhere to denote sample standard deviation, and the difference between signal and radiance is the radiometric calibration, which is momentarily held constant for the purposes of this discussion.

$$L_i = \int_0^{\infty} \Phi(\lambda) R_i(\lambda) d\lambda \quad (4.55)$$

Assuming a Gaussian form for the moment, the equation can be rewritten as shown in equation 4.56. When a shift error S_{λ_0} and width error $S_{\Delta\lambda}$ are present, the error in the resulting signal can be expressed by equation 4.57.

$$L_i = \int_0^{\infty} \Phi(\lambda) e^{-\pi\left(\frac{\lambda_i - \lambda_{i,0}}{\Delta\lambda_i}\right)^2} d\lambda \quad (4.56)$$

$$\begin{aligned} \Delta L_i = \hat{L}_i - L_i &= \int_0^{\infty} \Phi(\lambda) e^{-\pi\left(\frac{\lambda_i - \lambda_{i,0} \pm S_{\lambda_{i,0}}}{\Delta\lambda_i \pm S_{\Delta\lambda_i}}\right)^2} d\lambda \\ &\quad - \int_0^{\infty} \Phi(\lambda) e^{-\pi\left(\frac{\lambda_i - \lambda_{i,0}}{\Delta\lambda_i}\right)^2} d\lambda \end{aligned} \quad (4.57)$$

The ultimate goal is a model that can produce the sensitivity of sensor-reaching radiance to errors in band center and/or band width. A spectral calibration error simulation was performed by Green (1995), whose result for a 100% reflector is reproduced in figure 4.12. The conclusion was that spectral calibration to within 0.1–0.5 nm was required to prevent spectral effects from dominating the instrument error.

The strong dependence of perturbed radiance on each variable will be demonstrated. As is seen in figure 4.12, spectral calibration errors are most apparent

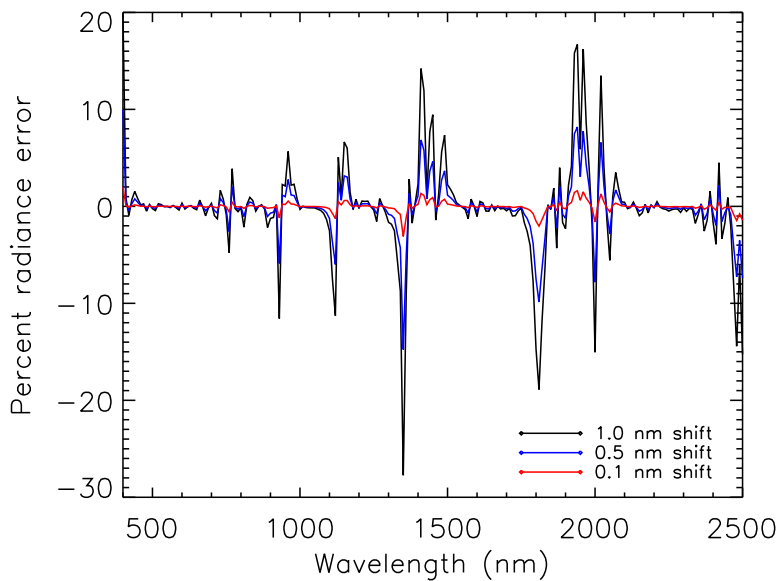


Figure 4.12: Percent error in radiance as a function of band center shift

in the typical water vapor, carbon dioxide, and oxygen atmospheric absorption bands, where the absorption features create strong slopes. However, many target reflectance spectra have strong features as well. Equation 4.57 is unworkable when constructing a rigorous model because the solution depends on not only the spectral response function, but also the shape of the reflectance curve being sampled.

In cases where atmospheric transmission curves produce steeper slopes than spectral reflectance curves, generalizations can be made that apply to a wide range of possible targets. To this end, seven representative reflectance spectra, shown in figure 4.13, were simulated along with 3 spectrally uniform reflectors: a 100%, a 50%, and an 18% reflector. The sample ground cover targets include asphalt, concrete, grass, dirt, deciduous vegetation, painted steel, and two linear mixtures of some of these common classes.

Although several of the curves exhibit strong slope features, the features in the sensor-reaching radiance spectra are largely (but not wholly) attributable to atmospheric absorption. This claim is supported by inspection of the radiance curves for the chosen ground cover targets, shown in figure 4.14. It is magnitude, not spectral features, that is the prime determiner of how spectral calibration errors will manifest, though the “red edge” present in several of the target reflectance spectra

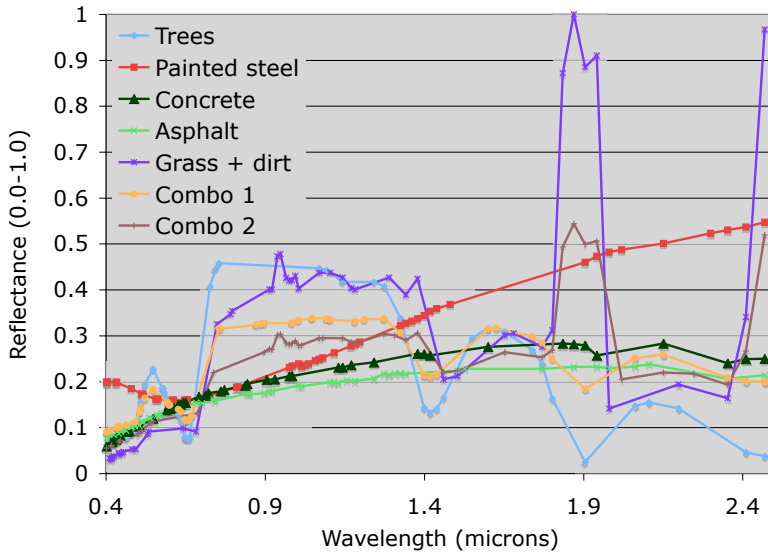


Figure 4.13: Reflectance curves used to simulate spectral cal errors

serves as a prominent exception. This feature is strong enough to co-dominate, yet atmospheric effects still appear prominent in the results of the original simulation in figure 4.12. The conclusion is that strong spectral features can induce error in retrieved reflectance, but significant error will exist anyway for any target because of the atmosphere and overall target brightness. This error concentrates near the various atmospheric absorption features, which are spectrally invariant (though their width may change with atmospheric composition).

A simulation was conducted using a notional band model, a ± 2 nm shift in band center, and the ground cover targets presented in figure 4.13. The band model uses 211 bands, ranging between 400 and 2500 nm on 10 nm centers and Gaussian response curves, with 10 nm between 50% response points (full-width half-max, or FWHM). Results for the band center shift study are shown in section 5.4.

4.12.3 Ground radiometer

A dual-input ground radiometer is a sensor configuration meriting individual attention. A dual-mode reflectometer measures both the ground-reaching irradiance and the ground-leaving radiance. It can determine the target reflectance despite frequent time-domain changes in the radiance environment because the two inputs

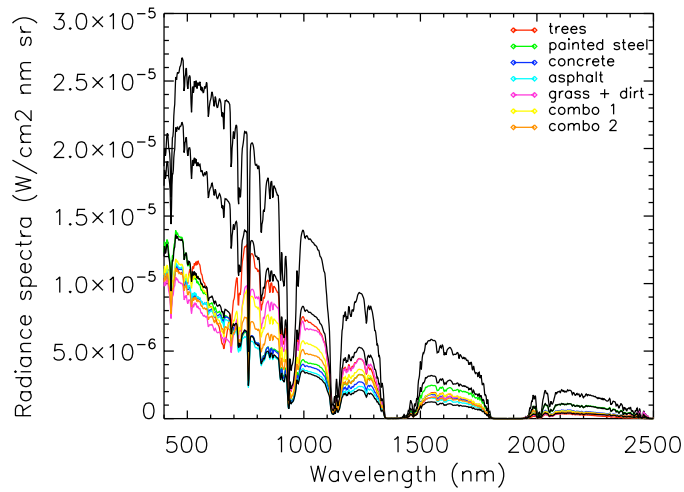


Figure 4.14: Radiance curves used to simulate spectral cal errors. The black curves represent results for a 100%, a 50%, and an 18% reflector. The colored curves correspond to results for each of the 7 target types shown in figure 4.13.

sense the same illumination at all times. A notional illustration of this configuration is shown in figure 4.15. In the figure, one input head points towards a target to measure ground-leaving radiance. The other points straight up with a cosine head attachment (depicted as a hemispherical diffuser, though they are also flat) to measure total irradiance.

A simple derivation of ground instrument error is provided for this case so that it these types of ground instruments can be incorporated into the error propagation model to study error reduction scenarios. Other than the geometric configuration allowing a reduction in mathematical complexity, the error considerations for these sensors is the same as for the instruments described above. The irradiance head measures total irradiance as shown in equation 4.58. The other head measures the same energy as radiance after it is reflected off the ground target. This is shown in equation 4.59, where E indicates spectral irradiance in units of W/m^2 , M is spectral exitance in the same units, and the G subscript indicates energy incident to or leaving the ground. The signals from each head are indicated by v_1 and v_2 . The ratio of these signals can be used to determine the target's Lambertian reflectance per equation 4.60.

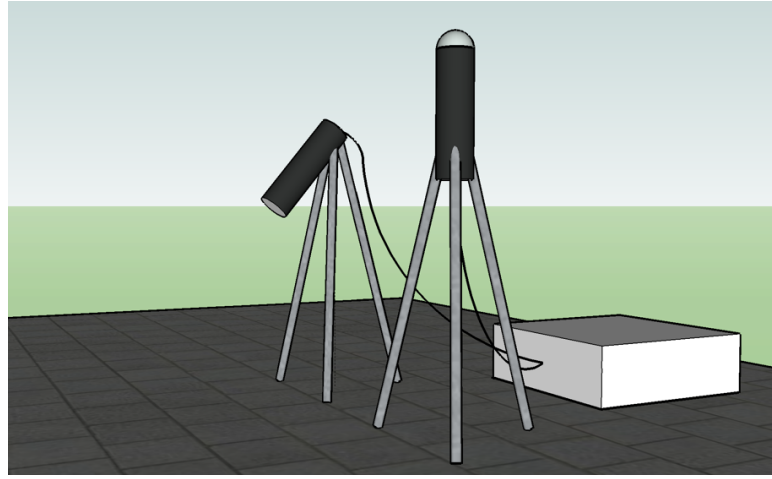


Figure 4.15: Ground reflectometer in dual-input configuration

$$v_1 = E_G = E_s \tau_1 + \int_0^{2\pi} \int_0^{\frac{\pi}{2}} L_d(\sigma, \phi) \cos \sigma \sin \sigma d\sigma d\phi \quad (4.58)$$

$$v_2 = L_G = \frac{M_G}{\pi} = r \frac{E_G}{\pi} \quad (4.59)$$

$$r = \frac{v_2 \pi}{v_1} \quad (4.60)$$

The error analysis is applied in the usual manner, as seen in equation 4.61. Although both radiometer heads are assumed to have the same instrument noise, it is necessary to use equation 4.59 to convert one measurement into the units of the other.

$$\begin{aligned} S_r^2 &= \left(\frac{\partial r}{\partial v_1} S_{v_1} \right)^2 + \left(\frac{\partial r}{\partial v_2} S_{v_2} \right)^2 \\ &= \left(\frac{-v_2 \pi}{v_1^2} \right)^2 S_{v_1}^2 + \left(\frac{\pi}{v_1} \right)^2 S_{v_2}^2 \\ &= \left(\frac{r}{v_1} \right)^2 S_{v_1}^2 + \left(\frac{\pi}{v_1} \right)^2 \left(\frac{r}{\pi} S_{v_1} \right)^2 \\ &= \frac{2r^2 S_{v_1}^2}{v_1^2} \end{aligned} \quad (4.61)$$

If instrument noise is reported as a spectrally flat percentage of the signal, a further simplification is possible. If the noise factor is k , where k would be 0.03 for an example noise level that is 3% of the signal, then equation 4.62 shows the final form. In reality, just as for imaging spectrometers, spectral noise response for field instruments is not flat, though some report the constant factor merely as an upper bound for the noise.

$$S_r = \sqrt{2}kr \quad (4.62)$$

4.12.4 Mechanical factors

Knowledge of the sensing platform's physical environment is an obligatory piece of the remote sensing equation. Each piece of information is measured with one or more truth instruments and stored along with the image as engineering, navigation, or other metadata. The quantities include inertial position, airspeed, roll, pitch, heading, time, temperature, pressure, and altitude. Instrument, lamp, black body, and scan motor voltages and/or temperatures may also be recorded as applicable. Each piece of metadata indirectly affects the final reflectance solution, and each reading has an uncertainty attached.

The main effect of physical factors is to change the pixel location and size relative to its assumed position on the ground. This is the case with roll, pitch, heading, altitude, and absolute location. However, the error caused by imaging the wrong spot on the ground is something the error propagation model was not designed to handle. Even if a radiometric signature is indexed to the wrong ground spot, it can still be accurately inverted to reflectance.

These same factors can also affect how the radiometric signature is inverted, primarily by changing the assumed path length. They are usually ignored because the differences are small—on the order of 3 degrees or less for the angles and tens of meters in altitude (Clark et al., 1998). Then, if they are included, errors in knowledge of these parameters amount to an even smaller effect.

A similar situation exists with voltage stability of the calibration standards and scan hardware (if applicable). Whereas small voltage variations can cause slight differences in the performance of these components, they can be compensated for down to the level where the voltage stability introduces random error that cannot be compensated for, but this error is extremely tiny.

As a result, uncertainty in knowledge of physical factors are mostly excluded from rigorous propagation under the assumption that their effects reside at a level or two below the detail level included in the rest of the model. There does exist a capability to specify random error in pointing angle, whether it arises from a

stabilized platform or control of a rotating mirror. Even so, with errors possibly on the order of $1 \mu\text{rad}$ for the stabilized platform or 1 mrad for the direct pointing, even this error source was found to be extremely small when placed in the larger context of inversion to reflectance.

4.13 Environmental error models

Environmental errors are parts of the imaging chain whose sources cannot be modeled mathematically. The factors referred to here are target tilt relative to the local terrestrial normal, off-nadir sensor pointing, clouds, and background objects. Their effects are part of the governing equations, but the variables themselves are not predictable; they are organic parts of the imaging environment. This has two critical implications:

1. The error is not reasonably bounded
2. To be fully accounted for, the physical quantity must be measured at every spatial location in the image, or else there will be a guaranteed error

The first assertion refers to the fact that an environment variable can take on any value within a certain range, with the resulting change in apparent reflectance taking on values anywhere from 0 to 100% or more. This theoretical freedom is restricted in practice by behavioral tendencies either in the variables themselves or by how imaging is accomplished, and this alone salvages the situation. The second assertion points to the fact that statistical models are ill-suited for predicting the variability of an environmental term because their variability does not obey a random probability distribution. Hence, spatial propagation techniques can propagate the uncertainty but not the values themselves.

Furthermore, this failure to account for these types of effects introduces a new category of error: systematic bias. Assuming a term is not present when it is creates a direct bias that is mathematically carried along as a separate term, and systematic bias terms are not incorporated into the partial derivative method of computing random error. Although imperfect knowledge of the term does increase the amount of random error, leaving it out completely does not affect the random error. An intuitive example of this is taking a series of measurements with a ruler. The measurements themselves will vary according to some random measurement error, but if the ruler has an inch of wood sawed off the back end, all of the measurements are biased in a deterministic way. Whereas random error is denoted as S , a Δ is used to indicate a systematic or non-random bias. Equation 4.63 recalls the basic

expression of this fact for reflectance. The variable r represents the true value, and the variable \hat{r} represents the imperfect estimate. Keeping with this convention, variables with the hat are also imperfect estimates or, in this case, values that do not fully account for one of the environmental effects.

$$\Delta r = \hat{r} - r \quad (4.63)$$

These concepts will now be discussed in the context of each environmental term, and the methodology by which each was modeled is presented. The final forms for reflectance bias were previously presented in section 4.6.4. What follows is a discussion of how the component terms were actually determined.

4.13.1 Target tilt

The target tilt is part of the variable $\sigma_{s'}$, the solar zenith angle from the target plane's frame of reference. Figure 4.16 shows the angular relationships between the solar zenith angle σ_s and the local solar incidence angle σ'_s . The model for bias error resulting from assuming the target plane is the same as the local tangent plane is given in equation 4.40. The change in direct solar irradiance is simple to adjust for, but the model does not automatically adjust the diffuse radiance for the loss of downwelled sky radiance and the addition of terrain-based background radiance (however, the model allows this to be set manually). It is also assumed that the tilt is low enough such that the target is not placed into shadow.

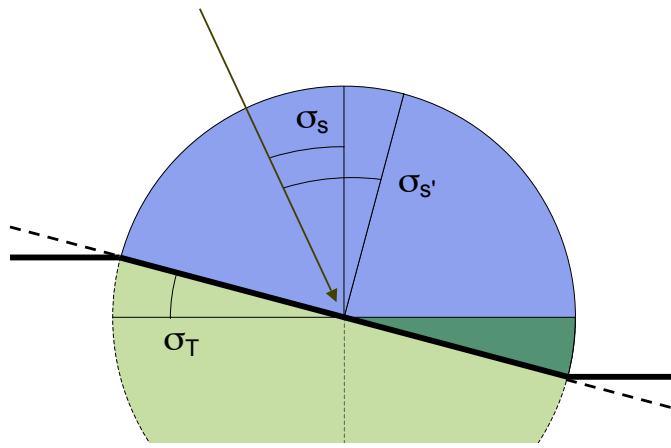


Figure 4.16: Tilted target relative to the local horizon

The tilt of the local normal can range from 0–90°, which in turn can cause the apparent reflectance to range from 0 to over 100% of its actual value. This is mitigated by the fact that terrain normally does not contain sharp inclines, but there is no reason why this could not be the case. Geologic and human features both cause spatial discontinuities statistical models are powerless to predict. Additionally, the process of building a statistical model strong enough to adequately describe an area produces the kind of full-scene data set required by the second assertion. The statistical model must adequately capture not just the altitude variability, but also the *angle* variability, and they two are very different things.

A simple terrain scenario, shown in figure 4.17, was constructed to illustrate a limitation of elevation measurement with respect to sample spacing. It shows a piece of terrain in which a hill causes a 10 meter change in elevation over a 20 meter distance (a 26° incline). The terrain is sampled at 30 meter intervals, which corresponds to an SRTM product.

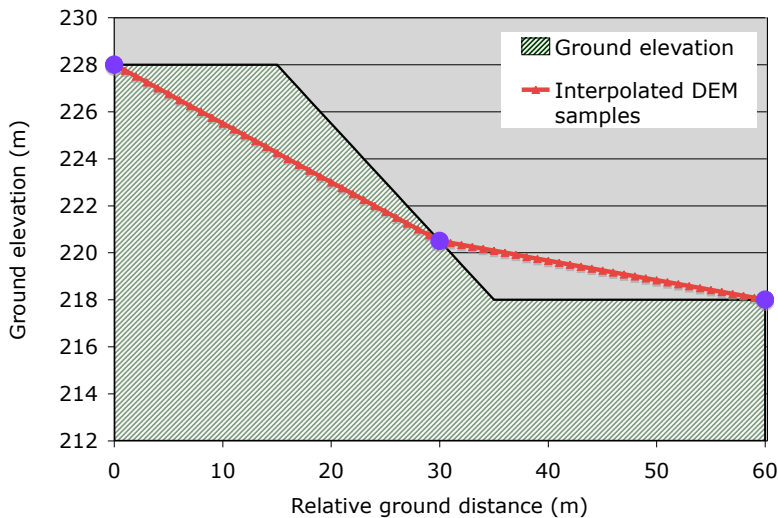


Figure 4.17: Elevation measurement scenario

In this simple demonstration, the elevation and angular deviations are computed and presented. Linear interpolation is performed between the sample locations to produce an assumed elevation for each point in between. The local terrain angle is also calculated for each point. The differences are presented in figures 4.18 and 4.19. Using the numbers from the example, the elevation is never more than 5 meters away from the true value.

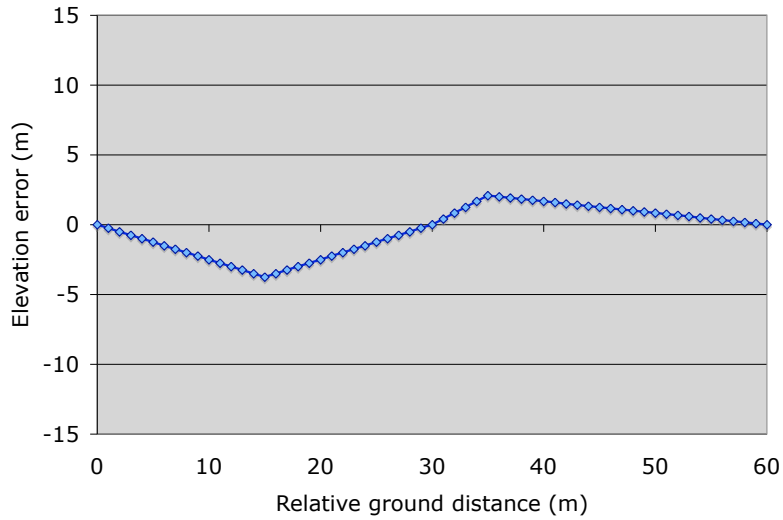


Figure 4.18: DEM interpolation error in elevation

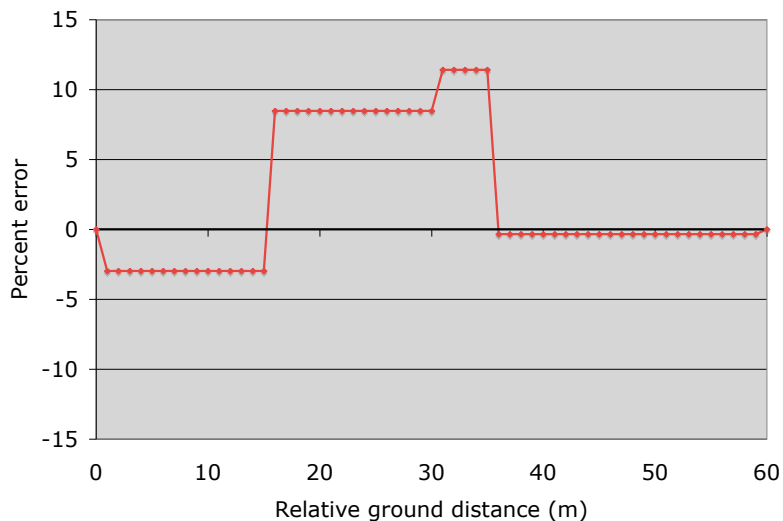


Figure 4.19: DEM interpolation error in direct solar term

When using the altitude as an input to atmospheric modeling, the DEM uncertainty is far below the uncertainty attributable from other sources (as will later be shown), showing the DEM's sufficiency for that purpose. However, the angular differences are more pronounced. The ratio of the cosines of both angles was taken to show how the changes in angle would affect the direct solar irradiance term where the cosine of the tilt angle plays a part.

Even though the DEM sampling is never more than 15 meters away from a change in terrain elevation, including one sample point directly on the incline, there is still a great deal of error in the tilt angle. The sample point that falls directly on the slope is also the region with the highest angular error, which was a 12% difference in the cosine term. Using equation 4.40, this translates to between roughly 4% and 8% reflectance error depending on spectral band. Since blind usage of DEMs has been invalidated, there is little recourse with respect to predicting the terrain angle. The error propagation model accommodates tilt angle errors in two ways. First, it provides a gross bias error estimate based on the assumption that the tilt angle is 0° . When the scenario specifies an actual tilt of 0° , the bias error is also zero. When the target's true tilt angle is non-zero, this error term is permitted to grow. Secondly, an input is provided to specify tilt angle knowledge error. The model is agnostic as to the source of the knowledge error: it may be due to simple measurement error or something more complex, such as a study attempting to statistically parameterize angle error as a function of DEM resolution and terrain variability. While physical-world drivers of tilt angle error are not handled, the error source itself can be given specification values to compare with other sources and provide a threshold at which this source becomes dominant.

4.13.2 Clouds

Clouds are a difficult subject to treat. Their spatial positions and frequency are not predictable, they come in several different varieties, and sometimes change faster than they can be measured. Their abundance frequently runs the full range from clear sky to full coverage, eliminating direct solar irradiance and possibly greatly reducing diffuse sky radiance. Alternately, they can increase the radiance of some spectral bands. Unpublished empirical data suggest that clouds that graze direct solar rays may even increase the total irradiance above 100% of the sun's irradiance. Airport observations provide percent cover, layer thickness, and altitudes, but no positional information. It is possible to visually estimate cloud position, but not in a way that produces radiometric accuracy. It has also been shown empirically that clouds can cause extraordinary spatial variability in ground-reaching radiance over distances on the order of 1 km or less (Klempner et al., 2006). Because clouds have

a potentially drastic effect on the results and their temporal and spatial variability make them extremely difficult to model, measure, or predict, it can be safely said that clouds truly are the bane of remote sensing in the visible and near infrared spectrum.

Clear days are sometimes called “good remote sensing days,” and cloudy days are not. The fact that an overcast sky eliminates direct solar irradiance is counterbalanced by the fact that data collects for radiometry are never carried out on overcast days. Regardless, the factors described above make clouds not only hard to compensate for in imaging, but they also greatly complicate the modeling process. The modeling approach here will be approximate in the hope that it can at least provide representative results and act as a guidepost for future modeling research. It may be possible in the future to parameterize cloud characteristics to radiance variability, but it is currently not possible. A very narrow subset of the wide range of cloud conditions will be modeled using a numerical approach published by Fairbanks (1999) and extended by Bartlett (2006).

Cloud type selection

Four different types of cloud conditions are illustrated in figure 4.20. The first (figure 4.20(a)) is a monolithic slab of infinite horizontal dimension simulating an overcast day. This is the type of cloud MODTRAN uses. Because the code is geared towards calculating the radiance onto a single point rather than a 3-dimensional scene, this is the most appropriate type of cloud for it to use. The fact that the code calculates radiance coming from the entire 3-dimensional hemisphere may make this fact to be counterintuitive. Regardless, the user can specify the altitude, thickness, and composition of the cloud layer; MODTRAN does the rest. The other end of the realism spectrum is shown in figure 4.20(b). Clouds are 3-dimensional objects floating in air. They receive radiance directly from the sun at a slant angle, diffuse sky radiance, and reflected radiance from the ground underneath. The radiance is absorbed, scattered, and reflected in all directions. Depending on the angle to the viewer, radiance leaving the cloud may be transmitted solar radiance or reflected sky radiance, or a combination of both. Finally, clouds can have “texture,” meaning they have fine spatial structure that has both highlights and shadows. The wide domain of cloud types led to the decision to pare the field down to cumulus, stratus, and altostratus clouds. For each type, dark (figure 4.20(c)) and bright (4.20(d)) variants were created to simulate the highlights and shadows that result from direct and indirect solar illumination as well as absorption or transmission through the cloud itself. This gives a bare-bones toolset to start building cloudy skies.

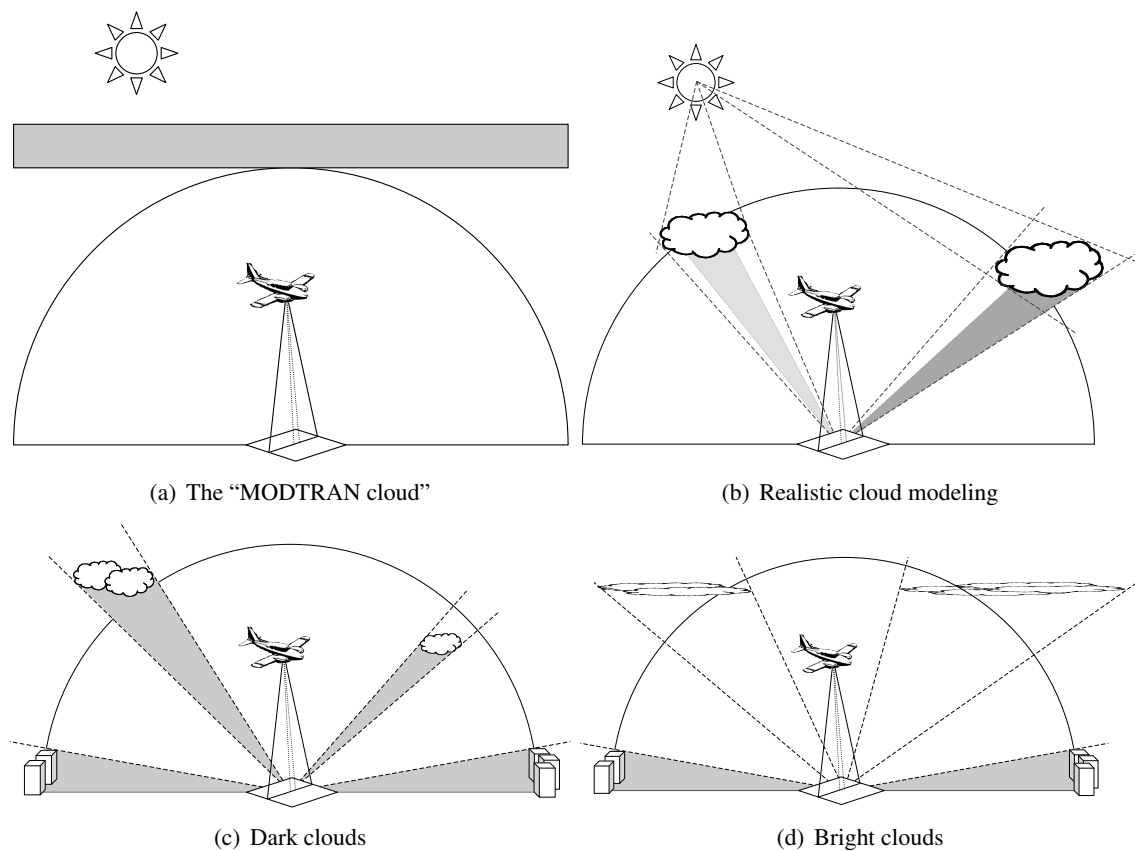


Figure 4.20: Cloud concepts

Cloud modeling approach

Although it seems primitive, the “MODTRAN cloud” is enough to provide basic radiometry information needed to model cloud variability. The sky is divided up into equiangular quads defined by azimuth and zenith angles. For each azimuth and zenith angle combination a MODTRAN run is generated where the sensor view angle is defined by the azimuth and zenith. For dark clouds, the sensor looks from underneath the cloud deck looking up. For bright clouds, the sensor is placed above the cloud deck looking down. From the run the total sky (direct and diffuse) radiance from that particular direction is saved into a database. Global simulation scenario settings determine the spectral bin sampling, time of day, and time of year, so the resulting spectrum database is portable to different azimuths but not different zenith angles. An “endcap” for each hemisphere is used to simulate the radiance directly overhead.

Two quad division schemes were used. The low resolution quad database uses 6 zenith positions, 12 azimuth positions, and a 15° endcap for a total of 72 quads. The high resolution quad database uses 17 zenith positions, 72 azimuth positions, and a 5° endcap for a total of 1224 quads. Figure 4.21 shows the populated clear-sky databases. The brightest spot in each figure corresponds to the sun’s location, and the brightness of each quad represents the scaled panchromatic radiance. Figures 4.21(c) and 4.21(d) show a two dimensional representation of the quad map. Radial distance from the center represents zenith angle ranging from 0° in the center to 90° at the edge. Azimuth angle is represented by the angular distance around the circle, with 0° aligned with the +x-axis. Figures 4.21(a) and 4.21(b) show the same information in vertical relief to show the relative contribution of quads close to and far away from the sun. The last pair of figures, 4.21(e) and 4.21(f), present the most intuitive view, where each quad is spatially placed relative to an observer or target in the center. In all cases, the endcap circle is clearly visible. The simulation results also agree with similar results presented elsewhere (Schott, 1997).

To model a desired sky configuration, quads are turned “on” or “off” in a simple configuration array. An integer number for each position tells the sky builder code to use clear sky, a dark cloud, a bright cloud, or nothing at all. This interface is highly extensible and lends itself well to other applications, such as automated modeling of sky hemisphere photos that have been processed into cloud maps and thresholded. The sky builder then calculates the downwelled radiance. The basic expression for downwelled irradiance is given as equation 4.64, where radiance L from any direction in a clear sky is a function of the scattering phase function and the angles. The function $L(\sigma, \phi)$ is shown in figures 4.21(a) and 4.21(b), with the angles ϕ and σ coming from the spatial positions of each point.

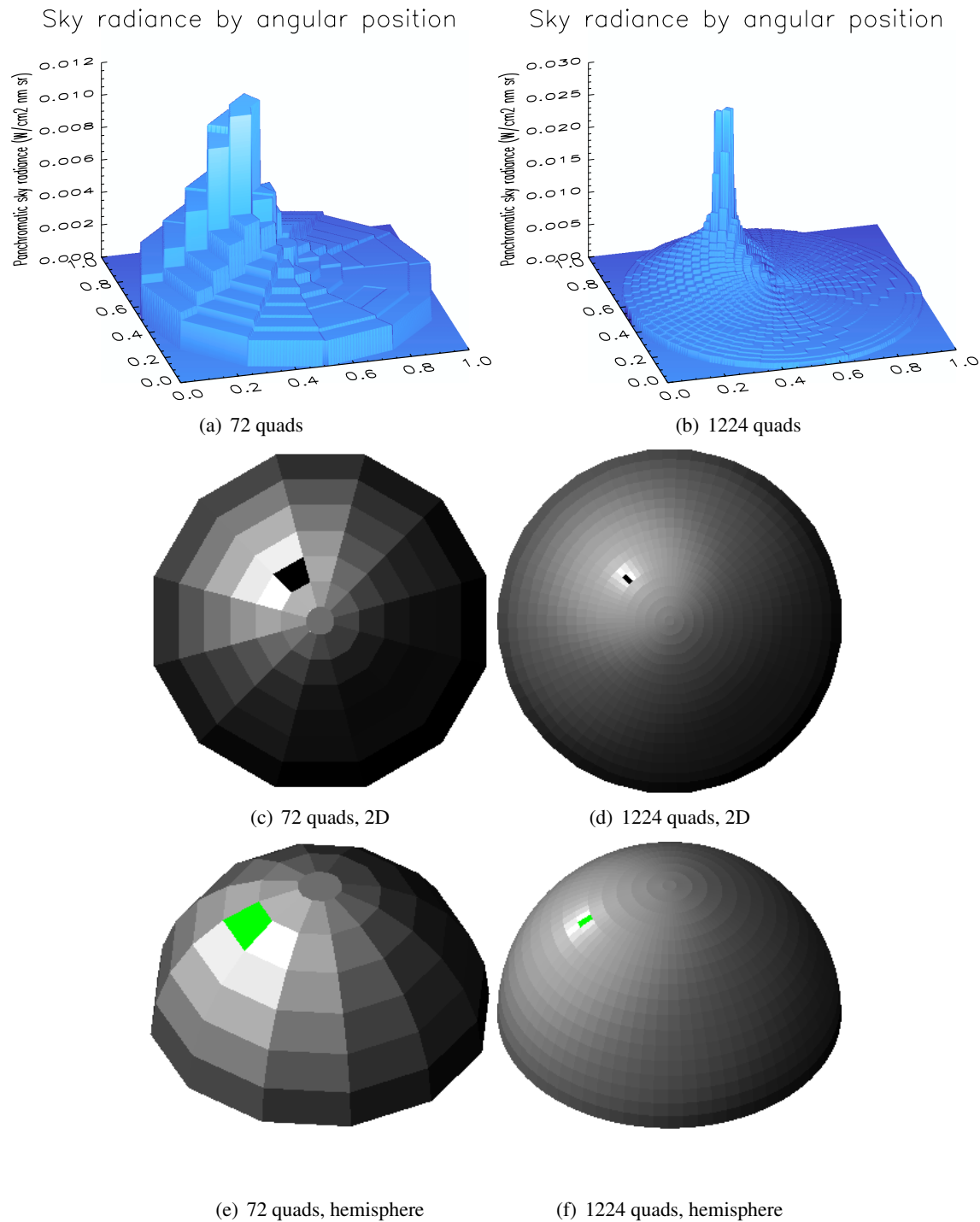


Figure 4.21: Clear-sky radiance results for 72 and 1224 quads

$$E_d = \int L(\sigma, \phi) \cos \sigma d\Omega = \int_{\phi=0}^{2\pi} \int_{\sigma=0}^{\frac{\pi}{2}} L(\sigma, \phi) \cos \sigma \sin \sigma d\phi d\sigma \quad (4.64)$$

The discrete approximation form of equation 4.64 is shown in equation 4.65. The terms on the right replace the differential terms of the earlier form and represent degrees per quad in both the azimuth and zenith directions: n_ϕ is the number of azimuthal quads, n_σ is the number of zenith quads, and *endcap* is the angular diameter of the endcap portion of the hemisphere. The expression is straightforward to calculate.

$$L_d = \frac{E_d}{\pi} = \frac{1}{\pi} \sum_{i=0}^{n_\phi} \sum_{j=0}^{n_\sigma} L(\phi_i, \sigma_j) \cos \sigma_j \sin \sigma_j \left(\frac{2\pi}{n_\phi} \right) \left(\frac{\pi - \text{endcap}}{2n_\sigma} \right) \quad (4.65)$$

Redefining the half-endcap as σ_e in equation 4.66, the expression for the endcap radiance is given by equation 4.67. $L(0, 0)$ is the radiance coming from directly overhead; it is a constant. The two π terms are kept to clarify that the first converts directional irradiance to directional radiance, and the second is part of the solid angle calculation.

$$\sigma_e = \frac{\text{endcap}}{2} \quad (4.66)$$

$$\begin{aligned} L_{d,\text{endcap}} &= \frac{L(0, 0)}{\pi} \int_{\phi=0}^{2\pi} d\phi \int_{\sigma=0}^{\sigma_e} \cos \sigma \sin \sigma d\sigma \\ &= \frac{L(0, 0)}{\pi} \pi \sin^2 \sigma_e \end{aligned} \quad (4.67)$$

Cloud error simulation

The discussion so far provided the guts of the cloud radiance model. It has limitations, but it has enough fidelity to fulfill its stated purpose of quantifying the variability in reflectance inversion due to certain types of cloud cover, namely the types that are modeled here. In other words, the model sets its sights low but soundly delivers. The error propagation methodology can exercise the cloud model to provide additional reflectance bias error due to clouds. To enable this, a cloud error simulation is prepared as follows:

1. Minimum and maximum cloud cover values are chosen in terms of number of quads set to cloud
2. A statistically large number of random cloud configurations are generated
3. A total sky radiance spectrum is numerically integrated for each configuration
4. The root sum square of the difference between each cloudy sky radiance spectrum and the clear sky spectrum is taken
5. The percent sky coverage is calculated for each quad configuration
6. The results are parameterized and saved according to fraction of the sky covered by clouds

As mentioned earlier, a quad is “set” to be a cloud or to clear sky by changing its integer index in the cloud map. In this simulation, 0 in the cloud map represents clear sky, a 1 is a dark cloud, a 2 is a bright cloud, and a -1 is zero radiance (used for obscuration calculations elsewhere in the model). Each random configuration has a certain number of quads active. For example, the first group of random configurations all have exactly 4 quads set to clouds, the next all have 5, and so on until the maximum number is reached. In summary, the following statements are true:

- The number of activated quads in each random configuration set is gradually incremented until the maximum value is reached (roughly half the total number of quads)
- The cloud location and subtype (bright or dark) is random according to a uniform distribution
- The basic cloud type (cumulus, stratus, etc.) is chosen at the outset and not changed
- The multiple scattering algorithm (ISAAC 2-stream or DISORT 8-stream) is chosen at the outset and not changed
- The quad containing the sun is never permitted to be obscured

A statistical approach was chosen as a way to sample the space of possible results. The prime alternative would be to simulate one of every possible quad configuration. Even when optimizing for symmetry, the combinatorial requirements

are staggering, taking more than 4 years for the 72 quad case at 100 radiance calculations per second. The number is incalculable for the 1224 quad case.

The sky fraction is calculated based on the two-dimensional size of each quad relative to the whole hemisphere. Quads at lower zenith angles are smaller than those at higher zenith angles, therefore random configurations of any n quads will contain quads of different sizes, and each n -quad result will be paired with a slightly different sky cover fraction.

Because the cloud type and multiple scattering algorithm are intrinsic to the simulation, each different setting is saved as a separate simulation dataset, available for use depending on the error propagation scenario. However, preliminary results suggest that the multiple scattering algorithm and cloud type have basically zero bearing on the overall error. Factors not considered include the cloud height and transparency. Cloud height (technically cloud *range*) changes the amount of path radiance observed, and transparency allows a more realistic mixture of sky radiance and cloud radiance within a quad.

Finally, cloud shadows were not allowed. Although they are common in scenes, allowing clouds to obscure the sun makes radiometric calculations next to impossible. In short, there is no single thing that can be called a “cloud shadow.” Empirical evidence shows that the radiance within a shadow is constantly changing, even exceeding clear-sky radiance under certain conditions. Other shadows are modeled as equation 3.3 minus the exoatmospheric solar irradiance term; this is not the case with cloud shadows.

Cloud error incorporation

To use the cloud error databases in the error propagation code, the scenario must specify a cloud cover amount and sampling slice width. The sampling slice is conceptually identical to spectral sampling that a sensor does, only with cloud cover. A nominal value of 2% is sufficient to specify sufficient data for a robust error calculation. The bias error for reflectance as a result of cloud-induced changes in downwelled radiance is found from equation 4.43.

All spectra matching the requested sky cover fraction are retrieved and used to calculate bias error. Then, the entire ensemble of bias errors is carried through to the end. No summary statistics are calculated on the bias spectra because the goal is to observe the effect of any one of these possible configurations on the final result. Averaging the cloud spectra together eliminates much of the variability that makes clouds so invidious. Using the average and reporting the variability as standard deviation would merely require another apparatus to communicate the variability, whereas keeping the whole dataset already accomplishes that purpose.

4.13.3 Background objects

Interestingly enough, a separate background radiance term is absent from equation 3.3, the main radiative transport equation. Background objects are often ignored, and rightly so. They are restricted to the horizon, meaning their angle of incidence is usually low. Instead, it is incorporated into the downwelled radiance term of equation 3.5. Their radiance contribution, just like the sky radiance they replace, is always a small contribution to the overall downwelled radiance term. For open space, a terrain masking angle (as illustrated in figure 3.1) of 15° or less requires a 30 ft (9.1 m) tall object to be only 112 ft (34 m) away. At 15° elevation or 85° zenith, the irradiance is less than 25% of what it would be at zenith. However, these are just example calculations, and the situations actually encountered may or may not be greatly affected by background objects. The assumption that terrain masking angle is low is not universally valid. Often, images contain structures, and those structures have pixels next to them, and likewise for trees. Research has been conducted concerning the effects of “treeshine” on target detection algorithms (Raqueno et al., 2005), and whether it is because they can change the spectral character and magnitude of sky radiance or shade the ground from direct solar irradiance, background objects deserve attention.

The mathematical contribution from background objects was detailed in equation 3.5. They are nominally part of the diffuse downwelled radiance term in that they block a portion of the sky that would normally be providing scattered sky radiance and replace it with their own radiance. In a process that is very similar to the cloud error propagation model described earlier, the background object model performs a rudimentary series of simulations to determine that background object radiance and compares it to the clear sky downwelled term.

The background object

Just like with cloud modeling, there is an infinite variety of ways a background object can look to a ground target. The primary equation governing background radiance is equation 4.73. It is a miniature version of the main radiance expression in equation 3.3. The main sources of irradiance incident on a background object are identical to those onto any flat target: direct solar irradiance, integrated diffuse sky radiance, and radiance reflected from the ground. This formulation does not explicitly include radiance that might be coming from other background objects, but implicitly accounts for it in the way ground reflected radiance is determined.

$$\begin{aligned}\frac{L_{bkg}}{r_{bkg}} &= \frac{E_s}{\pi} \cos \sigma'_b \tau_1 + \int_{\phi_b - \frac{\pi}{2}}^{\phi_b + \frac{\pi}{2}} \int_0^{\frac{\pi}{2}} L(\sigma_b, \phi) \cos \sigma_b \sin \sigma_b d\phi d\sigma_b \\ &+ F_{gnd} r_{gnd} \frac{E_s}{\pi} \cos \sigma_s \tau_1\end{aligned}\quad (4.68)$$

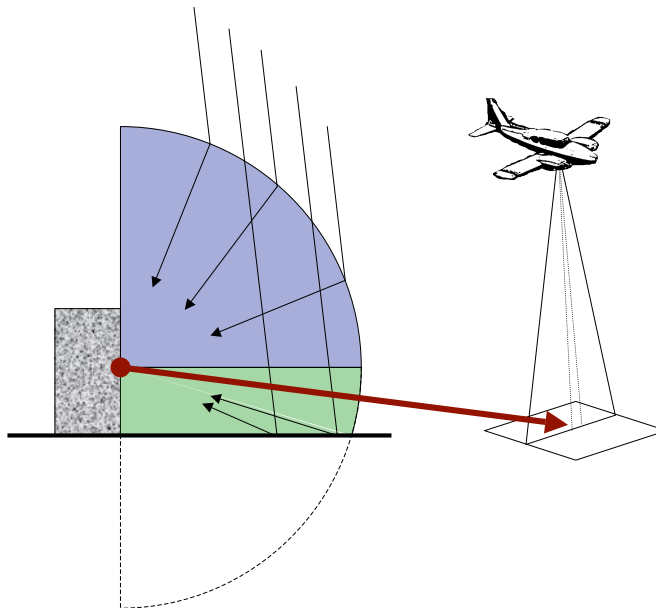


Figure 4.22: Radiance sources for a background object

Figure 4.22 illustrates the terms in equation 4.73. The downwelled radiance term is present, but it is calculated somewhat differently than for a flat target. Only radiance from the half-hemisphere facing the object can reflect off the vertical face. Also, the zenith angle is now rotated by 90° such that rays from directly overhead barely graze the object. Direct solar radiance is also present, but only if the local zenith angle is less than 90°.

The other half hemisphere now views distant background objects and radiance reflecting off the ground. This ground source is significant due to the presence of direct solar radiance reflecting off of it. What is normally downwelled sky radiance for a flat target is now a half-hemisphere of earth albedo. Equation 4.69 shows the half-hemisphere integration for an assumed constant ground albedo. In

reality it is different for each point on the ground, however for modeling expediency a representative spectral profile was chosen. This representative curve was then propagated through MODTRAN to produce total radiance leaving adjacent ground at a 45° slant angle, which was then used as L_{gnd} .

$$\begin{aligned} L_{d,gnd} &= \frac{L_{gnd}}{\pi} \int_{\phi=0}^{\pi} d\phi \int_{\sigma_b=0}^{\frac{\pi}{2}} \cos \sigma_b \sin \sigma_b d\sigma_b \\ &= \frac{L_{gnd}}{\pi} \pi \left(\frac{\sin^2 \frac{\pi}{2} - \sin^2 0}{2} \right) = \frac{L_{gnd}}{2} \end{aligned} \quad (4.69)$$

A single albedo curve was used to model adjacent ground reflectance, and another spectrum was used for the background object reflectance. To attempt to account for statistical variability, each curve was constructed with a linear mixture of representative material type reflectance curves. The curves were taken from the DIRSIG spectral library (Ientilucci and Brown, 2003), linearly mixed according to set, arbitrarily-chosen fractions thought to be representative of typical scenes, and downsampled to MODTRAN's preferred number of spectral points. For adjacent ground, the target was composed of 60% asphalt, 10% concrete, and 40% dirt and grass, assuming that manmade structures would be surrounded by parking lots, streets, and sidewalks, while background trees would be surrounded by dirt and grass. The background object albedo was constructed with 55% trees, 20% painted steel, 20% concrete, and 5% asphalt, again assuming background objects were roughly evenly divided between natural and manmade structures.

Empirical spectrometer measurements of vertical background targets were made and compared with the resulting object-leaving radiance curves. This validation result is shown in figure 4.23. Two side-looking sun-illuminated tree spectra and two mixed tree/asphalt spectra were taken. At the same time a sky radiance spectrum was taken from a portion of the sky 90° of azimuth away from the solar azimuth angle. A simulated downwelled radiance spectrum and four sun-illuminated simulated background object radiance spectra are overplotted on the figure. The simulated and empirical curves roughly match in magnitude and spectral features, with a notable deviation between 400-500 nm, which is believed to be due to path length differences between the simulated and measured spectra. The path length differences would result in differing amounts of path flare caused by molecular scattering, and the spectra with greater path flare would have higher signal in the blue spectral regions, where path scattering is most prominent. This preliminary result provides a degree of confidence that background objects are adequately modeled and can be used in the error propagation simulation.

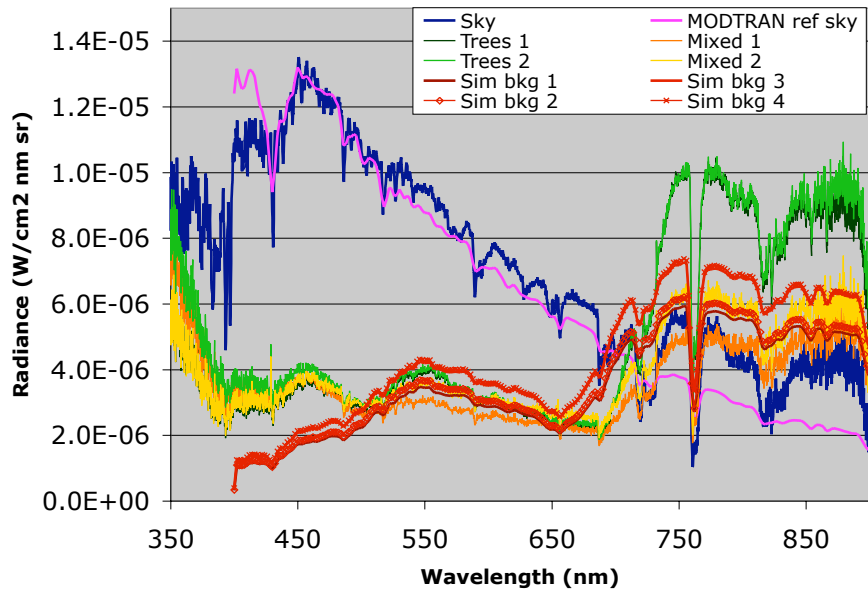


Figure 4.23: Background radiance, measured vs predicted

Background object error incorporation

Building a library of background object radiances follows a procedure very similar to how cloudy-sky downwelled radiance spectra were made. The object was assumed to receive a half-hemisphere's worth of directionally-dependent sky radiance and a constant, isotropic half-hemisphere's worth of ground radiance. The setup is notionally illustrated in figure 4.24, except the angular separation between the solar azimuth and the local normal azimuth is not shown. Since a quad-indexed database will be populated with the results of calculating the adapted form of equation 4.65, and it is known that the half-hemisphere seen by the vertical object is azimuth-dependent, this must be accounted for when building up the quad database.

The azimuthal rotation is implemented by introducing a local axis convention and angular rotation. There is a distinct set of angular rotations for each azimuthal position. This would not normally be so critical, however the dominance of the solar irradiance on the eventual result makes it more important to model direct solar illumination, grazing solar illumination, and shaded cases of background radiance. A full set of background objects placed at each of the different azimuth angles is

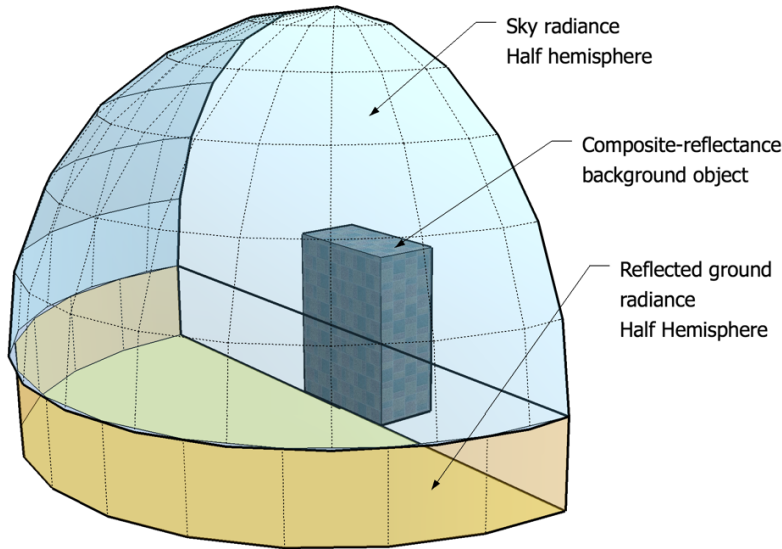


Figure 4.24: Quad integration approach for background objects

shown in figure 4.25.

No matter what azimuth rotation scheme is used, there must be at least one coordinate transformation to account for the change from a flat target to a vertical target. The local reference system is comprised of an x-axis unit vector pointing in the 0° azimuth direction, a z-axis unit vector pointing up in the direction of the local normal, and a y-axis unit vector oriented to make a right-handed system. The axis rotation is accomplished by rotating $+90^\circ$ about the local x-axis. The generic transformation matrix about the x-axis is given as follows, where θ_x is a generic angle of rotation about that axis:

$$\mathbf{T}_x = \begin{bmatrix} 1 & 0 & 0 \\ 0 & \cos \theta_x & \sin \theta_x \\ 0 & -\sin \theta_x & \cos \theta_x \end{bmatrix}$$

To orient the object's face with a particular azimuth, the face is rotated about the z-axis before the x-axis rotation. This would be equivalent to performing a y-axis rotation after the x-axis rotation. The z-axis coordinate transform is defined as:

$$\mathbf{T}_z = \begin{bmatrix} \cos \theta_z & \sin \theta_z & 0 \\ -\sin \theta_z & \cos \theta_z & 0 \\ 0 & 0 & 1 \end{bmatrix}$$

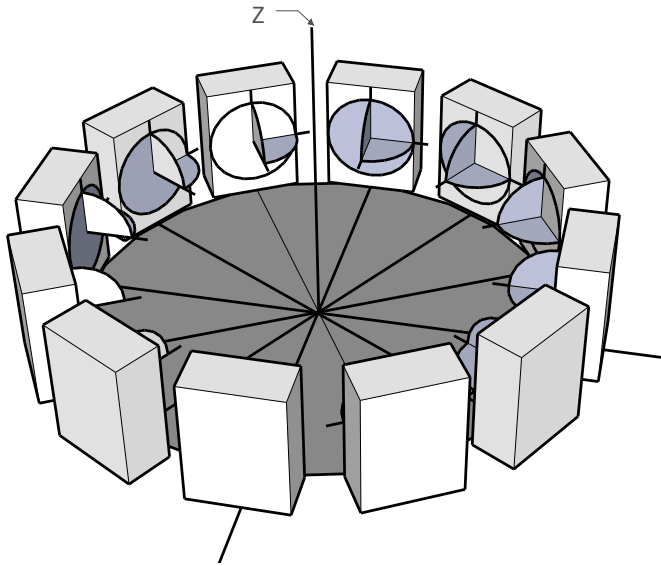


Figure 4.25: Azimuthal variation in simulated background objects

In this case, the generic rotation angle θ_z is replaced by $\phi - \pi/2$, where ϕ is the azimuth to the object. Thus, an object at 0° azimuth relative to the final target faces back towards the center at an azimuth of 180° . The angle used for ϕ in the transform is 0° .

Implementation of the transforms is accomplished in equation 4.70. The vectors \mathbf{X} and \mathbf{X}' are relative to a three-axis orthogonal reference. They relate to the polar coordinates being used through equation 4.71.

$$\mathbf{X}' = \mathbf{T}_x \mathbf{T}_z \mathbf{X} \quad (4.70)$$

$$\begin{bmatrix} x \\ y \\ z \end{bmatrix} = \begin{bmatrix} \rho \cos\left(\frac{\pi}{2} - \sigma\right) \cos \phi \\ \rho \cos\left(\frac{\pi}{2} - \sigma\right) \sin \phi \\ \rho \sin\left(\frac{\pi}{2} - \sigma\right) \end{bmatrix} \quad (4.71)$$

Following transformation to the rotated frame, the rotated angles are obtained through 4.72. In practice only the new zenith angle is required, but it is a function of both the original azimuth and zenith that were relative to the local horizontal.

$$\begin{bmatrix} \rho' \\ \phi' \\ \sigma' \end{bmatrix} = \begin{bmatrix} \sqrt{x'^2 + y'^2 + z'^2} \\ \arctan \frac{y'}{x'} \\ \frac{\pi}{2} - \arcsin z' \end{bmatrix} \quad (4.72)$$

Following this method, a different set of quads can be set to be “visible” by the vertical background object for each azimuth position. The quads visible by the tilted object were chosen in the local horizontal reference frame to be the half-hemisphere of quads directly opposite the object. Those radiances are indexed to the unrotated frame and do not require transformation so long as the correct quads are activated and the other quads are set to zero radiance contribution. The rotated angles are used in the cosine and sine terms of the calculation.

$$L_{sky,bkg} = \sum_{\phi} \sum_{\sigma} L(\sigma, \phi) \cos \sigma' \sin \sigma' d\phi d\sigma \quad (4.73)$$

Once the database of background object-filled quads has been built, using the database to generate sets of randomly configured quads is identical to the process used to index sky fraction obscured by clouds to cloudy-sky radiance. A key difference is that in this specific implementation of background object radiance simulation, background objects were assumed to only occupy the lowest elevation (highest zenith) ring of quads. Since all quads corresponding to a particular zenith are the same size, the relation of sky fraction obscured by background objects to number of quads takes on discrete values; a certain number of quads set to background always produces the same sky fraction. This could change in subsequent simulations if more zenith rings were permitted to take on background object radiances. Other than this, the process of generating random quad configurations and collecting their effects on downwelled radiance is identical to the process used to model clouds. The propagation of bias error into final reflectance is accomplished using equation 4.43.

4.13.4 Pointing

Off-nadir sensor pointing is a self-limiting exception among environmental effects. First, while it is possible to drive the radiance reflected off the ground to zero by sufficiently increasing the view angle, this is impractical because the image pixel would no longer be in the image. Second, it is trivial to know the exact pointing angle (within a degree of random error) for every pixel in the image, so the intractability introduced by the second implication above does not apply. Third, model-based inversion algorithms can account for off-nadir pointing effects

without external adjustment because an off-nadir effect is functionally identical to a spatial variation in the atmospheric parameters.

The nadir vector originates at the sensing platform and is collinear with but has the opposite sign of the normal vector of the terrestrial point directly below the platform. The pointing angle, which will be called ψ , is the angle between this vector and the vector along which photons travel into the sensor. Depending on the sensor's basic architecture, the details of how this is precisely defined varies. However, the vector's definition is external to the sensing platform. The setup is shown in figure 4.26.

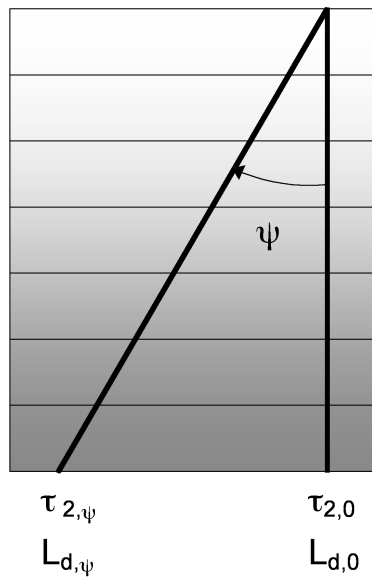


Figure 4.26: Nadir and off-nadir pointing terms

To account for the effects of pointing off-nadir, changes in upwelled radiance (L_u) and ground-sensor transmissivity (τ_2) due to path length differences must be modeled. The same MODTRAN scenario is run multiple times using different zenith angles. In the terminology here, nadir-pointing corresponds to a zenith angle of 180° . It is also possible to vary the azimuth angle. Figure 4.27 shows the result of sampling this parameter space for upwelled radiance at 550 nm. The figure takes on the shape of a bowl where each azimuthal position around the bowl corresponds to an azimuth and distance from the center represents a different pointing angle, which ranged from -45° to $+45^\circ$ off nadir. The bowl appears to be symmetrical,

but this is just a result of how the space was sampled. The actual center of the bowl for upwelled radiance is off-center based on the position of the sun. The “off-nadir bowl” for τ_2 actually is symmetrical and points downward rather than upward. This figure has a distinct realization for every wavelength.

Upwelled radiance by azimuth and angle

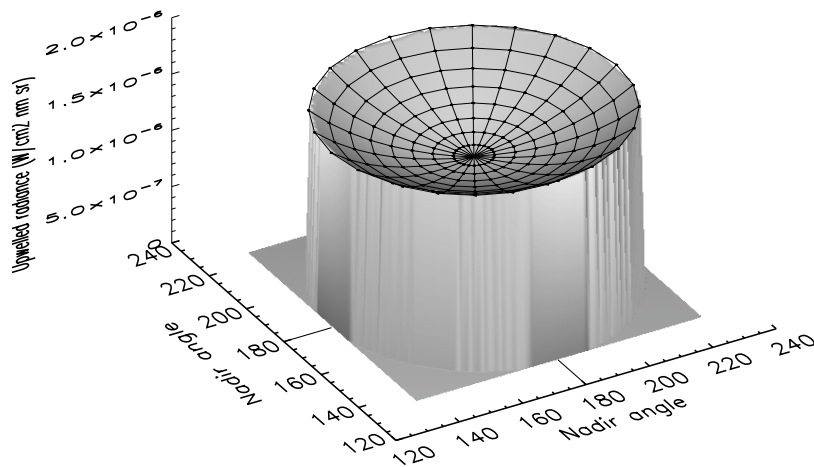
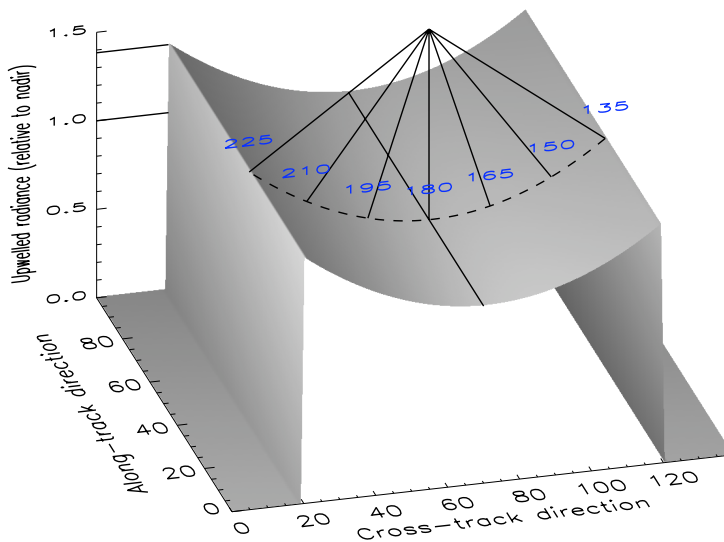
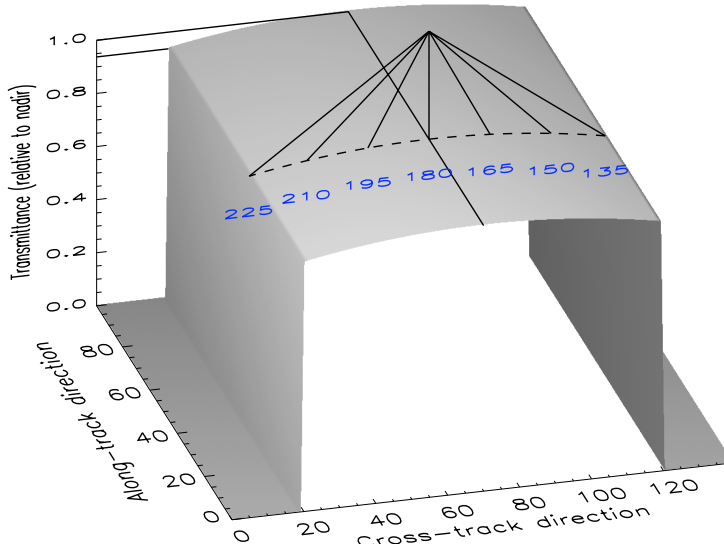


Figure 4.27: Upwelled radiance by azimuth and nadir angle

In practice it is unnecessary to sample different azimuths because a sensing platform’s motion will define an along-track and cross-track direction. The along-track direction will define the azimuth used for the off-nadir angle sampling. The cross-track off-nadir pointing results are assumed to be the same for every imaging line, meaning the sensing platform altitude and sun angle do not change across the image. This smearing of one azimuth in the along-track direction is shown in figures 4.28(a) (upwelled radiance) and 4.28(b) (transmissivity).

Results were generated for a sensor at 792 m (approximately 600 m above ground level), 4 km, 11 km, and 100 km and will be presented in section 5.5. The altitude used is user-selectable. Once the desired dataset is unpacked, a fourth-order polynomial curve is fit to each wavelength and sent to the error propagation model, which uses the coefficients to reproduce the off-nadir L_u and τ_2 results for

(a) Upwelled radiance, L_u (b) Transmissivity, τ_2 Figure 4.28: Variation in L_u and τ_2 by pointing angle, relative to nadir

any angle. The sensing scenario specifies the off-nadir pointing angle, for which the bias error is calculated using equation 4.38. Random error due to pointing angle knowledge uncertainty is analytically calculated from the first derivative of the curve fit, with the result added in quadrature with other types of errors in these two terms.

A final note on pointing error is that the multiple scattering algorithm was found to be significant. The two options built into the model are Isaac's fast-but-inaccurate two-stream algorithm and the more rigorous discrete ordinate (DISORT) algorithm using 8 streams. The two-stream algorithm was found to be adequate in calculating a numerical derivative using the relative differences in close proximity to a central value (section 4.7). However, discrepancies of up to 1% of the upwelled radiance were observed at lower wavelengths, so, as with the numerical derivatives, the DISORT multiple scattering algorithm was used out of prudence.

4.14 Scenario setup

Given a full set of error models capable of covering each term in the governing equation, a baseline set of parameters was established for all error modeling efforts. Any results are anchored to specific scenario parameters, particularly the geometric conditions, so this scenario baseline is necessary to a controlled and comprehensible approach to generating results. The tradeoff of restricting modeling to one specific scenario is a loss of generality, but this cannot be avoided. Second, third, or more scenarios can be added at any time and are left to future work. It is sufficient for this work to demonstrate and validate the modeling method and use the results to draw conclusions about this set of scenario parameters and perhaps others similar to it. The specific scenario parameters are presented in tables 4.1, 4.2, and 4.3. It is key to fix the geometry and atmospheric baseline because in a non-linear system, the sensitivity curves change in response to changes in these parameters. In a developmental context, fixing a single set of parameters facilitated exploration of the research space, requiring tens of thousands of MODTRAN runs. Once the methodology is established, less than 10 MODTRAN runs are required to establish the radiometric modeling baseline, which must be reconstructed for the particular geometry of each image.

Table 4.2 includes several parameter options that are selectable at run-time. These exist only for model demonstration purposes and would be unnecessary in an operational version of the model. Altitude selection allows the model presentation to show any differences between airborne and spaceborne sensors with regards to uncertainty caused by systematic and random nadir angle errors. The sample sensor

Table 4.1: Baseline Scenario Geometry

Parameter	Value
Date	May 12, 2006
Time	15:35:35 GMT
Latitude	42.93° N
Longitude	78.73° W
Ground altitude	0.218 km

Table 4.2: Baseline Sensor Parameters

Parameter	Value	Options
Sensor altitude	100 km	792 m, 4 km, 11 km for pointing errors only
Sensor pointing	nadir (0°)	0–45°
Band model	400–2500 nm (2 nm centers)	-
Band response	triangular, 4 nm FWHM	-
Noise model	none	AVIRIS (1997-9 cals), Hyperion, HYDICE

Table 4.3: Baseline MODTRAN Atmospheric Parameters

Parameter	Value	Model Capability
Atmospheric profile	1976 Standard atmosphere	Complete control at 36 altitude levels
Water vapor profile	midlatitude summer	any
Multiple scattering	ISAAC 2-stream (at ground)	DISORT 8-stream
Target altitude	0.218 km	0–5 km
Visibility	15 km	2–100 km
Water vapor	2.0 g/cm ²	0–2.63 gm/cm ² (varies by model)
CO ₂ concentration	373 ppm	any

noise models exist to exercise the portion of the model that accounts for calibration uncertainty. Finally, table 4.4 lists several other model options that are not included in the baseline configuration but can be added to predict the relative magnitudes of various effects in relation to the standard error sources. These include ground tilt, cloud cover, and background object cover. The modeling methodology for these was described in earlier sections, and the input ranges are listed in the table. Finally, it is critical to note target reflectance can be specified either as a spectrally constant scalar or as a spectrum.

Table 4.4: Other Selectable Parameters

Parameter	Specified As	Range
Ground tilt	Angle in degrees	0–45°
Cloud cover	Sky fraction, 0–1.0	0–0.45
Cloud cover knowledge	Sky fraction uncertainty	0–0.2, 0–0.05 typical
Background objects	Sky fraction, 0–1.0	0–0.25
Background object knowledge	Sky fraction uncertainty	0–0.1, 0–0.05 typical
Target reflectance	Scalar or spectral vector	0.0–1.0

The default scenario conditions were chosen to blend conditions at Buffalo International Airport and Rochester Institute of Technology. Buffalo’s location and altitude were used so the results could be correlated with historical meteorological data collected at the National Weather Service station, in particular the temperature, pressure, dew point, and radiosonde data. Sensing geometry was taken from an airborne imagery collect over RIT so that radiance results could be compared to the collected data. These parameters include primarily date and time, but one of the sensor altitude options built into the model matches the aircraft altitude during the collect. The collected imagery and metadata together did not produce a useful data set that could be used to validate this work, so the scenario selection rationale is now immaterial. In general, the important thing is that the scenario parameters used match the actual or expected collection geometry treated by the model’s application.

4.15 Validation

Validation is a key task for any scientific work. It was listed as an objective of this investigation, and both simulation results and real-world collection data were

planned to be part of the validation process. Because claims are made regarding uncertainty in absolute terms rather than relative terms, it is imperative that some level of confidence in these results is generated. MODTRAN simulation is used to generate statistical distributions of retrieved reflectance resulting from uncertainty in atmospheric constituents. Despite the initial plan to also use actual collection data to validate these and other results (such as the environmental effects), it was discovered that parts of this approach bordered on the impossible. It is feasible to perform atmospheric inversion with actual constituent determination and perturb these constituents to increase the error, but validating effects such as cloud and background radiance using statistical language and real-world data introduces a host of approximations and imprecisions that tend to negate the value of the validation effort. The assumption here is that if simulation can be used to validate the analytical techniques of error propagation, then higher confidence can be placed in other parts of the model employing the same error propagation techniques.

It is claimed that the error propagation model delivers the ability to tie constituent errors with environmental errors and propagate both into reflectance space. Despite the many plug-in sub-models built to hang off it, the core engine is the most critical piece to validate. Thus, a final validation approach was selected that balances effectiveness with simplicity, focusing on just the core propagation capability. The ability to predict a statistical distribution without instantiating random variables is the model's primary value. The validation approach will compare the deterministic results with actual random results for identical atmospheric and geometric scenarios.

A Monte Carlo-style simulation was constructed in which a retrieved reflectance error is simulated by inducing error in the atmospheric parameters. The simulated situation is shown by equations 4.74 and 4.75. Equation 4.74 represents the truth state, and equation 4.75 represents an erroneous retrieval. The total calibrated radiance is the same, but due to supposed errors in atmospheric constituent determination, the estimated reflectance (and by extension the estimated component radiance) is off by some amount. The terms r and \hat{r} represent the true reflectance and the erroneous retrieved reflectance. The atmosphere operator is fixed but imperfectly estimated quantity during this process.

$$L = L_{gnd}r + L_U \quad (4.74)$$

$$\hat{L} = \hat{L}_{gnd}\hat{r} + \hat{L}_U \quad (4.75)$$

The definition of L_{gnd} is given by equation 4.76:

$$L_{gnd} = \left(\frac{E_s}{\pi} \cos \sigma_s \tau_1 + L_d \right) \tau_2 \quad (4.76)$$

Equation 4.77 shows the method by which the validation scenario is simulated. Because reflectance errors induced by constituent uncertainty can only be indirectly treated by the radiative transfer modeling process, error in atmospheric constituent knowledge must be simulated as a perturbation in the MODTRAN input parameters. The effect must then be detected in the radiance outputs. Whereas reflectance retrieval errors would not affect sensor-reaching radiance, the indirect simulation method keeps reflectance constant, instead collecting these errors in the sensor-reaching radiance term. To return to the situation in equation 4.75, the original radiance is substituted for the perturbed radiance and inverted. Terms \hat{L}_{gnd} and \hat{L}_U are obtained from input-perturbed MODTRAN runs. Then, it is assumed the defect exists in r , not L , so reflectance errors are isolated according to equation 4.78, where each term corresponds to the terms in equation pair 4.77.

$$\hat{L} = \hat{L}_{gnd} r + \hat{L}_U \quad (4.77)$$

$$\hat{r} = \frac{(L - \hat{L}_U)}{\hat{L}_{gnd}} \quad (4.78)$$

For each scenario, a mean value, distribution width, and distribution shape were assumed for the input parameter under study. An arbitrarily large (nominally 600) random sample of parameter values was constructed by accessing a random distribution possessing the characteristics in table 4.5. Note that for the translation of optical depth error to visibility, ± 0.02 translated to $+0.8$ and -0.7 km. These were averaged together for brevity's sake. MODTRAN was run with each input parameter in the random sample, and the reflectances were calculated according to equation 4.78. The first run in each scenario was unperturbed and provided the “truth” radiances required by equation 4.78. Results for 100% and 20% reflectors will be presented in chapter 5.

Table 4.5: Validation scenario summary

	Validation parameter	Distribution	Mean	Std dev
V1	water vapor - dry	normal	0.75 cm	0.2 cm
V2	water vapor - dry	normal	0.75 cm	0.1 cm
V3	water vapor - wet	normal	2.0 cm	0.2 cm
V4	water vapor - wet	normal	2.0 cm	0.1 cm
V5	density altitude	normal	0.218 km	0.02 km
V6	density altitude	normal	0.218 km	0.01 km
V7	aerosol optical depth	log-normal	0.447 (15 km)	0.04 (1.55 km)
V8	aerosol optical depth	log-normal	0.447 (15 km)	0.02 (0.75 km)
V9	multiple parameters			
	water vapor	normal	2.0 cm	0.2 cm
	density altitude	normal	0.218 km	0.045 km
	aerosol optical depth	log-normal	0.456	0.02

Chapter 5

Results and Discussion

An approach has been presented that allows the estimation of atmospheric inversion error using basic error propagation theory and radiative transfer modeling techniques. The statistical approach used here recognizes that any values obtained are governed by an uncertainty distribution. The fundamental premise of this work is that any reflectance result is also governed by a statistical distribution, and the purpose of the method presented is to determine both the magnitude and traceability of error as it moves through the system, accumulating in the final spectral reflectance result. The final product of the process is a basic statistical description of the final result in reflectance units. This chapter presents the results of error propagation process at each step, building to a final body of reflectance uncertainty results. Validation and sensitivity study results will also be presented.

Error propagation is a multi-step process. The results of each step are now presented individually so as to provide insight into the implications of the final results. Figure 5.1 shows how the components are combined to produce retrieved reflectance errors. According to the error propagation method described in section 4.4, any propagated error requires both a system sensitivity, defined by the mathematical relationship between variables, and a system driver, defined by the injected error input. In the case of model output uncertainty, the atmospheric partial derivatives (section 5.1) are driven by atmospheric constituent uncertainty (section 5.2). The errors in the model outputs (L_d , L_u , τ_1 , and τ_2) are shown for a variety of input drivers in section 5.3. Sensor calibration error modeling results for several representative sensing platforms are shown in section 5.4. A variety of results for the modeled environmental components are presented in section 5.5. Finally, fully combined end-to-end error propagation results are presented in section 5.6.

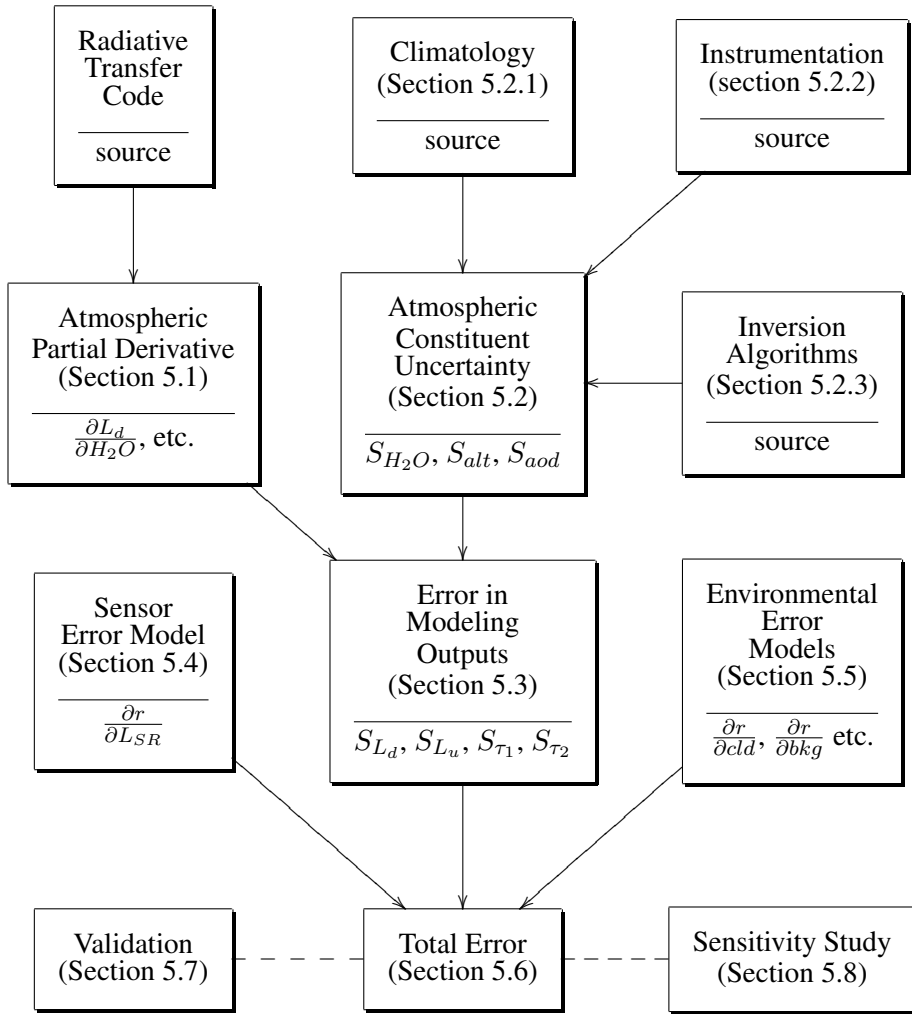


Figure 5.1: Map of Component Results

5.1 Atmospheric partial derivatives

5.1.1 Step size selection

Determining the partial derivatives was a two-step process. First, the proper numerical derivative step size for each constituent was determined. This is not normally thought to be a hazardous process, but if done incorrectly it could lead to some serious problems. Step size determination results are presented fully in figures 5.2, 5.3, and 5.4 and summarized in table 5.1. These plots show the basis for choosing the step sizes that were eventually used to numerically compute the first derivatives of each model output with respect to each atmospheric parameter. A vertical line on the plot indicates the step size eventually chosen in calculating the derivatives. A single number was used for all bands in each case. The different plot curves represent a sampling of wavelengths between 400 nm and 2500 nm, roughly 300 nm apart.

Table 5.1: Partial Derivative Settings Summary

Parameter	Setting
water vapor	0.25 cm
density altitude	0.1 km
visibility	2 km

Judgments were made empirically, keeping in mind the error regime considerations illustrated in figure 4.7. Both the functional error and machine noise regimes are clearly visible in the step size plots. Each plot is best read from right to left in that large step sizes on the right are generally smoothly sloping curves, giving way on the left to more erratic behavior.

Figure 5.2 shows the most interesting behavior, clearly highlighting the potential pitfalls in conducting a numerical analysis of this sort. Several effects are visible: highly erratic machine noise in figure 5.2(a), zig-zag behavior in same, highly-sloping functional noise, and what appears to be three distinct slope regimes punctuated by a discontinuity just under 1.0 cm step size. Machine noise regimes and zig-zag lines also appear in figures 5.3 and 5.4.

The highly erratic machine noise in all of the τ_1 derivative plots stems from how τ_1 is calculated from the MODTRAN results. It is the only result not directly available as a scaled difference of tape 7 columns. It is found as a quotient of

columns, meaning it is highly sensitive to machine noise.

The zig-zag behavior was investigated and found to be a quantization issue. Because the default MODTRAN output is limited to a set number of decimal places, it is possible for two slightly differing inputs to produce output whose values differ by an amount smaller than the 3 or 4 decimal output precision. The expected result is that the slope is constant in this small change regime because outputs and inputs change by about the same amount, no matter what they are. However, when the slopes are calculated from this output, the unchanging output is divided by the changing input, producing a different slope. Once the sub-precision residual accumulates past the quantization limit, the least significant decimal place increments (or decrements), and the quotient suddenly changes, producing a step discontinuity. The entire process repeats, creating a zig-zag appearance. From an error propagation standpoint, all of these answers are “correct” because the distance between max and min is bounding the quantization noise. Technically speaking, it is probably most correct to use one of the zig-zag extrema as a reference value, but the results need to be examined manually to determine which extremum to use.

The most peculiar aspect of the water vapor step size graph is the appearance of 3 different behaviors: a typical functional noise sloped region on the left, a scalloped region in the middle, and a opposite-sloping discontinuity on the right. This is most likely explained by how MODTRAN handles excess water in constructing its profiles. The model uses the 1976 Standard Atmosphere because it is the basis for correlating changes in temperature and pressure with density altitude. However, the midlatitude summer vapor profile is used to better match wetter conditions expected in the US northeast. The key difference is that despite similar temperature and pressure profiles, each model atmosphere has a different saturation limit, with midlatitude summer saturating at 4.95799 g/cm^2 and the 1976 standard atmosphere saturating at 2.61107 g/cm^2 . It is likely the discontinuities arise from MODTRAN reacting unpredictably in response to approaching this limit.

Final step size selection attempted to find the place that optimally avoids the worst error of the many sources discussed. Primarily, the limit was placed at the outer edge of the machine noise regime. A single number was selected for each constituent, and because selection was dominated by machine and quantization noise, it is believed that this number should be viable for many different geometric configurations.

5.1.2 Slope determination in MODTRAN functional space

The partial derivatives of each modeling output with respect to each atmospheric constituent are absolutely crucial to the functioning of the error propagation model.

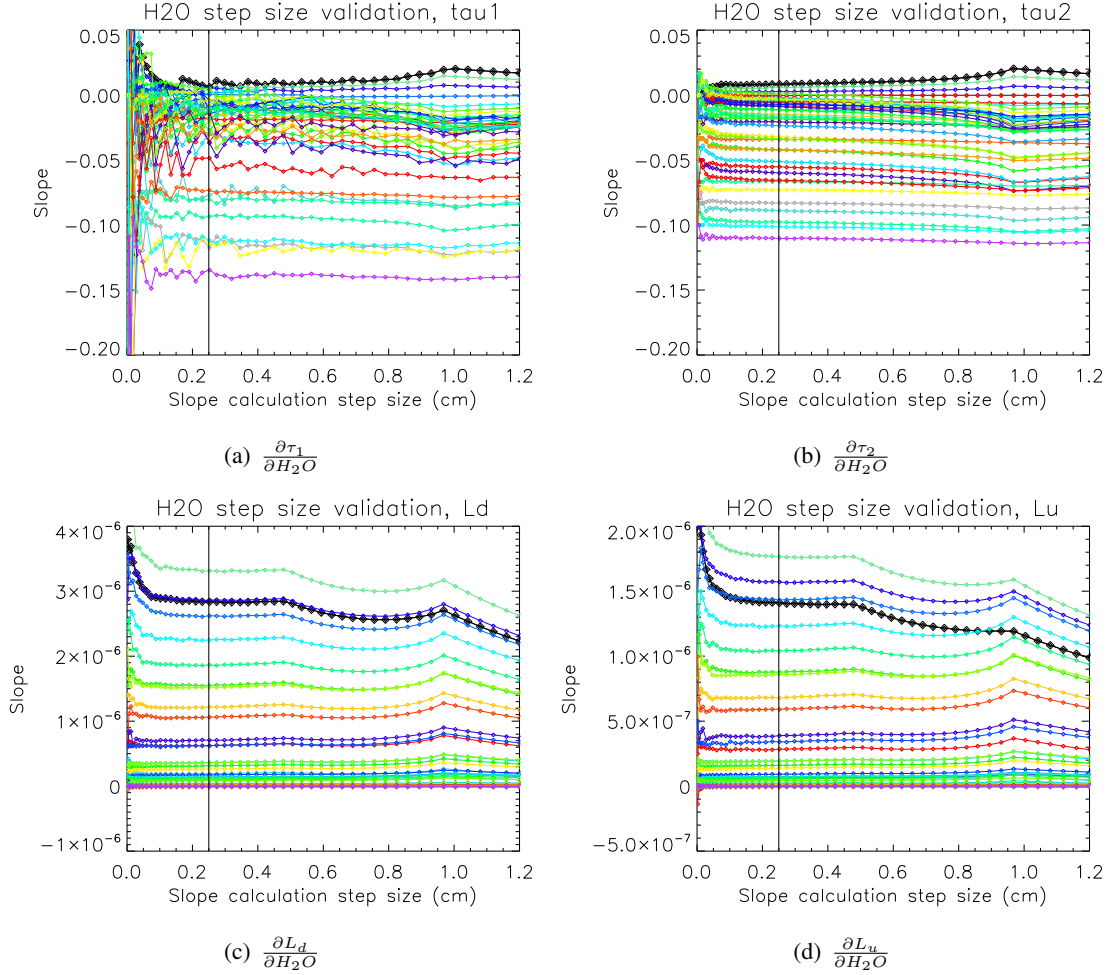


Figure 5.2: Water vapor slope step size sensitivity. Each curve represents one wavelength chosen to sample the entire spectral range on 50 nm centers, *i.e.* 400, 450, ..., 2450, 2500 nm. The purpose of the plot is to show in-family behavior for all curves in relation to the chosen step size (the vertical black line), so individual identification of each curve is not important. The functional error regime is visible as a slope change at the extreme right of each plot, and the machine error regime is visible as erratic slope behavior on the extreme left of each plot.

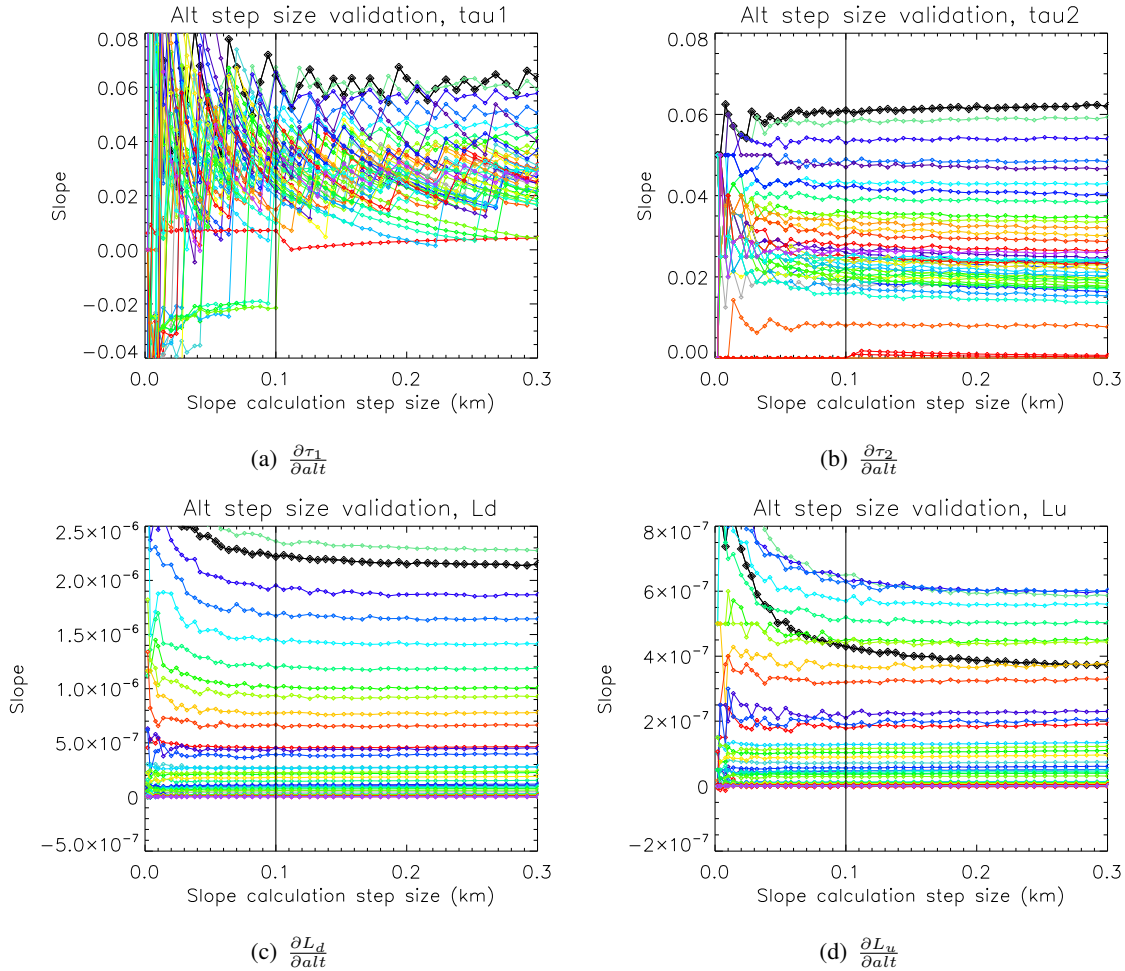


Figure 5.3: Altitude slope step size sensitivity. Each curve represents one wavelength chosen to sample the entire spectral range on 50 nm centers, *i.e.* 400, 450, ..., 2450, 2500 nm. The purpose of the plot is to show in-family behavior for all curves in relation to the chosen step size (the vertical black line), so individual identification of each curve is not important. The functional error regime is visible as a slope change at the extreme right of each plot, and the machine error regime is visible as erratic slope behavior on the extreme left of each plot.

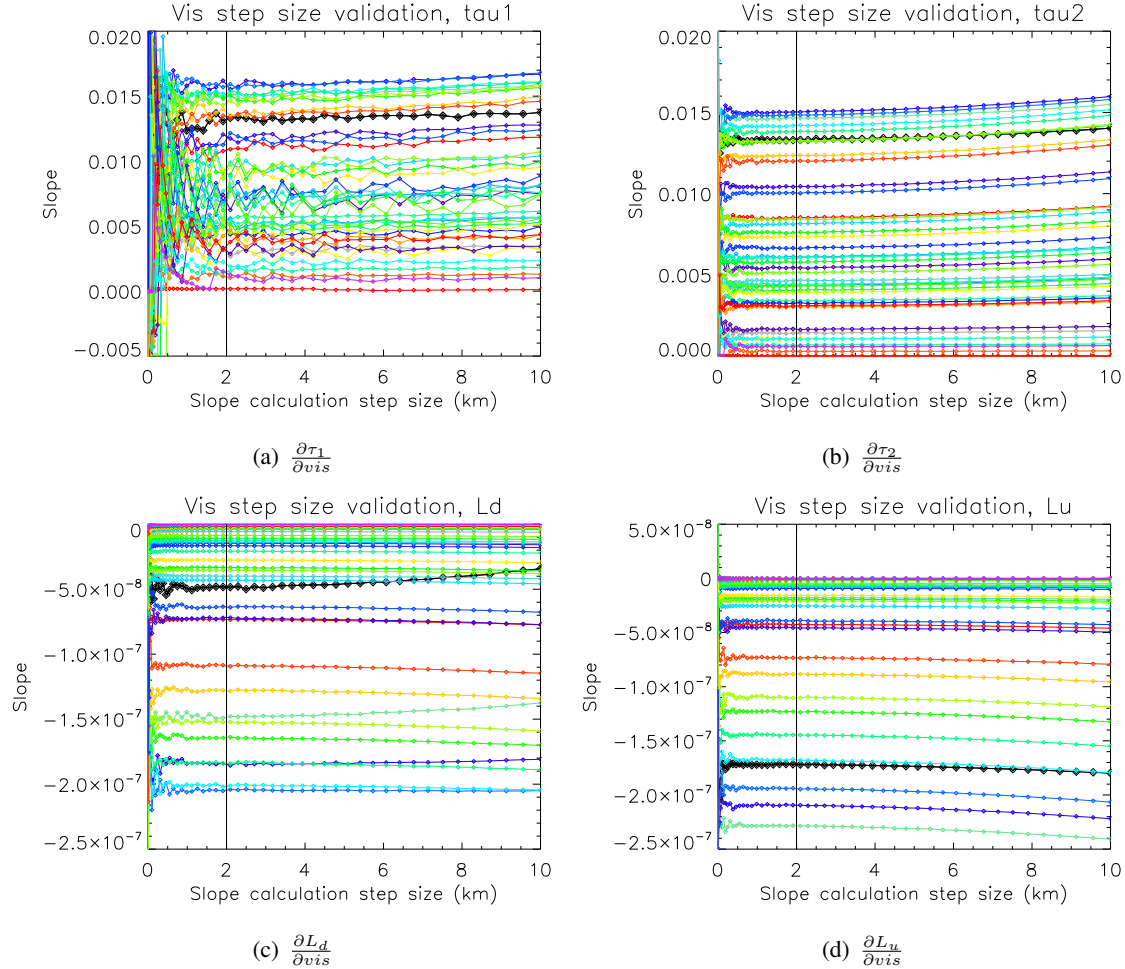


Figure 5.4: Aerosol/Visibility slope step size sensitivity. Each curve represents one wavelength chosen to sample the entire spectral range on 50 nm centers, i.e. 400, 450, ..., 2450, 2500 nm. The purpose of the plot is to show in-family behavior for all curves in relation to the chosen step size (the vertical black line), so individual identification of each curve is not important. The functional error regime is visible as a slope change at the extreme right of each plot, and the machine error regime is visible as erratic slope behavior on the extreme left of each plot.

Although they are not intuitively comprehensible by themselves, they are what essentially “carry” error inputs forward through the model to the next stage. It would be tempting to call them meaningless as standalone results, but because they represent the inner workings of the error propagation model and represent a significant portion of the new technique presented in this research, they deserve some scrutiny.

The slope computation results are shown in figures 5.5 through 5.8. These curves are specific to the initial conditions listed in tables 4.1, 4.2, and 4.3, but they are independent of any error scenarios. Thus, they are the last application-independent results that will be presented.

It needs to be pointed out that both visibility and aerosol optical depth (at 550 nm) are presented together. Visibility is directly relatable to optical depth via an exponential relationship. The exact relationship applicable to the baseline geometric and atmospheric modeling parameters selected for the sample scenarios is shown in figure 5.9. In the figure, the baseline 15 km visibility corresponds to an optical depth of 0.447. Visibility is an intuitive, single-parameter input to MODTRAN (given an acceptable default aerosol model), whereas direct aerosol definition is not. Aerosol optical depth (at 550 nm) is available in the output, therefore both inputs produce acceptable partial derivatives. Visibility, however, is a terrible quantity to measure, the reasons for which will be elaborated upon in section 5.2.1. Aerosol optical depth is used as the working quantity after this point.

The absolute magnitudes of the partial derivatives are not useful for comparison purposes because they are of different units with different typical values. In figure 5.5, the partial derivative of τ_1 with respect to aerosol optical thickness is much larger than the partial with respect to visibility because the typical variability of AOT is two orders of magnitude less than that of visibility.

As would be expected, figure 5.5 closely matches 5.6. Because the time of day is near local noon, τ_1 should be nearly identical to τ_2 . Note the signs of the curves with respect to water vapor and aerosols are opposite those with respect to visibility and altitude. This is due to the fact that transmissivity increases with higher visibility and altitude (less scatterers) and decreases with higher water vapor and aerosols (more scatterers). An exception to this observation occurs with water vapor in the low visible wavelengths, where it is thought that the water vapor’s lower-than-air density starts to emerge as a more dominant effect. Figures 5.7 and 5.8, both scattered radiance results, share the same general tendencies but differ in magnitude.

All curves are pocked with absorption dips (and spikes, in the case of water vapor). It should be noted that the apparent low sensitivity in these regions is

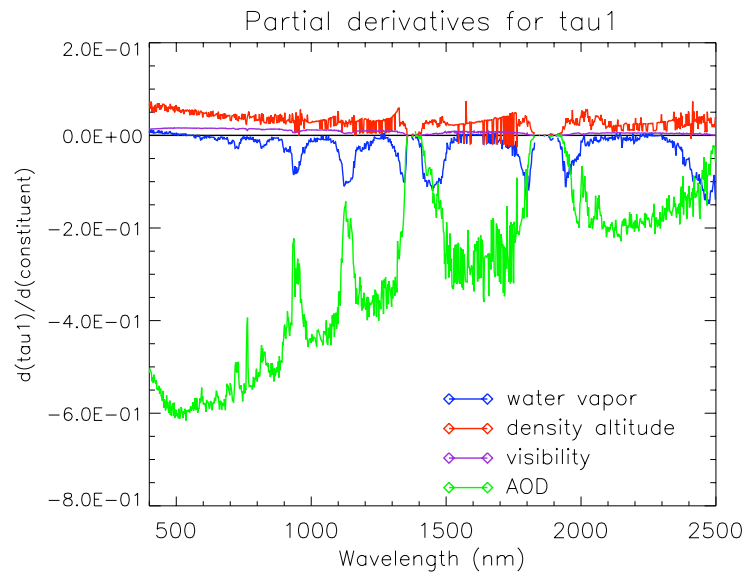


Figure 5.5: Derived slopes for τ_1 with respect to each constituent

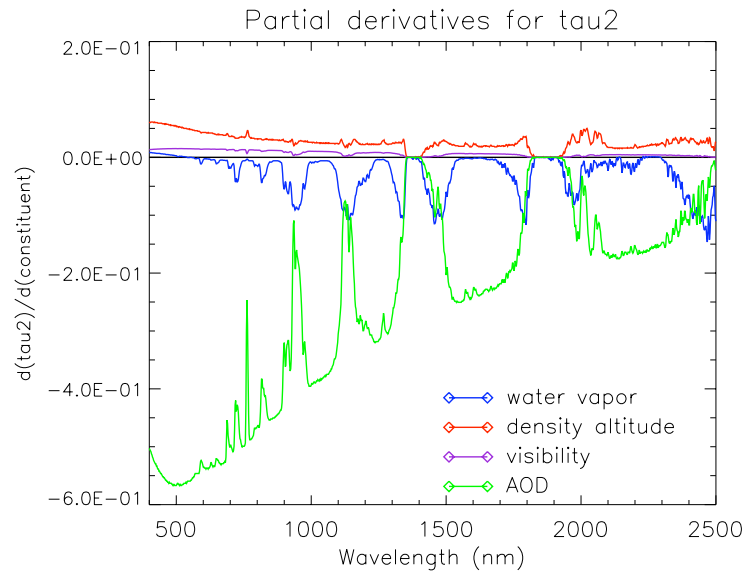


Figure 5.6: Derived slopes for τ_2 with respect to each constituent

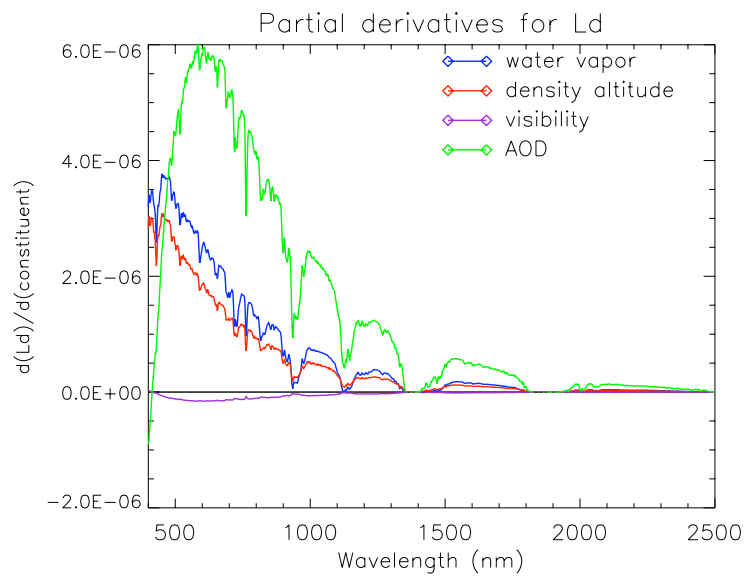


Figure 5.7: Derived slopes for L_d with respect to each constituent

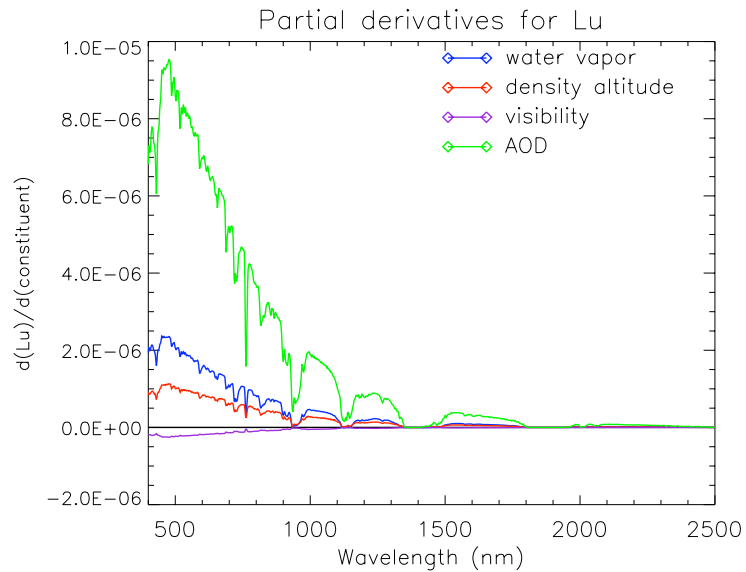


Figure 5.8: Derived slopes for L_u with respect to each constituent

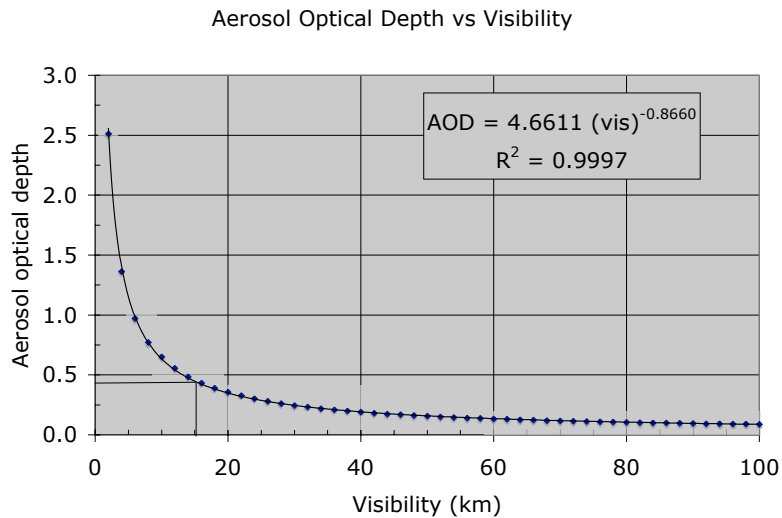


Figure 5.9: Relationship between aerosol optical depth and visibility. The plot shown here uses default MODTRAN aerosol settings and the geometric settings listed in table 4.1. Optical depth is indexed to a particular wavelength, commonly 550 nm. Other parameters are required to describe the spectral character of aerosols' effect.

counterbalanced by the low signal and high noise in the actual radiance curves, removing any hope of useful results in these regions.

5.2 Atmospheric constituent uncertainty

The other half of error propagation is the atmospheric constituent uncertainty being propagated forward. The three sources referenced by figure 5.1 are climatology, instruments, and inversion algorithms, each one providing atmospheric constituent inputs to MODTRAN. The constituents—water vapor, well mixed gas density, and aerosol optical depth—are known to varying degrees of certainty. These uncertainties were reduced to the standard deviation of a normal, uniform, or log-normal distribution (depending on the observed physical phenomenology), so as far as the error propagation model is concerned, they're all just numbers. However, each source was selected to illustrate a specific point, which will be discussed before combining the constituent uncertainties with the partial derivatives to produce reflectance error predictions.

5.2.1 Constituents from Climatology

It was proposed that modeling could be attempted without *a priori* knowledge using an approach called “blind modeling.” Often atmosphere modeling is used to support imaging research without much consideration of how using MODTRAN’s default values (“very blind modeling,” perhaps) and the midlatitude summer atmosphere really change the results, though that is certainly “better than nothing.” The use of local historical data also falls within the “better than nothing” category but provides modeling settings that could plausibly be believed to have degree of closeness to actual conditions. The results presented here show that a climatology approach to constituent error produces a viable result that will be used in forward propagation. These propagated errors will be compared to results from the other sources of constituent uncertainty.

Historical climate data were compiled and analyzed for Buffalo Niagara International Airport, which benefits from several collocated data collection activities. Airport observations, twice-daily radiosonde launches, and a nearby automated GPS water vapor station were all investigated for suitability. Table 5.2 summarizes the results of the climate study, with the results themselves shown in Appendix B starting on page 201.

The results themselves are straightforward to interpret with some minor discussion warranted. First, the results were aggregated by month. This was an arbitrary decision chosen so as to capture seasonal cycles. Further aggregation by time of day was also desired, but the observations were thought to be insufficient to support this. Table 5.2 only shows results for May, which corresponds to the baseline geometry listed in table 4.1. A second discussion point in these results is that visibility observations cannot be used as a source measurement for reasons exposed by figure B.9. Visibility observations at an airport exist to detect conditions that may interfere with takeoffs and landings. Thus, they are at least bimodal, with low-end results caused by weather and high-end results caused by haze, though this could be fixed by truncating the lowest observations. However, airports also do not care about the visibility if it exceeds 10 or 15 km. Indeed, figure B.9 shows a partial distribution tail where most of the clear-weather observations are all binned at 10 km rather than made more accurately. Simply put, aerosols must be measured directly in order to support remote sensing operations.

This section does not fully explore the many interesting nuances discovered when using these data sources for blind modeling; the main point here is that these should *not* be used. Table 5.8 shows the uncertainty here is generally 10× as large as any of the other data sources used here. This bound on the “better-than-nothing” option is an important result, considering its prevalence in support to

imaging science research (though if no other alternative exists, be sure to do it in winter). Propagated results will be shown starting in section 5.3.

Table 5.2: Climatology Results Summary (Month 5)

Parameter	Source	Mean value	Std deviation	Figure
water vapor	GPS	1.87 cm	1.06 cm	B.1
	radiosonde	1.90 cm	1.07 cm	B.2
	MODIS	1.55 cm	0.62 cm	B.3
density altitude	airport obs	0.21 km	0.21 km	B.4
	GPS synoptic	0.17 km	0.18 km	B.5
	radiosonde	0.16 km	0.22 km	B.6
aerosol optical depth	MODIS	0.37	0.39	B.7

5.2.2 Constituents from Instrumentation

As stated earlier, wireless communication enabling a potential paradigm shift where the previously impractical routine use of ground truth in remote sensing could become practical. A snapshot of the state of instrumentation uncertainty was obtained through a cursory catalog search and a dip into the body of information compiled by the Atmospheric Radiation Measurement (ARM) Program, a Department of Energy activity that operates a national infrastructure of highly instrumented ground stations (U.S. Department of Energy, 2004). The primary metric was the published uncertainty provided by each type of sensor, which was taken at face value (despite the obligatory warnings about trusting manufacturer's claims).

Tables 5.3 through 5.6 comprise a brief re-compilation of some of this data. It does not need to be comprehensive; as long as each constituent is covered by an instrument that can be described as typical of the field, then the purpose will be served. The measurement atmospheric quantities as ground truth is an incredibly important capability, and the performance of a instrument network-enhanced sensing result is based on the capabilities inherent in these instruments.

Density altitude is an indirect measurement designed to index well-mixed gas density. Altitude itself is indirectly measured through pressure and two types of temperature (both air temperature and dew point). In an operational environment, the three measurements are taken together. For the purposes of the results to follow, it was necessary to derive density altitude uncertainty by propagating uncertainty in

pressure and temperature. This calculation uses the baseline scenario's values for surface temperature and pressure but a monthly historical average for dew point.

A brief survey was conducted to determine the state of the industry with regards to ground instrument accuracy in sensing quantities of interest: temperature, pressure, aerosol optical depth, and integrated water vapor column height. This sampling of uncertainty values will form the foundation for error propagation analysis of ground truth networks. At this point, no consideration is given to cost or practicality, just possibility. Results are summarized in tables 5.3 through 5.6. In addition to the atmospheric measurement data, Michalsky (2001) notes pyranometer and shadowband radiometer irradiance accuracy as low as 3% for direct irradiance and 5% for diffuse irradiance after non-linearity correction. This ground instrument uncertainty will be used to predict incorporation of direct measurement of downwelled radiance, sun-ground transmission, and ground-reaching radiance into uncertainty reduction.

Table 5.3: Temperature

Source	Uncertainty	Source
Commercial weather station	0.5° C	Davis Instruments (2004)
NIST reference instrument	0.2° C	Davis Instruments (2005)
Vaisala RS-90	0.5° C	Vaisala (2006)
Vaisala RS-90 dew point	1.5° C	ibid.
Vaisala PTU300	0.2–0.4° C	Vaisala (2008)
GPS MET station	0.1–0.3° C	Feng and Herman (1999)

5.2.3 Constituents from In-scene Algorithms

The final source for uncertainty in a model-based approach comes from the in-scene model-based algorithms themselves. As described in sections 3.2.2 and 3.2.3, in-scene algorithms depend on band ratio methods to determine atmospheric constituents. Because inversion algorithm validation studies rightly focus on final reflectance results and seldom on the intermediate results of the algorithm's inner workings, band ratio studies provide the majority of the uncertainty data used to populate this source.

The correlation between band ratio and physical phenomenology is derived by constructing look-up tables with MODTRAN. The degree of error inherent in the

Table 5.4: Pressure

Source	Uncertainty	Source
Commercial weather station	1.35 hPa	Davis Instruments (2004)
NIST reference instrument	0.68 hPa	Davis Instruments (2005)
Vaisala RS-90	1.0 hPa	Vaisala (2006)
Vaisala PTU300	0.15–0.45 hPa	Vaisala (2008)
Vaisala PTB100	0.25–0.3 hPa	Deblonde et al. (2005)
Setra 270 pressure transducer	0.3 hPa	ibid.
GPS MET w/ synoptic meas.	0.66–1.4 hPa	ibid.
GPS MET station	0.13–0.44 hPa	ibid.

Table 5.5: Aerosol Optical Depth

Source	Uncertainty	Source
Cimel Sunphotometer	0.02–0.04	Rainwater and Gregory (2005)
Sunphotometer - high altitude	0.01	Halthore et al. (1999)
Multifilter rotation shadowband radiometer (MFRSR)	0.02	ibid.

process is the basis for a common comparison with other sources for atmospheric constituent data. This is not a bad comparison because the same assumptions that underly the main mathematical techniques of the work presented herein mirror those used to construct the lookup tables. Both rely on linearizing a smooth curve pegged to a certain set of geometric conditions, so the error inherent in the correlation process theoretically matches the functional error inherent in the slope determination process, which was too low to affect the results.

Therefore, error arising from the band ratio process is not inherent in the process itself, rather it arises from imperfect modeling of the atmosphere under test. It is further concluded that this imperfect modeling is not related to the variables treated by the algorithm, instead it is the assumed variables that are never verified. One example of this is provided by Gao and Goetz (1993), where the presence of liquid water fouls the in-scene water vapor determination method and subsequent spectral curve fit. The idea that an error in the assumed aerosol particle size distribution could manifest as error in retrieved water vapor (for example) presents an interesting implication for the comparisons made here. It suggests that, for model based algorithms only, constituent determination error may not cause random error in reflectance, instead it manifests as a bias due to a shift in the entire function space (that may or may not be linear across the entire parameter range). Linearity problems with band ratio algorithms, like those described by Hirsch et al. (2001), may also contribute. It is entirely possible that this underlies the empirical EF-FORT correction described by Boardman (1998). Modeling error due to bias as a random phenomenon potentially invalidates the approach by which ground truth instrument errors are directly compared to errors observed in the in-scene inversion process. Put another way, it is possible that because of the many effects built into FLAASH's lookup table, perfect knowledge of the constituents FLAASH finds would still result in retrieved reflectance errors. However, since the inner workings of the model based algorithms are beyond the scope of this study, this theory will need to be explored in future work. Errors related to model-based inversion algorithms are treated as random if reported as such.

According to Green et al. (1993), surface pressure altitude appears to closely follow the topography of the region. This might suggest that barring drastic extremes of weather, actual terrain elevation is more important than elevation adjusted for non-standard air column density. As an example, given a surface height of 220 meters, an atmospheric variation contribution of 5-10 meters is really within the noise of the surface elevation measurement in the first place. Figure 4.10 shows that for flat terrain, elevation-only error is generally bounded to 10 meters or less. Drastic terrain changes would have slightly higher error, and most of the area cov-

ered by the DEM would likely have significantly less. This makes 10 meters a conservative value to use for the determination of density altitude.

Alternately, Green (1991) also notes that in-scene altitude determination was precise to within 12% when performed pixel-by-pixel. Results were improved when multiple pixels were convolved together, presumably under the assumptions that density altitude slowly varies spatially and that high-frequency differences unrelated to the equivalent elevation could be safely removed to obtain a better local result. Using 12% as an upper bound, with the understanding that the precision for a spatially averaged in-scene determination should be somewhat lower, an *altitude-dependent* uncertainty range of 1–25 meters is assumed.

Because in-scene determination of atmospheric water vapor employs the use of a band ratio technique, it is possible to evaluate algorithm performance in this regard by examining the results of band ratio studies. A study performed to validate the AVIRIS water vapor retrieval method produced very useful results (Bruegge et al., 1990). It was based on synoptic collections using very precise ground instruments and a LOWTRAN-assisted band ratios algorithm. The benefit is that very precise, upward-looking instruments can determine the theoretical limit of band ratio reliability free of the need to account for instrument noise and ground constituents affecting what is assumed to be an atmosphere-only phenomenon. Sun-photometer and spectral hygrometer measurements were used to produce ratios that were then indexed against LOWTRAN predictions. Both types of ratios used the 940 nm absorption feature. These results were cross-checked by a Fourier transform spectrometer, agreeing with one another to within 2%. When used to support an AVIRIS collection, the results displayed random deviations restricted to within 0.05 cm. Although these results will not be directly applicable to a downward-looking retrieval with an imaging spectrometer, this provides the lower bound of error but does not provide typical performance for in-scene algorithms. One result that could be directly applicable is that an AVIRIS retrieval was also thought to have an uncertainty of 0.05 cm. The study was conducted in a dry atmosphere, so the entire range cited here is for the “dry” category of uncertainty predictions.

The band ratio algorithm that eventually became part of the ATREM inversion algorithm (Gao and Goetz, 1990b) and that used by the AVIRIS inversion algorithm (Bruegge et al., 1990) both use a continuum interpolated band ratio (CIBR) to determine feature absorption depth and correlate it to water vapor abundance. One comprehensive study of CIBR’s performance was conducted by Hirsch et al. (2001). This study examined the baseline CIBR model, repeated in equation 5.1, where L_F is the radiance at the bottom of the feature (at approximately 940 nm), and L_1 and L_2 are the radiances at the shoulders of the feature. The wavelength

terms correspond to the points at which these three radiances are taken and are used to perform the interpolation from shoulder to shoulder so as to estimate what the radiance should be for a zero-water vapor case.

$$CIBR = \frac{L_F}{\frac{\lambda_F - \lambda_1}{\lambda_2 - \lambda_1} L_1 + \frac{\lambda_2 - \lambda_F}{\lambda_2 - \lambda_1} L_2} \quad (5.1)$$

The baseline CIBR results were compared with a scene reflectance-corrected modified CIBR and Atmospheric Pre-corrected Differential Absorption (APDA) water vapor retrieval algorithm. The scene reflectance correction arises from an empirical observation that band ratios over dark targets are negative affected by upwelled radiance, whereas the higher reflected radiance bright targets tends to prevent path radiance from exerting dominance over the relevant spectral region. The same idea motivates APDA, where a path radiance correction attempts to remove the same effect, but in a way that should make the target reflectance irrelevant. The APDA model is given as equation 5.2, where the L_u terms represent the upwelled radiance terms for the corresponding spectral band. APDA requires iteration. All methods in this study looked at the 940 nm absorption feature.

$$APDA = \frac{L_F - L_{u,F}}{\frac{\lambda_F - \lambda_1}{\lambda_2 - \lambda_1} (L_1 - L_{u,1}) + \frac{\lambda_2 - \lambda_F}{\lambda_2 - \lambda_1} (L_2 - L_{u,2})} \quad (5.2)$$

The CIBR study presented by Hirsch et al. (2001) compiled a wide array of validation data, where in-scene band ratios derived from Multispectral Thermal Imager (MTI), and validation data were obtained from radiosondes and sun photometers located at several sites. The data are presented in figure 5.10.

CIBR and APDA produced accurate dry-atmosphere predictions but underestimated to varying degrees the water vapor in wet atmospheres. The study results were reduced by calculating the root mean squared error for each band ratio estimate compared to the corresponding ground truth measurement. Readings taken from different altitudes were removed. The divergence observed for wetter atmospheres is unsettling. It is possible that ground truth instruments perpetually overestimate water vapor content, but it has been noted that some algorithms have problems with high water vapor content (Goetz et al., 2003), suggesting the problem does not lie with the truth instruments. It is more likely that feature depth is underpredicted by MODTRAN, a phenomenon that was surely validated at one point and therefore deserves greater scrutiny in the future. Another possibility may be tied to how MODTRAN processes wet atmospheres. Each of the built-in models has an internal maximum water vapor content it can accommodate, and only two of six are capable of taking greater than 3 cm of integrated precipitable water vapor.

Table 5.6: Water Vapor

Source	Uncertainty	Source
Aeronet microwave radiometer	0.02-0.04 cm	Cimini et al. (2003)
Aeronet microwave radiometer	0.023 cm	Liljegren and Lesht (1996)
		Revercomb et al. (2003)
ROAB sonde/GPS cross-cal	0.1 cm	Mattioli et al. (May 2005)
ARM CART sonde/GPS cross-cal	0.2 cm	Santos et al. (2007)
GPS-MET network IPW – dry	0.1 cm	Deblonde et al. (2005)
GPS-MET network IPW – wet	0.2 cm	ibid.
International H2O Project GPS IPW	0.15 cm	Birkenheuer and Gutman (2005)
Australian GPS net/MWR cross-cal	0.13–0.24 cm	Santos et al. (2007)
Cimel Sunphotometer	10%	(Rainwater and Gregory, 2005)
		(Halthore et al., 1999)
Regan Sunphotometer	12%	(Bruegge et al., 1990)
Spectral Hygrometer	0.01 cm	ibid.

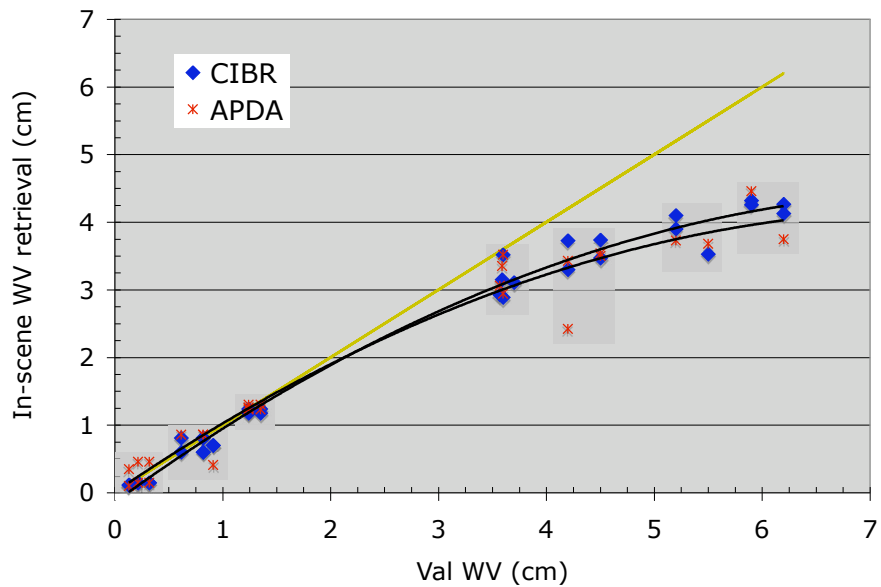


Figure 5.10: CIBR and APDA validation results

Additionally, MODTRAN has a separate procedure for vertically redistributing water vapor in response to layer saturation, which may produce unexpected results. Work by Felde et al. (2004) provides what is probably the best insight into this issue: the band ratios for the 820 nm, 940 nm, and 1130 nm water vapor absorption regions all lose sensitivity above approximately 2.5 cm of total water vapor. Put another way, retrieved water vapor is hypersensitive to small perturbations to band ratio. The above mentioned factors likely combine to produce small errors in band ratio that magnify errors. This presents another opportunity for future validation of the predicted *versus* observed behavior of atmospheres with high water vapor content.

CIBR produced an uncertainty of 0.11 cm for dry atmospheres and 1.23 cm for wet. After removing instances where APDA failed to produce a convergent solution, the algorithm gave an uncertainty of 0.12 cm and 1.29 cm, respectively. For both algorithms, the wet atmosphere uncertainty appears to include a non-linear bias, so these deviations should not be treated as random. An empirical fit to the data was determined, visible as the fit lines in figure 5.10, and used to de-bias the data set. It is against these de-biased values that random deviations can be computed. There is no claim made that this fit is universal; rather, it simply fits these data in this case. Additional data could continue to follow these trends or they could alternately display completely random behavior around the 1:1 ratio line. With the bias correction, random uncertainty for the wet atmosphere cases is 0.35 for CIBR and 0.36 for APDA.

Several other sources offer water vapor uncertainties in the form of a percentage, namely Gao and Goetz (1990b) and Kaufman and Gao (1992). The first cites approximately 5% error for a scene with mean 0.97 cm of water vapor, while the latter demonstrates 13% error with possible improvements that reduce it to 7%. In order to translate these into a range in centimeters of total precipitable/integrated/perceived water vapor, a standard dry atmosphere value of 0.75 cm was assumed, and a standard wet atmosphere with 2.0 cm of water vapor was assumed.

In-scene aerosol optical depth is accomplished using a dark pixel method that provides upwelled radiance as an indicator of scattering species. An algorithm of this type was developed for the Moderate Resolution Imaging Spectrometer (MODIS) instrument on NASA's Terra spacecraft and has grown into widespread use (Kaufman et al., 1997). The algorithm relies on band correlation relationships for low reflectance targets to estimate the aerosol contribution. In a nutshell, the 470 and 660 nm visible spectral regions were found to correlate in target reflectance with 2.1 and 3.8 micron spectral regions. In the absence of other factors, it is ex-

pected that spectral bands at or near these locations will correlate, particularly for dark targets. The benefit is that aerosols affect the visible region much more than the near or midwave infrared regions. Additionally, dark targets are less sensitive to direct radiation and highly sensitive to upwelled path radiance, which is heavily driven by aerosol interactions. Therefore, aerosol abundance is knowable through the degree of non-correlation between the selected visible and infrared bands.

The published uncertainty is $\Delta\tau_a = 0.05 \pm 0.02 \tau_a$, where τ_a is used by the authors to denote aerosol optical thickness. The uncertainty from this algorithm is tied to the value of the optical thickness, so a visibility range was chosen and converted to an exponent. 10 km is used as the low visibility case, chosen based on climatology analysis presented earlier. This is the lowest typical value not encroaching on weather effects. An upper value of 50 km was chosen to be arbitrarily large; past 25 km, the change in optical depth is small enough that any large value would be suitable. At 50 km, the aerosol optical depth is 0.15, and at 10 km it is 0.65. At these points, the aerosol uncertainty range becomes 0.053–0.63.

Table 5.7 summarizes the in-scene retrieval results. Each source has a low and high estimate. For water vapor estimation, the low estimate is for a dry atmosphere, and the high is for a relatively humid atmosphere. As stated earlier, for uncertainties reported to be a function of water vapor content, the dry atmosphere was defined as 0.75 cm, and the wet atmosphere was defined as 2.0 cm. For density altitude, the low and high uncertainties correspond to low and high altitude, roughly defined as sea level and 300 km.

Similar to the other constituents, aerosol optical depth has low and high estimates because the uncertainty is a function of the optical thickness itself. Low uncertainty corresponds to the high visibility case at 50 km, and high uncertainty corresponds to the low visibility case at 10 km. In the case of altitude, a cap was placed on the high altitude because the ubiquitous availability of low-error DEM data, even for high altitude terrain. The best in-family uncertainty values for each atmospheric constituent will be used to construct two scenarios simulating a model-based algorithm drawing upon each of these in-scene sources for atmospheric constituents.

Although it would be intuitive to assume low altitude regions are humid and hazy, while high altitude regions are dry and clear, no such assumption was made. Instead, the “low uncertainty” scenario uses all “low uncertainty” inputs and *vice versa*. In truth, the altitude uncertainty contribution is expected to be a minor contributor, so the results probably would be fine under either pairing scheme.

Table 5.7: Inversion algorithm constituent determination summary

Parameter	Source	Uncertainty range		source
		Low	High	
water vapor	LOWTRAN band ratio	0.015	0.05 cm	Bruegge et al. (1990)
	AVIRIS retrieval	0.05 cm	-	ibid.
	ATREM precursor	0.04 cm	0.1 cm	Gao and Goetz (1990b)
	CIBR validation	0.11 cm	0.35 cm	Hirsch et al. (2001)
	APDA validation	0.12 cm	0.36 cm	ibid.
	MODIS in-scene	0.05 cm	0.14 cm	Kaufman and Gao (1992)
density altitude	terrain dominance	0.004 km	0.01 km	Green et al. (1993)
	CIBR (12%)	0.001 km	0.04 km	Green (1991)
aerosols	MODIS validation	0.053	0.063	Kaufman et al. (1997)

5.2.4 Atmospheric Constituent Scenarios

An overall summary of the atmospheric constituent sources is given in table 5.8. Each line on the table will be used as the starting point for end-to-end error propagation scenarios, the results of which are presented in section 5.3. There is one scenario based on climatology, two on ground instrument networks of varying quality, and two on in-scene retrieval algorithms. These last 2 scenarios attempt to simulate how a model-based algorithm such as FLAASH might perform, which assumes that constituent retrieval is not the black-box process one might wish it to be. Indeed, without this “cracking-open” of the black box, direct comparison is impossible, but there are spatial and spectral smoothing effects or corrections particular to each inversion algorithm that cannot be accounted for in this manner. Scenarios will be referred to by the scenario numbers in the first column or the scenario descriptions in the second.

5.3 Error in Modeling Outputs

The atmospheric constituent errors and sensitivities presented earlier combine to produce propagated errors in the modeling outputs: τ_1 , τ_2 , L_d , and L_u . This step provides the solution to equations 4.32 through 4.35. Five basic scenarios are carried forth from here on out, one corresponding to each of the sources described in the preceding sections. From this point on, results cannot be generated without

Table 5.8: Atmospheric Uncertainty Scenario Settings

	Source	Water vapor	Density altitude	Aerosols
1	Climatology	1.06 cm	0.2 km	0.39
2	Instrumentation - field	0.2 cm	0.045 km	0.04
3	Instrumentation - ARM	0.03 cm	0.017 km	0.02
4	In-scene - wet/hazy	0.3 cm	0.040 km	0.063
5	In-scene - dry/clear	0.05 cm	0.004 km	0.053

a selection of input error drivers. This loss of generality will be accommodated by constructing multiple scenarios using the source error magnitudes described in table 5.8.

For the most part, error in each modeling output is not individually interesting. To be intuitively significant, it is necessary to fully propagate this error into reflectance space. Sample results showing the error in modeling outputs for scenario 1 are presented in figure 5.11. Results for all scenarios will not be presented because they all share the same general shape but differ in magnitude and, to a slight degree, relative magnitude. For each of the basic scenarios, the atmospheric constituent uncertainties tend to either all increase or decrease, but there are also differences in the relative uncertainty between instruments. As an example, the improvement in water vapor uncertainty between scenarios 2 and 3 is drastic because of the improvement gained by moving from field instruments to research instruments. By comparison, the improvement in aerosol optical density uncertainty, while halved between scenarios, is still not quite as drastic. This shift in relative magnitudes is first manifested in these results and carried throughout all scenarios.

5.4 Sensor Modeling Results

5.4.1 Radiometric precision

Sensor modeling was accomplished by using sensor noise cal results published by others. Several representative noise models are presented in figure 5.12. First flown in 1987, AVIRIS has defined the standard for hyperspectral imagery for years, leading the industry not only in instrument design, but also in calibration, processing and exploitation (Vane, 1987). Incremental changes to the system's configuration has resulted in improvements to calibration accuracy over time, with max

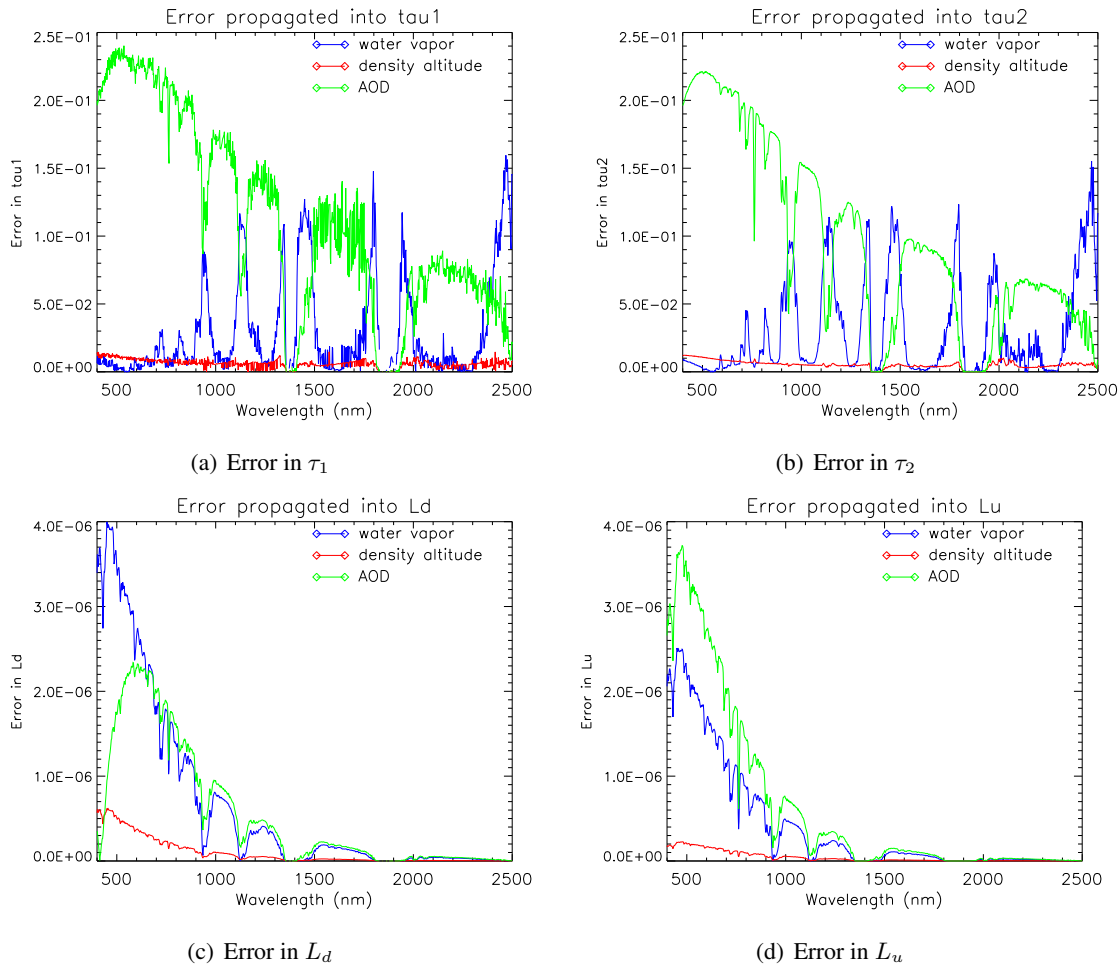


Figure 5.11: Sample results for error in modeling outputs. Results are shown for basic scenario 1. Each graph shows the error propagated into each radiative transfer modeling output by individual constituent.

SNR growing from about 50 to over 1000 (Green and Pavri, 2000). Of the curves that are available, figures 5.12(a) and 5.12(b) show selected results from the 1997 flight season (Green, 1997). Selecting an older performance data set puts the noise model more in line with what other, less advanced sensors are able to achieve. The AVIRIS noise is expressed in $ne\Delta L$.

The Hyperspectral Digital Imagery Collection Experiment (HYDICE) is an imaging spectrometer operated by the Department of Defense. It has a very similar configuration to AVIRIS but poorer noise performance (Mitchell, 1995). Whereas AVIRIS' SNR can range from 300-1200, HYDICE peaks at approximately 200 (Okin et al., 2001), although like AVIRIS, the baseline performance in later experiments was much improved (Nischan et al., 1999). HYDICE's noise performance was reported as SNR, but the illumination conditions were also reported: 6k altitude, 60° sun zenith angle, and 5% reflectance. The noise in radiance units was backed out by estimating the input spectrum using MODTRAN and reported as such in figure 5.12(c).

It is important to note that noise performance of instruments is generally dependent on the signal level used. Unless an instrument is dominated by fixed sources of noise (a sign of a very noisy instrument), then the noise is correlated to signal due to such sources as photon shot noise and gain-correlated noise. In the example instruments presented here, this was not given consideration. The goal of this research was to demonstrate that instrument noise can be propagated into reflectance space and compared with other sources. The model does not have the ability to process multiple noise curves, indexed to L_{SR} , for a given instrument, nor can it accept a functional expression of noise. Extension of the model to two dimensions would probably need to include this improvement so that instrument noise can be accurately processed over a scene that includes both bright and dark pixels.

The pre-ship lab performance of the Hyperion instrument flown on the EO-1 spacecraft is shown in figure 5.12(d) (Browne, 1999). It was also reported as an SNR curve, but again the input spectrum was estimated using MODTRAN for the reported illumination conditions: orbit altitude, 60° zenith, and a 30% reflector. It exhibits a similar shape to the HYDICE curve with somewhat noisier performance across the spectrum. In fact, Hyperion's noise performance was so different that a closer look was warranted. Figure 5.13 shows the results of an atmospheric inversion study presented by Goetz et al. (2003). It is claimed that the high noise seen in figure 5.12(d) both below 500 nm and above 2 microns manifests as high error in retrieved reflectance (departure from the nominal 50% reflectance line) in figure 5.13.

These 3 instruments provide a range of options for instrument noise perfor-

mance over a common spectral range when propagating error through other parts of the imaging chain.

5.4.2 Radiometric accuracy

In addition to instrument precision, an effort was made to account for unresolved radiometric calibration validation discrepancies, which are treated as a bias. Although an instrument can be calibrated in the laboratory and on the platform before and after each collection, there are still opportunities for calibration errors. Bias is a difficult subject to treat because after a calibration, it is assumed to not exist. After that, though one may suspect it exists, it cannot be detected until after a calibration validation. After this, the calibration is adjusted, in theory eliminating the bias once again until the next validation.

As will be seen with both the AVIRIS and Hyperion studies referenced here, part of the root problem is error in the calibration reference, though other error sources exist. These error sources are listed in Green and Pavri (2003) as imperfect knowledge of the calibration standard, drift of the calibration over time, and errors in the validation source (MODTRAN).

Calibration validation results for AVIRIS from 2002 are presented in figure 5.14. This will be used as a representative example of calibration accuracy, with general agreement to within 5% and the majority of the bands agreeing to within 2%. This was noted to be highly acceptable.

In contrast with AVIRIS, 2001 radiometric calibration accuracy results were reported for Hyperion to exceed 10-20%, depending on spectral regime (Green et al., June 2003). The primary driver for this discrepancy, shown in figure 5.15, was a problem with the original laboratory calibration reference. Following this discovery, Hyperion's calibration was adjusted to within 3% of the assumed reference value: an 11% negative bias in the VNIR spectral region was corrected by 8%, and a 21% negative bias in the SWIR spectral region was corrected by 18%. Both the AVIRIS band-by-band results and a straight 3% negative bias will be used as error model inputs.

5.4.3 Spectral calibration

It is possible to simulate the effect of any degree of bias and jitter for any target spectrum for any atmosphere. The baseline atmosphere described in tables 4.1, 4.2, and 4.3 was used for all cases. Although different atmospheres and viewing geometry would change the actual curves, the absorption features would all be in the same places, the general shapes would be the same, and the atmosphere would

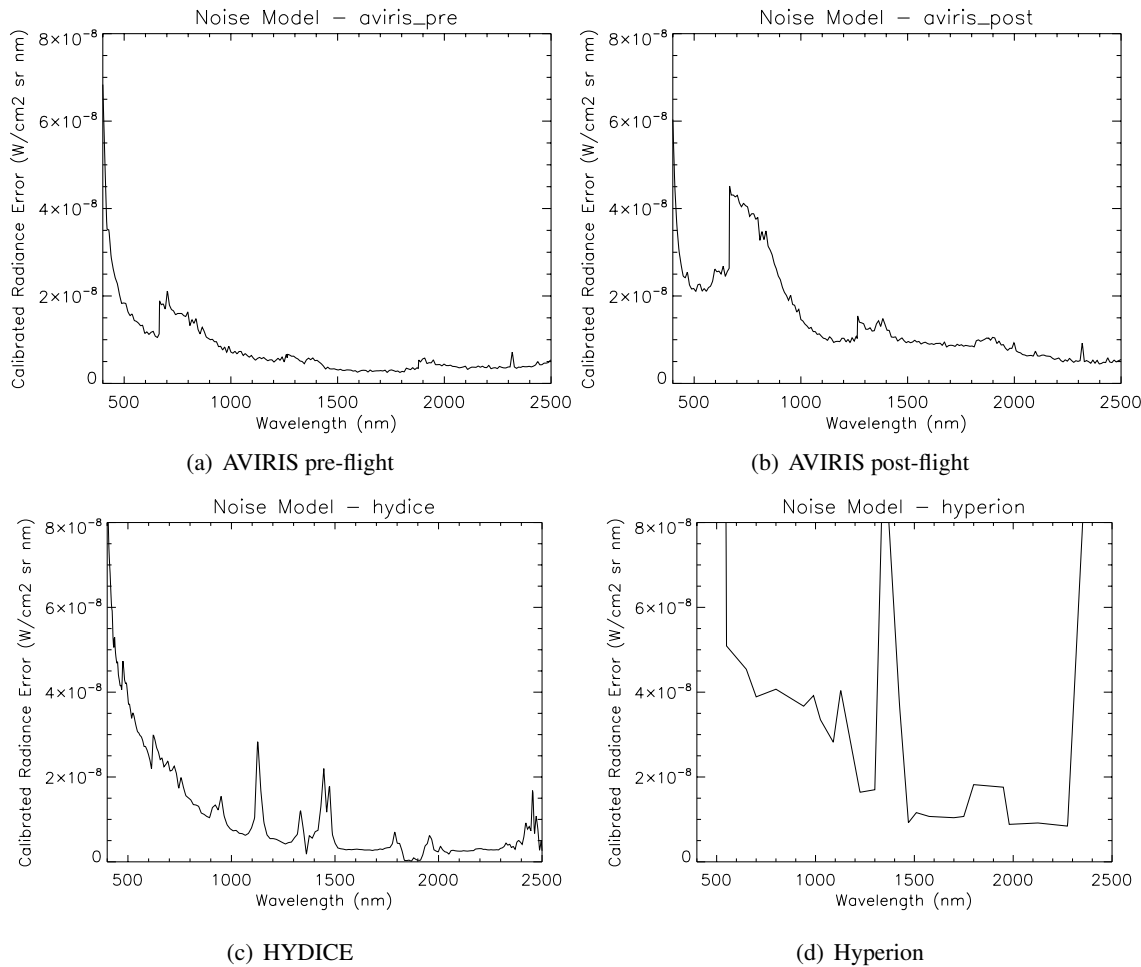


Figure 5.12: Instrument radiometric calibration noise models

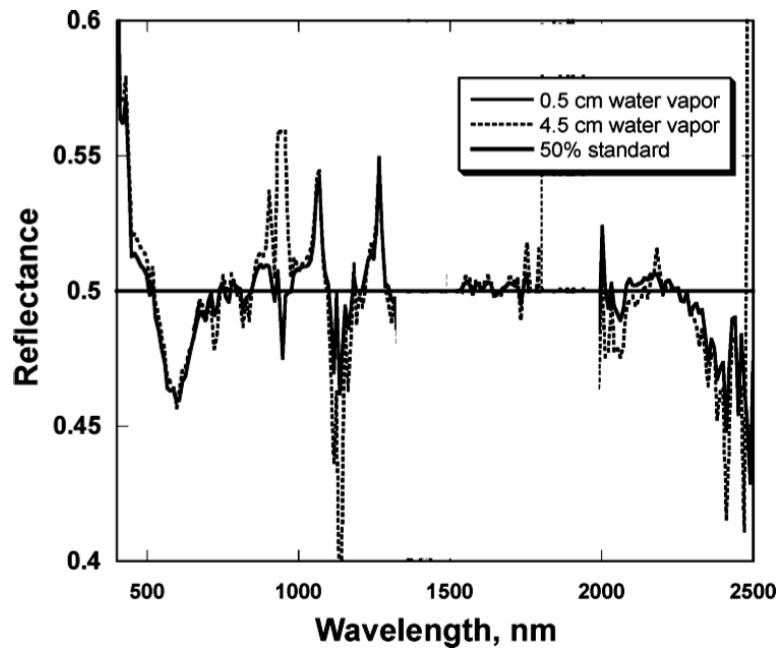


Figure 5.13: Reflectance retrieval from Hyperion imagery. Figure taken from Goetz et al. (2003).

continue to be the primary contributor to the radiance error. Therefore, it was determined to not be useful to show the variation of spectral misregistration errors over a range of atmospheres. In contrast, a moderate degree of radiance change was observed to depend on the target spectrum used, and the highest degree of change resulted from the amount of spectral shift.

These observations are supported by figure 5.16. A family of curves is shown in each plot, where the two black curves represent a 100% and an 18% reflector. The 100% reflector curve creates the outer envelope, while the 18% radiance curve shows the least amount of change. The colored curves represent the same 7 ground cover types mentioned earlier, which span the space between the two enveloping curves. Between 700 and 800 nm, the red edge effect causes the radiance bias for the vegetation targets to exceed that of the 100% reflector. Together, these features demonstrate that absolute reflectance as well as spectral shape determine the effect on sensor radiance.

Figure 5.16(a) shows a result for a 0.25 nm shift for all bands, whereas 5.16(b)

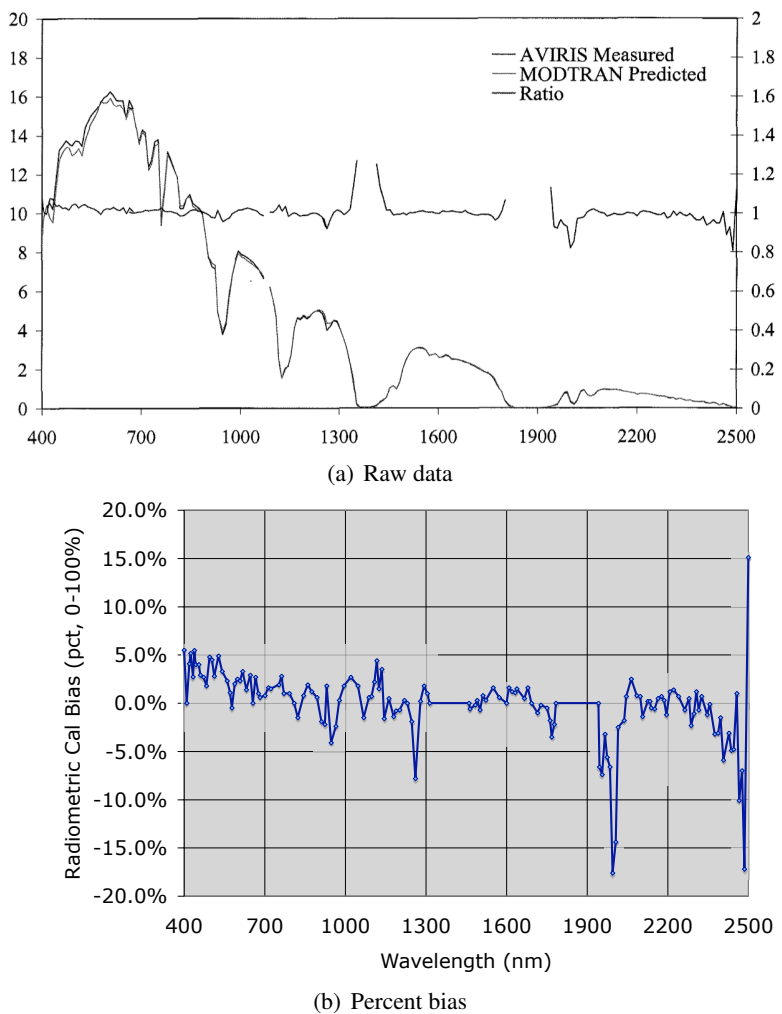


Figure 5.14: Estimated 2002 AVIRIS radiometric calibration bias model. Figure 5.14(a) comes from Green and Pavri (2003).

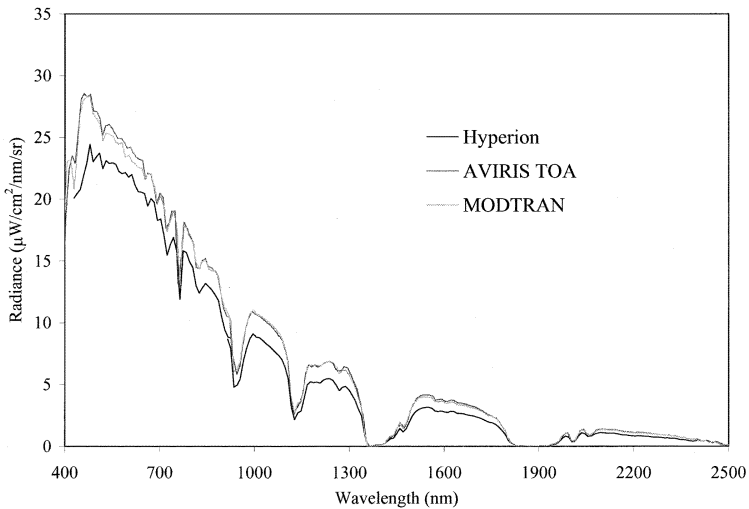


Figure 5.15: Observed 2001 Hyperion radiometric calibration bias. Figure is taken from Green et al. (June 2003).

shows the effect of a 0.5 nm shift. Whereas the various target types show small variation within the envelope created by the bright and dark gray reflectors, the degree of shift has a very strong macro-level effect. The 0.5 nm shift nearly doubles the effect on sensor-reaching radiance for some bands. For affected bands, the effect tends to increase with increased shift. A band center shift in the negative direction produces nearly identical results, except the signs are reversed.

This information is presented another way in figure 5.17, which shows the standard deviation of all ground target types with respect to the percent error in radiance. In other words, the sensor-reaching radiances for all 7 target spectra and 3 gray reflectors (100%, 50%, and 18%) were reconvolved with the shifted band model, and the standard deviation of the 10 results was taken as a function of wavelength and degree of shift. Any changes in radiance due to atmospheric features will be common to all of the spectra, so variation in the results should be a result of the unique contributions of each spectrum relative to the others. This can be verified by inspection of figures 4.13 and 5.17. Those points in figure 4.13 where the slope is highest correspond to the points of highest variation in figure 5.17. They do happen to fall within atmospheric absorption bands, but this most likely the result of sensor artifacts from when the spectra were originally measured. Because of the reduced importance placed on the atmospheric absorption bands

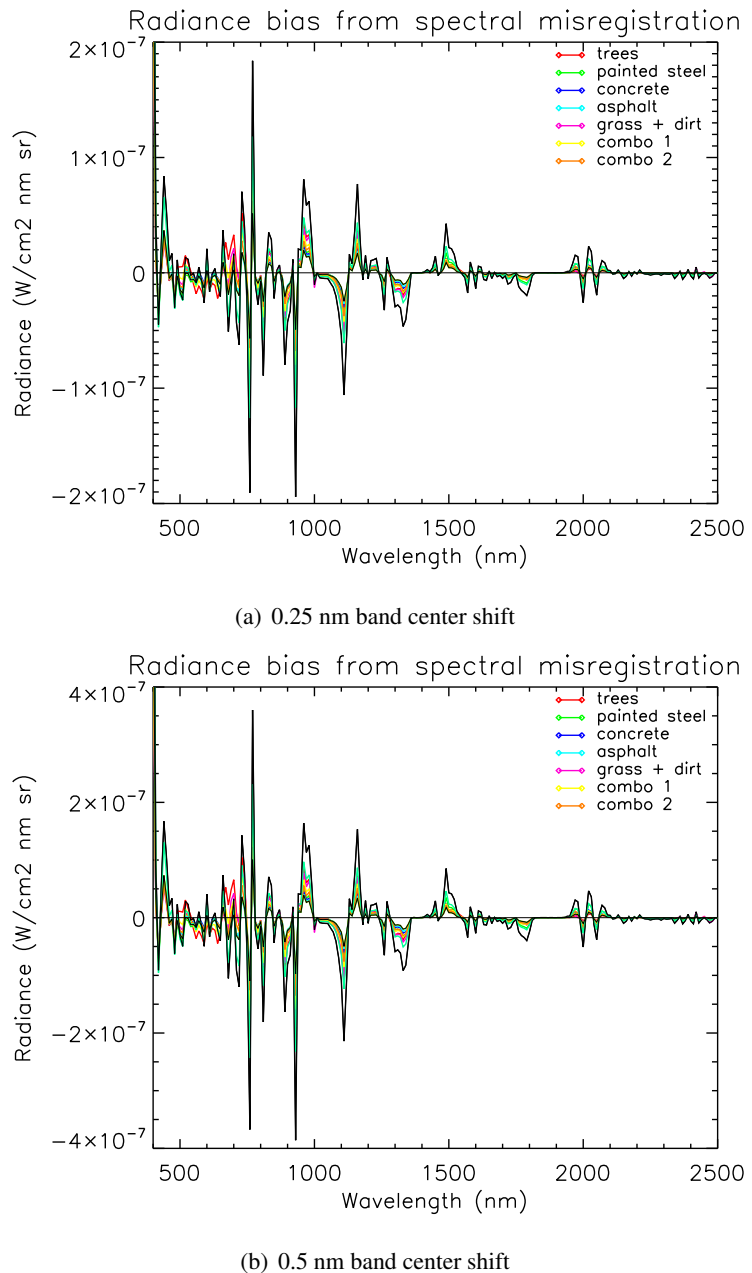


Figure 5.16: Radiance bias error due to spectral misregistration. The black curves bounding the family represent results for a 100% and an 18% reflector. The colored curves correspond to results for each of the 7 target types shown in figure 4.13.

(especially the 1390 and 1900 nm regions), it can be argued that choice of target reflectance spectrum skewed the results, depressing the significance of spectral character on spectral misregistration-induced radiance shifts. But, it must be noted that because the most typical types of ground cover were chosen, it is acceptable to conclude dominance of atmospheric absorption features is a natural state.

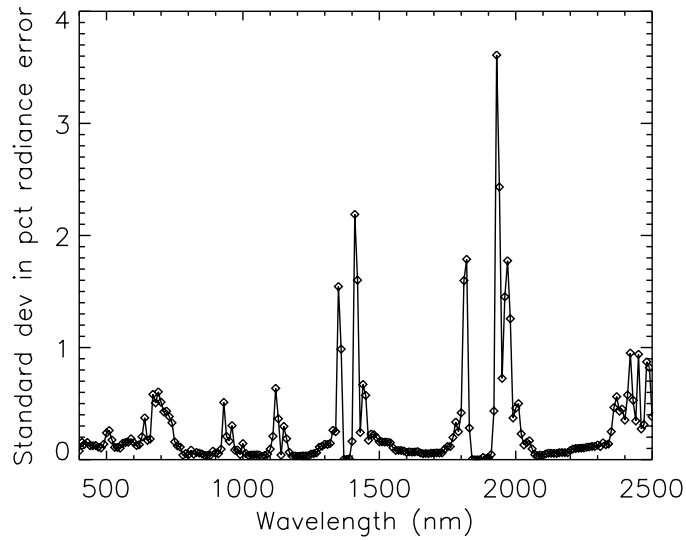


Figure 5.17: Standard deviation in percent radiance error due to the variability of target spectra

The modeling of spectral jitter effects was accomplished by generating a normal probability density function centered on the band's nominal central wavelength with the standard deviation set to 0.5 nm. Radiance curves were generated by shifting the Gaussian response curve center over ± 4 standard deviations, subtracting the mean from each result, squaring it, multiplying by the probability density function, and finally summing it. This process, shown in equation 5.3, approximates the second central moment or variance, of a function given its probability density function. The width of the probability density function was chosen to correspond to observed jitter for HYDICE according to Nischan et al. (1999), albeit on the high end of the reported range. The jitter was recorded as fractions of a channel corresponding to approximately 0.3–0.6 nm, but it could be as bad as 4.5 nm, depending on spectral band. An offset of approximately 0.15 nm was also reported.

$$\sigma_L^2 = \sum_{i=1}^n (L(\lambda) - L(\lambda_0))^2 p_i \quad (5.3)$$

Figure 5.18 shows the resulting uncertainty curves for the two bounding spectrally flat cases—the 100% and 18% reflectors—as well as for the 7 ground cover targets. The 100% reflector produces an upper bound on the uncertainty, showing that target brightness is again a significant contributing factor. Even though the target is spectrally flat, the atmosphere imparts the spectral shape driving the uncertainty, and brighter targets have deeper absorption features, stronger slopes, and ultimately a greater sensitivity to spectral misregistration effects. Contributions from the shape of the reflectance spectra are again seen in the visible region, where some of the ground cover curves exceed the envelope limits of the flat reflectors. In these spectral regions, the ground cover curves have slopes strong enough to show up in the radiance uncertainty results. Overall, it is noteworthy that spectral jitter, seen in figure 5.18, is of the same order of magnitude as radiometric calibration uncertainty, as seen in figure 5.12.

Because change in radiance due to spectral calibration errors is highly sensitive to multiple factors, it is difficult to abstract the behavior into a generalized model. Any model used is dependent on amount of bias or jitter, the target brightness, and the spectral shape, and while general behaviors can be described based on the first two factors alone, the “wildcard” nature of the target reflectance spectrum reduces the utility of attempting to predict error performance. This situation is similar to the problem presented by modeling clouds and backgrounds, but not as nicely behaved. Results will be presented that show the radiance errors presented so far propagated into reflectance space. Two scenarios were crafted to treat the effect of spectral misregistration on retrieved reflectance, one for bias and one for jitter, based on a notional case crafted for investigative purposes. However, as with background objects, the top level error propagation model provides no interface to model specific target spectra. A two-dimensional predictive tool able to operate on actual imagery could provide this capability, but that task is left to future work.

5.5 Environmental error modeling results

Although the naming may seem unintuitive, recall that “environmental errors” refer not to elements of the atmosphere, but instead to elements of the remote sensing environment. They were segregated from atmospheric uncertainty for two reasons: they are unpredictable according to any equation or functional relationship, and

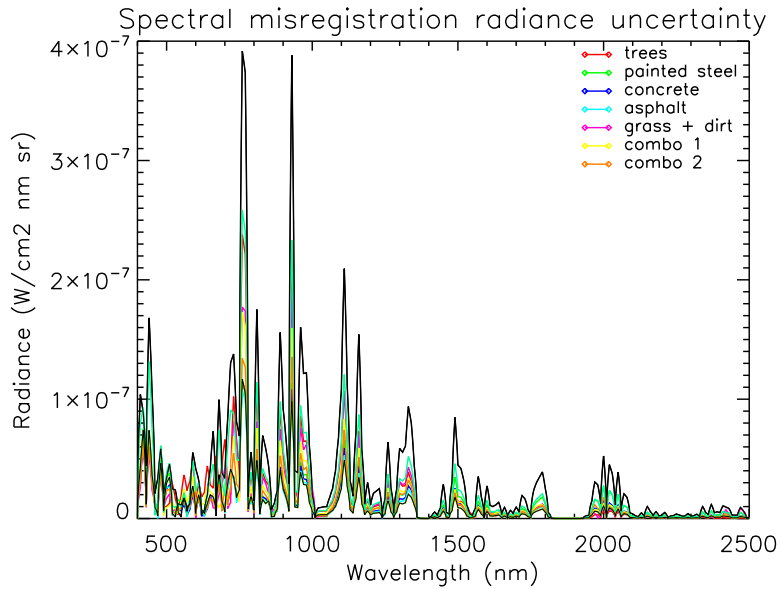


Figure 5.18: Uncertainty in radiance due to 0.5 nm spectral jitter

their error is unbounded. Despite these considerations, it is necessary to illustrate the effects on retrieved reflectance error.

It was unnecessary to build a model for ground tilt angle because it appears directly in the final reflectance expression, and there is no connection to antecedent sources. The models for instrument pointing angle, clouds, and background objects permit specification of the effect, and they will propagate their contribution forward into reflectance space. Results are presented that show their effects on the modeling outputs L_d , L_u , and τ_2 .

5.5.1 Pointing angle modeling results

Off-nadir pointing produces bias error in L_u and τ_2 . The fourth-order equation fit technique was used to produce analytical relationships for L_u and τ_2 as a function of pointing angle ψ and wavelength. Representative examples of these are shown in equations 5.4, which is for upwelled radiance at 550 nm for a platform at 792 m, and 5.5, which is for transmissivity at the same point. It would be impractical to list all equation fit coefficients for all altitudes. Although it may seem odd to keep the higher order terms, it must be noted that the input units for ψ is in degrees, and

the values for downwelled radiance are on the order of 10^{-5} to 10^{-7} . When the input variable is put to the third or fourth power, multiplying it by such a small coefficient still produces output just large enough to affect the final result, so 5 coefficients were carried for this fit technique. There would be negligible computational penalty for carrying even higher order terms, but this was felt to be a good cut-off point.

$$\begin{aligned} L_u(\psi; 550) = & 4.01 \times 10^{-5} - 7.98 \times 10^{-7}\psi + 6.29 \times 10^{-9}\psi^2 \\ & - 2.26 \times 10^{-11}\psi^3 + 3.15 \times 10^{-14}\psi^4 \end{aligned} \quad (5.4)$$

$$\begin{aligned} \tau_2(\psi; 550) = & -1.85 + 5.70 \times 10^{-2}\psi - 4.51 \times 10^{-4}\psi^2 \\ & + 1.63 \times 10^{-6}\psi^3 - 2.26 \times 10^{-9}\psi^4 \end{aligned} \quad (5.5)$$

Propagated error in L_u and τ_2 as a result of off-nadir sensor pointing is presented for the various available altitudes starting with 792 m in figure C.1, 4 km in figure C.2, 11 km in figure C.3, and finishing with 100 km in figure C.4. Both absolute and results relative to nadir are shown. There is a general trend that as the absolute value of the modeling output decreases, the effect of off-nadir pointing increases. Thus, as upwelled radiance increases with altitude, the percent change at 45° pointing angle decreases from about 40% to 30%. However, below 25° from nadir, there is a much smaller change (<10%) that is relatively insensitive to altitude.

Transmissivity shows similar behavior. As the absolute value decreases with increasing altitude, the percent difference with increasing ψ increases quite a bit, from -5% to -23%. The insensitivity range only applies within $\pm 5^\circ$ of nadir.

A final set of results is presented in figure C.5, which compares multiple scattering algorithms. There is the barest hint of a difference at 45° off-nadir in the lowest wavelengths, an effect that just exceeds 1% of upwelled radiance. It may seem so small as to be insignificant, but as this work tries to expose effects operating in the sub- to few-percent regime, it was considered worthwhile to avoid an unnecessary 1% hit to upwelled radiance.

These modeling results for the off-nadir pointing effect show a great deal of sensitivity of the parameter to off-nadir pointing, but the effect in reflectance space is unknown at this time. The implication of this variability is not obvious without carrying the propagation all the way forward into reflectance space. While a 30% increase in upwelled radiance or 15% decrease in transmissivity from nadir

to $\pm 20^\circ$ off-nadir may seem severe, the change in one parameter does not guarantee a significant addition of bias error or random uncertainty to the final retrieved reflectance.

5.5.2 Cloud modeling results

Cloud cover causes bias error in L_d . The product of the cloud model process is shown in figure 5.19. The Monte-Carlo style simulation produced 24,000 spectra, each of which corresponded to a certain number of sky quads filled with cloud and a certain percentage of the sky dome obscured by cloud. Because it was not reasonable to study every possible sky quad configuration, the sampling in figure 5.19 attempts to adequately span the configuration space.

Each spectrum was produced by specifying the independent variable, number of quads, but they must be re-indexed to sky fraction because the model specifies clouds according to sky fraction. As an example, all points corresponding to 20 cloud quads are boxed in figure 5.19(a). Although the quads are equiangular, they have different areas, so different combinations of a given number of quads will have different combined areas, which accounts for the vertical spread in the box in figure 5.19(a).

The spectra were then regrouped by sky fraction, which is shown by example in figure 5.19(b). In the example, all spectra covering 25-30% of the sky are boxed. The results to follow are aggregated in 5% bins, but in the model, any custom range specification can be applied to the entire dataset and these results are regenerated on-the-fly.

Figure C.6 shows the effect of the cloud simulation on downwelled radiance. The radiance curves in figure C.6(a) are grouped by quad, and those in figure C.6(b) are grouped by sky fraction. Each grouping was compared against the clear sky downwelled radiance and had its root-mean-square deviation calculated. These curves are calculated for presentation purposes only. In practice, the model carries all spectra forward in raw form and individually calculates their effects on the final result. Also, note that because the root mean square is shown, all results are presented as positive. However, actual bias errors are positive or negative depending on conditions, and all calculations carry the correct sign throughout.

Finally, several types of clouds were tested. Figure C.7 shows relative effect on downwelled radiance for stratus and altostratus clouds. There are minor differences on the order of single-digit percentages in the most affected wavelengths. High altitude cirrus clouds, both visible and invisible, would be a welcome addition to the cloud simulation model. Wylie and Menzel (1989) estimate that not only is

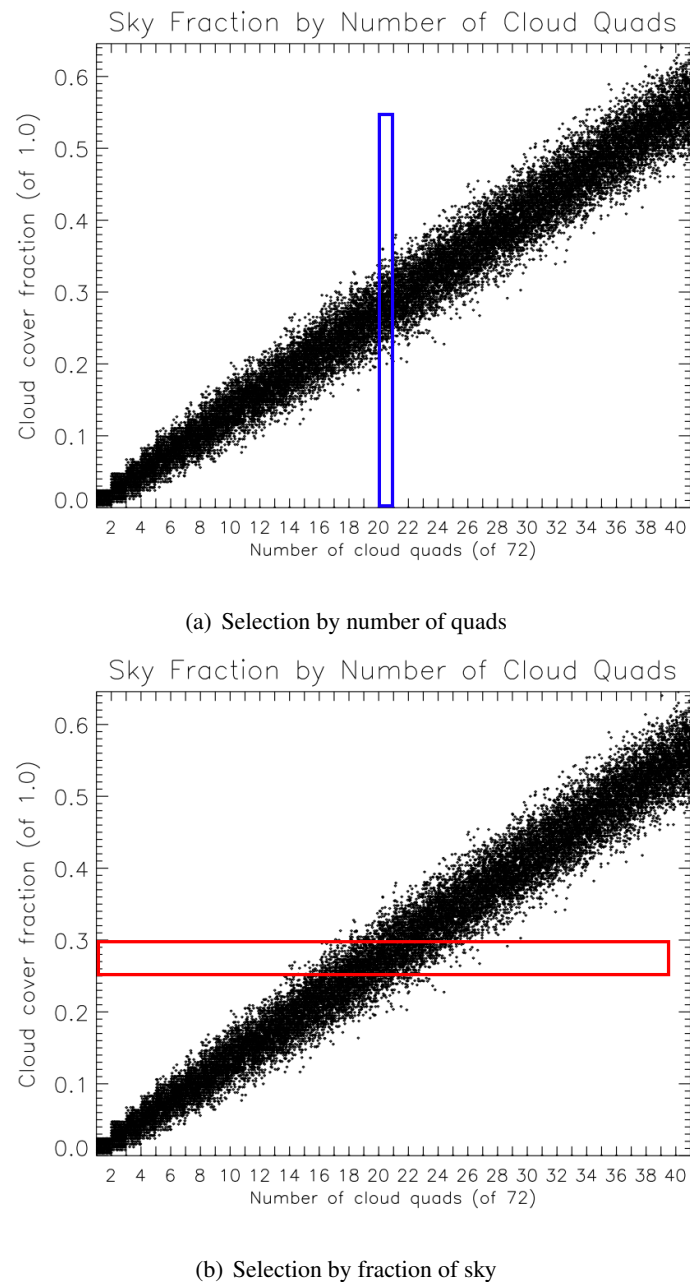


Figure 5.19: Relationships between cloud quads and sky fraction

45% of the United States is covered by opaque clouds at any time, but also that an additional 20–30% is covered by thin, semi-transparent cirrus clouds.

Clouds are critical contributors to the remote sensing environment. These results merely give a hint as to the potential variability clouds provide, and further research is required into the validity of the current modeling technique with different cloud types and geometries, especially partially transparent clouds. For a remote sensing user attempting to estimate cloud cover, it is clear that not only does cloud cover have the potential to greatly influence one or more remote sensing parameters, but that “perfect estimation” is a multi-dimensional problem. Even if the amount of cloud cover were perfectly known, these results show that geometry causes great variability in the effects on the downwelled radiance. If both cloud amount and location were both known, then cloud type and opacity become important variables. If all cloud parameters are perfectly known, the time-varying nature of cloud cover very quickly invalidates the estimate. If clouds cannot be modeled, and they cannot be avoided, the only remaining course of action of a user is to look for remote sensing regimes for which the impact of cloud cover is minimized. Presented later are results where these error spectra are propagated into reflectance space will provide pointers to conclusions of this nature.

5.5.3 Background object modeling results

Sky obscuration by background objects also causes variability in L_d . However, because the simulation was restricted to the lowest-elevation ring of quads, the 12 quads subject to background obscuration are equal in size. As a result, figure 5.20 shows much less diversity in sky fraction than did figure 5.19. The implications of this result are shown in the figure. The vertical blue box encloses all output spectra corresponding to 6 of the 12 quads being filled with background objects, identically to the cloud simulation. However, because there is no area diversity in the activated quads, there are fractions with zero corresponding radiance spectra. Although this would only happen for certain cases with narrow sky fraction ranges, it is possible. An example is shown with the magenta box in figure 5.20, which attempts to enclose spectra covering $20\% \pm 1\%$. No background radiance spectra meet the hypothetical specification, so the range would need to be widened for the model to function properly. The red box encloses the spectra that would be retrieved by a specification of $10\% \pm 1\%$, just as with the cloud simulation.

Figure C.8 shows the effect of background objects on downwelled radiance. Because the clear sky quad was replaced with a composite ground object spectrum, the change in downwelled radiance is quite differently shaped from the cloud spectra. However, the magnitude of this change, as shown in figure C.8(d), is at least an

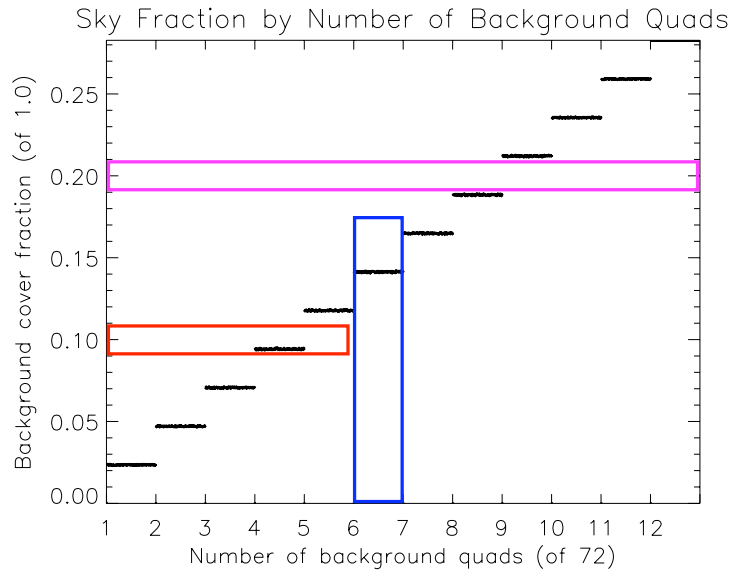


Figure 5.20: Correlation between background quads and sky fraction

order of magnitude lower than the effects of clouds and thus of much lower concern. Again, the root mean square curves are all positive, but actual bias errors are positive or negative depending on conditions.

5.5.4 Environmental error scenario summary

The environmental effect modeling presented in the preceding sections was applied to propagate bias and random uncertainty into the final reflectance retrieval. Baseline values and uncertainty ranges were selected for each and propagated into reflectance space. For each scenario listed in table 5.9, results will be presented that show the effect on reflectance error and that compare the relative magnitude of these contributions to those induced by atmospheric uncertainty. Note the scenario numbering continues from table 5.8.

5.5.5 Combined effects

Although not strictly an environmental condition, one final scenario was created. It combines the random contributions from basic scenario 2 with reasonable envi-

Table 5.9: Environmental Error Scenario Settings

	Environmental Effect	Scenario baseline	Uncertainty range
6	Nadir angle bias	792 m	0–15°
7	Nadir angle bias	4 km	0–15°
8	Nadir angle bias	100 km	0–15°
9	Nadir angle uncertainty	4 km, 0° nadir	0–1°
10	Nadir angle uncertainty	4 km, 15° nadir	0–1°
11	Ground tilt bias	0°	0–15°
12	Ground tilt uncertainty	5° tilt	0–10°
13	Ground tilt uncertainty	20° tilt	0–10°
14	Cloud cover knowledge	10% cumulus cover	1–5%
15	Cloud cover knowledge	20% cumulus cover	1–5%
16	Background objects	10% obscuration	1–5%
17	Background objects	20% obscuration	1–5%
18	Sensor random noise	none	AVIRIS, HYDICE, Hyperion
19	Sensor calibration bias	none	AVIRIS (2002), Hyperion (−3%)
20	Spectral bias	0.25 and 0.5 nm bias	by target type
21	Spectral jitter	0.5 nm uncertainty	by target type

ronmental contributions taken from the environmental scenarios. The results are a synthesis of atmospheric constituent uncertainty, environmental bias effects, environmental random effects, sensor bias, and sensor random effects. Thus, this final scenario attempts to simulate the most likely best-case result if a field sensor network were used to feed a model-only inversion. Table 5.10 summarizes the parameters used.

5.6 Total error

Scenario error propagation results reside in Appendices D and E. All scenarios were run using both a 100% reflector and a 20% reflector. Scenarios are grouped into three categories. “Basic” scenarios simulate *only* contributions from errors in atmospheric constituent determination. “Environmental” scenarios simulate a wide variety of environmental effects contributing bias or uncertainty, one scenario per effect. These effects include ground tilt, sensor pointing, clouds, background ob-

Table 5.10: Combined Effect Scenario Settings

	Parameter	Value
22	Water vapor uncertainty	0.2 cm
	Density alt. uncertainty	0.045 km
	Aerosol uncertainty	0.04
	Sensor random noise	AVIRIS (1999 post-season cal)
	Sensor calibration bias	AVIRIS (2002)
	Nadir angle	0°
	Nadir angle uncertainty	1 milliradian
	Ground tilt	0°
	Ground tilt uncertainty	5°
	Cloud cover	15% cumulus cover
	Cloud cover knowledge	to within $\pm 5\%$
	Background objects	5% obscuration
	Spectral bias	0 nm
	Spectral jitter	0 nm

jects, and instrument noise. The “combined” scenario is the final category, in which error from all sources are combined at realistic magnitudes into a single scenario. Each scenario from the first two categories attempts to examine a single source at a time so that the relative influence can be studied. Error contributions do not sum linearly, so it is necessary to study each effect in isolation. The final scenario shows the effect of combining effects. Because of the endless permutations possible when combining effects, the magnitudes were set to their most likely, most reasonable, or most useful values.

The basic scenarios listed in table 5.8 produced the modeling results shown in figures D.3 through D.12. The results show total reflectance error predictions along with error contributions from each individual output. The correlated error contributions are also shown by individual component on separate plots. Summary results are presented here as figure 5.21. Uncertainty in retrieved reflectance is shown for 100% and 20% reflectors, with all 5 scenarios plotted together. The black curve corresponds to the first scenario, which uses climatology-only sources for atmospheric constituents. The red and green curves correspond to ground instruments of low and high quality, respectively. The blue and cyan curves show the predicted approximate uncertainty present in model-based algorithms such as

FLAASH. The two curves attempt to bound the performance between worst case (humid and hazy) and best case (dry and clear) atmospheric conditions. Each scenario will be presented and discussed individually.

The environmental effect scenarios listed in table 5.9 produced the results shown in figures E.1 through E.11. These show the outcome of parametric studies focusing on the error contributions of various degrees of injected environmental effects. Because single effects are shown, the single factor contributions always match the total output, therefore only total random error or total bias error is shown at any one time. These results are so diverse and unique to the physical factor being simulated that summation is not possible.

It is extremely important to remember that random error results are intended to indicate, by spectral band, the width of a random statistical distribution from which random errors are taken, but bias errors represent a literal increase or decrease in the retrieved reflectance.

The remainder of this section is a detailed discussion of each of the 22 scenarios, presented either individually or grouped by effect, as appropriate.

5.6.1 Scenario 1 – Climatological sources

Appendix D, starting on page 217, contains the detailed results for the 5 basic scenarios. Scenario 1 reflects the use of *a priori* climatology data without support from in-scene estimation or ground truth measurements. This starting point does not serve a practical purpose, but it shows the effects on a much larger scale and may serve as a rough measure of the validity of using default inputs in scene modeling. The predicted standard deviation of random uncertainty error ranges from 0.1–0.7 reflectance units for a 100% gray reflector (figure D.3(a)) and 5–30 reflectance units for a 20% gray reflector (figure D.3(b)). For the lower reflectance target, this uncertainty exceeds the actual target reflectance.

Some noteworthy effects that will run across scenarios are best visible in the results for this scenario. An intuitively obvious difference between the contributing effects for 100% and 20% reflectors is easily shown here. For the 100% reflector, error in both transmissivity terms dominates, but for the 20% reflector the upwelled radiance dominates as it is unaffected by the change in reflectance, and the other terms are reduced by a factor of 5.

The other interesting effect is the contribution of correlation terms. There are six correlation terms described in appendix A, and the sum total of these terms is shown in figures D.3(a) and D.3(b).

The actual correlation curve shown is more accurately described as a "signed square root" in that the sign of each term is recorded, the square root of the absolute

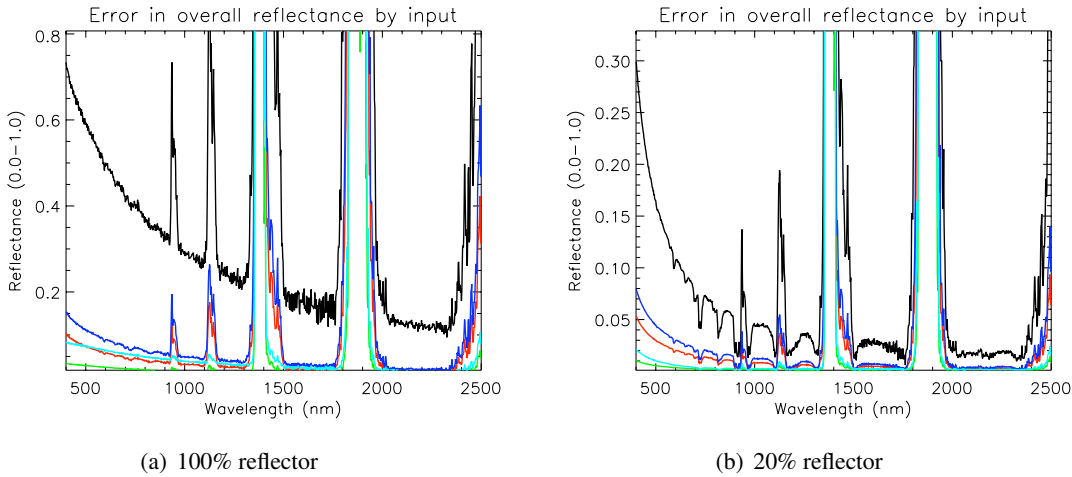


Figure 5.21: Total reflectance uncertainty summary for basic scenarios 1-5. Color coding shows total reflectance error for basic scenarios 1-5 in the following order: black (1), red (2), green (3), blue (4), and cyan (5).

value is taken, then the sign is applied to the result. Unlike the other terms, the sign of the correlation terms is key, so it is preserved before the square root is taken. Because correlation terms are added directly without squaring, their sign is critical to understanding the results. The other uncertainty terms contribute to final error as squared error, so their sign is not important. However, the other error terms are all combined when squared but presented as square roots of the squared error to provide intuitive context for the magnitude of the results. The correlations are not technically squares of any term, but they also need to be shown as a square root so that the relative magnitude of their contributions is placed in proper context.

There is a high negative error contribution from cross-correlation, confirming the common knowledge that there is high positive correlation between the two radiance modeling outputs and the two transmissivity modeling outputs and high negative correlation between each radiance/transmissivity combination. These positive and negative correlations have a net effect of reducing the total uncertainty.

The underlying component correlation terms are presented later in the same appendices, as figures D.4(a) and D.4(b). For all scenarios, it can be seen that the τ_1/τ_2 and L_d/L_u correlation terms are positive and the others are generally negative (except for a quirk in water vapor and aerosol behavior at the low end of the visible spectrum, explained for the next scenario).

Because of the near-overhead sensing geometry, the correlation between the two transmissivity terms is directly dependent on target reflectance. The correlation between the two radiance terms has a smaller dependence on reflectance. In contrast, the negative cross-correlations between transmissivity and scattered radiance consistently match each other across the range of scenarios and reflectances.

The noteworthy observation regarding correlation effects is seen in figure D.3(b), where the upwelled radiance contribution actually exceeds the total predicted reflectance error. The correlation term reduces the overall error below the upwelled contribution for low reflectance targets, an effect that repeats in other scenarios.

5.6.2 Scenario 2 – Field-quality ground instruments

Scenario 2 predicts the retrieved reflectance uncertainty from a “commercial-quality” sensor network, which is to say ground truth measurements are fed into MODTRAN to accomplish model-only inversion. This is the “poor man’s” inversion method, used by someone who cannot afford either science-quality instruments or a hyperspectral sensor but still needs surface reflectance. “Poor man” is definitely a misnomer though, as any organization that is trying to extend the use of existing platforms that lack sounding capabilities, needs to make use of ad-hoc ground truth networks, and is interested in reflectance inversion is subject to the constraints of this type of scenario regardless of resources.

“Commercial quality” instruments describes the smaller, lower-accuracy commercially available instruments that can be field-deployed in an unattended network. “Field quality” is another way of describing this type of network. In truth, instruments placed into this category are not low quality, rather they are the state of the art.

As seen in figure D.5(a), the error propagation model predicts 4–10 reflectance units of uncertainty in the visible spectrum for a 100% reflector. Figure D.5(b) shows a prediction of 1–5 reflectance units of uncertainty in the visible range for a 20% reflector. Again, with the lower reflectance target error in upwelled radiance dominates the result with a shape that suggests aerosol contributions (this is studied in more detail in later results).

The other main feature to observe here is the sign inversion in the correlation term. A comparison of figures D.6(a) and D.6(b) shows that the downwelled radiance correlation terms exert increased influence for the 100% reflector and that they are responsible for the sign inversion below 550 nm. From experience this is known to be a joint aerosol/water vapor effect. The aerosol model used is known to drop off in scattering below 500 nm. Also, it is concluded here that water vapor’s absorption effects give way to density effects in the lower end of the visible

spectrum. Water vapor is significantly less dense than dry air, and this decrease in density is in constant tension with water vapor's tremendous absorption capability, though density ultimately loses this fight for dominance. However, the density effects are visible far enough away from those absorption bands. The main conclusion from this observation is that lower target reflectances exhibit more nonlinear error behavior than higher reflectances. This conclusion is validated by the validation results for this scenario, shown in figures F.3 and F.4.

5.6.3 Scenario 3 – Research quality ground instruments

Scenario 3 employs the best ground sensor network available to drive the model-only inversion method. These sensor capabilities are intended to match the Department of Energy's ARM program, though the program is much more extensive than the sensor survey results in section 5.2.2. Their ability to filter multiple observations from multiple instruments during intensive observation periods is not reflected here.

Figures D.7(a) and D.7(b) show error model predictions for the 100% and 20% reflectors, respectively. There are some minor differences that contrast with scenario 2, namely an increased contribution from the correlated error terms, a greatly increased relative contribution from upwelled radiance for the low reflectance target, and a change in dominance for the high reflectance target. This change in dominance is more of a shift from upwelled dominance to co-dominance for all the terms, and it is seen by the more linear slope in the overall reflectance term in comparison to either the lower reflectance target or the previous scenario.

Other than magnitude, there do not appear to be any significant shifts in behavior in the underlying correlation terms shown in figures D.8(a) and D.8(b).

The jagged appearance of the line is a machine precision artifact inherent in how τ_1 is calculated by the model. Any curve where the τ_1 contribution is nontrivial also takes on this appearance, which only provides information already in evidence by the relative magnitude of the curve itself.

5.6.4 Scenarios 4 and 5 – In-scene sources

Scenarios 4 and 5 simulate in-scene methods working at opposite ends of their precision ranges. Scenario 4 simulates a humid, hazy atmosphere, and scenario 5 simulates a dry, clear atmosphere. Because most uncertainty types were found to be positively correlated with constituent abundance, scenario 4 is the poorer performer of the two, and scenario 5 performs very well. These results should be taken to bound the precision of model-based inversion algorithms.

Considering scenario 4 first, the wet and hazy atmosphere results in figure D.9(a) were below 15 reflectance units for a 100% reflector in the visible range, dropping to below 5 reflectance units in the SWIR region. This is very high, but it is also the absolute worst case. Even so, 5% error is still well-within the family of reported results for the performance of model-based inversion (Kruse, 2004; Kerekes, 1998). At 20% target reflectance, as seen in figure D.9(b), the uncertainty is cut in half, down to below 1 reflectance unit in the SWIR.

In the scenario 4 20% result, the classic upwelled radiance contribution (the cyan curve) is prominent, suggesting aerosol dominance in the visible region according to common knowledge. However, later analysis in section 5.8 will show that water vapor also contributes to upwelled radiance. Relative to their typical values, there is an imbalance in favor of water vapor uncertainty. Put another way, aerosol uncertainty in this scenario was moderate while water vapor uncertainty was very high. This is quantitatively supported. Using the scenario definitions established earlier, the signal-to-noise ratio (SNR) for water vapor was $2.0 \text{ cm} / 0.3 \text{ cm}$ or 6.67. For aerosols it is $0.65/0.063$ or 10.3. This condition leads to upwelled radiance driven by water vapor despite aerosol's traditional assertiveness in this regard. Aerosol's general relationship to upwelled radiance is unchanged; it is the uneven conditions imposed by the scenario that skew the results. As an aside, the later analysis will also show that 20% reflectance is not quite dark enough to manifest aerosol dominance. Negative correlations between the model output terms actually reduces the error quite a bit in the aerosol-only case. At 20% the error is actually at a minimum. Below 20% the correlations disappear, and the aerosol-driven upwelled radiance error contribution is fully visible. A tidbit of usefulness here is to conclude, then, that water vapor should be a high priority for augmented measurement in humid environments, especially for dark targets like vegetation.

Scenario 5 represents the best that model-based algorithms can do (without considering any spatial and spectral convolution or correction tricks). For the 100% reflector, figure D.11(a) shows decent performance starting at just above 8 reflectance units, dropping quickly to below 3 reflectance units of uncertainty in the near IR and short wave IR. Again, this is consistent with literature observations of in-scene inversion algorithms. The 20% reflector results, shown in figure D.11(b), show retrieved reflectance uncertainty under 2 reflectance units, and most often less than half of a reflectance unit. As with the previous scenarios, there is a strong component from upwelled radiance counteracted by strong negatively correlation terms. In this case, the water vapor uncertainty is much lower, but the aerosol uncertainty is more or less the same as for the hazy case. It is expected that aerosol uncertainty would dominate because of this, except the presence of the

correlation terms makes it hard to predict exactly which effects are the most active.

It may be striking just how different the results these two cases are from one another, but the modeling methodology easily exposes the cause: the water vapor and density altitude parameter uncertainties each spanned an order of magnitude. It may be standard to see this level of variability between different classes of ground instruments, but it was also demonstrated earlier that in-scene constituent retrieval can vary dramatically depending on atmospheric conditions and, in some cases, scene content.

The final key observation is that the uncertainties for the in-scene inversion algorithm scenarios are higher than for the previous scenarios. The best-possible atmospheric determination uses the ARM-grade instrumentation. The reflectance random uncertainty for scenario 3 was 1 reflectance unit at its maximum in the visible region, and quickly dropped to 1 or 2 tenths of a reflectance unit for the rest of the spectral range. The best in-scene performance from scenario 5 is roughly double this, meaning improvement from truth-augmentation would be possible and beneficial.

5.6.5 Scenarios 6 through 8 – Off-nadir pointing bias

Appending E, beginning on page 229, contains the results for the environmental effect scenarios. Scenarios 6, 7, and 8 are grouped together because they all explore the effect of off-nadir pointing on retrieved reflectance. Off-nadir pointing increases the path length of the atmospheric column, decreasing the target/sensor transmissivity τ_2 and increasing the path radiance L_u . A larger path length than what was assumed by the model has the overall effect of decreasing the retrieved reflectance as a negative bias effect.

Figure E.1 shows the magnitude of this bias for several different altitudes and pointing angles over a 100% reflectance target. Different sensor instruments have a wide range of architectures such that one instrument would never capture a scene outside more than a degree or two field of view, whereas another may scan a viewing swath of 30° or more. These sensors may be based on aircraft or spacecraft. For the worst case studied, which is a 15° off-nadir shift from 100 km, the negative reflectance bias was less than 1–2 reflectance units. For a 20% reflector, the bias was both positive and negative but with a generally less pronounced effect. For the 100% reflector, the effect from the decrease in transmissivity, which is reflectance dependent, dominated the effect from increase in path radiance, which is not. When the target reflectance is lower, the transmissivity and path radiance effects are more in balance, causing the surprising curve shapes seen in figure E.2. For the aircraft height, the differences were almost negligible, and from the spacecraft height, the

bias was small but nontrivial.

Because the position of the sensor is known, this error source is a geometric effect that can and should be removed systematically. Modeling should account for the path length changes either by directly specifying them or by detecting the increased quantities of water vapor or aerosols using in-scene methods. Even if the bias is ignored, both narrow and wide field-of-view spacecraft should not suffer greatly in reflectance retrieval, unless of course accuracy to within 2 reflectance units of 1σ uncertainty is desired.

5.6.6 Scenarios 9 and 10: Off-nadir pointing uncertainty

Scenarios 9 and 10 show the effect of inaccurate knowledge of pointing angle. Figure E.3 shows bias error on the order of 8×10^{-5} for a 100% reflector and 1° pointing knowledge. Typical pointing accuracy is on the order of milliradians, and can be as low as microradians. This effect can be safely ignored.

5.6.7 Scenario 11: Ground tilt bias

Ground tilt bias is one of the most problematic effects that can be modeled. The cosine effect causes rapid change to perceived ground target reflectance after a small change in relative tilt angle. This is clearly seen in figure E.4(a), where negative bias approaches 20 reflectance units for a 100% reflector and 15° tilt. However, in the more restrained case of a 3° tilt, the negative bias to retrieved reflectance is 2–3 reflectance units. The results for the 20% reflector case, shown in figure E.4(b), are exactly one fifth of those for the 100% reflector.

It is dangerous to underestimate the impact of bias error effects. Whereas a 1 sigma random error result would predict that 68% of the time the result will fall within ± 3 reflectance units of the true value, often very close to the true value. With a bias error, there is a 100% guarantee that the retrieved value will differ from the true value by 3 reflectance units. A 20 reflectance unit difference for a 100% reflector is 20% guaranteed error on top of all random uncertainty that applies to the retrieval.

5.6.8 Scenarios 12–13: Ground tilt knowledge uncertainty

It is charity to limit tilt angle knowledge to 10° or less. Even in cases where the actual angle is small (5° or less, as shown in figures E.5(a) and E.5(b)), knowing that the ground tilt angle is bounded to within 10° , a pittance for hilly ground, introduces uncertainty of 10–12% reflectance in final retrieved reflectance for a

100% reflector. A more ambitious assumption of 2° angle knowledge results in a more manageable 2 reflectance unit uncertainty in final reflectance.

The impact of knowledge error in the case of inverting reflectance of highly sloped terrain (figures E.5(c) and E.5(d)) is considerably worse in all but the best of situations. This represents a case where a slope is known to exist, but it may vary by a couple of degrees. If inversion is being conducted over a sloped surface known with 2° uncertainty, the same 2–3 reflectance unit uncertainty is predicted to be present.

Other than the tendency for the ground to be flat, there is no limit to the havoc hills and slopes can wreak on the remote sensing of bright targets. In general, the imaging scientist has zero knowledge of the local ground tilt angle. Model-based algorithms are powerless to detect and compensate for non-systematic ground tilt variations without the help of active sensors, though it may be possible to detect and correct for a constant slope across a scene. When it comes to darker targets, the outlook is more optimistic. As shown in figure E.5(d), the impact of ground tilt uncertainty is bounded to within approximately 3–4 reflectance units for the 20% reflector, with a most likely best case impact of half a reflectance unit or less.

There is no refuge for the imaging scientist other than to use apparent reflectance or hope that an assumption of flatness to within 2° (184 feet of elevation change per mile) is valid. Apparent reflectance is a time-stable material property that affects reflectance in a manner similar to a target being in shadow. Many imaging algorithms can deal with a shadowed targets, either explicitly as a separate class or by using brightness-insensitive metrics such as spectral angle (though this is not to say that targets are not spectrally altered by either shadow or tilt effects – they are). Therefore, the overall contribution of target tilt to absolute reflectance error can be high but the impact to perceived reflectance and, subsequently, the imaging science application of the retrieval, can be low.

5.6.9 Scenarios 14–17: Bias error due to cloud cover and background objects

Clouds and background objects are both difficult to model and discuss. It is nearly impossible to generalize about clouds because their geometric and radiometric character are so variable that any analysis and conclusions are applicable only to the conditions modeled and those specific results. The attempt here was to divide the variability space into cloud type families and show a bias spread based on geometric configuration. The contributions of cloud cover to reflectance retrieval error are obvious, but because they add direct bias to the retrieved reflectance, it is difficult to integrate them into a sensor network based on uncertainty reduction. In

other words, adding a diffuse radiance sensor to the network should theoretically reduce single-point cloud/background bias to zero, a simple and elegant solution to the problems cloud cover and terrain masking pose. The validity of this approach has not been fully explored.

Figures E.6 and E.8 show cloud and background bias results for a 100% reflector. Figures E.7 and E.9 show the same for the 20% reflector.

Because clouds are volatile, it is futile to model a given sky configuration and hope to match it to actual conditions if the imagery is collected over any appreciable time span. The statistical approach provides a family of curves, each of which corresponds to the quantity specified, *i.e.* 10% or 20% cloud cover. There is no specification of where those clouds are located in the sky, and if the 10% cover is at the horizon, then the contribution is much different than if the clouds are overhead or near (but not blocking) the sun. The same is true for background objects to a lesser extend, with the exception that terrain masking can be known and measured for each point in the image. The spatial component is captured by the width of each curve family. The maximum and minimum curves are the theoretical limits to the contribution of clouds and background, outliers (see figure E.6(c)) notwithstanding.

The cloud and background object modeling results also show the effects of coverage knowledge. For 10% cloud cover over a 100% reflector, retrieved reflectance was negatively biased between 1-10 reflectance units, again depending on the geometric configuration, opacity, and shape of those clouds. For a given percentage of cloud cover, in this case 10%, the uncertainty in the coverage estimate was also varied. Figure E.6(a) shows $10\% \pm 1\%$, meaning the true sky fraction was accurate to within 1% of the sky. Figure E.6(b) shows $10\% \pm 5\%$, or an estimate accurate to within 5% of the sky dome area.

Random error in sky fractions F_1 and F_2 still manifests as a bias effect on final reflectance. Specifically, it has the effect of widening the family of curves for each result. For simplicity, the uncertainty is modeled as a uniform distribution in that spectra are included or excluded in a binary fashion, but are never scaled. Put another way, increasing the uncertainty of the sky fraction merely increases the size of the bounding box in figure 5.19(b) to include more spectra.

For 20% cover, the bias ranged from 4–15 reflectance units. Both cases represent a very significant source of error, and they themselves are subject to a great deal of variability. As with the 10% cloud cover case, increasing from $20\% \pm 1\%$ to $\pm 5\%$ sky fraction random uncertainty results in a corresponding increase in the curve family width. This has little effect on the average cloud bias, but the maximum and minimum cloud contributions now move to greater extremes.

For the 20% reflector, the effect of downwelled radiance is greatly reduced, so the negative bias induced by clouds drops from 1–10 reflectance units down to 2–3 reflectance units for either 10–20% cloud cover.

Background objects were modeled using a composite spectrum that combines reflectances from vegetation, asphalt, and building materials. Therefore, this result is not universally applicable because no actual object actually has these spectral characteristics. Because background objects were restricted to the horizon, there was much less variability in bias curves due to geometric configuration. Also, specular reflectance is not modeled, only Lambertian downwelled radiance. This is a major weakness of the background object module that can be addressed in future work.

There is a pronounced spectral character in the background object bias results that results from the composite background object being darker than the sky in the visible spectrum and brighter than the sky in the NIR/SWIR spectral range. This manifests as the bias sign inversion seen in all background bias results for both reflectors. The general conclusion here is that the background can both contrast sharply or blend in nicely with the diffuse sky radiance it obscures depending on conditions.

Unlike clouds, background objects have a small effect, with up to ± 0.5 reflectance units of bias error for a 100% reflector and ± 0.2 reflectance units for the the 20% reflector. However, unlike random errors, these biases are directly added to or subtracted to the final result. This makes them powerful drivers in precision remote sensing.

5.6.10 Scenario 18: Sensor noise

Industry-best instrument precision is assumed by using noise curves for AVIRIS and HYDICE. Figure E.10 shows the impact of sensor noise propagated to final retrieved reflectance (via sensor reaching radiance L_{SR}). Error is generally limited to 0.2 reflectance units or less, which amounts to basically zero contribution when added in quadrature to the other sources. Although these results show little contribution for the instruments chosen in this study, there is nothing inherent that limits the noise for the hardware part of the imaging chain – sensor noise should never be ignored.

5.6.11 Scenario 19: Sensor radiometric calibration bias

Calibration bias was injected into the error propagation model in such a way that attempts to match reported bias results for AVIRIS and Hyperion. The result

is shown in figure E.11. Accuracy for the industry standard instruments hovers around 3% or less, and as can be seen in the result, this is not trivial at all. Reflectance bias as a result of bias in the sensor-reaching radiance is extremely simple to model: the difference in radiance is a simple linear adjustment factor to the sensor-reaching radiance term, which is then combined with the upwelled radiance term. This gives an indicator as to why the cal bias can produce such dramatic effects.

In figure E.11(a), the AVIRIS bias for the 100% reflector shows a change in reflectance of 1–10% in response to a 2–5% bias in radiance, with maximum impact at 400 nm. In the VNIR and SWIR, the effect on radiance stays within ± 2 reflectance units, increasing past -5 reflectance units after 2400 nm. In figure E.11(b), the 20% reflector causes the sensor radiance term is lower in relation to the path radiance term to begin with. Therefore, changes in the sensor radiance term do not produce as much of a change in reflectance as with the 100% reflector. Except for the green, blue, and far SWIR spectral regions (where reflectance bias climbs to as much as 4 reflectance units), the effect on reflectance is within ± 2 reflectance units.

Hyperion’s hypothetical 3% negative bias in sensor-reaching radiance manifests as a decrease in retrieved reflectance. The effect takes on the shape of the upwelled radiance contribution to retrieved reflectance, as it is relatively larger compared to a spectrally constant reduction in the sensor radiance contribution. A 3% reduction in radiance results in a 5.5 reflectance unit drop for the 100% reflector worst case at 400 nm and a 4 reflectance unit drop for the 20% reflector at 400 nm. The negative bias improves with increasing wavelength until a steady state is reached past 1000 nm.

This result is striking when compared to the tiny contributions the other sources of error and uncertainty have had on retrieved reflectance. The AVIRIS instrument in particular has a reputation for being well-calibrated and low-noise (look no further than the previous scenario for proof of this). Atmospheric uncertainty and many environmental errors can be reduced to less than 1 reflectance unit using best-available instrumentation and modeling. However, if spectrally unpredictable biases of 2-5 reflectance units are unavoidable due to an undetectable instrument calibration bias, then attention is warranted here. The mitigating factor is that the calibration bias could be over-reported, and some of the bias exists in the MODTRAN model used as the reference. On the other hand, Hyperion’s 11-21% bias that had gone undetected or had drifted since the pre-launch calibration, corrected down to approximately 3% bias, is a major source of error regardless of the inversion technique used.

5.6.12 Scenario 20: Bias error due to spectral misregistration

This scenario was run using two values for spectral band center shift, 0.25 and 0.5 nm. Results for all target types tested are shown on a single plot. Figure E.12 shows the effect on reflectance for these conditions. In general, spectral misregistration for both cases fails to cause a bias more than half of a reflectance units except for the atmospheric absorption bands. For the two major water vapor absorption regions at 1390 and 1900, the effect exceeds 10 reflectance units, but for the other water vapor regions and the oxygen, ozone, etc. the effect is to perturb retrieved reflectance by no more than 2-4 reflectance units.

It is already known that spectral misregistration can adversely affect applications that use absorption bands such as atmospheric constituent estimation. It may not be useful to propagate errors into reflectance space because applications affected by spectral cal errors use radiance to compute band ratios. While some algorithms can detect and correct misregistration effects, others are powerless to do either.

A study was conducted to measure the effect of spectral registration bias on such applications. The continuum-interpolated band ratio (Hirsch et al., 2001) uses a water vapor absorption feature at 940 nm, shown in figure 5.22, to estimate the total integrated water vapor in the imaging column. The technique is very straightforward and is described by equation 5.1. More complex methods exist to estimate water vapor from a band ratio, but this study only intended to show a simple case for discussion purposes. Using the notional band model described in section 4.12.2, the spectrum was convolved using perfect spectral registration and perturbations up to ± 1 nm. This limit was selected to envelope real-world cases of noted misregistration as discussed earlier.

For the default atmosphere used in this investigation, a wide range of water vapor values ranging from 1.4 to 2.6 cm were substituted for the default water vapor value, and the resulting at-sensor radiance spectra were convolved with the band model. The continuum-interpolated band ratio was then computed for the perfectly-registered, convolved spectrum for each water vapor input. Then, a simulation was conducted where the band model was biased by some amount and used to reconvolve the total radiance spectrum. For each degree of spectral shift, the shifted, convolved spectrum was then used to produce a band ratio, which differed from the unshifted ratio to some degree. The relationship between the unshifted spectrum band ratio and the corresponding water vapor input was used as a lookup curve against which each shifted spectrum band ratio was compared. In this manner, each shifted spectrum, which corresponded to a true water vapor input, produced a different water vapor retrieval according to the unshifted lookup

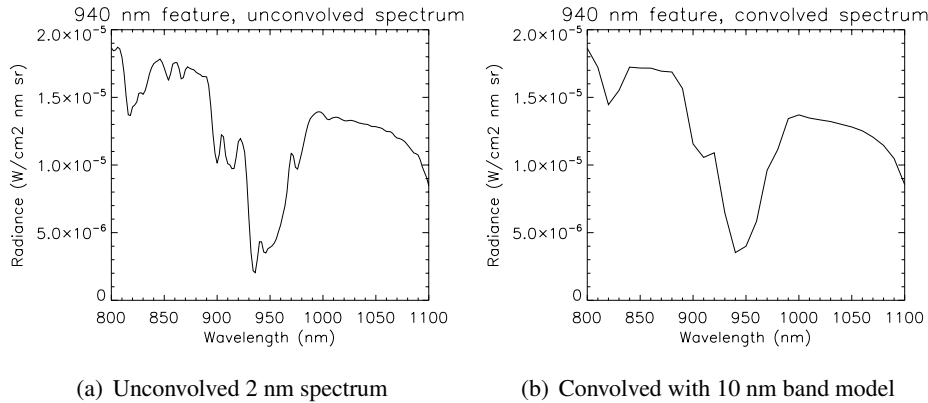


Figure 5.22: 940 nm absorption feature

table. The difference between true water vapor and retrieved water vapor is shown in figure 5.23. The change in slope at the wet end of the curves is an artifact in the MODTRAN modeling process corresponding to saturation at the lower altitudes. The ± 1 nm shift produced small errors in retrieved water vapor, on the order of hundredths of a millimeter. Except for the most extreme cases, measurement error of these quantities is an order of magnitude higher, and these errors would not dominate the error propagation process. Green's original observation regarding spectral registration is verified: keeping spectral bias to below 1 nm is necessary to control errors attributable to it. Spectral misregistration bias in excess of ± 1 nm produces correspondingly greater errors in retrieved water vapor.

5.6.13 Scenario 21: Spectral jitter uncertainty

Spectral jitter was the final effect examined as a standalone scenario. Figure E.13 shows random radiance uncertainty propagated forward into reflectance space. Unlike the spectral bias case, the effect on band ratio-type applications is not as serious because the expected value of the radiance (and reflectance) more or less matches the actual value, though inversion algorithms may require modification to account for this. For non-absorption band spectral regions, the added uncertainty is less than 1 reflectance unit. For the lower-wavelength absorption regions, retrieved reflectance uncertainty grows from 4–6 reflectance units at the edges and exceeds 10 reflectance units at the extrema. Because the fundamental mechanism for simulating jitter is the same as for band center bias, the same sensitivities apply as with

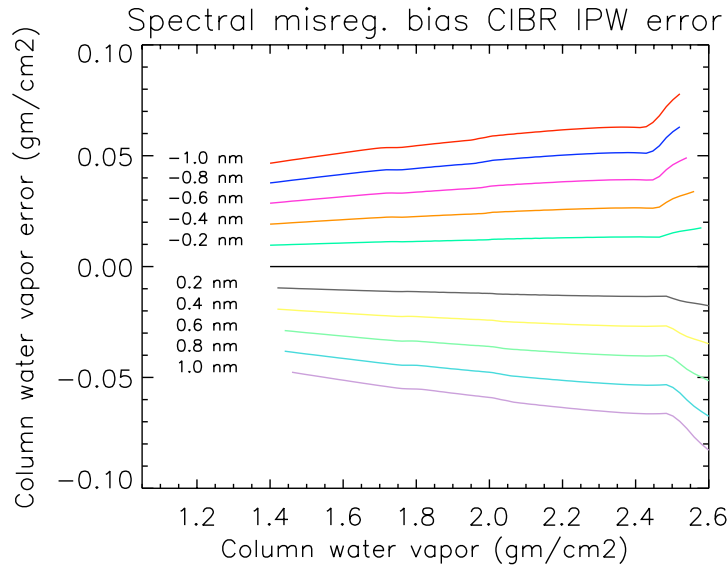


Figure 5.23: Bias in retrieved CIBR water vapor resulting from spectral misregistration bias. The degree of spectral misregistration is noted next to each curve.

the previous scenario, namely that target spectra with high overall brightness or sharp changes in reflectance produce higher uncertainty. Additionally, increasing the magnitude of the jitter increases the overall reflectance uncertainty.

5.6.14 Final Scenario: Mean squared error for combined effects

In each of the previous scenarios, single effects were studied, and there was no need to create a term that combined both random uncertainty and bias error. For most of the scenarios, one of these sources was zero anyway. For this case, both bias error and random uncertainty are contributors to the result. The parameters used for this scenario were listed in table 5.10. To summarize, atmospheric uncertainty for field quality ground instruments was used, an AVIRIS-quality instrument was used to define sensor noise, nominal pointing uncertainty and ground tilt knowledge were assumed, and modest cloud and background obscuration were used. Clouds were set to 15% with knowledge uncertainty to within $\pm 5\%$, while background terrain masking was set to 5%. These contributors are nearly omnipresent, so it is key to ensure their contributions are captured.

Mean squared error was introduced earlier as the commonly used standard that combines the squared bias with variance (equation 4.7). Bias error and random error each have distinct meanings in the context of measurement uncertainty, so combining the random components with the bias components creates more of an uncertainty metric rather than a statistically meaningful quantity. Both components will first be shown separately for the given scenario and finally together as mean squared error.

Both clouds and background reflectance bias spectra are affected not only by the total sky fraction but also by the spatial component of the sky and non-sky elements. As was explained earlier, there is an entire family of sky geometries that are all valid solutions to a given sky fraction specification. In the error propagation model, all curves in the family generated by the cloud and background modeling modules are carried forward to the final results. To simplify presentation of these results, the family of curves is described statistically by 5 summary curves: the minimum, maximum, mean, and the mean \pm 1 standard deviation. Figures 5.24 and 5.25 show the curve families generated for this final scenario for reflectance bias caused by clouds and background objects. Cloud and background effect were earlier shown to be dependent on target reflectance, so results for 100%, 20% and 5% reflectance targets are shown. The 5% reflectance target was added to fully expose a trend related to final mean squared error and cloud variability, which will be seen shortly.

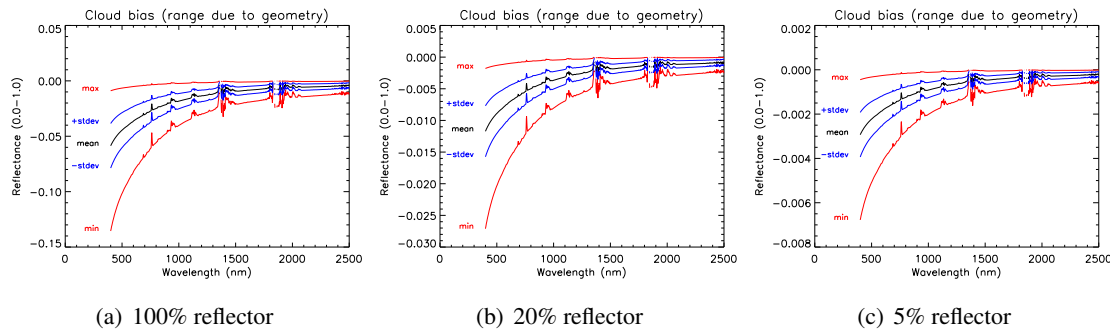


Figure 5.24: Final scenario reflectance bias, 15% \pm 5% cloud cover

The cloud and background reflectance bias spectra were added to the other sources of bias error to produce the total bias error. These results are presented for 100%, 20%, and 5% ground reflectance targets as figure 5.26. The most significant effect that can be seen at this point is that the range of bias error caused by cloud

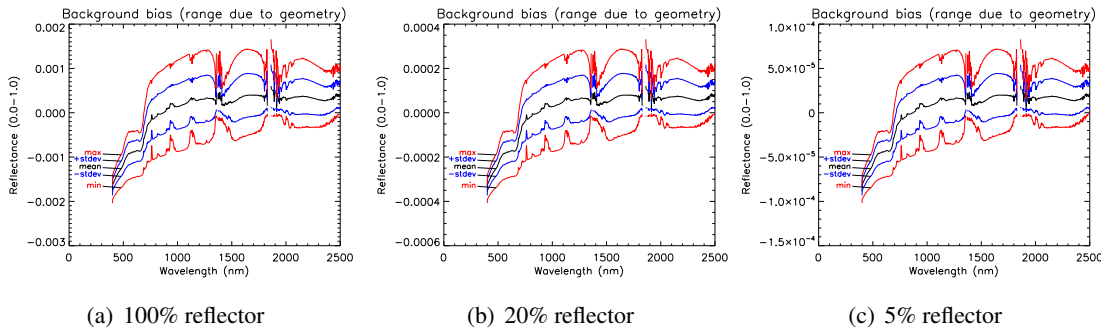


Figure 5.25: Final scenario reflectance bias, 5% terrain masking

and background object geometry ranges 10 reflectance units, from roughly -5 to +5 in the scenario shown here. However, this is only true for the 100% reflector. For the 5% reflector, there is virtually no variability caused by sky fraction geometry, on the order of tenths of a reflectance unit.

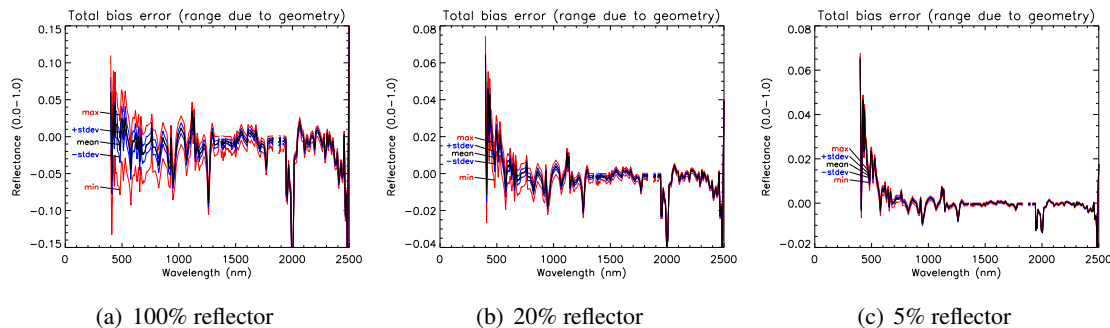


Figure 5.26: Total reflectance bias error for final scenario

These bias results were combined with the random component to produce the curves in figure 5.27. In this case, the average bias error was used to compute the mean squared error. The purpose of this result is to show the random error for the final scenario and how it notionally combines with the bias component to produce mean squared error. The random error is shown in red, and the square root of the mean squared error is the black curve. The components combine in quadrature, so it is easy to see how one component can dominate the other when its magnitude is significantly larger. For the conditions used in this scenario, it is coincidental

that the cloud bias tends to be negative on the same order of magnitude that the sensor and other bias sources tend to be positive. Because of this, the bias error is close to a minimum when compared with the random component. Strengthening or weakening the cloud contribution would greatly affect the bias contribution to the mean squared error, as will be seen presently.

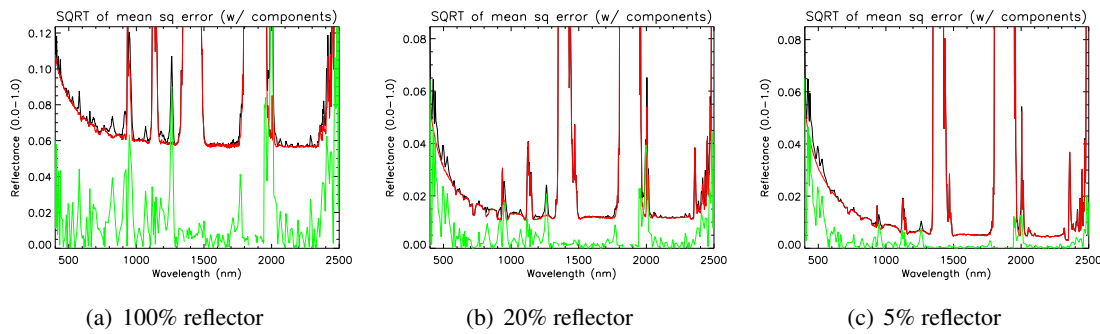


Figure 5.27: Final scenario mean squared error. Square root of the MSE is in black. The random component is in red, and the bias component is in green.

The final set of results for the final scenario is presented as figure 5.28. The square root of the mean squared error for a 100%, 20% and 5% reflector are shown in a way that relates the variability caused by the geometric variation in cloud and background object configuration. In the figure, the black curve is labeled “mean,” the red curve labeled “min,” and the green curve labeled “max.” The designations “min” and “max” refer to the original magnitude of the cloud or background reflectance bias spectrum. In this case, “min” refers to the most negative curve, and “max” refers to the most positive curve. As was seen in figure 5.24, the curve of greatest value (“max”) was actually closest to zero, while the most negative curve (“min”) actually had the greatest absolute value. In calculating the mean squared error, all terms are squared, and the curve labeled “min” becomes quite large in value.

It may seem surprising that the mean value curve produces the lowest mean squared error. This is due to the cancelation mentioned earlier between the negative clouds and the positive biases from the sensor and other sources. When the cloud contribution goes closer to zero (“max”), the overall bias grows positive, and when the cloud contribution goes highly negative (“min”), the overall bias grows more negative (but higher in magnitude). The cancelation effect is best seen in figure 5.26(a) where the average curve hovers around zero, but the “min” and “max”

have higher absolute value.

In figure 5.27, a striking contrast is revealed. For the bright target shown in figure 5.28(a), the variability in mean squared error due to cloud and background object geometry can be as high as 2 reflectance units – but ultimately not as large a factor as earlier results like figure 5.26 might have suggested. For the dark target in figure 5.28(c), geometry variability is no longer expressed in the final mean squared error. It is notable that the bias error is still present, but it no longer varies. It is masked by the sensor bias, which makes a lot of sense – clouds bias down-welled radiance, whose error contribution depends on target reflectance, whereas the sensor’s contribution does not.

Some overall conclusions can be drawn from these results. First, it can be said that the random error sources are most important. Bias did exert some influence in figure 5.28(a), but even in that regime the magnitude and shape of the mean squared error was driven by the random component (and even more so in other regimes). The mean squared error varied greatly as a function of target reflectance as it does for the random component alone. The square root of the mean squared error overall magnitude went as high as 10 reflectance units, but for the most part it hovered around a few reflectance units.

These results confirm behavior seen in other work, where differences between predicted and truth data are consistently to within this bound. It also illustrates how the errors introduced by atmospheric uncertainty can eclipse the benefits of having an instrument with superb noise characteristics, as was mentioned at the start of the last chapter.

Final scenario variant

The last set of observations to be made for this case requires a modification of the scenario parameters. Whereas the final scenario used “field quality” instruments corresponding to those used in basic scenario 2, it is demonstrative to reduce the atmospheric random uncertainty by switching to the “ARM quality” instruments corresponding to those used in basic scenario 3 (per table 5.8). In the baseline final scenario, it was seen that random uncertainty dominated the bias contributions. In the modified version, the random uncertainty from atmospheric measurements will be greatly reduced, showing what the transition from a cheaper, low-precision network to a more expensive, high-precision network might look like.

Because only random components have changed in this modified scenario, the bias errors are identical to the baseline final scenario. The new mean-squared error plots in figure 5.29 show new interactions when the errors are combined. With the lower atmospheric contribution, the other error sources are more easily seen in the

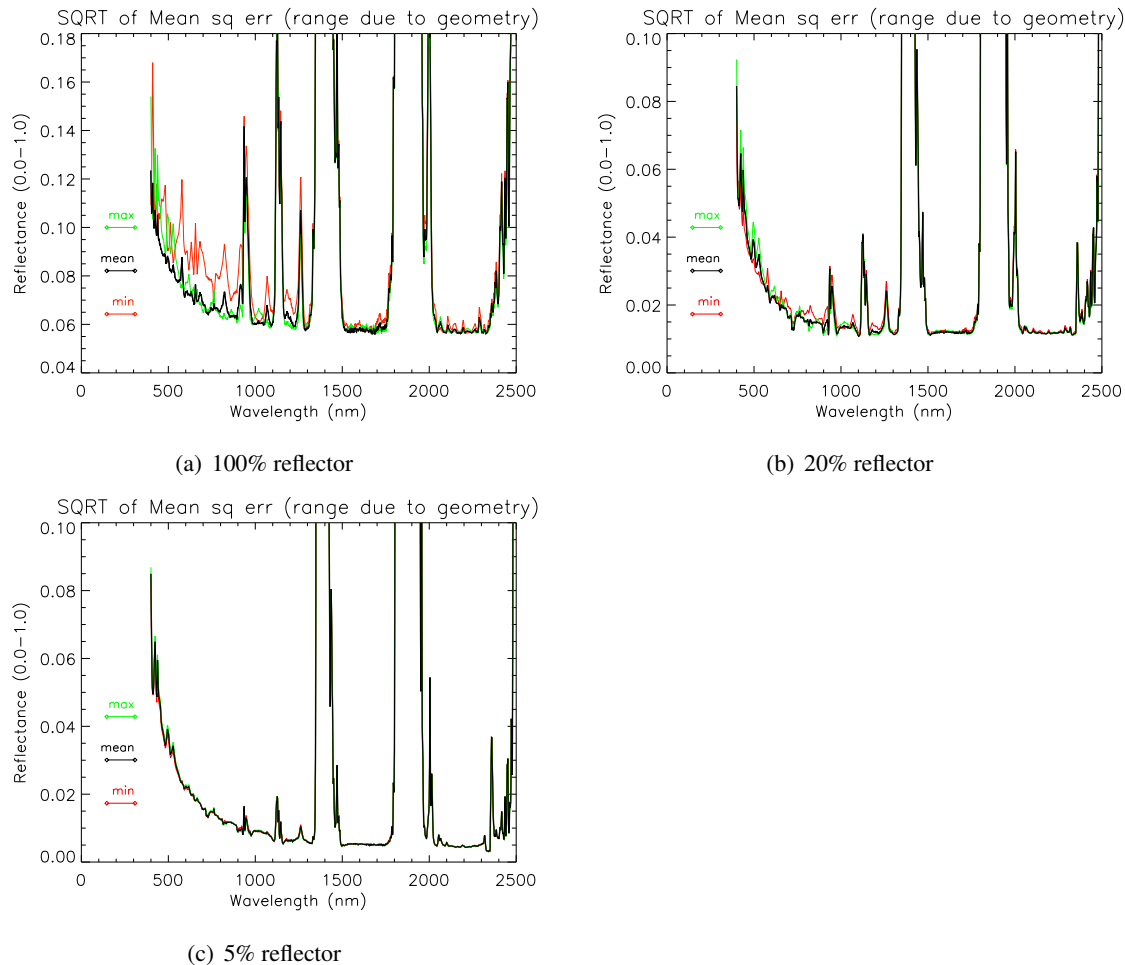


Figure 5.28: Square root of mean squared error for the final scenario (with geometric variability for clouds and background objects)

combined mean squared error. For the 100% reflector, the random component still dominates, but isolated spikes attributable to the sensor bias affect the combined result. The random component has a different shape, however, as the characteristic upswing in uncertainty in the blue spectrum is gone. This indicates a shift in dominance from atmospheric sources to environmental sources of uncertainty, namely the 5° random uncertainty in ground tilt. As the target reflectance decreases, the ground tilt random uncertainty also decreases, allowing bias error to again become the prime contributor, mainly in the blue spectral region.

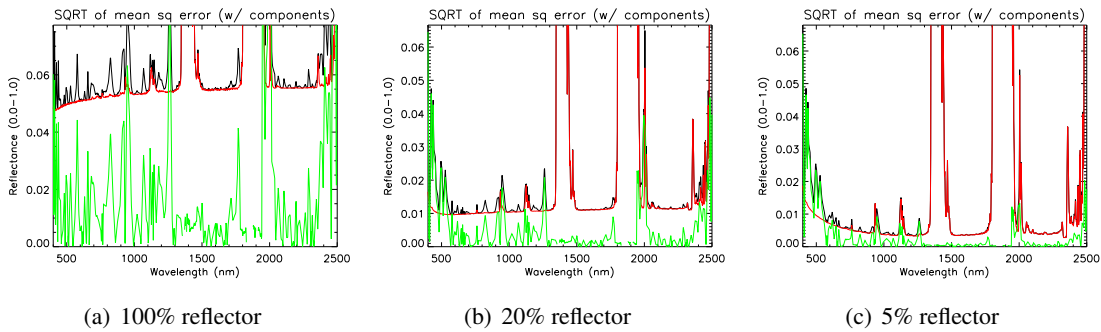


Figure 5.29: Final scenario variant mean squared error. Highly precise atmospheric instruments are modeled, as opposed to the lower-precision instruments modeled in the baseline final scenario. Square root of the MSE is in black. The random component is in red, and the bias component is in green.

Although the simulated ground sensor suite was upgraded to a better set of instruments for this modified scenario, the shift in dominance to other error contributors suggests a “noise floor” that proves difficult to break through. Bright ground targets in the blue spectral region are the exception, where the reduction in random uncertainty from the atmosphere does improve the system performance.

Figure 5.30 shows how the modified final scenario’s mean squared error behaves in response to geometric variability in cloud and background objects. The increased contribution from bias error sources over random sources can be seen in the increased range of final results due to the geometric variability. In figure 5.30(a), the cloud geometry causes the error estimate to change by 3-4 reflectance units in the visible spectral region, in comparison with the 2 reflectance units for the baseline scenario. Again, just like the baseline scenario, darker targets appear to have negligible sensitivity to the sky fraction geometry, though the effect is more pronounced than before.

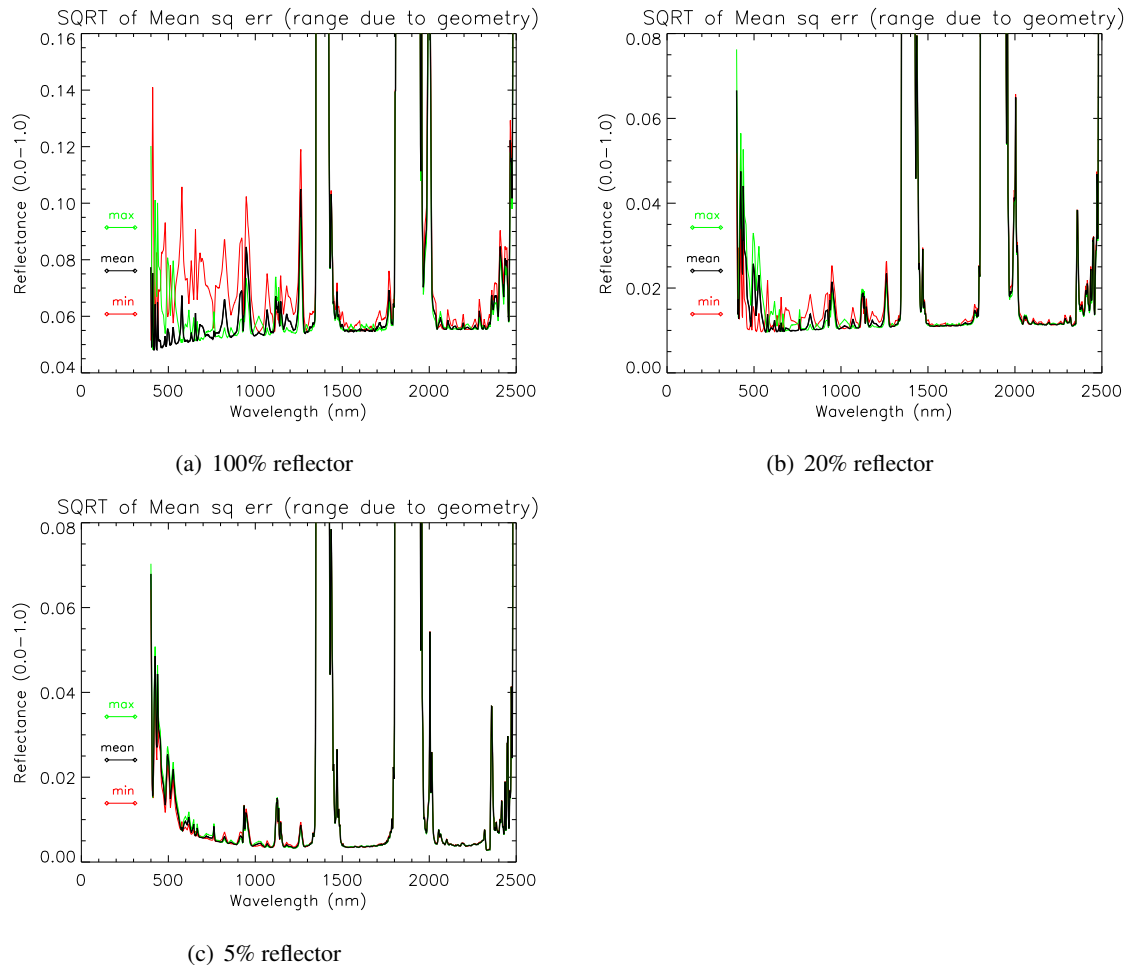


Figure 5.30: Square root of mean squared error for the final scenario (with geometric variability for clouds and background objects)

5.7 Validation

Validation results are presented in appendix F, starting on page 243. The list of validation cases is repeated in table 5.11. For each of the validation cases, a simulation run was conducted using the error propagation model, and one set of runs conducted according to the methodology described in section 4.15. For the Monte-Carlo style runs, each of the reported atmospheric constituents was validated against the intended input distribution.

Table 5.11: Validation scenario summary

	Validation parameter	Mean	Std dev
V1	water vapor - dry	0.75 cm	0.2 cm
V2	water vapor - dry	0.75 cm	0.1 cm
V3	water vapor - wet	2.0 cm	0.2 cm
V4	water vapor - wet	2.0 cm	0.1 cm
V5	density altitude	0.218 km	0.02 km
V6	density altitude	0.218 km	0.01 km
V7	aerosol optical depth	0.447 (15 km)	0.04 (1.55 km)
V8	aerosol optical depth	0.447 (15 km)	0.02 (0.75 km)
V9	multiple parameters		
	water vapor	2.0 cm	0.2 cm
	density altitude	0.218 km	0.045 km
	aerosol optical depth	0.456	0.02

Each validation result is the product of 600 MODTRAN runs using the discrete ordinate transfer (DISORT) algorithm. Each random distribution of atmospheric characteristics was verified against the corresponding desired distribution prescribed by the scenario list. Preliminary research using the less accurate Isaac 2-stream multiple scattering algorithm resulted in a significant underestimation of the variability on the order of 0.5–1.5 reflectance units. This was due to the underestimation of scattered radiance in the shorter visible wavelengths.

In some cases, the sample size of 600 proved to be too small. The target variability listed in table 4.5 was not achieved exactly, and in most cases the difference was large enough to affect the results. In those cases, the conditions simulated in the validation process differed from the uncertainties used to generate the error propagation model predictions. When this was found to be the case, the error prop-

agation model inputs were adjusted to match the conditions actually simulated, with the actual values used annotated in the appendix. The improvement in model performance was frequently significant.

The validation results agree well with the model predictions. Although there is not perfect correspondence, the values are well within the same order of magnitude, and the curve shapes are virtually identical. No component contribution data was compiled from the validation runs, so no basis for comparison exists for the contribution of the individual modeling outputs.

Each validation scenario includes a plot showing absolute difference in absolute reflectance units and one showing percent difference in relative units. The absolute differences are generally very satisfying, on the order of less than half of a reflectance unit. The percent differences tell a different story. Because the validation scenarios produce such small reflectance uncertainty to begin with, uncertainty on the order of tenths or hundredths of a reflectance unit can correspond to 5–10% of the comparison magnitude. The best correspondence exists within the visible spectrum, where the model predictions generally fall to within $\pm 5\%$ of the validation result. In the non-absorption regions past 1 micron, there are places where the predictions match to within $\pm 10\%$, but generally the small values involved result in wide disagreement.

The fact that the difference plot sometimes takes on the shape of one of the component curves may indicate a systematic source of error, the determination of the exact source of which would require further study. The effect is worst in validation scenario 3 (water vapor at 2.0 cm with an uncertainty of 0.2 cm) and scenario 6 (density altitude at 0.218 km with an uncertainty of 0.01 km), both at 20% target reflectance. However, most of the water vapor and density altitude scenarios showed at least a slight bias or spectrally-correlated shape at both 100% and 20% reflectance. In general, the model performed worse in comparison to the validation runs for the 20% reflector across the board. For the aerosol optical depth scenarios, there was no spectrally-correlated bias, but the spread in the results was much greater for the 20% reflector than for the 100%.

All of the validation scenarios tested a single parameter except for the last, which set each parameter to the uncertainty values used in scenario 2. The simulation parameters were corrected to match the actual statistical distributions generated in the validation process. The final validation scenario had the best correspondence between the model and simulation results. In the visible spectrum, the discrepancy was below $\pm 3\%$, which is considered extraordinary. Furthermore, the percent difference was below $\pm 10\%$ up until the first major absorption region at 1390 nm and above the second major absorption region at 1900 nm.

Vagaries of the error modeling process could explain the discrepancies between validation and prediction results. The most likely candidate is machine precision in MODTRAN's outputs. Because these results are so small, they would be sensitive to a loss of significant bits. It has been shown that the precision of slope determination is affected by the limited number of significant figures provided by MODTRAN output (and possibly carried along in the computation itself). An adjustment of parameters within the significant precision limits of the model would definitely cause discrepancies, though the exact contribution of these errors is probably not possible to determine without examining the inner workings of the radiative transfer code.

In addition, the τ_1 term is a term not directly accessible in the MODTRAN output, rather, it must be derived from several other outputs. It routinely shows the effects of precision truncation. This is most clearly visible in figure D.3(a), where the red τ_1 curve shows a jagged appearance where the other curves are smooth. Any curve to which the red curve is a significant contributor also picks up this high frequency "noise," as the correlation term and total error curves do in that plot. This jaggedness is visible in the correlation term curves for many of the validation scenarios and qualitative appears to be responsible for the many outliers in the percent difference plots.

The other possible source of error is from the assumptions inherent in the modeling approach. First is the truncation of the Taylor series that serves as the foundational process of the error propagation model. The correlation terms are plainly seen to make significant contributions to the final result. The loss of higher order terms usually means a change in precision 2 or 3 orders of magnitude below the level of real impact, but again, the differences involved here operate within that error regime. Similarly, the assumption of linearity may or may not have an impact, depending on the non-linearity of the parameter. Despite the differences observed, the overall level of agreement between model predictions and the Monte Carlo-style simulation results leads to the conclusion that constituent error is validly and correctly propagated into reflectance space.

5.8 Error sensitivity study

The results in appendices D and E show traceability to the modeling outputs and environmental effects, but not to the atmospheric constituents. A study was performed in which each the uncertainty for each atmospheric constituent was set to zero, and the reduction in total uncertainty was recorded.

The concept is that the relative magnitudes of uncertainty reduction, peak nor-

malized to the starting uncertainty, shows the relative strength of each constituent in driving total uncertainty in retrieved reflectance. It should be possible to conclude that one constituent or another is the most important to measure for a given set of conditions.

In addition to measuring the three primary constituents under study, a fourth scenario was added, namely the simultaneous direct measurement of downwelled radiance and sun-to-ground transmissivity. This attempts to simulate the addition of a ground photometer that only measures these quantities. It is possible to have constructed another scenario case around this configuration, but this format was just as convenient and allows direct comparison between constituent measurement or model output measurement.

Appendix G (starting on page 263) shows results of the study, with one set of results for each of the 5 basic scenarios listed in table 5.8. For each of the 5 basic scenarios, results are presented for three target reflectances, with a 5% reflector added to the usual 100% and 20% reflectors. This is because an effect was discovered where the interaction between correlation terms causes error to reach a minimum not at 0% target reflectance, but closer to 20%. It was necessary to show a truly dark target, in the form of the 5% reflector, to show how the error behavior shifts first in one direction and then in the other.

In addition to the direct study results, summary plots are included for each scenario that show the total uncertainty as a function of target reflectance and constituent. This was necessary because while the water vapor error contribution produces a simple monotonic decrease in error as a function of target reflectance, the aerosol error contribution shows a minimum around 20% target reflectance. Finally, this same information is re-presented in much greater detail (in the form of complete results for each target reflectance and error constituent) to elucidate this more complex interaction.

5.8.1 Scenario 1

The first set of results are for scenario 1, which is the climatology-based model-only inversion. Although the magnitudes of the errors are extreme compared to the more likely scenarios, the general behavior is the same and worth discussing, since the conclusions will be broadly applicable. Figure G.2 shows the individual contributions of each constituent. The red curve corresponds to the error contribution of density altitude uncertainty. The sensitivity of the final result to each constituent depends on the relative magnitudes of the input uncertainties, and for this scenario the air column density uncertainty is much smaller than the other uncertainties. This will change in later scenarios, where the uncertainties balance out better. Ad-

ditionally, the low contribution of density altitude allows the scenario 1 analysis to focus on opposing contributions from water vapor vs aerosol.

The blue and green curves correspond to the error contribution of water vapor and aerosol respectively. To be more specific, the blue curve is the percent reduction in reflectance error when the uncertainty contribution from the water vapor is set to zero. With perfect knowledge of the water vapor, the aerosol optical depth uncertainty greatly dominates the uncertainty in the retrieved reflectance. When water vapor uncertainty is set to zero, there is a small reduction in final reflectance uncertainty for the 100% and 5% reflectors but a large reduction for the 20% reflector. By contrast, when aerosol uncertainty is set to zero, there is a great reduction in overall error for the 100% reflector but a small reduction for the 20% reflector, at least in the visible spectral region. For the dark 5% reflector, the aerosol contribution again becomes dominant, but not by much. It is also thought that the starting water vapor uncertainty is larger than the aerosol uncertainty such that removing water vapor error produces greater improvement in the total uncertainty result. However, no metric has been proposed to prove this. Because of the exponential relationship between optical depth and visibility, direct differences in signal-to-noise may not be valid.

5.8.2 Explanation of counterintuitive results

The trend seems counterintuitive: for a bright target, effects linked to τ_1 and τ_2 should dominate. These terms are driven by water vapor, not aerosols. Alternately, for dark targets, the scattered radiance terms L_d and L_u should dominate. These terms are driven by aerosols, not water vapor. A closer look at the underlying results resolves the seeming reversal of intuition.

Figure G.3 shows the total reflectance uncertainties for multiple reflectances when each type of error is zeroed out. In figure G.3(a), the aerosol uncertainty is zero, meaning the results are driven by water vapor. Despite the intuitive link between aerosols and scattering, water vapor does cause a significant amount of path radiance. The monotonic decrease in total reflectance uncertainty with decreasing reflectance in the presence of water vapor uncertainty is driven by path radiance. To prove this, detailed results for each individual run were included in figure G.4. The cyan line in figure G.4(a) represents the upwelled radiance contribution to total uncertainty. Although aerosol uncertainty is zero in this figure, the upwelled radiance contribution is significant. It stays constant all the way through figure G.4(f), where it is the *only* contributing factor. Stated explicitly, in figure G.4(f), the total reflectance error contribution is from upwelled radiance, and upwelled radiance is driven by water vapor. This runs counter to the intuitive thinking that aerosols drive

path radiance and water vapor does not.

However, this is not to say that aerosol uncertainty does not have a significant path radiance contribution. Indeed, moving on to figure G.5(f), a high upwelled radiance contribution is the only driver of reflectance uncertainty. Figure G.5 shows the results for zero water vapor uncertainty contribution, so aerosols are the driver here. The upwelled radiance contribution is actually higher for aerosol error than water vapor, as it should be.

The resolution of the discrepancy is now assisted by reviewing the other plots in figures G.5 and G.4. First, the red and green transmissivity curves in figure G.4 are extremely low when compared to the scattered radiance terms. This is not expected behavior for water vapor-induced uncertainty. The behavior starts back all the way in figures 5.5 and 5.6, which show the slope of τ_1 and τ_2 with respect to each atmospheric constituent. The slope for water vapor is very low in most of the spectral region, whereas the slope for aerosol optical depth is very large. These slopes are combined with the constituent uncertainties to produce an error in a modeling output. For scenario 1, the aerosol optical depth uncertainty is 40% of the water vapor uncertainty, but the sensitivity of the transmission terms to water vapor is much less than 40% than that of aerosols. Later in the propagation chain, slopes are calculated to determine the relationship between each modeling output and the uncertainty in the final reflectance retrieval. These sensitivities are shown in figure 5.31. In this figure, the red and green curves correspond to τ_1 and τ_2 , while the blue and cyan curves correspond to L_d and L_u . Note the logarithmic scale on the y-axis. Just based on the equations derived in appendix A, there are at least 4 orders of magnitude between the transmission terms and the scattered radiance terms. By itself, this is not meaningful because the error in the radiance terms are several orders of magnitude below the error in the transmission terms. But, when traced forward to this point, the slope differences noted earlier are magnified. This produces the unintuitive but true result that aerosols do have a significant effect on transmission even when water vapor does not. The intuitive behavior is upheld, but the relative magnitudes of the numbers involved cause the term dominance to vary by situation.

The red and green transmissivity curves in figure G.5 show what happens when the aerosol uncertainty is the dominant term. As explained earlier, a sufficiently high aerosol uncertainty can drive transmissivity independently of water vapor and to degrees in excess of the water vapor's influence. This is shown in figures G.5(a) through G.5(e), where decreasing reflectance causes a decreasing contribution from the transmission terms. The upwelled radiance contribution is constant, however, until figure G.5(f), where it is the only contributor. Indeed, the transition in influ-

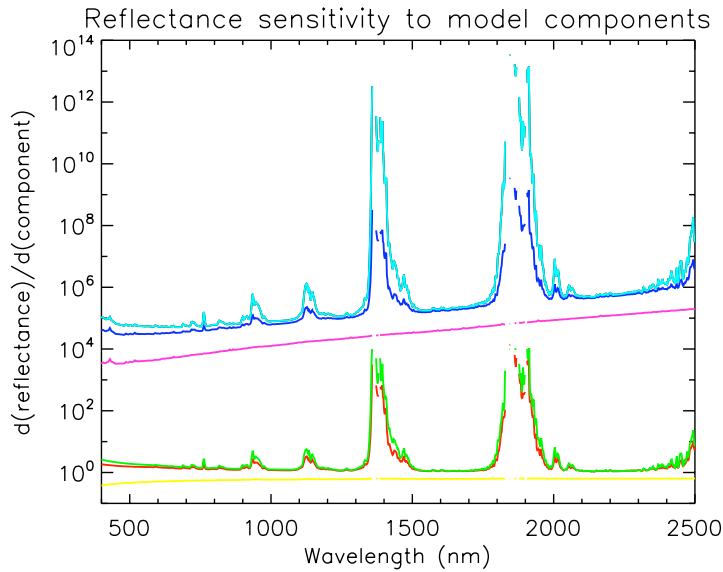


Figure 5.31: Reflectance uncertainty sensitivity to component terms. The curves are colored according to the legend in figure D.1.

ence from transmission to path radiance is seen in figure G.3(b), where the jagged curves (driven by jaggedness in the τ_1 contribution) give way to the smooth exponential slope for 20% and 0% reflectors (driven by the upwelled radiance contribution).

The correlation terms are the other major factor at play. The violet line represents the sum of all correlation terms. There is a strong negative correlation for all of the aerosol-only plots in figure G.5 that pulls the final uncertainty below some of the component uncertainties. The decrease in correlation with lower reflection actually allows the reflectance uncertainty to increase for the aerosol-only plots in figure G.5. In figure G.4, the correlation is positive and stays positive, so there is no trend reversal in reflectance uncertainty.

The combined effect of these various factors causes aerosols to remain the dominant error contributor for the 100% reflector. The black curve of figure G.5(a) shows a max error contribution in the low wavelengths of approximately 0.6 or 60 reflectance units. Figure D.3 shows the full error total in this spectral region of approximately 70 reflectance units. By contrast, the reflectance result in figure G.4(a) shows a max error contribution of only approximately 43 reflectance units.

When the reflectance drops to 20%, the highly negative correlations present in the zero-water vapor error case show a greatly reduced contribution from the aerosol uncertainty. The maximum contribution is seen in figure G.5(e) to be only approximately 12.5 reflectance units. In contrast, the error contribution from water vapor uncertainty is seen in figure G.4(e) to have decreased by much less down to approximately 27 reflectance units. The higher error contributor in each regime becomes the larger percent reduction in figure G.2.

Another effect caused by the correlation factors is that the percent reductions will not add to 100%. When one term or another dominates, the correlation factors serve to either boost or depress the total reflectance uncertainty, depending on the specific atmospheric contributions. This is an inherently non-linear process. For example, throughout this discussion, density altitude has been barely mentioned. In figure G.2, it barely registers a change because it is dwarfed by the other contributors. One might expect the density altitude-only situation to produce a very small reflectance uncertainty. However, when density altitude is the only error contributor, the maximum overall reflectance uncertainty in the visible regime is approximately 10 reflectance units (compared to approximately 70 for all constituent contributions). The interaction between atmospheric constituents via correlation terms makes a linear combination model impossible to construct.

5.8.3 Scenarios 2 and 3

Results for scenarios 2 and 3 are shown in figures G.6 and G.10. The supporting plots of underlying contributors are included for completeness, but they show the same general trends discussed earlier. In fact, the same conclusions can be made for these scenarios. For bright targets and this geometric configuration, aerosols contribute the most uncertainty (except for the water vapor absorption bands), while water vapor contributes the most uncertainty for the 20% reflector.

An interesting effect occurs between scenarios 2 and 3 for the truly dark target at 5% reflectance. In scenario 2, water vapor is the heaviest error source in the 5% case, but in scenario 3, the aerosol contribution is completely dominant, as would be expected. The explanation for this again focuses on the initial uncertainties. Scenario 2 uses low-quality instrument sources. However, because the trade space for aerosol profile sensors does really not have a “low-end,” scenario 2 actually has much higher quality (and higher cost) aerosol sources than it should. Scenario 2 baseline aerosol’s uncertainty is lower than the water vapor uncertainty, which is quite high, relatively speaking. Because of this, reducing the aerosol uncertainty in scenario 2 does not produce a drastic effect because the constituents were not on equal footing to begin with.

In scenario 3, the instruments are all high-quality, and the starting uncertainty contributions are more balanced to begin with. Reducing the aerosol uncertainty has the expected effect of greatly reducing the overall uncertainty for the 5% reflector. Even in the 20% case water vapor uncertainty has a reduced influence compared to scenario 2.

Because the overall precision of the instruments used to measure water vapor and aerosols is greatly improved for scenario 3, density altitude becomes a non-trivial contributor for the 20% target. However, it does not dominate water vapor uncertainty in this regime. For darker targets, density altitude again fails to significantly influence the results.

5.8.4 Scenario 4

The error reduction studies for the model-based inversion algorithm scenarios produce results that are in accordance with behavioral observations made elsewhere. In scenario 4, the 100% reflector shows in figure G.14(a) that aerosols are the greatest contributor for the majority of the spectral region. For a bright target, it is expected that water vapor effects dominate, and they do in the short wavelength visible region. In the NIR and SWIR, water vapor rapidly falls in influence, allowing aerosols to take over in that region.

For the 20% reflector (figure G.14(b)), the same seemingly strange water vapor dominance is again present. The key to understanding this behavior lies in figure G.15. For the water vapor-only error plots, there is a tight distribution ranging from 6–12 reflectance units, so at the low reflectances there is still a high degree of water vapor-induced error. In contrast, the error attributable to aerosols is much more volatile in response to changes in reflectance. As was stated earlier, this is due to the cross-correlation interactions between the modeling outputs. This error decreases with decreasing target reflectance, reaches a minimum around 20% target reflectance, then increases again with even darker targets. It is safe to conclude that for this geometric configuration, the heuristic of associating dark targets with aerosol scattering is probably only valid for truly dark targets, defined as those under 10% reflectance. Value is gained in measuring water vapor very accurately first, then aerosols.

5.8.5 Scenario 5

Scenario 5 produced some unusually shaped results. Figure G.18 shows that for both the 100% and 20% reflectors, aerosols are worth measuring for visible target

applications. Due to the unbalancing in relative magnitudes in the error inputs chosen for each scenario, scenario 5 sees a shift in favor of highly accurate water vapor over less accurate aerosols. Recall that for scenario 4, the water vapor uncertainty was higher than aerosols in relation to the assumed constituent abundances. Therefore, as can be seen in figure G.19, the aerosol-only errors start at 8 reflectance units for the brightest targets. In contrast, water vapor again has a very tight range that stays between 1 and 2 reflectance units, depending on target brightness. Therefore, aerosol is clearly the main contributor, and reducing it produces the greatest improvement in retrieved reflectance uncertainty.

For the 20% reflector, aerosols show that drastic decline as target brightness decreases, eventually reaching parity with the always-low water vapor contribution. At this lower brightness, aerosols only dominate at the lowest wavelengths. In figure G.19(b) the highly sloped curve below 500 nm allows that brief span of aerosol dominance, but note that the aerosol error contribution dips nearly to zero. This is again due to the interaction of cross-correlation terms. Because the aerosol contribution is so low locally, the water vapor contribution spikes around 750 nm. For the remainder of the spectral region, the aerosol and water vapor contributions appear to be fairly well balanced, with aerosols remaining the dominant contributor (except for the water vapor absorption bands).

For the 5% reflector, scenarios 4 and 5 show the same dual nature as was seen in scenarios 2 and 3. In scenario 4, water vapor was the highest error contributor, but not as high as for other target reflectances. In scenario 5, the aerosol contribution absolutely crushes the others. Because the only difference between these scenarios are the starting constituent uncertainties, the shift in behavior for dark targets is attributed to this change in starting uncertainties.

Again, for balanced inputs, it is expected that aerosols are the dominant contributor for dark targets. For the other regimes, it was shown in the amplification plots that the tight monotonic range of water vapor error contributions exerts influence over a narrow range in retrieved reflectance error, while the aerosol error contribution varies non-monotonically over a wide range. The magnitudes of the respective ranges depend on the initial uncertainties. Both the range location and width determine which effects will be dominant for any given scenario.

5.8.6 Direct measurement of τ_1 and L_d

The final component of this study was to examine the possibility of reducing the uncertainty in the modeling inputs by adding a direct measurement of the output. The two terms that can be measured from the ground are downwelled radiance and sun-ground transmission. Literature on ground radiometers describes a best-case

3% uncertainty for direct radiance and 5% uncertainty for diffuse radiance (Michalsky, 2001). The uncertainty in the measurement is treated as a simple substitution, and its effect on the error is computed. More complex schemes of averaging or filtering (by inverse weighting each input by its estimated uncertainty) the multiple sources was not considered.

As the atmospheric constituent uncertainties improve, the value of adding ground measurements decreases. For scenario 1, the ground measurements cut the uncertainty in half for a bright target. For the dark target, there is significant improvement to be had in the SWIR bands, but none in the visible bands. For scenario 2, a 10–40% improvement in error is possible for the bright target, but very little improvement is possible for the dark target. For scenario 3, the ARM-grade measurements are so precise that the light measurement equipment actually makes the results worse, except for bright targets in the lower wavelength visible spectral region (which may be really important to the application).

For both types of targets in scenario 4, the direct radiance improvement curve shows direct radiance/transmittance measurement is very effective for this scenario, with 5–50% potential reduction in uncertainty, depending on scene brightness.

In scenario 5, direct measurement of the downwelled radiance and sun-ground transmittance is less effective here because the radiometer instrument error is closer to the low-end achievable uncertainty from the in-scene methods. Benefits exist for bright targets, but they disappear for the darker ones.

An effect not studied here is the elimination of bias error. The true value of adding direct measurement instruments to a ground truth network is to compensate for clouds. The state of cloud modeling needs to advance before any results presented on this topic would be meaningful. However, the benefit of trading a bias of up to 10 reflectance units for a 3% uncertainty in modeling output terms should be an easy trade to make.

Not counting the potential benefits of bias adjustment, it was not clear that direct measurement of these factors was always better than reducing atmospheric uncertainty. In reality, instruments that measure these quantities may also have the ability to perform accurate measurement of one or more atmospheric constituents. When considering this capability as a theoretical stand-alone addition to a ground truth network, there are better ways to improve performance.

5.9 Optimal network design

Undertaking the construction of a network of inversion-assisting instruments assumes certain things. First, the area covered by the network is a place of continuing long-term and repeated imagery operations. The cost and effort of establishing a network, populating it with sensors, and setting up back-end processing needs to be lower than simply performing repeated human data collects, implying a lack of access or need to travel, that requires the system be automated. Finally, the remote sensing instrument used greatly influences the framework by prescribing an inversion method and general requirements for data quality.

General considerations

The major obstacle to creating an operational instrument-only inversion method or using instruments to augment in-scene inversion methods is that taking good ground truth is hard (Clark et al., 1995; Smith, 2004). It is labor intensive and difficult to do correctly and consistently. If detailed procedures are not developed to use the ground instruments correctly, the resulting data will have nowhere near the published precision. This is especially true for equipment that primarily measures radiance. Instruments that measure the atmosphere's physical properties are simpler, cheaper, more accurate, and more reliable. However, with the exception of water vapor, it was found that these instruments provide less-than-useful data: density altitude never drives retrieved reflectance uncertainty.

Spatial applicability of any measurement is a problem across the board. Two-dimensional propagation of error is driven by the atmospheric variability across the scene and the effects of clouds. As distance from a point sensor increases, uncertainty should be modeled as increasing as well. A network of instruments can work together to create an “error topology” that has pockets of high and low uncertainty, bound on the low end by the instruments themselves and on the high end by the distance between the sensors and atmospheric volatility, both temporal and spatial. Analysis of 2D effects would be an ideal and logical next step toward extending this work.

Field-quality instruments can augment or match in-scene algorithms at the low end of their performance. Because humid conditions have the ability to seriously confound band ratio techniques, water vapor measurement is always a good option for humid areas, as well as all other areas, depending on scene brightness. They cannot augment in-scene algorithms performing at their best.

Aeronet-quality instruments can augment any inversion method or serve as the foundation for an instrument-only algorithm that rivals any in-scene algorithm.

Their quality is unmatched, as is their cost. Both grades of ground instruments can readily be incorporated into Kalman-type filtering algorithm that incorporates many measurements of differing qualities. While this was not examined in this work, it would be an excellent investigation for future work.

ELM is so popular because, despite its basic nature, is based in first-principle physics and consistently works well. Panels would theoretically provide the best overall performance, limited to a best case reflectance uncertainty of approximately 0.5 reflectance units, driven by the radiometer used to calibrate the panels (Smith, 2004). The 2D spatial applicability of the calibration is affected just like any other method, but it avoids any problems involved in the modeling process. Additionally, network communications are not needed because in-scene spectra provide the required ELM constants. However, it is also the most volatile option – as soon as a layer of dust or mud settles on the panel, the calibration is useless. Because the panels require periodic re-calibration, they do not integrate well into an unattended ground sensor network and are considered only partially network compatible.

An alternative to panel ELM would be ground reflectometer ELM. Both require a ground reflectometer instrument, but the alternative concept would leave the instrument in the field to provide continuous measurement of a selected ground target. This concept trades the temporal problems of the calibration panels with instrument durability, cost, and network complexity problems associated with radiometers.

Evaluation factors

Each sensor is qualitatively evaluated against criteria critical to the success of a network. Data quality refers to the precision and accuracy of the measurements taken. The body of work preceding this section provides a way to cast actual precision into a common quantitative evaluation framework. The qualitative evaluations in the figure stem from that analysis. The next factor is cost. Cost data were taken from actual system costs either through vendor documentation or interaction with those familiar with the hardware. Temporal stability is another key factor that refers to how long a sensor can remain unattended without repeated calibration or adjustment. If a sensor cannot hold a calibration, then it is not useful in a ground network. The 2D spatial factor refers to how well a single point reading applies to the rest of the scene. These were all set to the same color because the relevant drivers are generally not sensor dependent, though in truth there might [literally] be fine shades of distinction between the candidates. Net readiness is a factor that evaluates how well a sensor can be inserted into a network and run in an autonomous fashion. Sensors that require regular human interaction were downgraded in this category.

It was assumed that data acquisition and network communications hardware could be adapted to any sensor; this reflects truth unless some extenuating circumstance comes into play. Finally, sensor durability was evaluated. Any unattended sensor needs to potentially be able to withstand some degree of stressing weather, water, temperature variation, wild animals, and/or human activity. Sometimes sensors can be ruggedized, while others have inherent durability.

Because the show-stopper for building ground networks is not necessarily the instrument's inherent accuracy, other factors become essential in the decision-making process. Instruments must be able to produce quality data, but logistics, automation, and reliability are key. Figure 5.32 shows these considerations for the leading sensor candidates.

The qualitative evaluation of practicality factors for each instrument is supplemented by a quantitative evaluation of each instrument's relative error reduction potential, shown in table 5.12. The table shows a best case improvement over an existing field network or over model-based algorithms alone. The numbers represent the decrease in reflectance error (0-100), averaged over the visible spectral region. The table is also broken down by target reflectance; results are provided for 100% reflector, 20% reflector, and a 5% reflector. Although absolute values are not given, results can be related to the reflectometer, which is pegged to 1 reflectance unit of uncertainty.

Option analysis

The quantitative demonstration in table 5.12, while not comprehensive, does confirm key judgments regarding data quality. The calibration panels and *in situ* reflectometer configurations were held as the control case, with an uncertainty in

Table 5.12: Instrument improvement analysis (averaged over visible bands)

Instrument	Over field instruments			Over in-scene methods		
	100%	20%	5%	100%	20%	5%
Sun photometer	3.3	1.7	1.5	6.3	2.7	2.7
GPS water vapor	0.5	0.5	0.4	1.1	1.5	1.0
Cal panels	4.7	1.1	1.2	7.7	2.1	2.3
Reflectometer	4.7	1.1	1.2	7.7	2.1	2.3
Radiosonde	0.0	0.0	0.0	0.7	1.0	0.7

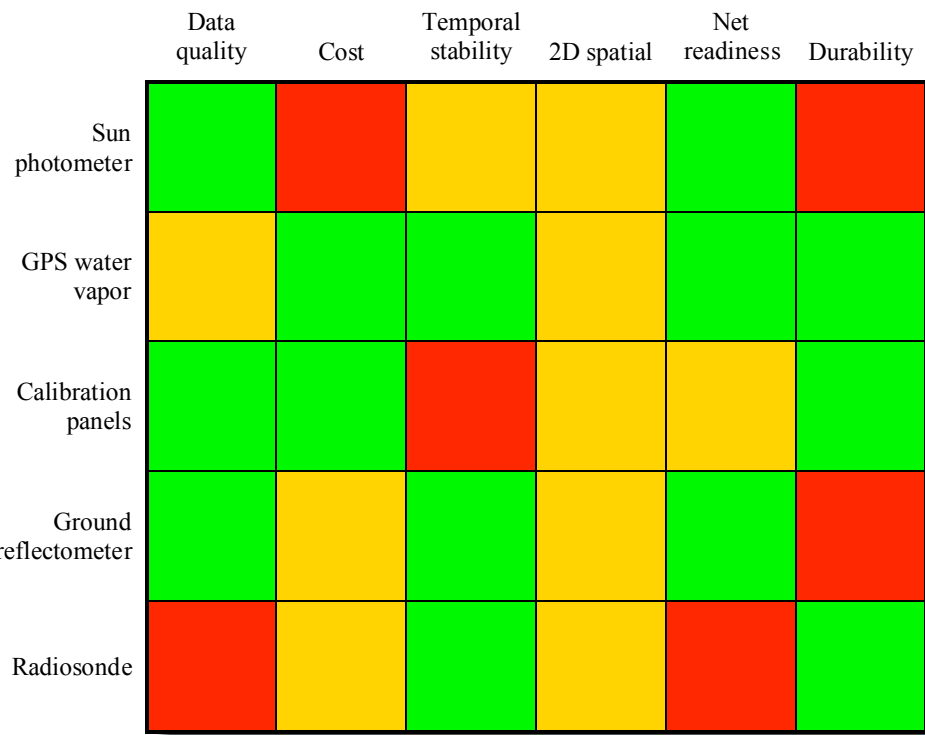


Figure 5.32: Instrument Tradeoff Matrix. Color coding indicates satisfaction of the evaluation parameter. Red indicates a “show-stopper” or disqualifying factor. Yellow indicates suboptimal performance or difficulty, but one that may still provide benefit. Green indicates satisfaction of the evaluation criterion with few caveats.

reflectance measurement of 1 reflectance unit for all spectral bands. All reflectometer results in the table show reductions in reflectance uncertainty down to 1 reflectance unit, which is on the order of expected performance in all but the most favorable conditions. Any table entries greater than those of the reflectometer indicate a reduction in uncertainty below 1 reflectance unit. The sun photometer does this for darker targets. GPS-based instrumentation provides a modest reduction but not greater than either the reflectometer or photometer. The radiosonde, whose data are perpetually suspect to begin with, did not provide much improvement at all.

Sun photometers provide a lot of high quality data, depending on number of bands and construction. As ground-based radiometric instruments, they can be used to provide water vapor, aerosol content, and transmissivity independently of the scene content. They are expensive instruments, from 5-50 times the cost of simpler instruments, therefore the risk of damaging one carries high consequences. The instrument needs to be protected from damage and drastic alignment disturbances. The degree of calibration stability is an instrument dependent risk factor, but it would be acceptable even if on the order of a handful of months. If it were not for the cost, this instrument would be the obvious choice for network use.

GPS water vapor instruments provide an excellent mix of operability attributes at the expense of data quality. Because they measure radio signals, as long as the instrument has line-of-sight access to one or more GPS satellites, they function. The sensors are simple, can be made durable, and are already in continuous reliable, autonomous networked operation. These sensors are also inexpensive to set up and operate (Santos et al., 2007).

Because they are so easily changed by the environment, calibrated reflectance panels simply do not have the ability to serve in an autonomous, high-accuracy ground truth networks. They are suitable to augment instruments that do not have atmospheric sounding bands (low accuracy) or in areas where they can be frequently re-calibrated or cleaned (not autonomous).

A calibration reference with a resident reflectance instrument is a significant improvement over calibration panels alone in that the updated reflectance measurements account for changes in the reference over time. The measurement can be automated and provides good accuracy, on the order of 0.5 to 4 reflectance units depending on target brightness and the instrument itself. Although calibrated in-scene targets provide ELM constants rather than atmospheric constituents, 2D spatial stability of the retrieved values remains the main problem with the ground truth network. Though they can cost significantly less than sun photometers, fielded spectral radiometers share the same durability and alignment issues. A single-

input radiometer configuration requires a time-stable instrument calibration to provide useful results. A dual-input radiometer configuration would provide relative data not dependent on the instrument's absolute calibration stability, but there are tradeoffs. The instrument needs to measure the much greater direct solar irradiance yet still be sensitive to changes in the downwelled radiance. The second input has an independent alignment requirement, making the system even more sensitive to physical disturbance. Therefore, increase in system complexity and dynamic range considerations may prevent a dual input configuration from being the better alternative despite the better reflectance results. Also, it should be noted that calibration targets require at least two measurements per image, which multiplies the hardware requirements for this option.

Although reflectometers and sun radiometers appear to be very similar in both operation and the types of data they produce, there is a significant difference in providing an atmospheric constituent and a pixel reflectance. While the pixel reflectance is the desired end product for the entire scene, extrapolating an ELM result can be tricky. It requires multiple ground truth measurements for a range of target brightnesses, and the measurement precision is potentially brightness-dependent. In contrast, atmospheric constituents are a physical quantity, not a radiometric quantity. They are non-spectral, only require a single measurement to use, and can be determined with a precision independent of scene content. So, while the sun photometer products require radiative transfer modeling to be effective, they would actually be preferable to measuring ground target reflectance at a limited number of points.

Radiosondes are relatively simple instruments that can be stored in a weatherproof enclosure. Their suspect data quality and considerable cost are not the driving factors in rejecting these for more widespread use. Their main problem is the fact that their operation cannot be automated and require a continuous human presence to launch the instruments, defeating the purpose of building an automated ground truth network.

Final Evaluation

If the imaging spectrometer being used to take imagery cannot support an in-scene inversion method, two options exist. The low-cost, low-quality option is to populate the network with GPS water vapor instruments and perform aerosol estimation with climatology methods, primarily global aerosol products (such as MODIS data). The products are *not* suitable for pixel-by-pixel in-scene use, but they are better than nothing. The field-quality water vapor measurements provide good water vapor information. Driven by the high aerosol uncertainty, performance in the

range of 10–15 reflectance units of uncertainty is predicted in the visible region and below 10% in the NIR and SWIR regions. The high cost, high accuracy option is to add a sun photometer, microwave radiometer, or combination instrument to provide performance on the order of 1 reflectance unit or less. Unfortunately, there is not much trade space in between these two points because of the difficulty in measuring aerosols.

If the remote sensing instrument has sufficient spectral resolution to support an in-scene inversion method, it might not be worth it to establish a ground network. If the application requires an improvement from the native 5 reflectance units of uncertainty down to below 1-2, then any single instrument would suffice. After adding a water vapor ground sensor, uncertainty improvements of 2 reflectance units are possible for bright targets; drastic improvements from 8 down to below 4 reflectance units are possible in the visible, and uncertainty below half of a reflectance unit in the other spectral regions. The high cost option of using a radiometer nets better performance, but not drastically so (on the order of scenario 3's uncertainty).

5.10 Summary of results

Results have been presented that show how the modeling theory described in the last chapter was assembled into a error propagation framework capable of integrating modular error sources into a cohesive prediction tool in reflectance space. Additionally, this model was exercised using realistic inputs to allow detailed analysis of error propagation as it related to inversion of hyperspectral imagery.

In order to correctly model the contributions of each atmospheric constituent, a partial derivative was required for each. Using the radiative transfer code MODTRAN, results were presented that demonstrate the process of numerically calculating the partial derivatives of each modeling output with respect to each atmospheric constituent. Step size selection was discussed and presented, and the slopes themselves were shown.

Three diverse sources for atmospheric constituent error were used to illustrate the flexibility of the model. Atmospheric constituent determination by using historical climate data, ground instruments, and in-scene algorithms operate very differently but produce identical outputs. Survey results were presented to show the approximate quality of constituent determination using each source. These results were then crafted into 5 basic scenarios used to frame the analysis of hyperspectral imagery inversion.

When constituent uncertainties are combined with the partial derivatives, error

in each modeling output is produced. Because this is an intermediate step, only representative results were shown for one of the five basic scenarios, but the applicability of these results to the other scenarios were discussed.

The radiative transfer equation was decomposed into its individual components. The error in modeling outputs accounted for just the action of the atmosphere on the light, but modeling techniques for the many non-atmospheric effects was also discussed. These included off-nadir pointing on a slant path through the atmosphere, clouds, and background objects. The remaining effect, ground tilt, was not presented as a standalone effect due to its simplicity: it directly perturbs the cosine term in the big equation. The other environmental effects required more involved calculations, and the results in radiance space were presented and discussed for each. Additionally, three sensor calibration effects were presented: radiometric accuracy (bias), radiometric precision (noise), and spectral calibration (which contained both systematic and random effects). Sensor error models were taken from literature to be representative of the state of the remote sensing community. The effects of these sensor error models on radiometry were shown.

Once all the pieces of the governing radiative transfer equation were established with regards to impact on the radiometric environment, all error sources were propagated into the common reflectance space. Putting together these pieces involved iteratively applying the same basic error propagation steps described earlier: the error inherent in each term is combined with the partial derivative of reflectance with respect to each term. The partial derivatives, which are scenario dependent, were calculated analytically and used to produce total error.

Total error results were the centerpiece of this work. There were 5 basic scenarios designed to show the model predictions of how well each source of atmospheric inversion data fared. However, a detailed parametric study was also performed, and results for 16 additional scenarios were presented. Each of these additional scenarios focused on one of the environmental or sensor error sources and tracked how the error contribution varies as the parameter does. One final scenario was produced that attempted to model a realistic situation using ground sensors and realistic environmental and sensor noise sources.

Model validation is an extremely important activity, and results were presented that showed close agreement between the model predictions and a detailed validation study consisting of 9 scenarios. Because of known issues with machine precision and the small numbers involved, agreement based on percentage appeared to show significant discrepancies, while agreement based on absolute deviation showed close similarity in both magnitude and spectral shape. Thus, the results were mixed but ultimately deemed to be acceptable.

Finally, a sensitivity study was performed and presented that attempted to trace error in retrieved reflectance back to atmospheric constituents. The results were counterintuitive, but upon detailed examination were shown to be correct. The relative magnitudes of the atmospheric constituent contributions did not fully support intuitive notions of which constituents dominate which modeling outputs for two reasons. First, it was found that the definition of “dark” targets perhaps should include 10% reflectors and below – at 20% reflectance, opposing factors work to reduce aerosol error effects. Additionally, the relative magnitudes of the errors used to construct each scenario heavily affected how much error reduction could take place. In other words, if an error is as low as it can go to begin with, and another constituent suffers from high error, then that relationship governs the result, rather than universal principles regarding aerosols or water vapor. However, the choice of parameters and targets did produce unexpected results, and it is perhaps in situations like this that the surprising results are the most valuable.

Chapter 6

Conclusions and Future Work

6.1 Modeling Work and System Behavior

A foundational body of work has been presented that explores a subject of intense interest in a novel fashion. The study of radiometric accuracy of remotely sensed imaging and any derived products flows from the traditional study of measurements and uncertainty. The field of remote sensing is one of constant interaction between remote sensing instruments and the environment in which they function. Predicting the characteristics of any element of this interaction is a recursive spiral of calibration and validation to increasingly reliable methods and standards. Operating in this environment demands a constant awareness of error and uncertainty. The penalty for ignorance is not only not knowing whether or not a result is accurate, but also not knowing when to distrust or reject the results. While this state is not unique to remote sensing, specialized study of radiative transfer and atmospheric inversion is needed to enable comprehension of the nonlinear system and modeling challenges inherent in this task. The remote sensing product examined here was a reflectance image produced by estimating atmospheric effects and applying them as an inverse operator to a radiance image.

A method has been developed that models the uncertainty inherent in hyperspectral imagery inversion. Every link of the imaging chain from source to detector to inversion algorithm has been simulated in error space with respect to electromagnetic wavelength. The modeling approach presented here allows the unique specification of the uncertainty in each link in the chain and propagates all error sources into the common framework of reflectance space. Input parameters are described as the width of statistical distributions governing the uncertainty of the individual terms, and the final output is the width of the statistical distribution gov-

erning the uncertainty of retrieved reflectance. The presentation of this model is the first major conclusion of this investigation. The ability to describe retrieved reflectance error using statistical language rather than as a single deviation is the novel aspect of the approach.

Background material was introduced to describe common inversion methods and the physics behind radiative transfer. The statistical underpinnings of error propagation were also presented, including careful treatment of correlations of multiple variables. Then, these two relatively simple concepts were combined and applied to the various physical phenomena affecting the spectra reaching an airborne or spaceborne sensor. Individual models for each phenomenon were built and assembled in modular fashion, allowing for flexibility and future growth.

This analytical model was validated to the point where it credibly reproduces statistical distributions generated through discrete simulation using MODTRAN. This self-validation shows that the model's key mechanism, the non-linear slope determination, functions properly. It also validates the mathematical theory used to propagate error from precursor sources into retrieved reflectance space. The validation did not treat any of the environmental models, but for the most part these were calculated in a very straightforward manner. Cloud modeling results were not validated, but these results were generated for a very specific case using an external methodology. In other words, the purpose of this work was not to study cloud modeling *per se*, rather given a valid cloud model, these effects needed to be correctly propagated into reflectance space. A similar situation exists with background radiance.

Populating the component models with sample data was alternately simple and difficult. Those portions relating to the atmosphere and sensing geometry simply require scenario settings as inputs but otherwise retained their generality. The portions relating to cloud and background radiance could not be used without specifying geometric and spectral configurations for the objects themselves, so sample spectra and random geometry were used to create a set of results that were instructive but not general. Similarly, spectral calibration error presented a modeling difficulty. Except for spectrally correlated noise, which is not currently modeled, spectral calibration error is the only effect in which the spectral bands are not independent. While a degree of generality can be achieved by parameterizing by a spectrum's first derivative, the overall effect is unique to both the atmosphere and targets. The loss of generality is unavoidable at times but compensated for by the model's customizability.

Aside from these intricacies, the model was exercised to provide insights into how different effects interact and what relative magnitudes fall out of a sample sce-

nario. Because this has been shown to be a valid approach to predicting uncertainty, it becomes much simpler to use the model as a tool for studying uncertainty, as opposed to a Monte Carlo style method. Therefore, the second major conclusion of this work is that observations have been made possible by running the model with representative inputs in a plausible set of scenarios. Although these results were examined in detail earlier, major findings are summarized here:

- Confirming common knowledge, error in retrieved atmospheric transmissivity dominates for bright targets, while error in upwelled radiance dominates for darker targets. Downwelled radiance does not dominate, and its contribution scales according to target brightness.
- Correlation contributions drastically affect the results. This is not an artifact of the modeling process; these terms are mathematically necessary. The sum of the correlation terms may be positive or negative, depending on their relative magnitudes.
- Although there is an intuitive tendency to equate aerosols with scattered radiance and water vapor with transmissivity losses, all atmospheric constituents contribute to every modeling output. The relative magnitude of these contributions is so highly volatile that it is very difficult to predict which effect dominates the other. Another factor obscuring relationships that match intuitive tendencies is that when cast into reflectance *uncertainty* space, uncertainty inputs are rarely “balanced;” in fact, differences in the quality of one estimate over another can quickly skew the relative uncertainty contributions.

Finally, the model was used to show what improvements could be possible by establishing a network of one or more ground truth sensors to augment imaging by a primary remote sensing instrument. To consistently achieve better than the few percent reflectance that serves as the current approximate retrieval limit (depending on spectral region), it is necessary, but not sufficient, to drive down atmospheric sources of uncertainty. The results for the final scenario and its variant point to several different ways of approaching 1 reflectance unit of error as well as obstacles to doing so.

For bright targets, any single error source, whether bias or random, is capable of driving the error above the few percent that serves as the current lower limit. However, it is not as important to drive error so low for bright targets as it is for darker ones. When compared to dark targets, the ratio between retrieved reflectance and the error in retrieved reflectance greatly favors bright targets. For example, using

performance numbers seen in the previous chapter's final scenario, 4 reflectance units of error for a 100% reflector is five times better than 1 reflectance unit of error for a 5% reflector.

For darker targets, atmospheric uncertainty, ground tilt uncertainty, instrument noise (both random and non-random components), and cloud effects can all be driven reasonably low enough to permit reflectance retrievals with 1-2 reflectance units of uncertainty. Atmospheric contributions are the largest contributor, and driving these as low as possible (within the confines set by this research) enables retrievals at or below the 1 reflectance unit threshold, given that all other parameters are at the modeled values and depending on target reflectance. Several contributors are highly volatile. It has been shown what the results *could* be given the example parameters, but it would not be prudent to generalize further based on the particular sensor chosen for this scenario, nor the cloud type or amount. The conclusion here is that assuming the other parameters are behaving normally, there is value in pursuing a reduction in atmospheric constituent uncertainty.

Considerations for the use or rejection of several major types of ground truth instruments were discussed, and guiding principles for how to construct a network architecture were offered. Performance improvements for atmospheric inversion are highly possible but dependent on the ability of the instrument to provide adequate in-scene data to run one of the model-based algorithms. High cost and low cost options were presented and generally quantified, giving a decision-maker the tools to weigh the application-criticality of very accurate reflectance data with the cost of obtaining it.

The low cost and modest improvement produced by ground water vapor instruments such as dual-band GPS made this instrument the best marginal improvement option. Substantial gains in aerosol and direct irradiance measurement can be had at much greater cost using a photometer. The photometer's improvement in performance was unmatched, but it was only recommended if the performance need justified the cost. Using both in concert, of course, is better still, and was predicted to produce uncertainties on the order of ± 1 reflectance unit.

If the remote sensing instrument is capable of supporting model-based inversion, ground truth augmentation really isn't necessary unless the application requires accuracy below 2 reflectance units or the scenes are consistently humid. In that case, the same order of prescription applies: add a water vapor sensor first, especially for wet areas where model based inversion has trouble, then a sun photometer if the budget allows.

6.2 Future Work

The ultimate desire of this type of science is to get as close to the unknowable absolute truth as possible. Truly understanding the phenomenology behind why algorithms fail or why band ratios fail is really the best direction to proceed. The type of radiative transfer modeling performed today was until recently simply impossible because of the computing power required. Today's radiative transfer is limited by the shortcuts and assumptions made in the process. Tomorrows modeling will certainly take advantage of the computing tools available then to provide even better modeling capabilities, but only if the problems with the current approaches are understood. For example, there are hints as to why and under what conditions water vapor prediction from in-scene band ratios have problems, especially with wet atmospheres, but the underlying causes and modeling oversights are not understood well enough to move forward.

Still in the modeling vein, it would be very helpful to better understand the impacts of background and cloud radiance. Simple, homegrown models were presented here, but there is no well-established methodology for simulating cloud scenes of different cloud types and opacities. Clouds will continue to be the bane of remote sensing in the visible and near infrared spectral regimes until their effects can be better modeled – not necessarily from a spatial standpoint, which would be nearly impossible, but from a statistical one.

Also in the area of improving model fidelity, it would be useful to study the effects of non-Lambertian reflectors. The model would need to accept a target BRDF or at the very least a factor that accounts for the non-Lambertian reflectance for the angles under study. Ground targets that are brighter or darker than an equivalent Lambertian reflector in certain geometries would behave in error space like brighter or darker targets. The previously demonstrated trends in error propagation between bright and dark targets would come into play, and it would be useful to see, for example, under what conditions a target's specularity causes a crossover in the relative importance of its error sources.

Pollution modeling is an interesting area of study. The huge molecules associated with pollution greatly affect the radiance results, but these are not explicitly treated when aerosols are discussed in remote sensing literature. For that matter, aerosol particle size distribution and phase functions were not treated. These can have significant effects on the aerosol modeling results if the wrong type of aerosols are used. Unfortunately, no “plug-in” data or methodologies were available to handle these properties in this work, but they should be developed.

Since pollutants are invariant neither temporally nor spatially, if error analysis

ever reaches the point of predicting extreme accuracy, this might be a fertile future study area.

Atmospheric constituents were assumed to not be correlated, but a quick look at climatology plots across seasons shows this is clearly not the case. However, determining proper coefficient values falls in the realm of meteorology, not remote sensing. As an aside, during the course of isolating a programming error, a cursory study was conducted using nonzero atmospheric constituent correlation coefficients, and the effect on the final results as presented here is small.

With regards to using MODTRAN as a slope generator, options exist but were not pursued to examine the internal machine precision of the MODTRAN code. Significant problems were encountered when using MODTRAN in this manner, but they seem to be rectifiable.

In terms of operating the model in support of error prediction, three major paths of future work almost scream out. First is the need to examine other geometries and locations. A single geometry was chosen to focus the work and its conclusions as well as for simplicity. To apply the model to produce actual error predictions and sensitivity information, the geometry needs to be reset and MODTRAN slopes need to be recomputed and is otherwise trivial.

Secondly, the simple method of combining inputs could be improved through the use of a Kalman filter. This type of filter uses data from all sources regardless of quality, weighting each by its noise. It recognizes that all inputs are useful in influencing the estimate.

Ultimately, two-dimensional modeling is an almost mandatory next step. It would model the propagation of uncertainty spatially outward from the measurement point. A distance function for each error source and distance maps for each source would be combined to create a unique uncertainty profile for each pixel. The uncertainty spectrum would be combined with the pixel spectrum to predict errors by band and by pixel as a function of brightness and spectral character. The product of this process is a spatial/spectral error cube. Future work from that point would include the addition of cloud and terrain masks to fold in the kind of environmental modeling presented here. Finally, the use of multiple atmospheric derivatives would enable the capability to predict error in a non-uniform in-scene atmosphere, though that's probably looking too far ahead.

Appendix A

Full Expressions for Selected Equations

A.1 Partial derivatives of reflectance

The following equations expand the relevant generalized terms listed equation 4.20:

$$\begin{aligned}
 S_r^2 &= \left(\frac{\partial r}{\partial E_s} S_{E_s} \right)^2 + \left(\frac{\partial r}{\partial \sigma_{s'}} S_{\sigma_{s'}} \right)^2 + \left(\frac{\partial r}{\partial \tau_1} S_{\tau_1} \right)^2 \\
 &+ \left(\frac{\partial r}{\partial \tau_2} S_{\tau_2} \right)^2 + \left(\frac{\partial r}{\partial L_d} S_{L_d} \right)^2 + \left(\frac{\partial r}{\partial L_{cld}} S_{L_{cld}} \right)^2 \\
 &+ \left(\frac{\partial r}{\partial L_{bkg}} S_{L_{bkg}} \right)^2 + \left(\frac{\partial r}{\partial F_2} S_{F_2} \right)^2 + \left(\frac{\partial r}{\partial F_1} S_{F_1} \right)^2 \\
 &+ \left(\frac{\partial r}{\partial L_u} S_{L_u} \right)^2 + \left(\frac{\partial r}{\partial L_{adj}} S_{L_{adj}} \right)^2 + \left(\frac{\partial r}{\partial L_{SR}} S_{L_{SR}} \right)^2 \\
 &+ 2\rho_{(\tau_1, \tau_2)} S_{\tau_1} S_{\tau_2} \frac{\partial r}{\partial \tau_1} \frac{\partial r}{\partial \tau_2} + 2\rho_{(\tau_1, L_d)} S_{\tau_1} S_{L_d} \frac{\partial r}{\partial \tau_1} \frac{\partial r}{\partial L_d} \\
 &+ 2\rho_{(\tau_1, L_u)} S_{\tau_1} S_{L_u} \frac{\partial r}{\partial \tau_1} \frac{\partial r}{\partial L_u} + 2\rho_{(\tau_2, L_d)} S_{\tau_2} S_{L_d} \frac{\partial r}{\partial \tau_2} \frac{\partial r}{\partial L_d} \\
 &+ 2\rho_{(\tau_2, L_u)} S_{\tau_2} S_{L_u} \frac{\partial r}{\partial \tau_2} \frac{\partial r}{\partial L_u} + 2\rho_{(L_d, L_u)} S_{L_d} S_{L_u} \frac{\partial r}{\partial L_d} \frac{\partial r}{\partial L_u} \quad (\text{A.1})
 \end{aligned}$$

$$\frac{\partial r}{\partial E_s} = \frac{-\frac{1}{\pi} \cos \sigma_{s'} \tau_1 \tau_2}{\left(\frac{E_s}{\pi} \cos \sigma_{s'} \tau_1 \tau_2 + (F_2 (F_1 L_d + (1 - F_1) L_{cld}) + (1 - F_2) L_{bkg}) \tau_2 \right)^2} \quad (\text{A.2})$$

$$\frac{\partial r}{\partial \sigma_{s'}} = \frac{\frac{E_s}{\pi} \sin \sigma_{s'} \tau_1 \tau_2}{\left(\frac{E_s}{\pi} \cos \sigma_{s'} \tau_1 \tau_2 + (F_2 (F_1 L_d + (1 - F_1) L_{cld}) + (1 - F_2) L_{bkg}) \tau_2 \right)^2} \quad (\text{A.3})$$

$$\frac{\partial r}{\partial \tau_1} = \frac{-\frac{E_s}{\pi} \cos \sigma_{s'} \tau_1 \tau_2}{\left(\frac{E_s}{\pi} \cos \sigma_{s'} \tau_1 \tau_2 + (F_2 (F_1 L_d + (1 - F_1) L_{cld}) + (1 - F_2) L_{bkg}) \tau_2 \right)^2} \quad (\text{A.4})$$

$$\frac{\partial r}{\partial \tau_2} = \frac{-1}{\left(\frac{E_s}{\pi} \cos \sigma_{s'} \tau_1 \tau_2 + (F_2 (F_1 L_d + (1 - F_1) L_{cld}) + (1 - F_2) L_{bkg}) \tau_2 \right) \tau_2^2} \quad (\text{A.5})$$

$$\frac{\partial r}{\partial L_d} = \frac{-F_2 F_1 \tau_2}{\left(\frac{E_s}{\pi} \cos \sigma_{s'} \tau_1 \tau_2 + (F_2 (F_1 L_d + (1 - F_1) L_{cld}) + (1 - F_2) L_{bkg}) \tau_2 \right)^2} \quad (\text{A.6})$$

$$\frac{\partial r}{\partial L_{cld}} = \frac{-F_2 (1 - F_1) \tau_2}{\left(\frac{E_s}{\pi} \cos \sigma_{s'} \tau_1 \tau_2 + (F_2 (F_1 L_d + (1 - F_1) L_{cld}) + (1 - F_2) L_{bkg}) \tau_2 \right)^2} \quad (\text{A.7})$$

$$\frac{\partial r}{\partial L_{bkg}} = \frac{-(1 - F_2) \tau_2}{\left(\frac{E_s}{\pi} \cos \sigma_{s'} \tau_1 \tau_2 + (F_2 (F_1 L_d + (1 - F_1) L_{cld}) + (1 - F_2) L_{bkg}) \tau_2 \right)^2} \quad (\text{A.8})$$

$$\frac{\partial r}{\partial F_2} = \frac{-(F_1 L_d + L_{cld} - F_1 L_{cld} - L_{bkg}) \tau_2}{\left(\frac{E_s}{\pi} \cos \sigma_{s'} \tau_1 \tau_2 + (F_2 (F_1 L_d + (1 - F_1) L_{cld}) + (1 - F_2) L_{bkg}) \tau_2\right)^2} \quad (\text{A.9})$$

$$\frac{\partial r}{\partial F_1} = \frac{-(F_2 L_d - F_2 L_{cld}) \tau_2}{\left(\frac{E_s}{\pi} \cos \sigma_{s'} \tau_1 \tau_2 + (F_2 (F_1 L_d + (1 - F_1) L_{cld}) + (1 - F_2) L_{bkg}) \tau_2\right)^2} \quad (\text{A.10})$$

$$\frac{\partial r}{\partial L_u} = \frac{-1}{\left(\frac{E_s}{\pi} \cos \sigma_{s'} \tau_1 + (F_2 (F_1 L_d + (1 - F_1) L_{cld}) + (1 - F_2) L_{bkg})\right) \tau_2} \quad (\text{A.11})$$

$$\frac{\partial r}{\partial L_{adj}} = \frac{-1}{\left(\frac{E_s}{\pi} \cos \sigma_{s'} \tau_1 + (F_2 (F_1 L_d + (1 - F_1) L_{cld}) + (1 - F_2) L_{bkg})\right) \tau_2} \quad (\text{A.12})$$

$$\frac{\partial r}{\partial L_{SR}} = \frac{1}{\left(\frac{E_s}{\pi} \cos \sigma_{s'} \tau_1 + (F_2 (F_1 L_d + (1 - F_1) L_{cld}) + (1 - F_2) L_{bkg})\right) \tau_2} \quad (\text{A.13})$$

A.2 Correlation and error terms

In the following expressions, the uncertainty in each atmospheric parameter is obtained either from *a priori* statistical climate models of the area, from instrument measurements, or from inversion algorithm outputs. The partial derivatives of each modeling output with respect to each atmospheric parameter are non-linear functions that must be approximated numerically or through an appropriate curve fit. It is suggested that numerical methods be used because the curves tend to shift as the scenario parameters are changed.

$$\begin{aligned}
S_{\tau_1} S_{\tau_2} \rho_{(\tau_1 \tau_2)} &= S_{H_2O}^2 \frac{\partial \tau_1}{\partial H_2O} \frac{\partial \tau_2}{\partial H_2O} + S_{alt}^2 \frac{\partial \tau_1}{\partial alt} \frac{\partial \tau_2}{\partial alt} + S_{AOD}^2 \frac{\partial \tau_1}{\partial AOD} \frac{\partial \tau_2}{\partial AOD} \\
&+ S_{H_2O} S_{alt} \rho_{(H_2O, alt)} \left(\frac{\partial \tau_1}{\partial H_2O} \frac{\partial \tau_2}{\partial alt} + \frac{\partial \tau_1}{\partial alt} \frac{\partial \tau_2}{\partial H_2O} \right) \\
&+ S_{H_2O} S_{AOD} \rho_{(H_2O, AOD)} \left(\frac{\partial \tau_1}{\partial H_2O} \frac{\partial \tau_2}{\partial AOD} + \frac{\partial \tau_1}{\partial AOD} \frac{\partial \tau_2}{\partial H_2O} \right) \\
&+ S_{alt} S_{AOD} \rho_{(alt, AOD)} \left(\frac{\partial \tau_1}{\partial alt} \frac{\partial \tau_2}{\partial AOD} + \frac{\partial \tau_1}{\partial AOD} \frac{\partial \tau_2}{\partial alt} \right)
\end{aligned} \tag{A.14}$$

$$\begin{aligned}
S_{\tau_1} S_{L_d} \rho_{(\tau_1 L_d)} &= S_{H_2O}^2 \frac{\partial \tau_1}{\partial H_2O} \frac{\partial L_d}{\partial H_2O} + S_{alt}^2 \frac{\partial \tau_1}{\partial alt} \frac{\partial L_d}{\partial alt} + S_{AOD}^2 \frac{\partial \tau_1}{\partial AOD} \frac{\partial L_d}{\partial AOD} \\
&+ S_{H_2O} S_{alt} \rho_{(H_2O, alt)} \left(\frac{\partial \tau_1}{\partial H_2O} \frac{\partial L_d}{\partial alt} + \frac{\partial \tau_1}{\partial alt} \frac{\partial L_d}{\partial H_2O} \right) \\
&+ S_{H_2O} S_{AOD} \rho_{(H_2O, AOD)} \left(\frac{\partial \tau_1}{\partial H_2O} \frac{\partial L_d}{\partial AOD} + \frac{\partial \tau_1}{\partial AOD} \frac{\partial L_d}{\partial H_2O} \right) \\
&+ S_{alt} S_{AOD} \rho_{(alt, AOD)} \left(\frac{\partial \tau_1}{\partial alt} \frac{\partial L_d}{\partial AOD} + \frac{\partial \tau_1}{\partial AOD} \frac{\partial L_d}{\partial alt} \right)
\end{aligned} \tag{A.15}$$

$$\begin{aligned}
S_{\tau_1} S_{L_u} \rho_{(\tau_1 L_u)} &= S_{H_2O}^2 \frac{\partial \tau_1}{\partial H_2O} \frac{\partial L_u}{\partial H_2O} + S_{alt}^2 \frac{\partial \tau_1}{\partial alt} \frac{\partial L_u}{\partial alt} + S_{AOD}^2 \frac{\partial \tau_1}{\partial AOD} \frac{\partial L_u}{\partial AOD} \\
&+ S_{H_2O} S_{alt} \rho_{(H_2O, alt)} \left(\frac{\partial \tau_1}{\partial H_2O} \frac{\partial L_u}{\partial alt} + \frac{\partial \tau_1}{\partial alt} \frac{\partial L_u}{\partial H_2O} \right) \\
&+ S_{H_2O} S_{AOD} \rho_{(H_2O, AOD)} \left(\frac{\partial \tau_1}{\partial H_2O} \frac{\partial L_u}{\partial AOD} + \frac{\partial \tau_1}{\partial AOD} \frac{\partial L_u}{\partial H_2O} \right) \\
&+ S_{alt} S_{AOD} \rho_{(alt, AOD)} \left(\frac{\partial \tau_1}{\partial alt} \frac{\partial L_u}{\partial AOD} + \frac{\partial \tau_1}{\partial AOD} \frac{\partial L_u}{\partial alt} \right)
\end{aligned} \tag{A.16}$$

$$\begin{aligned}
S_{\tau_2} S_{L_d} \rho_{(\tau_2 L_d)} &= S_{H_2O}^2 \frac{\partial \tau_2}{\partial H_2O} \frac{\partial L_d}{\partial H_2O} + S_{alt}^2 \frac{\partial \tau_2}{\partial alt} \frac{\partial L_d}{\partial alt} + S_{AOD}^2 \frac{\partial \tau_2}{\partial AOD} \frac{\partial L_d}{\partial AOD} \\
&+ S_{H_2O} S_{alt} \rho_{(H_2O, alt)} \left(\frac{\partial \tau_2}{\partial H_2O} \frac{\partial L_d}{\partial alt} + \frac{\partial \tau_2}{\partial alt} \frac{\partial L_d}{\partial H_2O} \right)
\end{aligned}$$

$$\begin{aligned}
& + S_{H_2O} S_{AOD} \rho_{(H_2O, AOD)} \left(\frac{\partial \tau_2}{\partial H_2O} \frac{\partial L_d}{\partial AOD} + \frac{\partial \tau_2}{\partial AOD} \frac{\partial L_d}{\partial H_2O} \right) \\
& + S_{alt} S_{AOD} \rho_{(alt, AOD)} \left(\frac{\partial \tau_2}{\partial alt} \frac{\partial L_d}{\partial AOD} + \frac{\partial \tau_2}{\partial AOD} \frac{\partial L_d}{\partial alt} \right)
\end{aligned} \tag{A.17}$$

$$\begin{aligned}
S_{\tau_2} S_{L_u} \rho_{(\tau_2 L_u)} & = S_{H_2O}^2 \frac{\partial \tau_2}{\partial H_2O} \frac{\partial L_u}{\partial H_2O} + S_{alt}^2 \frac{\partial \tau_2}{\partial alt} \frac{\partial L_u}{\partial alt} + S_{AOD}^2 \frac{\partial \tau_2}{\partial AOD} \frac{\partial L_u}{\partial AOD} \\
& + S_{H_2O} S_{alt} \rho_{(H_2O, alt)} \left(\frac{\partial \tau_2}{\partial H_2O} \frac{\partial L_u}{\partial alt} + \frac{\partial \tau_2}{\partial alt} \frac{\partial L_u}{\partial H_2O} \right) \\
& + S_{H_2O} S_{AOD} \rho_{(H_2O, AOD)} \left(\frac{\partial \tau_2}{\partial H_2O} \frac{\partial L_u}{\partial AOD} + \frac{\partial \tau_2}{\partial AOD} \frac{\partial L_u}{\partial H_2O} \right) \\
& + S_{alt} S_{AOD} \rho_{(alt, AOD)} \left(\frac{\partial \tau_2}{\partial alt} \frac{\partial L_u}{\partial AOD} + \frac{\partial \tau_2}{\partial AOD} \frac{\partial L_u}{\partial alt} \right)
\end{aligned} \tag{A.18}$$

$$\begin{aligned}
S_{L_d} S_{L_u} \rho_{(L_d L_u)} & = S_{H_2O}^2 \frac{\partial L_d}{\partial H_2O} \frac{\partial L_u}{\partial H_2O} + S_{alt}^2 \frac{\partial L_d}{\partial alt} \frac{\partial L_u}{\partial alt} + S_{AOD}^2 \frac{\partial L_d}{\partial AOD} \frac{\partial L_u}{\partial AOD} \\
& + S_{H_2O} S_{alt} \rho_{(H_2O, alt)} \left(\frac{\partial L_d}{\partial H_2O} \frac{\partial L_u}{\partial alt} + \frac{\partial L_d}{\partial alt} \frac{\partial L_u}{\partial H_2O} \right) \\
& + S_{H_2O} S_{AOD} \rho_{(H_2O, AOD)} \left(\frac{\partial L_d}{\partial H_2O} \frac{\partial L_u}{\partial AOD} + \frac{\partial L_d}{\partial AOD} \frac{\partial L_u}{\partial H_2O} \right) \\
& + S_{alt} S_{AOD} \rho_{(alt, AOD)} \left(\frac{\partial L_d}{\partial alt} \frac{\partial L_u}{\partial AOD} + \frac{\partial L_d}{\partial AOD} \frac{\partial L_u}{\partial alt} \right)
\end{aligned} \tag{A.19}$$

Equations A.20 through A.23 show how the error in each individual modeling term is determined. The earlier note on how the piece components are obtained applies here as well.

$$\begin{aligned}
S_{\tau_1}^2 & = \left(\frac{\partial \tau_1}{\partial H_2O} S_{H_2O} \right)^2 + \left(\frac{\partial \tau_1}{\partial alt} S_{alt} \right)^2 + \left(\frac{\partial \tau_1}{\partial AOD} S_{AOD} \right)^2 \\
& + 2\rho_{(H_2O, alt)} \frac{\partial \tau_1}{\partial H_2O} \frac{\partial \tau_1}{\partial alt} S_{H_2O} S_{alt} + 2\rho_{(alt, AOD)} \frac{\partial \tau_1}{\partial alt} \frac{\partial \tau_1}{\partial AOD} S_{alt} S_{AOD} \\
& + 2\rho_{(H_2O, AOD)} \frac{\partial \tau_1}{\partial H_2O} \frac{\partial \tau_1}{\partial AOD} S_{H_2O} S_{AOD}
\end{aligned} \tag{A.20}$$

$$\begin{aligned}
S_{\tau_2}^2 &= \left(\frac{\partial \tau_2}{\partial H_2O} S_{H_2O} \right)^2 + \left(\frac{\partial \tau_2}{\partial alt} S_{alt} \right)^2 + \left(\frac{\partial \tau_2}{\partial AOD} S_{AOD} \right)^2 \\
&+ 2\rho_{(H_2O, alt)} \frac{\partial \tau_2}{\partial H_2O} \frac{\partial \tau_2}{\partial alt} S_{H_2O} S_{alt} + 2\rho_{(alt, AOD)} \frac{\partial \tau_2}{\partial alt} \frac{\partial \tau_2}{\partial AOD} S_{alt} S_{AOD} \\
&+ 2\rho_{(H_2O, AOD)} \frac{\partial \tau_2}{\partial H_2O} \frac{\partial \tau_2}{\partial AOD} S_{H_2O} S_{AOD}
\end{aligned} \tag{A.21}$$

$$\begin{aligned}
S_{L_d}^2 &= \left(\frac{\partial L_d}{\partial H_2O} S_{H_2O} \right)^2 + \left(\frac{\partial L_d}{\partial alt} S_{alt} \right)^2 + \left(\frac{\partial L_d}{\partial AOD} S_{AOD} \right)^2 \\
&+ 2\rho_{(H_2O, alt)} \frac{\partial L_d}{\partial H_2O} \frac{\partial L_d}{\partial alt} S_{H_2O} S_{alt} + 2\rho_{(alt, AOD)} \frac{\partial L_d}{\partial alt} \frac{\partial L_d}{\partial AOD} S_{alt} S_{AOD} \\
&+ 2\rho_{(H_2O, AOD)} \frac{\partial L_d}{\partial H_2O} \frac{\partial L_d}{\partial AOD} S_{H_2O} S_{AOD}
\end{aligned} \tag{A.22}$$

$$\begin{aligned}
S_{L_u}^2 &= \left(\frac{\partial L_u}{\partial H_2O} S_{H_2O} \right)^2 + \left(\frac{\partial L_u}{\partial alt} S_{alt} \right)^2 + \left(\frac{\partial L_u}{\partial AOD} S_{AOD} \right)^2 \\
&+ 2\rho_{(H_2O, alt)} \frac{\partial L_u}{\partial H_2O} \frac{\partial L_u}{\partial alt} S_{H_2O} S_{alt} + 2\rho_{(alt, AOD)} \frac{\partial L_u}{\partial alt} \frac{\partial L_u}{\partial AOD} S_{alt} S_{AOD} \\
&+ 2\rho_{(H_2O, AOD)} \frac{\partial L_u}{\partial H_2O} \frac{\partial L_u}{\partial AOD} S_{H_2O} S_{AOD}
\end{aligned} \tag{A.23}$$

A.3 Consolidated expressions

The following equation is the final expanded form of governing equation 4.20. It does not explicitly incorporate equations A.14 through A.15 or A.20 through A.23, which cannot be analytically expanded any further.

$$\begin{aligned}
S_r^2 &= \left(\frac{-\frac{1}{\pi} \cos \sigma_{s'} \tau_1 \tau_2}{\left(\frac{E_s}{\pi} \cos \sigma_{s'} \tau_1 \tau_2 + (F_2 (F_1 L_d + (1 - F_1) L_{cld}) + (1 - F_2) L_{bkg}) \tau_2 \right)^2} S_{E_s} \right)^2 \\
&+ \left(\frac{\frac{E_s}{\pi} \sin \sigma_{s'} \tau_1 \tau_2}{\left(\frac{E_s}{\pi} \cos \sigma_{s'} \tau_1 \tau_2 + (F_2 (F_1 L_d + (1 - F_1) L_{cld}) + (1 - F_2) L_{bkg}) \tau_2 \right)^2} S_{\sigma_{s'}} \right)^2
\end{aligned}$$

$$\begin{aligned}
& + \left(\frac{-\frac{E_s}{\pi} \cos \sigma_{s'} \tau_2}{\left(\frac{E_s}{\pi} \cos \sigma_{s'} \tau_1 \tau_2 + (F_2 (F_1 L_d + (1 - F_1) L_{cld}) + (1 - F_2) L_{bkg}) \tau_2 \right)^2} S_{\tau_1} \right)^2 \\
& + \left(\frac{-1}{\left(\frac{E_s}{\pi} \cos \sigma_{s'} \tau_1 + (F_2 (F_1 L_d + (1 - F_1) L_{cld}) + (1 - F_2) L_{bkg}) \right) \tau_2^2} S_{\tau_2} \right)^2 \\
& + \left(\frac{-F_2 F_1 \tau_2}{\left(\frac{E_s}{\pi} \cos \sigma_{s'} \tau_1 \tau_2 + (F_2 (F_1 L_d + (1 - F_1) L_{cld}) + (1 - F_2) L_{bkg}) \tau_2 \right)^2} S_{L_d} \right)^2 \\
& + \left(\frac{-F_2 (1 - F_1) \tau_2}{\left(\frac{E_s}{\pi} \cos \sigma_{s'} \tau_1 \tau_2 + (F_2 (F_1 L_d + (1 - F_1) L_{cld}) + (1 - F_2) L_{bkg}) \tau_2 \right)^2} S_{L_{cld}} \right)^2 \\
& + \left(\frac{-(1 - F_2) \tau_2}{\left(\frac{E_s}{\pi} \cos \sigma_{s'} \tau_1 \tau_2 + (F_2 (F_1 L_d + (1 - F_1) L_{cld}) + (1 - F_2) L_{bkg}) \tau_2 \right)^2} S_{L_{bkg}} \right)^2 \\
& + \left(\frac{-(F_1 L_d + L_{cld} - F_1 L_{cld} - L_{bkg}) \tau_2}{\left(\frac{E_s}{\pi} \cos \sigma_{s'} \tau_1 \tau_2 + (F_2 (F_1 L_d + (1 - F_1) L_{cld}) + (1 - F_2) L_{bkg}) \tau_2 \right)^2} S_{F_2} \right)^2 \\
& + \left(\frac{-(F_2 L_d - F_2 L_{cld}) \tau_2}{\left(\frac{E_s}{\pi} \cos \sigma_{s'} \tau_1 \tau_2 + (F_2 (F_1 L_d + (1 - F_1) L_{cld}) + (1 - F_2) L_{bkg}) \tau_2 \right)^2} S_{F_1} \right)^2 \\
& + \left(\frac{-1}{\left(\frac{E_s}{\pi} \cos \sigma_{s'} \tau_1 + (F_2 (F_1 L_d + (1 - F_1) L_{cld}) + (1 - F_2) L_{bkg}) \right) \tau_2} S_{L_u} \right)^2 \\
& + \left(\frac{-1}{\left(\frac{E_s}{\pi} \cos \sigma_{s'} \tau_1 + (F_2 (F_1 L_d + (1 - F_1) L_{cld}) + (1 - F_2) L_{bkg}) \right) \tau_2} S_{L_{adj}} \right)^2 \\
& + \left(\frac{1}{\left(\frac{E_s}{\pi} \cos \sigma_{s'} \tau_1 + (F_2 (F_1 L_d + (1 - F_1) L_{cld}) + (1 - F_2) L_{bkg}) \right) \tau_2} S_{L_{SR}} \right)^2 \\
& + 2\rho_{(\tau_1, \tau_2)} S_{\tau_1} S_{\tau_2} \frac{-\frac{E_s}{\pi} \cos \sigma_{s'} \tau_2}{\left(\frac{E_s}{\pi} \cos \sigma_{s'} \tau_1 \tau_2 + (F_2 (F_1 L_d + (1 - F_1) L_{cld}) + (1 - F_2) L_{bkg}) \tau_2 \right)^2} \\
& \cdot \frac{-1}{\left(\frac{E_s}{\pi} \cos \sigma_{s'} \tau_1 + (F_2 (F_1 L_d + (1 - F_1) L_{cld}) + (1 - F_2) L_{bkg}) \right) \tau_2^2}
\end{aligned}$$

$$\begin{aligned}
& + 2\rho_{(\tau_1, L_d)} S_{\tau_1} S_{L_d} \frac{-\frac{E_s}{\pi} \cos \sigma_{s'} \tau_2}{\left(\frac{E_s}{\pi} \cos \sigma_{s'} \tau_1 \tau_2 + (F_2 (F_1 L_d + (1 - F_1) L_{cld}) + (1 - F_2) L_{bkg}) \tau_2 \right)^2} \\
& \cdot \frac{-F_2 F_1 \tau_2}{\left(\frac{E_s}{\pi} \cos \sigma_{s'} \tau_1 \tau_2 + (F_2 (F_1 L_d + (1 - F_1) L_{cld}) + (1 - F_2) L_{bkg}) \tau_2 \right)^2} \\
& + 2\rho_{(\tau_1, L_u)} S_{\tau_1} S_{L_u} \frac{-\frac{E_s}{\pi} \cos \sigma_{s'} \tau_2}{\left(\frac{E_s}{\pi} \cos \sigma_{s'} \tau_1 \tau_2 + (F_2 (F_1 L_d + (1 - F_1) L_{cld}) + (1 - F_2) L_{bkg}) \tau_2 \right)^2} \\
& \cdot \frac{-1}{\left(\frac{E_s}{\pi} \cos \sigma_{s'} \tau_1 + (F_2 (F_1 L_d + (1 - F_1) L_{cld}) + (1 - F_2) L_{bkg}) \right) \tau_2} \\
& + 2\rho_{(\tau_2, L_d)} S_{\tau_2} S_{L_d} \frac{-1}{\left(\frac{E_s}{\pi} \cos \sigma_{s'} \tau_1 + (F_2 (F_1 L_d + (1 - F_1) L_{cld}) + (1 - F_2) L_{bkg}) \right) \tau_2^2} \\
& \cdot \frac{-F_2 F_1 \tau_2}{\left(\frac{E_s}{\pi} \cos \sigma_{s'} \tau_1 \tau_2 + (F_2 (F_1 L_d + (1 - F_1) L_{cld}) + (1 - F_2) L_{bkg}) \tau_2 \right)^2} \\
& + 2\rho_{(\tau_2, L_u)} S_{\tau_2} S_{L_u} \frac{-1}{\left(\frac{E_s}{\pi} \cos \sigma_{s'} \tau_1 + (F_2 (F_1 L_d + (1 - F_1) L_{cld}) + (1 - F_2) L_{bkg}) \right) \tau_2^2} \\
& \cdot \frac{-1}{\left(\frac{E_s}{\pi} \cos \sigma_{s'} \tau_1 + (F_2 (F_1 L_d + (1 - F_1) L_{cld}) + (1 - F_2) L_{bkg}) \right) \tau_2} \\
& + 2\rho_{(L_d, L_u)} S_{L_d} S_{L_u} \frac{-F_2 F_1 \tau_2}{\left(\frac{E_s}{\pi} \cos \sigma_{s'} \tau_1 \tau_2 + (F_2 (F_1 L_d + (1 - F_1) L_{cld}) + (1 - F_2) L_{bkg}) \tau_2 \right)^2} \\
& \cdot \frac{-1}{\left(\frac{E_s}{\pi} \cos \sigma_{s'} \tau_1 + (F_2 (F_1 L_d + (1 - F_1) L_{cld}) + (1 - F_2) L_{bkg}) \right) \tau_2}
\end{aligned} \tag{A.24}$$

Let the constant k be assigned to the denominator of equation 4.18:

$$k = \frac{E_s}{\pi} \cos \sigma_{s'} \tau_1 \tau_2 + (F_2 (F_1 L_d + (1 - F_1) L_{cld}) + (1 - F_2) L_{bkg}) \tau_2 \quad (\text{A.25})$$

The following is a simplified form of equation A.24, albeit one that does not permit convenient connection between error sources and terms in the equation:

$$S_r^2 = \frac{\left(\frac{1}{\pi} \cos \sigma_{s'} \tau_1 \tau_2\right)^2 S_{E_s}^2 + \left(\frac{E_s}{\pi} \sin \sigma_{s'} \tau_1 \tau_2\right)^2 S_{\sigma_{s'}}^2 + \left(\frac{E_s}{\pi} \cos \sigma_{s'} \tau_2\right)^2 S_{\tau_1}^2}{k^4}$$

$$\begin{aligned}
& + \frac{(F_2 F_1 \tau_2)^2 S_{L_d}^2 + (F_2 (1 - F_1) \tau_2)^2 S_{L_{cld}}^2 + ((1 - F_2) \tau_2)^2 S_{L_{bkg}}^2}{k^4} \\
& + \frac{((F_1 L_d + L_{cld} - F_1 L_{cld} - L_{bkg}) \tau_2)^2 S_{F_2}^2 + ((F_2 L_d - F_2 L_{cld}) \tau_2)^2 S_{F_1}^2}{k^4} \\
& + \frac{S_{L_u}^2 + S_{L_{adj}}^2 + S_{L_{SR}}^2 + \frac{S_{\tau_2}^2}{\tau_2^2} + 2\rho_{(\tau_2, L_d)} S_{\tau_2} S_{L_d} F_2 F_1 + \frac{2\rho_{(\tau_2, L_u)} S_{\tau_2} S_{L_u}}{\tau_2}}{k^2} \\
& + \frac{2\rho_{(\tau_1, \tau_2)} S_{\tau_1} S_{\tau_2} \frac{E_s}{\pi} \cos \sigma_{s'} + 2\rho_{(\tau_1, L_u)} S_{\tau_1} S_{L_u} \frac{E_s}{\pi} \cos \sigma_{s'} \tau_2 + \rho_{(L_d, L_u)} S_{L_d} S_{L_u} F_2 F_1 \tau_2}{k^3} \\
& + \frac{2\rho_{(\tau_1, L_d)} S_{\tau_1} S_{L_d} \frac{E_s}{\pi} \cos \sigma_{s'} F_2 F_1 \tau_2^2}{k^4}
\end{aligned} \tag{A.26}$$

A.4 Digital elevation model altitude error

The following set of equations provides a model for altitude error given a regularly-gridded digital elevation model (DEM). In this development, the DEM grid locations are at x_n and y_n , where n represents the n^{th} grid location in figure 4.9(b), with z_n representing the corresponding datum. Linear interpolation to a ground location (x, y) produces the coordinate triplet (x, y, z) . The λ terms are common linear interpolation notation, and the Δ terms simply represent the indicated differences. The S terms represent random uncertainty in the subscripted variable.

$$\lambda_x = \frac{x - x_1}{x_2 - x_1}, \quad \lambda_y = \frac{y - y_1}{y_2 - y_1} \tag{A.27}$$

$$\Delta_x = x_2 - x_1, \quad \Delta_y = y_2 - y_1 \tag{A.28}$$

$$\begin{aligned}
S_{elev}^2 &= \left[(1 - \lambda_y) \left(\frac{1 - \lambda_x}{\Delta_x} z_1 + \frac{\lambda_x - 1}{\Delta_x} z_4 \right) + \lambda_y \left(\frac{1 - \lambda_x}{\Delta_x} z_2 + \frac{\lambda_x - 1}{\Delta_x} z_3 \right) \right]^2 S_x^2 \\
&+ \left[(1 - \lambda_y) \left(\frac{\lambda_x}{\Delta_x} z_1 + \frac{-\lambda_x}{\Delta_x} z_4 \right) + \lambda_y \left(\frac{\lambda_x}{\Delta_x} z_2 + \frac{-\lambda_x}{\Delta_x} z_3 \right) \right]^2 S_x^2 \\
&+ \left[\frac{1 - \lambda_y}{\Delta_y} ((1 - \lambda_x) z_1 + \lambda_x z_4) + \frac{\lambda_y - 1}{\Delta_y} ((1 - \lambda_x) z_2 + \lambda_x z_3) \right]^2 S_y^2 \\
&+ \left[\frac{\lambda_y}{\Delta_y} ((1 - \lambda_x) z_1 + \lambda_x z_4) + \frac{-\lambda_y}{\Delta_y} ((1 - \lambda_x) z_2 + \lambda_x z_3) \right]^2 S_y^2 \\
&+ \left[(1 - \lambda_y)^2 (1 - \lambda_x)^2 + \lambda_y^2 (1 - \lambda_x)^2 + \lambda_y^2 \lambda_x^2 + (1 - \lambda_y)^2 \lambda_x^2 \right] S_z^2
\end{aligned} \tag{A.29}$$

Appendix B

Climatology Analysis Results

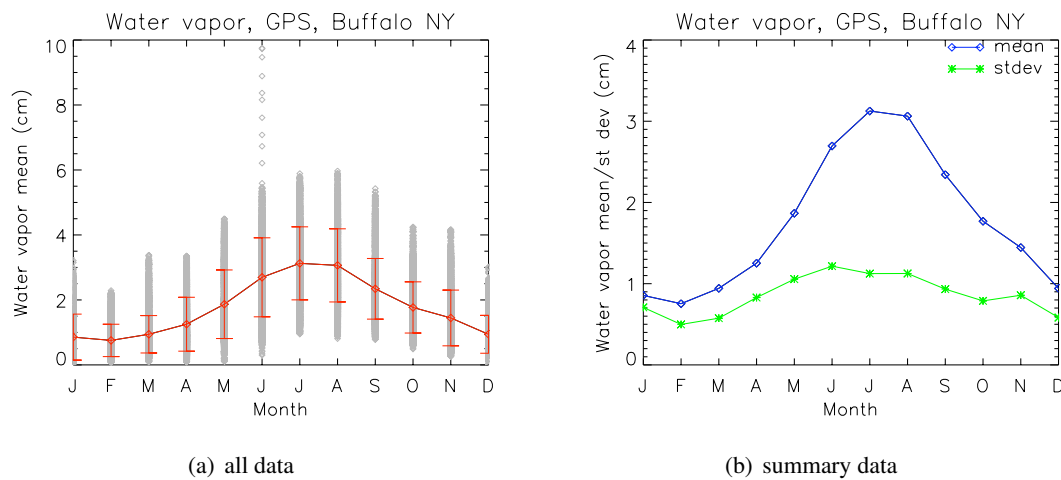


Figure B.1: GPS-based climate model for water vapor

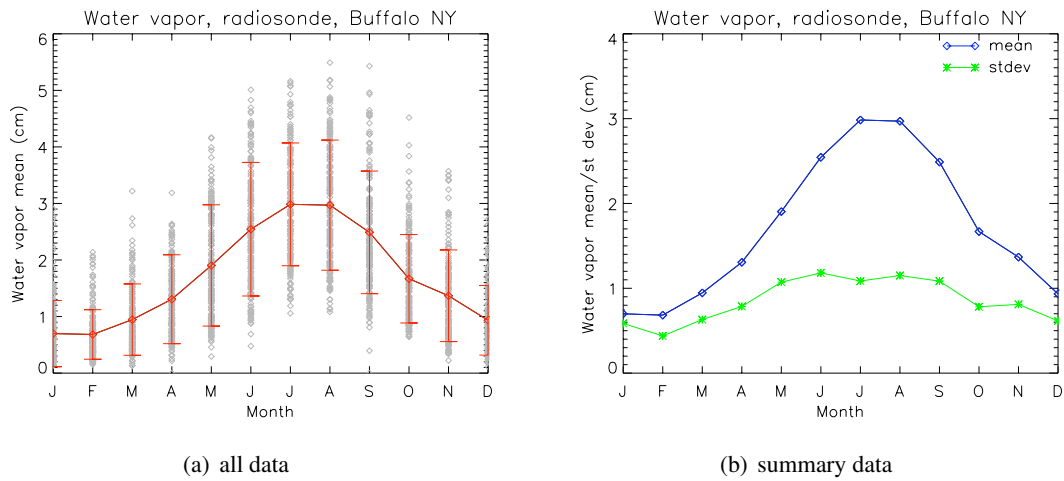


Figure B.2: Radiosonde-based climate model for water vapor

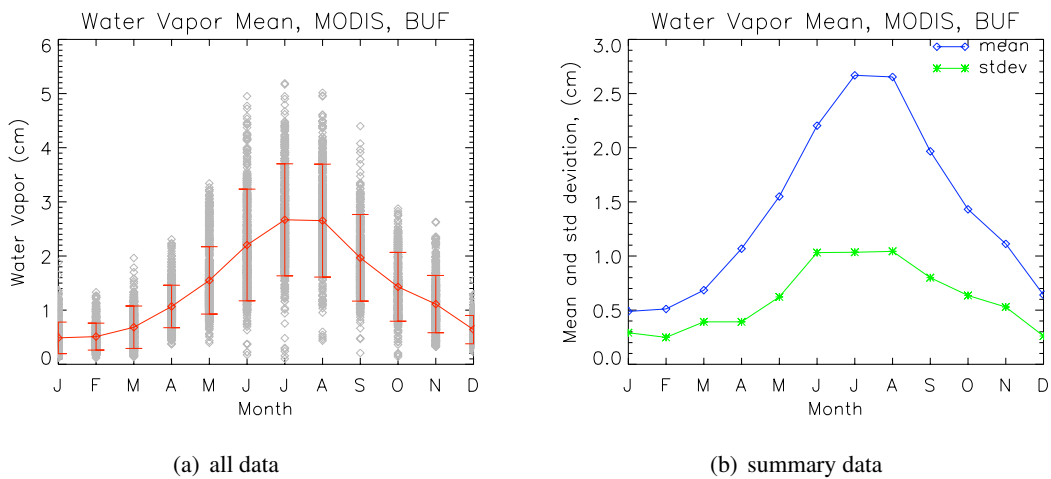


Figure B.3: MODIS-based climate model for water vapor

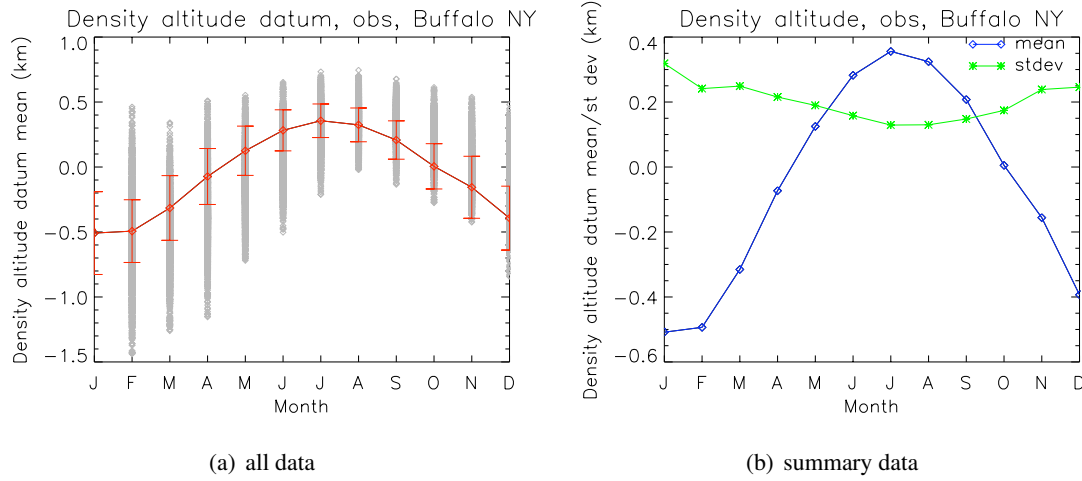


Figure B.4: Airport observation-based climate model for density altitude

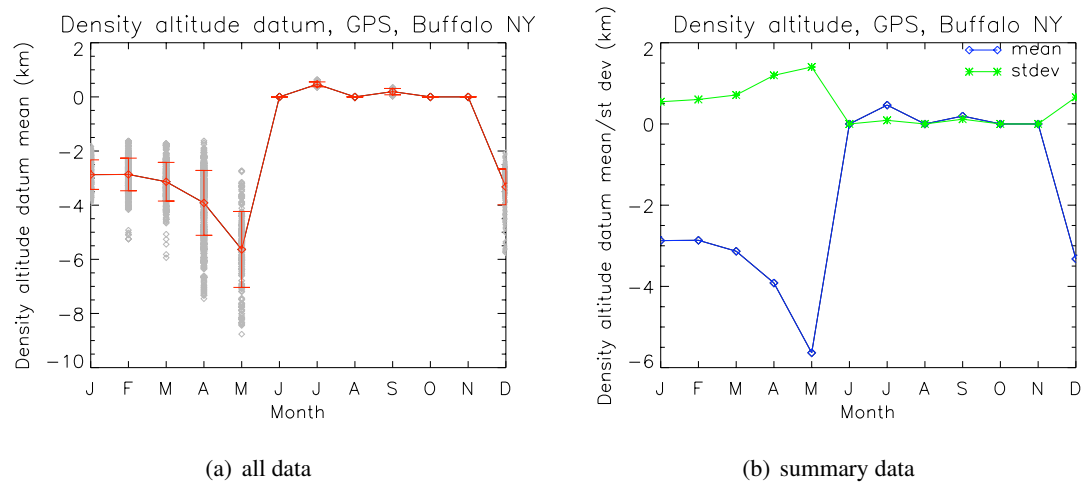


Figure B.5: GPS-based climate model for density altitude.
Note the lack of data between June and November

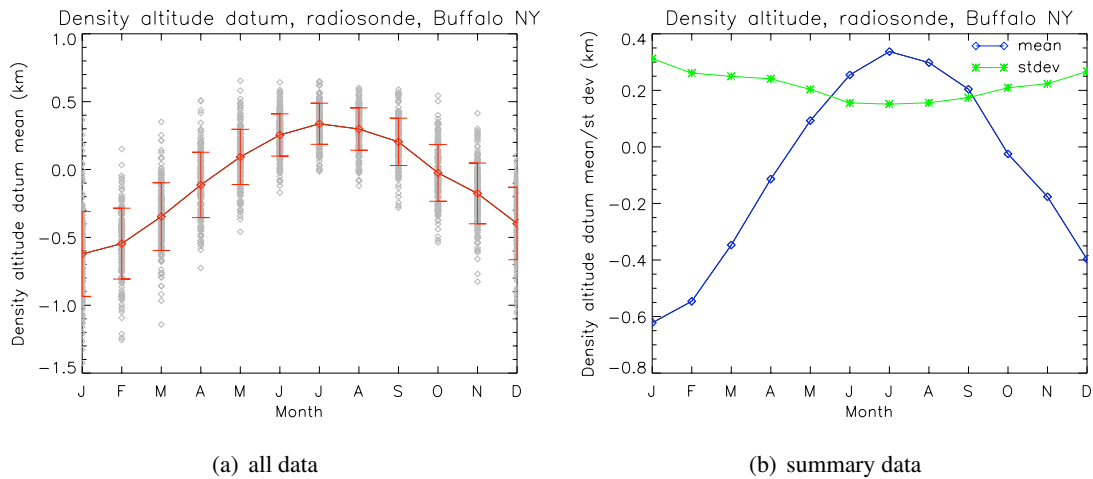


Figure B.6: Radiosonde-based climate model for density altitude

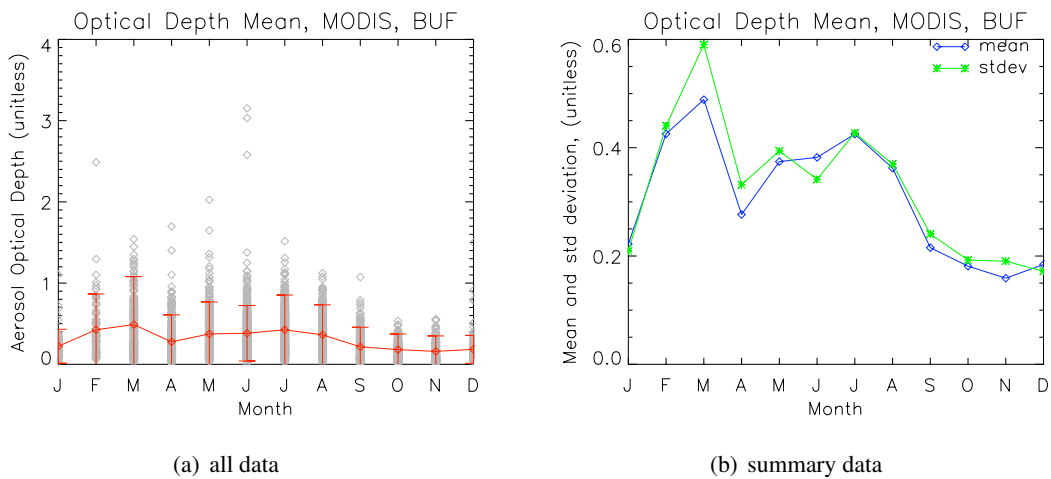


Figure B.7: MODIS-based climate model for aerosols

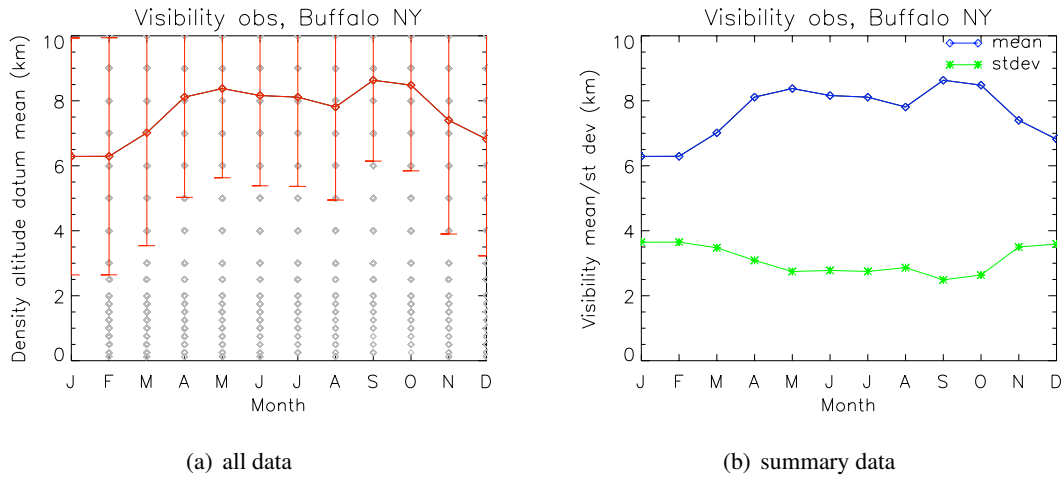


Figure B.8: Airport observation-based climate model for visibility

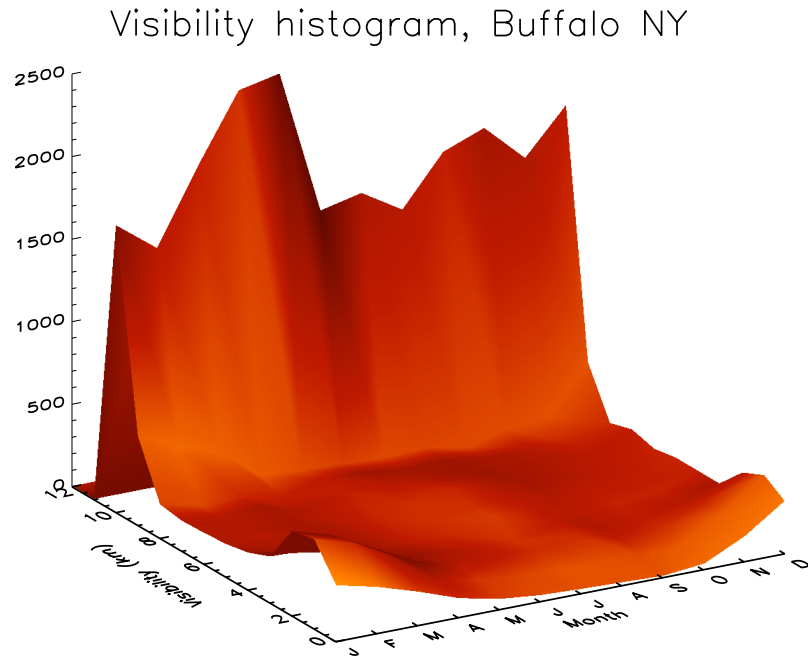


Figure B.9: Airport observation-based visibility histogram

Appendix C

Environmental Effect Modeling Results

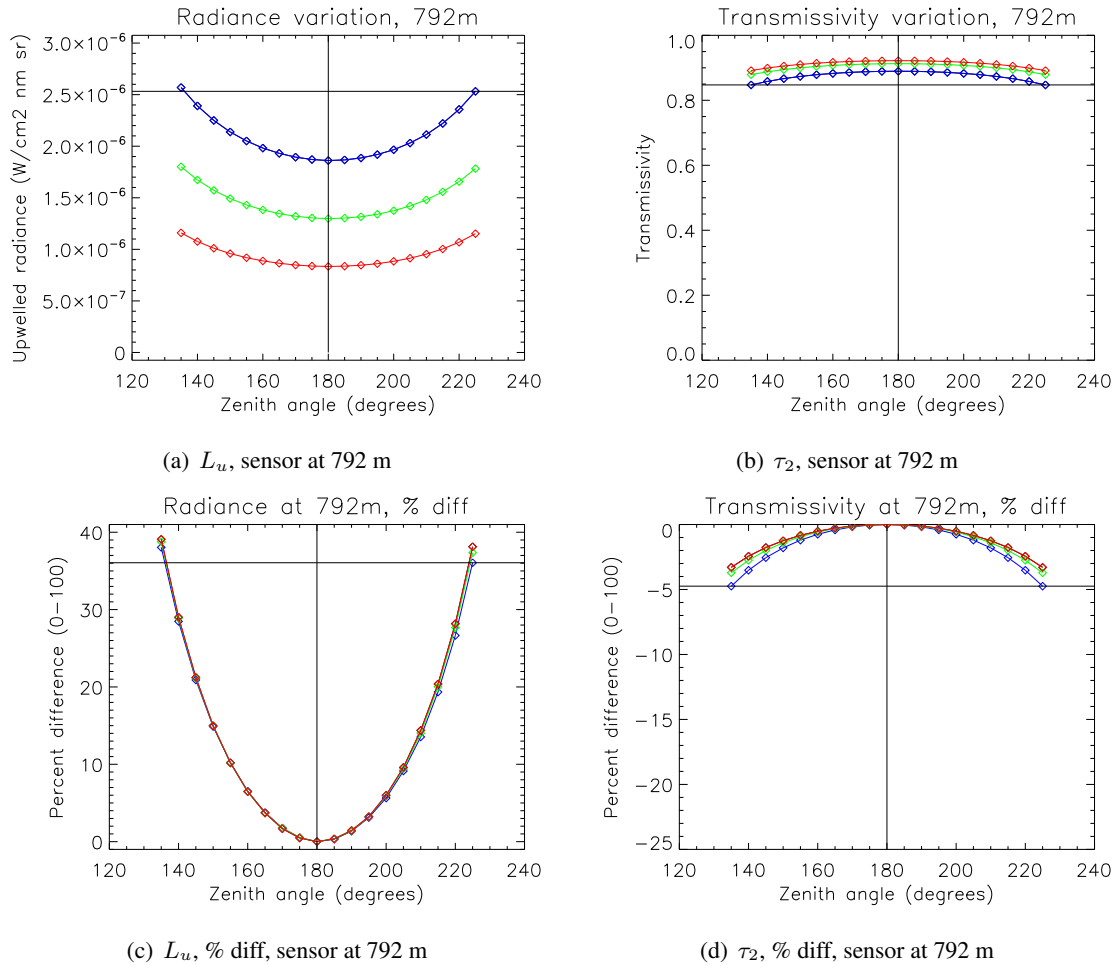


Figure C.1: Radiance and transmission variation due to off-nadir pointing at selected wavelengths.
Line color corresponds to blue (450 nm), green (550 nm), and red (650 nm) wavelengths.

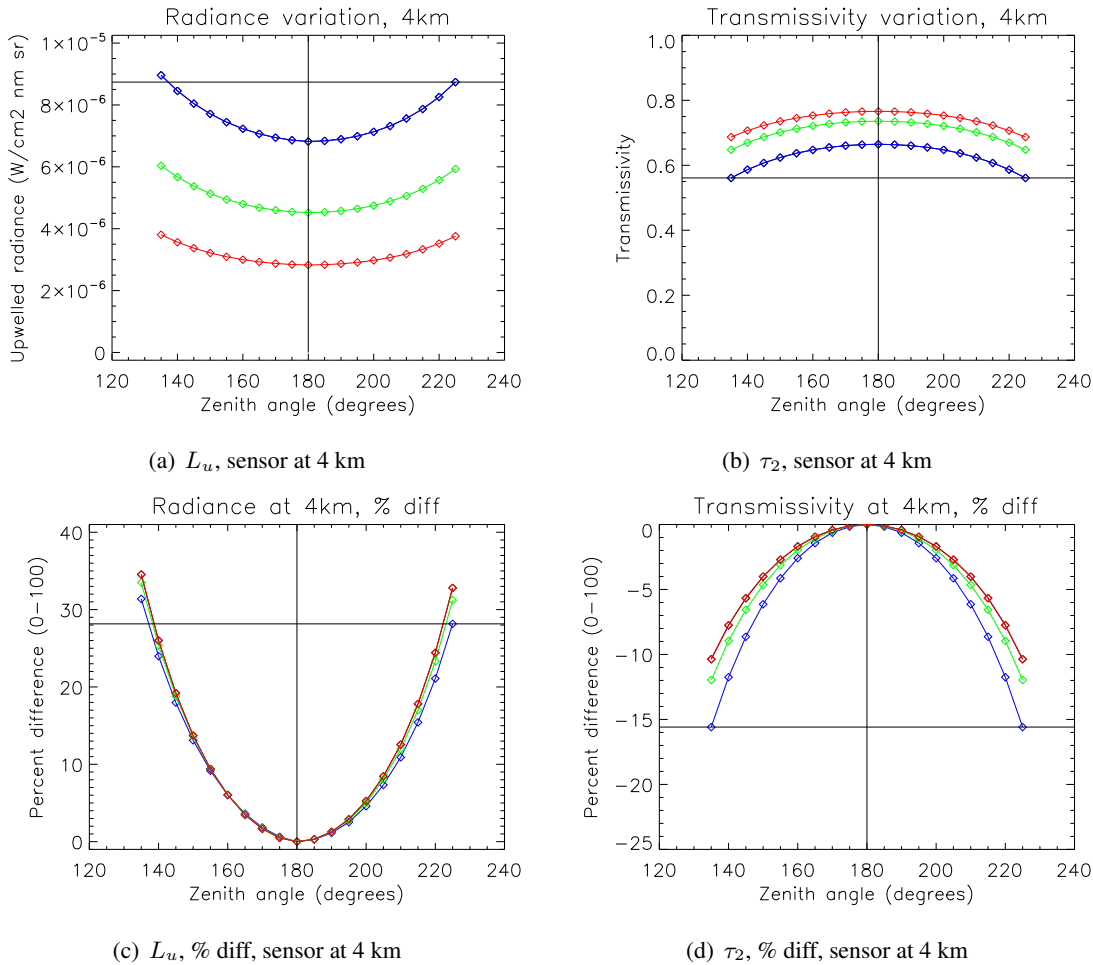


Figure C.2: Radiance and transmission variation due to off-nadir pointing at selected wavelengths.
Line color corresponds to blue (450 nm), green (550 nm), and red (650 nm) wavelengths.

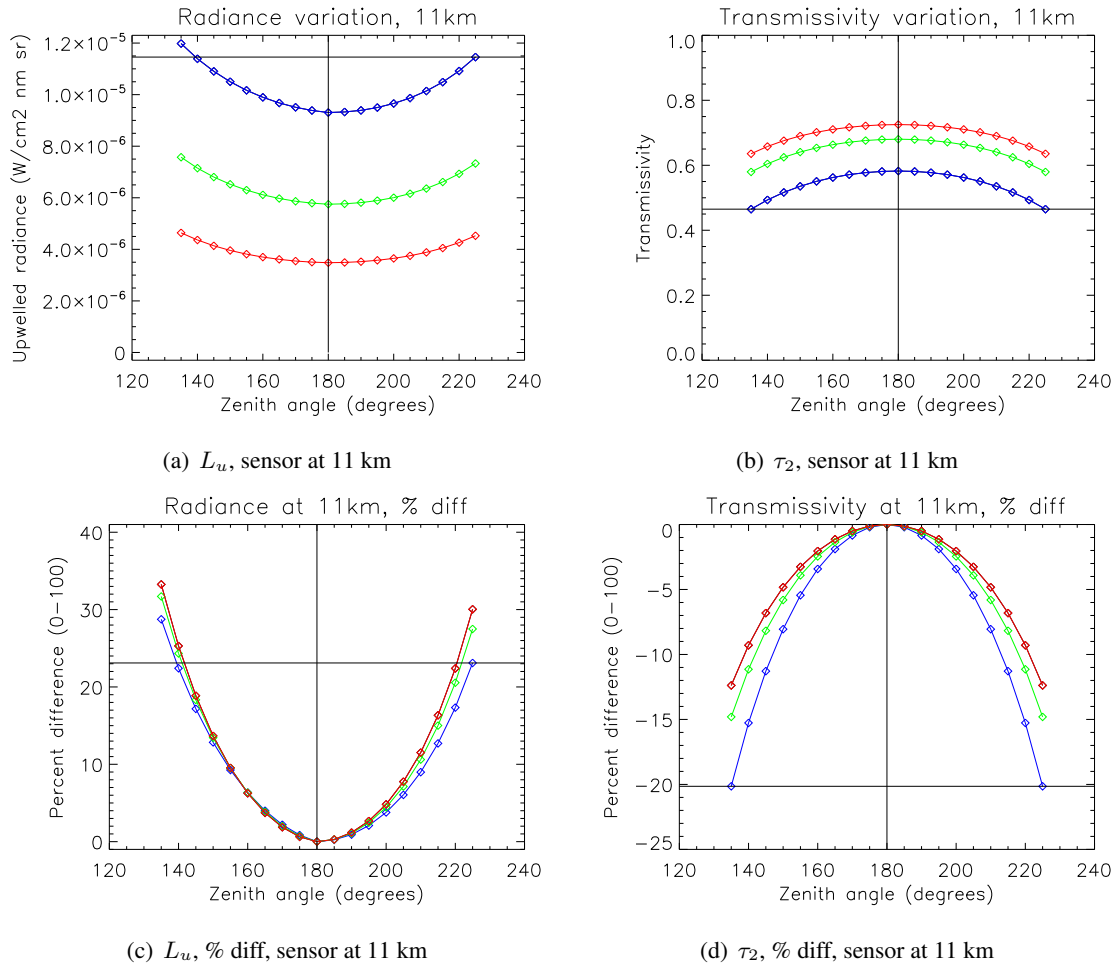


Figure C.3: Radiance and transmission variation due to off-nadir pointing at selected wavelengths.
Line color corresponds to blue (450 nm), green (550 nm), and red (650 nm) wavelengths.

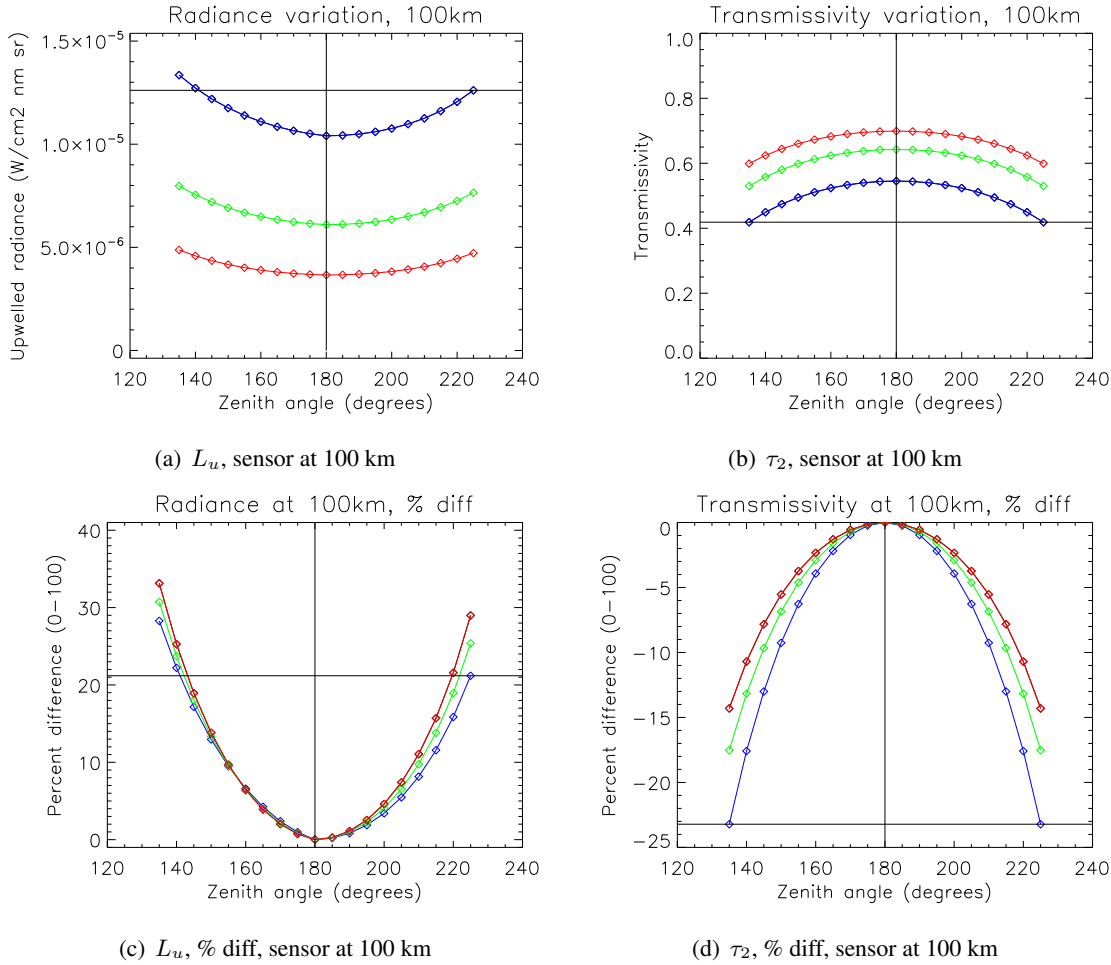


Figure C.4: Radiance and transmission variation due to off-nadir pointing at selected wavelengths.
Line color corresponds to blue (450 nm), green (550 nm), and red (650 nm) wavelengths.

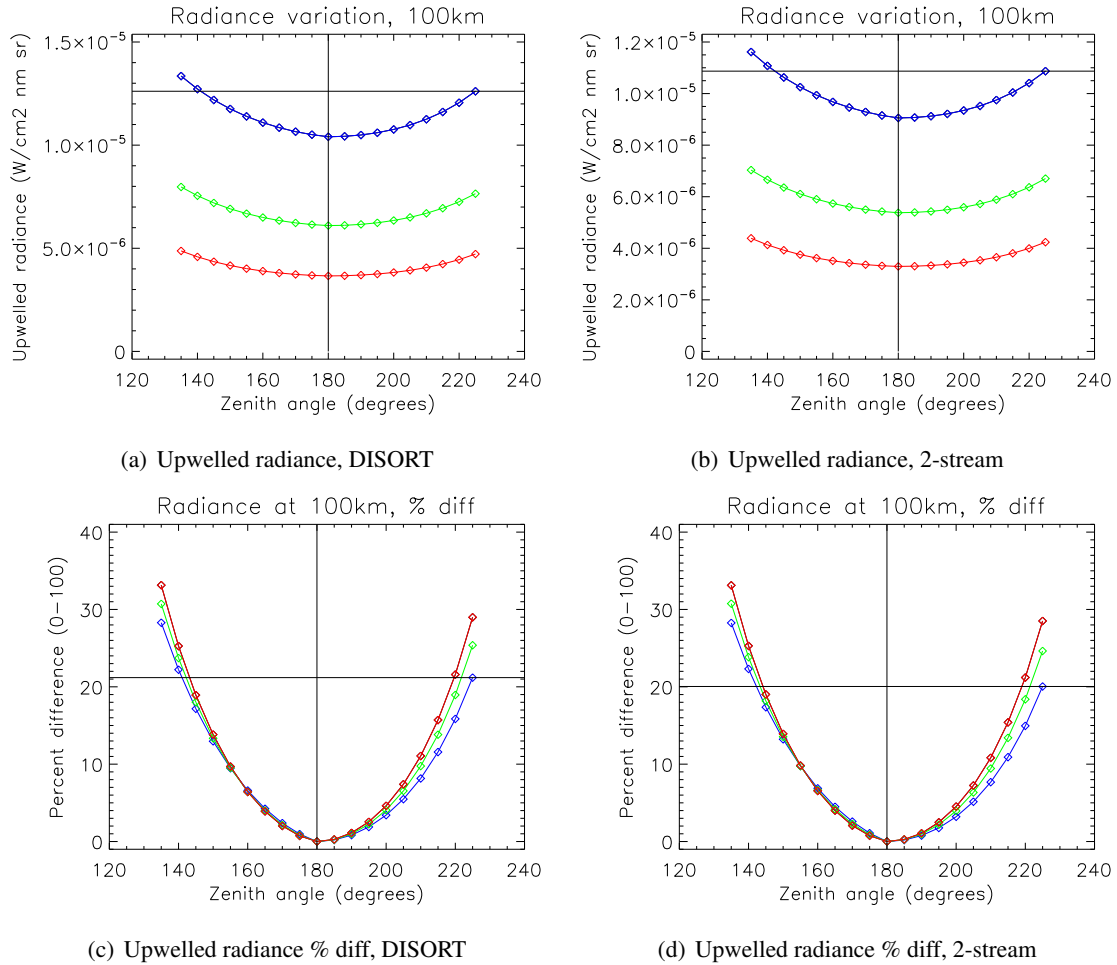


Figure C.5: Multiple scattering algorithm effect on off-nadir pointing, shown at 100 km altitude.

Line color corresponds to blue (450 nm), green (550 nm), and red (650 nm) wavelengths. A discrepancy of approximately 1% is visible for the 450 nm curve. Transmissivity is not affected in MODTRAN's implementation.

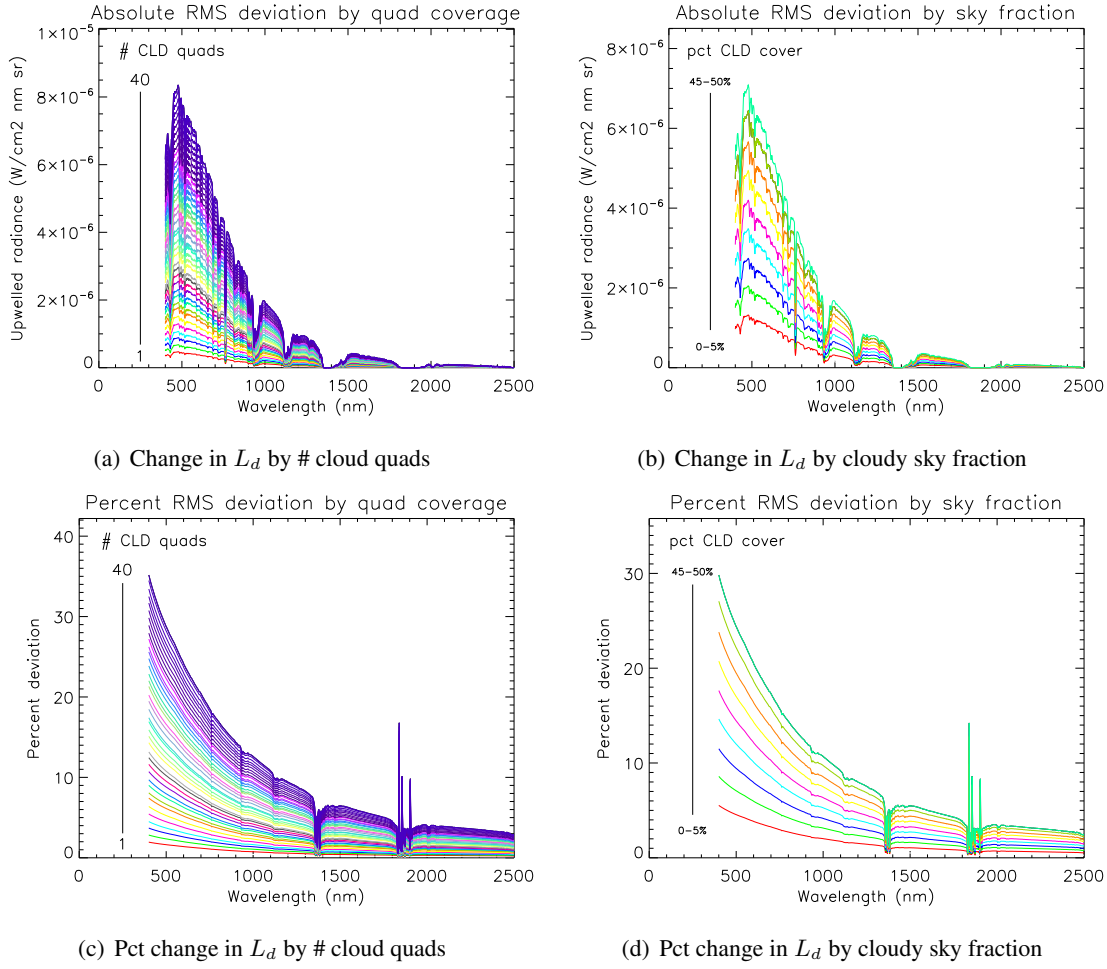


Figure C.6: Cumulus cloud modeling results using 72 total sky quads, with up to 40 filled with absorbing, scattering, and reflecting clouds. For figures C.6(a) and C.6(c), the smallest curve corresponds to 1 filled quad, increasing to 40 filled quads for the largest curve. For figures C.6(b) and C.6(d), the smallest curve corresponds to a 0–5% cloud cover bin, with bin value increasing by 5% per curve to a maximum bin size of 45–50% cloud cover.

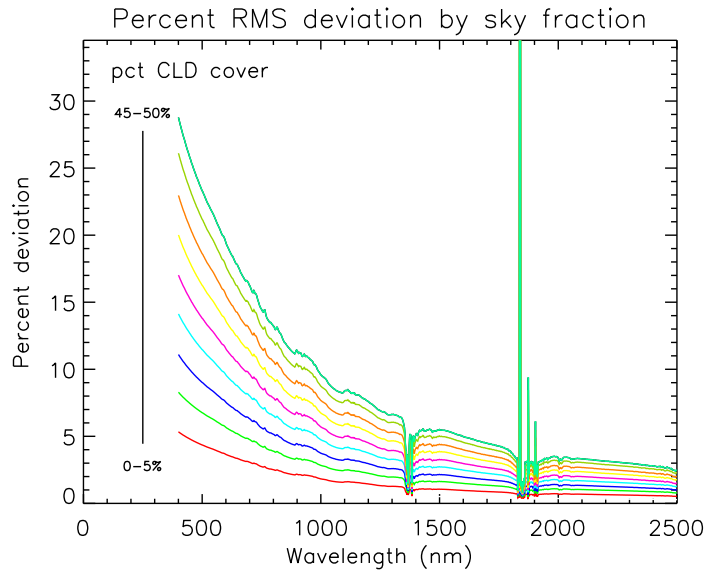
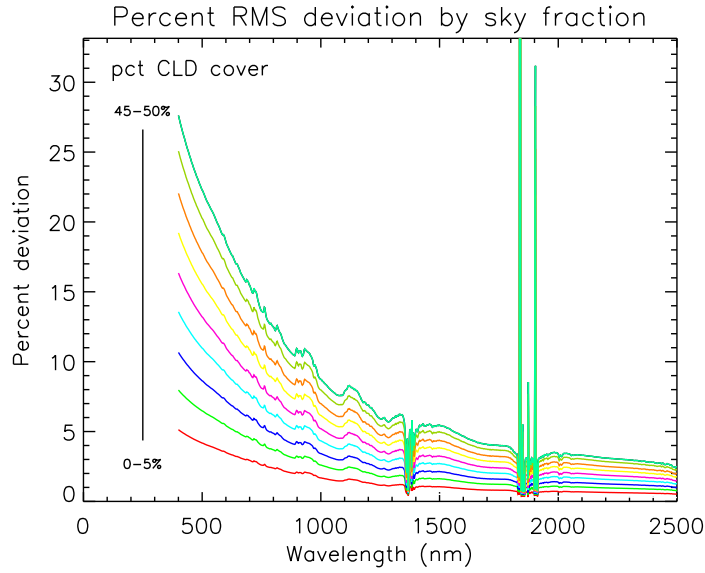
(a) Pct change in L_d , altostratus(b) Pct change in L_d , stratus

Figure C.7: Comparison between cumulus with stratus cloud types for effect on L_d . Compare to figure C.6(d). The smallest curve corresponds to a 0–5% cloud cover bin, with bin value increasing by 5% per curve to a maximum bin size of 45–50% cloud cover.

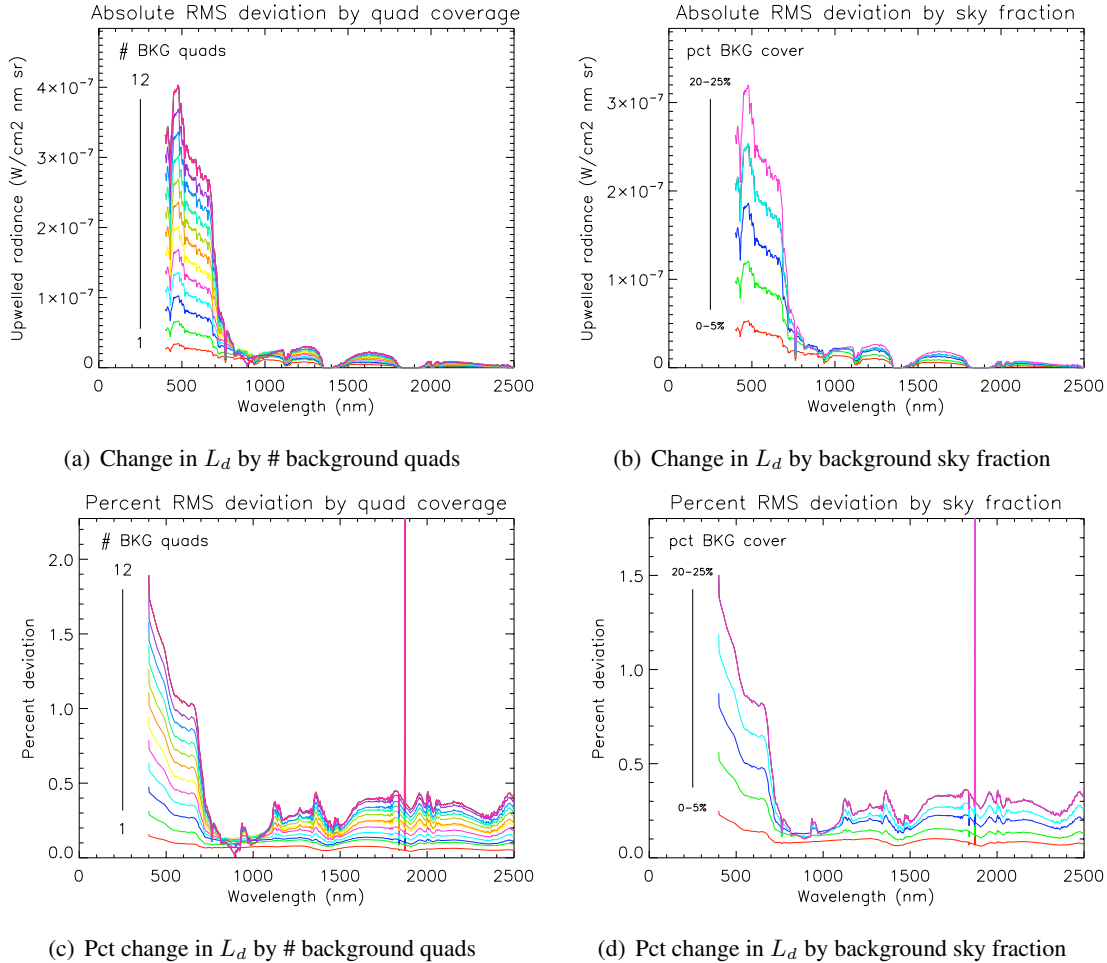


Figure C.8: Background object modeling results using 72 total sky quads, with up to 12 filled with a linearly-mixed composite background object. For figures C.8(a) and C.8(c), the smallest curve corresponds to 1 filled quad, increasing to 12 filled quads for the largest curve. For figures C.8(b) and C.8(d), the smallest curve corresponds to a bin of 0–5% sky masked by terrain, with bin value increasing by 5% per curve to a maximum bin size of 20–25% terrain masking.

Appendix D

Atmospheric Uncertainty Results

This appendix contains results for the atmospheric uncertainty scenarios listed in table 5.8. The legend below gives the color coding of the component curves. Each scenario was run for a 100% reflector and a 20% reflector. Results include a plot showing random reflectance error (along with the contributions from each modeling output) and a plot showing all of the individual correlation terms. Figure D.1 is the color legend for the reflectance error plots, and figure D.2 is the color legend for the correlation plots.

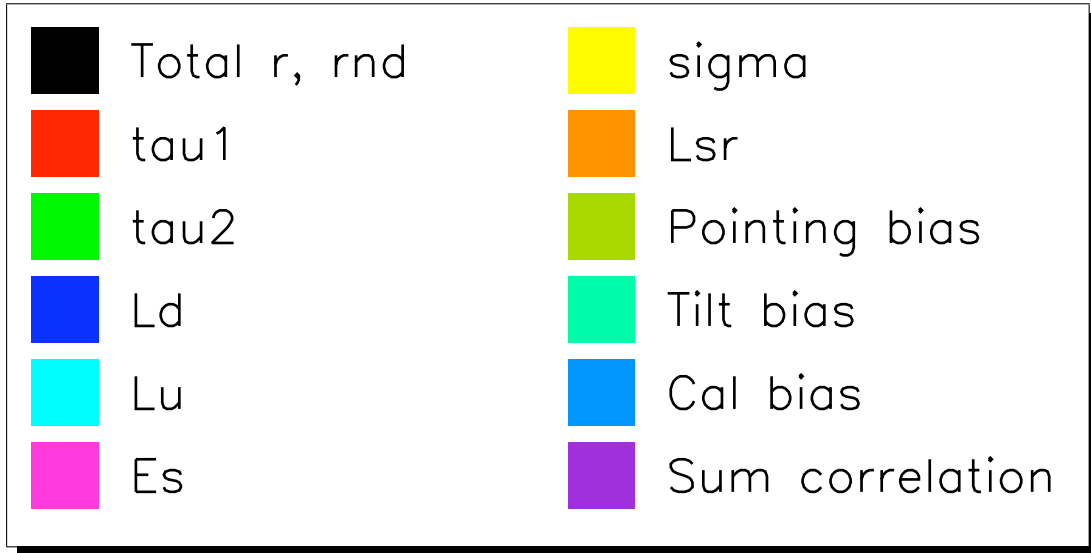


Figure D.1: Legend for reflectance results

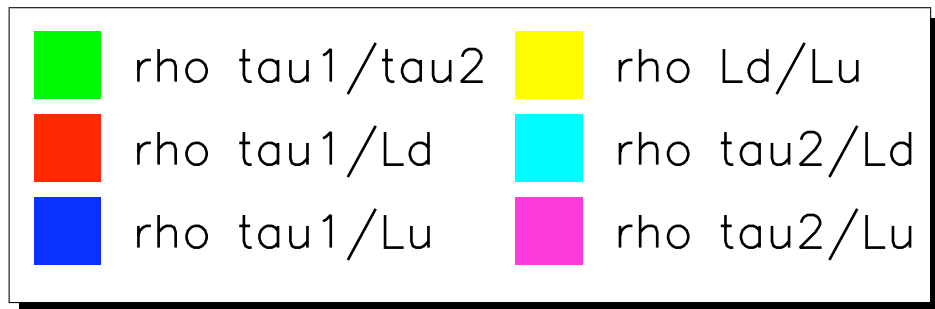


Figure D.2: Legend for correlation results

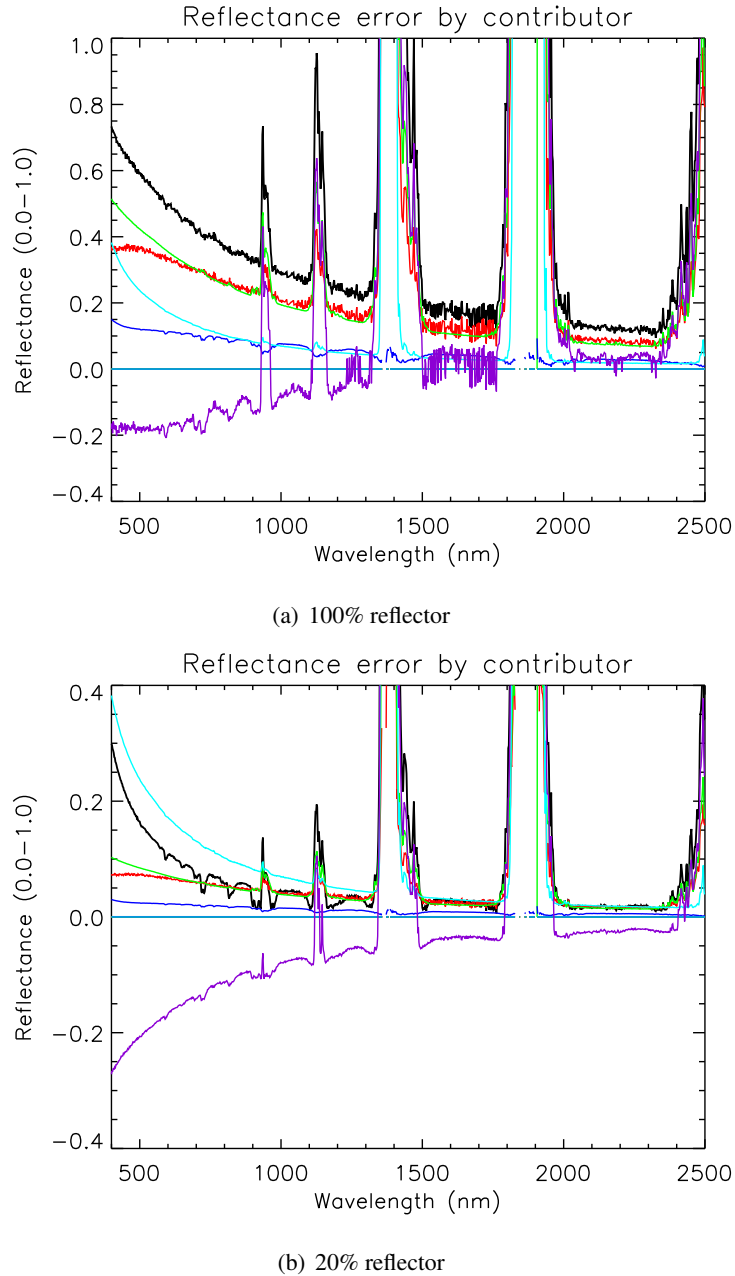


Figure D.3: Scenario 1 (*a priori* knowledge climatology inputs) – Total reflectance uncertainty (black curve) and contributing factors. Color coding for contributors: red = τ_1 , green = τ_2 , blue = L_d , cyan = L_u , and violet = sum of all correlation terms. Also see figure D.1.

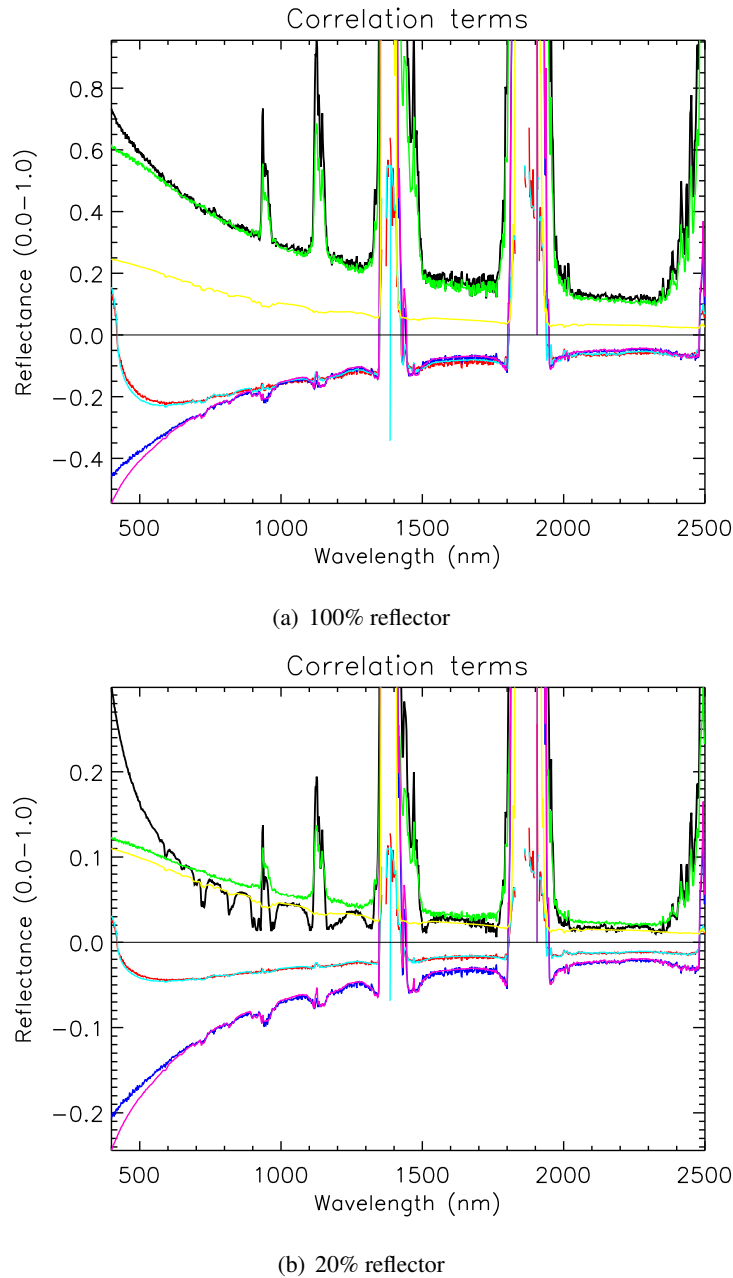


Figure D.4: Scenario 1 (*a priori* knowledge climatology inputs) – Individual correlation terms alongside total reflectance uncertainty (black curve). Color coding for correlations: green = $\rho_{(\tau_1, \tau_2)}$, red = $\rho_{(\tau_1, L_d)}$, blue = $\rho_{(\tau_1, L_u)}$, yellow = $\rho_{(L_d, L_u)}$, cyan = $\rho_{(\tau_2, L_d)}$, and magenta = $\rho_{(\tau_2, L_u)}$. Also see figure D.2.

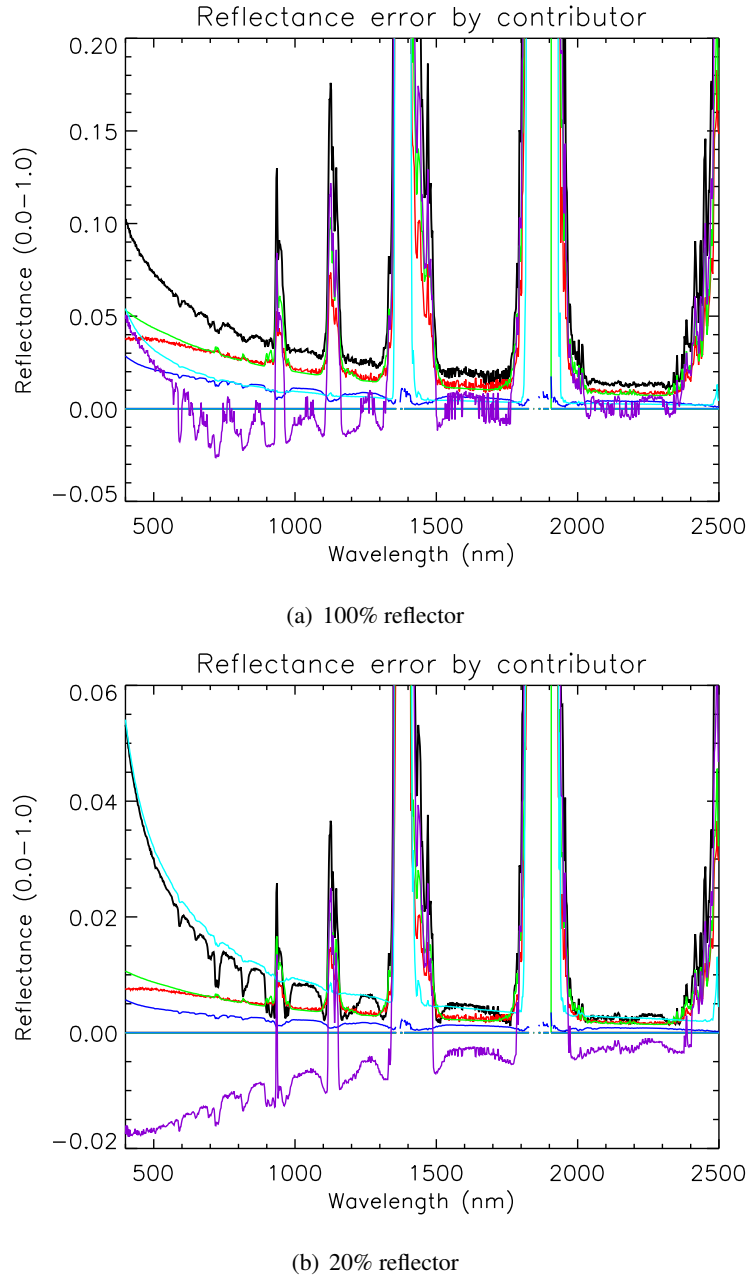


Figure D.5: Scenario 2 (inputs from commercial quality instrumentation) – Total reflectance uncertainty (black curve) and contributing factors. Color coding for contributors: red = τ_1 , green = τ_2 , blue = L_d , cyan = L_u , and violet = sum of all correlation terms. Also see figure D.1.

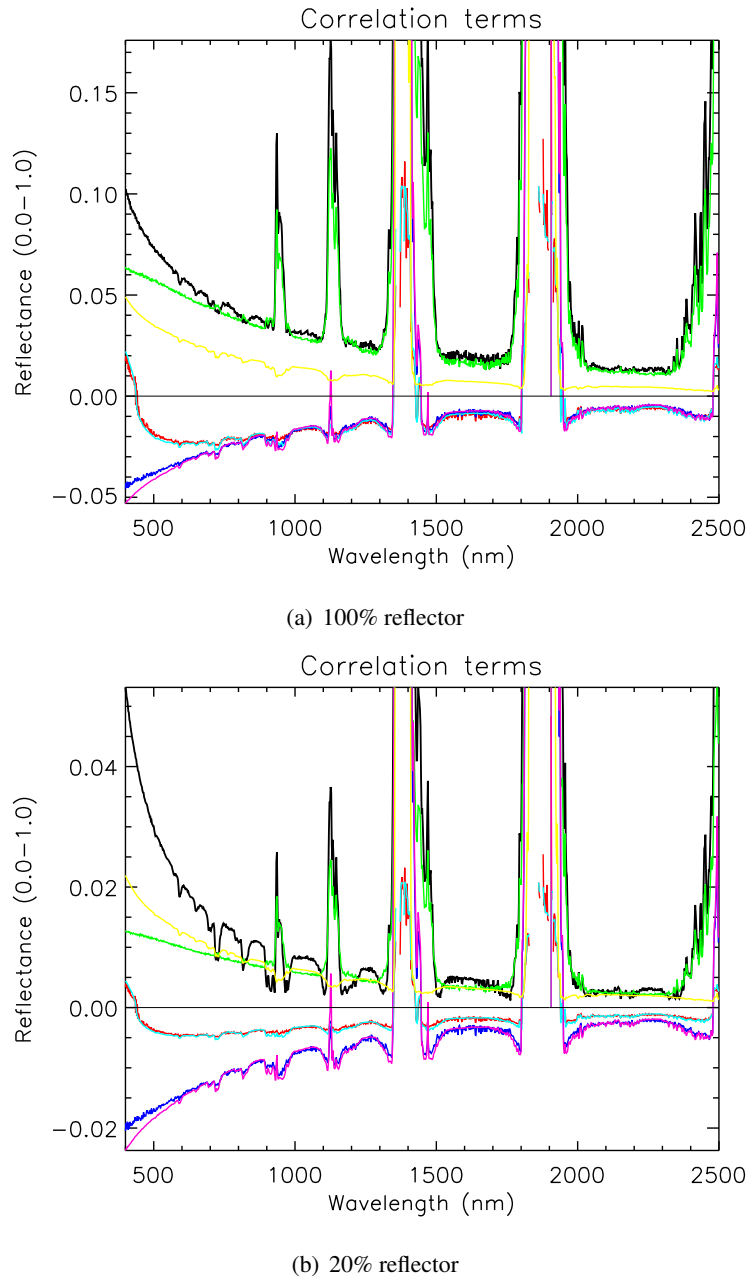


Figure D.6: Scenario 2 (inputs from commercial quality instrumentation) – Individual correlation terms alongside total reflectance uncertainty (black curve). Color coding for correlations: green = $\rho_{(\tau_1, \tau_2)}$, red = $\rho_{(\tau_1, L_d)}$, blue = $\rho_{(\tau_1, L_u)}$, yellow = $\rho_{(L_d, L_u)}$, cyan = $\rho_{(\tau_2, L_d)}$, and magenta = $\rho_{(\tau_2, L_u)}$ Also see figure D.2.

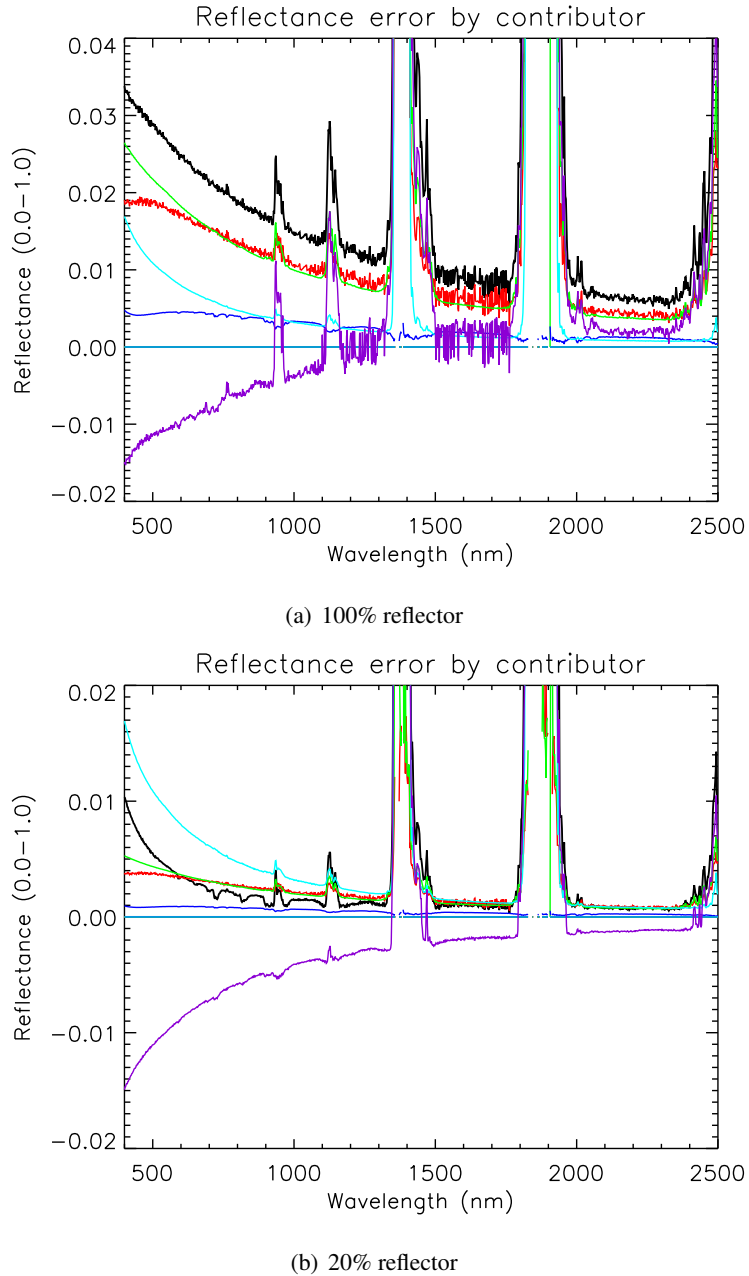


Figure D.7: Scenario 3 (inputs from ARM-grade instrumentation) – Total reflectance uncertainty (black curve) and contributing factors. Color coding for contributors: red = τ_1 , green = τ_2 , blue = L_d , cyan = L_u , and violet = sum of all correlation terms. Also see figure D.1.

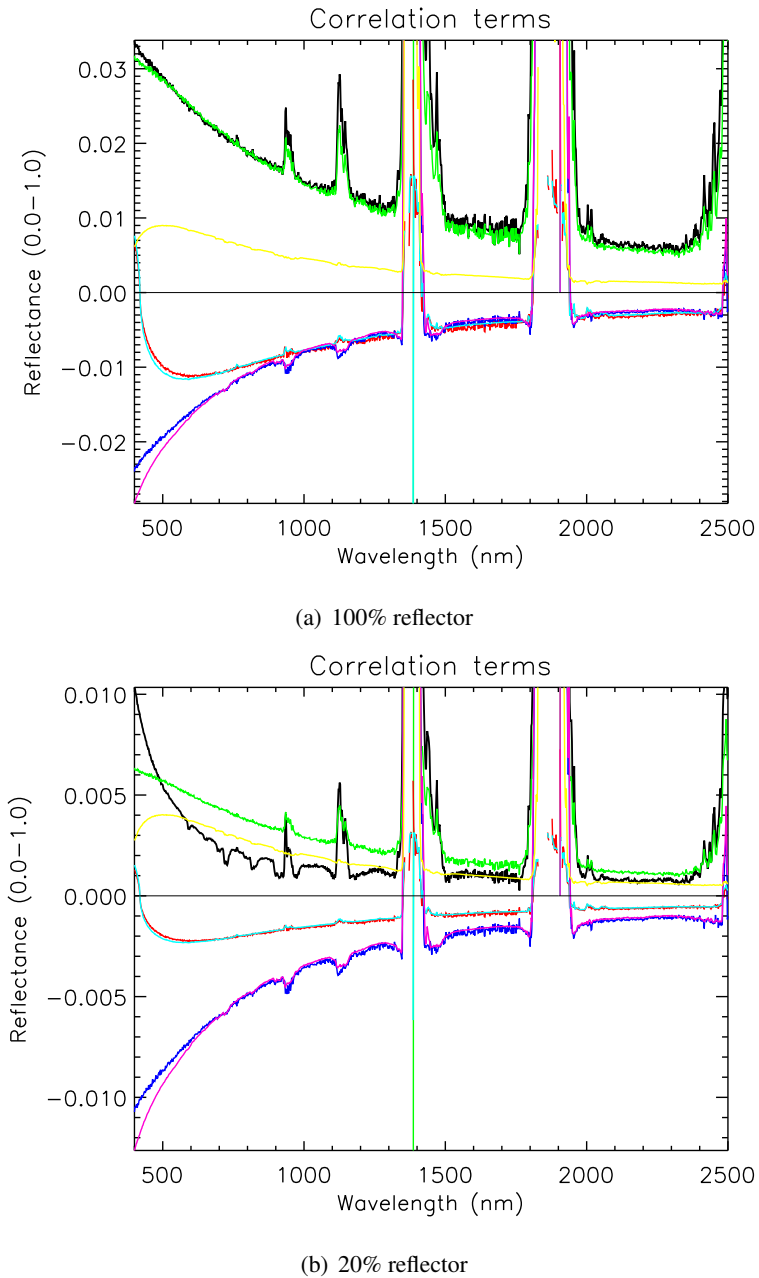


Figure D.8: Scenario 3 (inputs from ARM-grade instrumentation) – Individual correlation terms alongside total reflectance uncertainty (black curve). Color coding for correlations: green = $\rho_{(\tau_1, \tau_2)}$, red = $\rho_{(\tau_1, L_d)}$, blue = $\rho_{(\tau_1, L_u)}$, yellow = $\rho_{(L_d, L_u)}$, cyan = $\rho_{(\tau_2, L_d)}$, and magenta = $\rho_{(\tau_2, L_u)}$. Also see figure D.2.

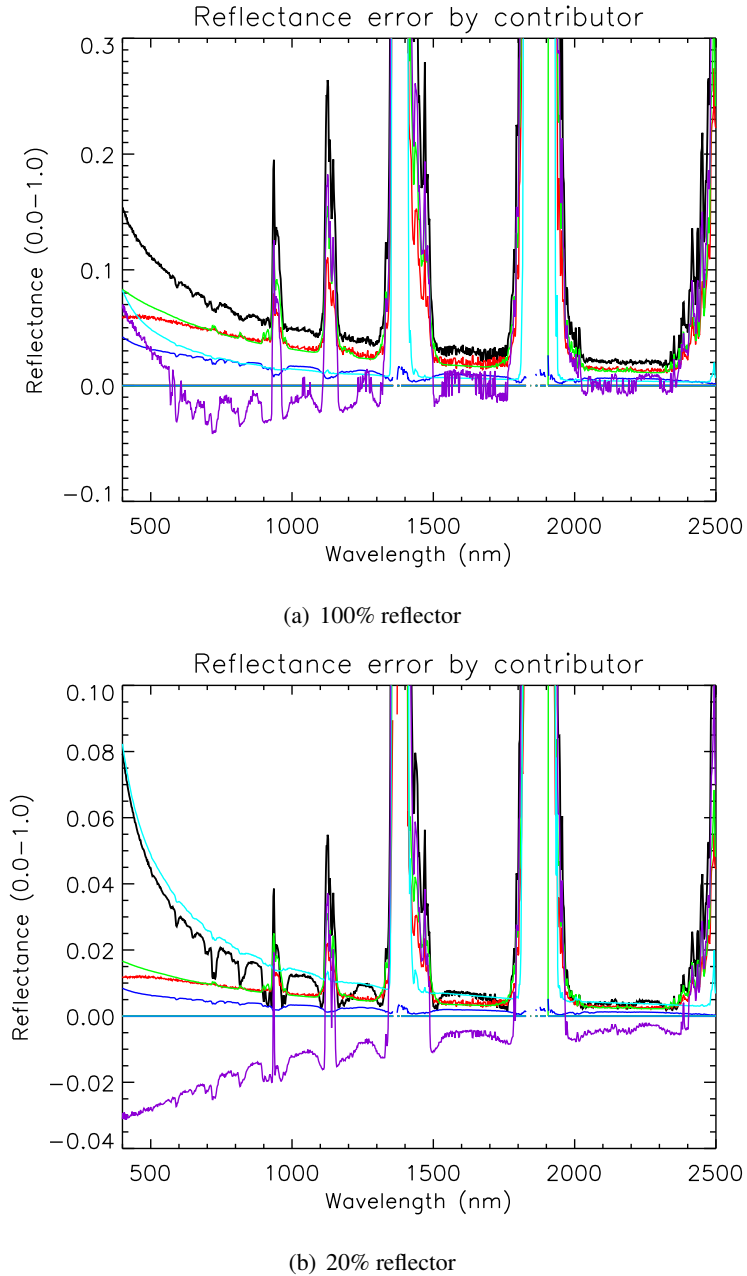


Figure D.9: Scenario 4 (wet atmosphere model inversion results) – Total reflectance uncertainty (black curve) and contributing factors. Color coding for contributors: red = τ_1 , green = τ_2 , blue = L_d , cyan = L_u , and violet = sum of all correlation terms. Also see figure D.1.

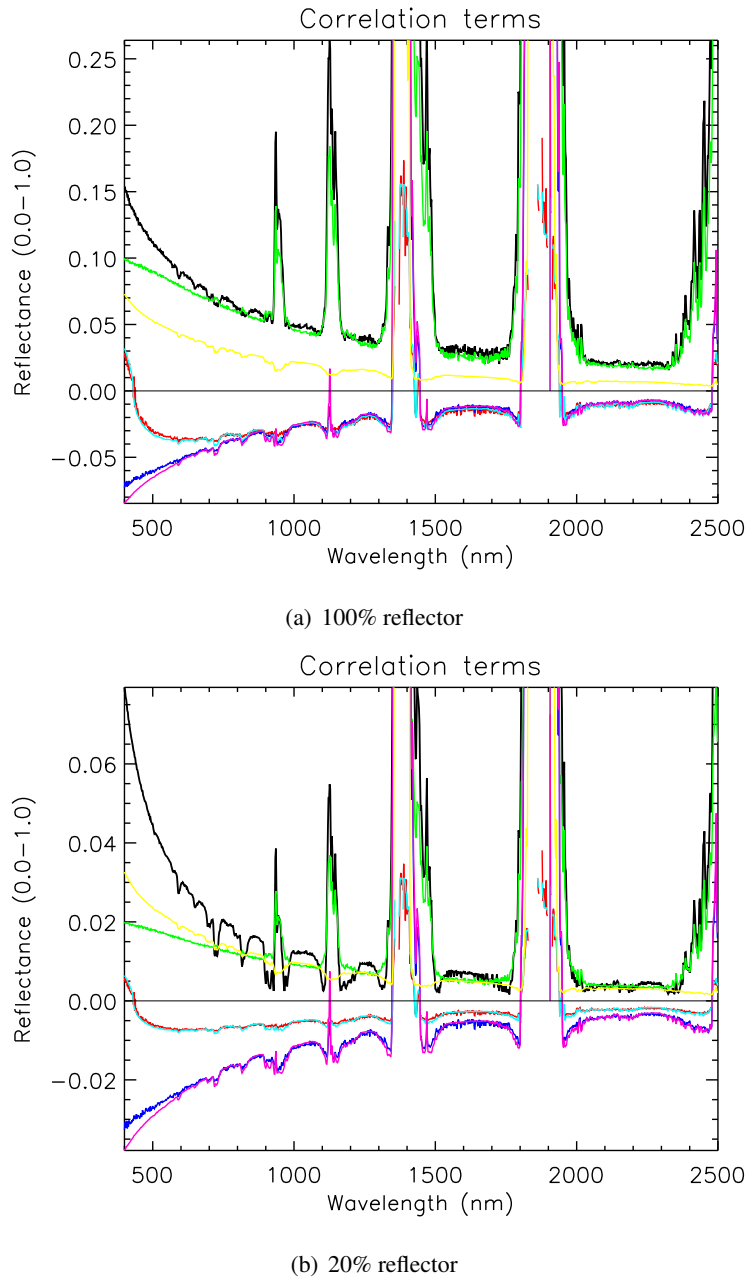


Figure D.10: Scenario 4 (wet atmosphere model inversion results) – Individual correlation terms alongside total reflectance uncertainty (black curve). Color coding for correlations: green = $\rho_{(\tau_1, \tau_2)}$, red = $\rho_{(\tau_1, L_d)}$, blue = $\rho_{(\tau_1, L_u)}$, yellow = $\rho_{(L_d, L_u)}$, cyan = $\rho_{(\tau_2, L_d)}$, and magenta = $\rho_{(\tau_2, L_u)}$. Also see figure D.2.

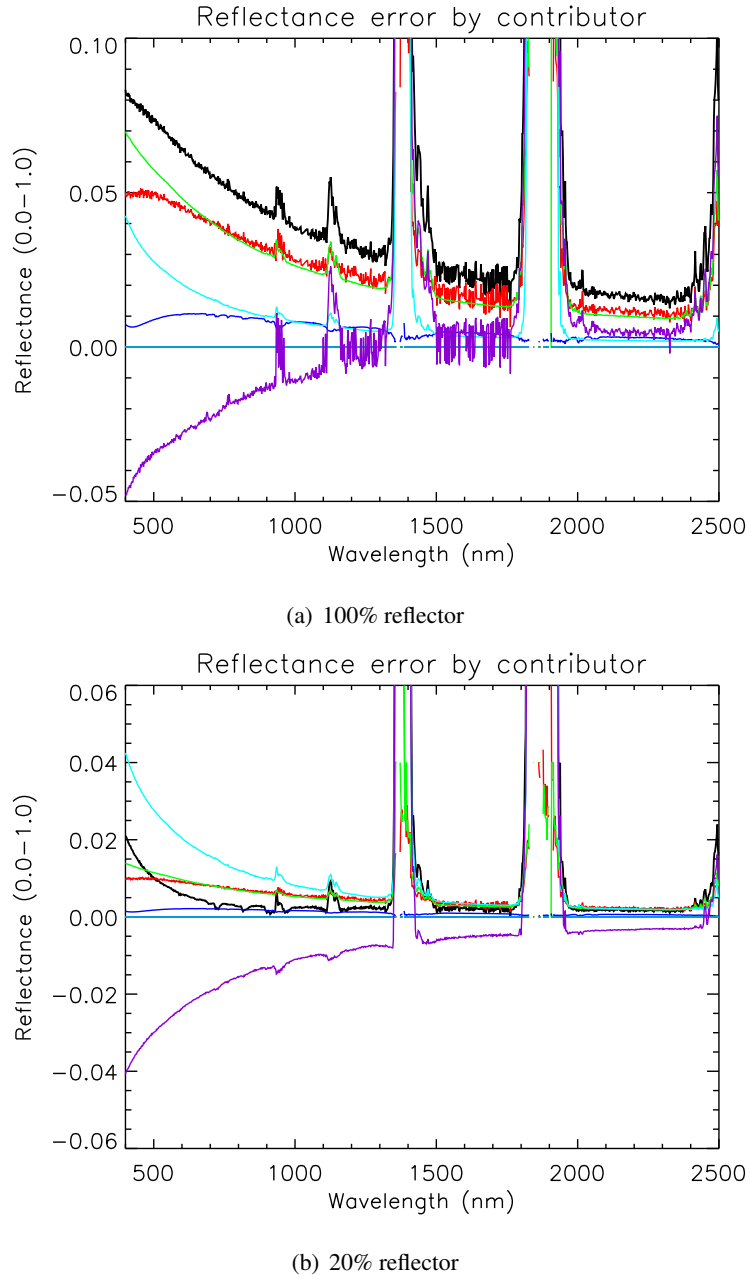


Figure D.11: Scenario 5 (dry atmosphere model inversion results) – Total reflectance uncertainty (black curve) and contributing factors. Color coding for contributors: red = τ_1 , green = τ_2 , blue = L_d , cyan = L_u , and violet = sum of all correlation terms. Also see figure D.1.

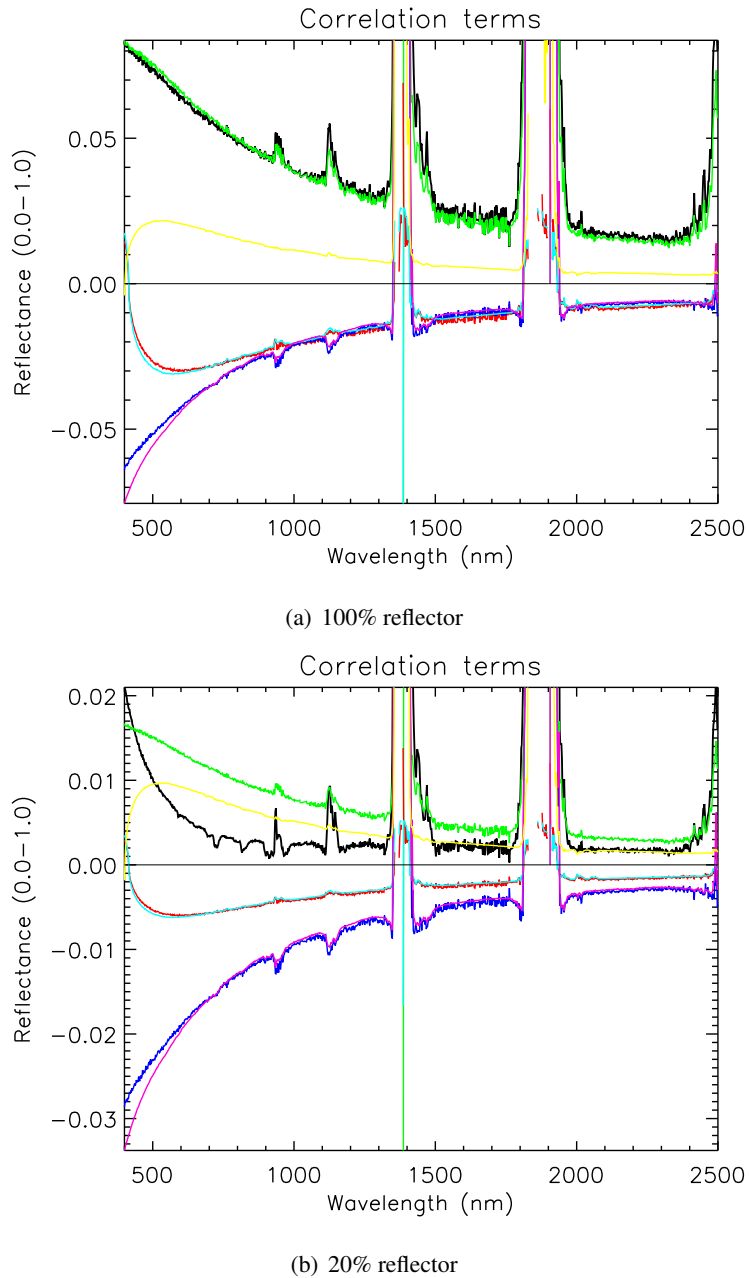


Figure D.12: Scenario 5 (dry atmosphere model inversion results) – Individual correlation terms alongside total reflectance uncertainty (black curve). Color coding for correlations: green = $\rho_{(\tau_1, \tau_2)}$, red = $\rho_{(\tau_1, L_d)}$, blue = $\rho_{(\tau_1, L_u)}$, yellow = $\rho_{(L_d, L_u)}$, cyan = $\rho_{(\tau_2, L_d)}$, and magenta = $\rho_{(\tau_2, L_u)}$. Also see figure D.2.

Appendix E

Environmental Effect Results

This appendix includes total reflectance uncertainty and bias for several major environmental effects. For each effect, a key parameter was varied over a range of values, and the final reflectance results were combined on a single plot for comparison purposes. There is no significance to the colors in these plots other than to provide visual distinction between curves. The black curves generally represent the most extreme value of the set.

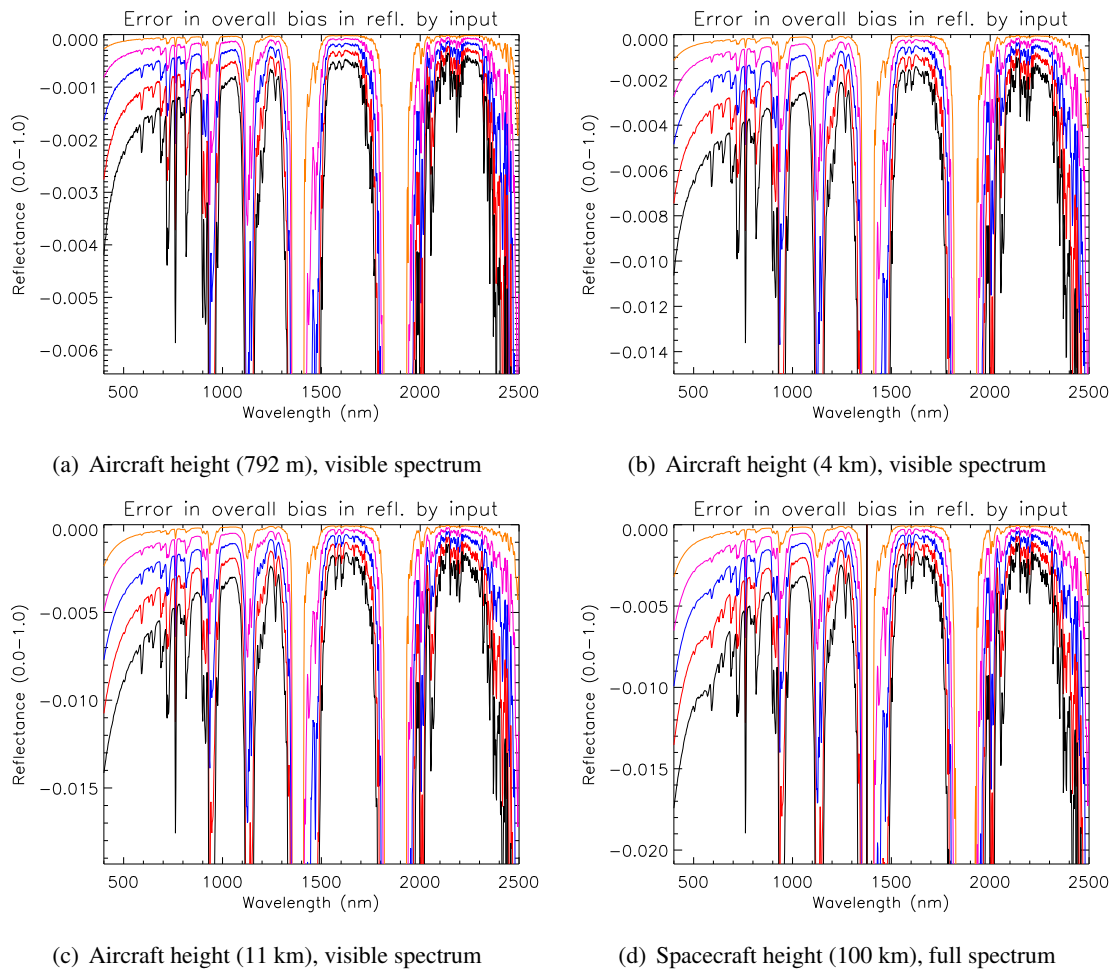


Figure E.1: Scenarios 6-8, bias error for a 100% reflector caused by off-nadir pointing effects
Nadir angles are 0° , 3° , 6° , 9° , 12° , and 15°

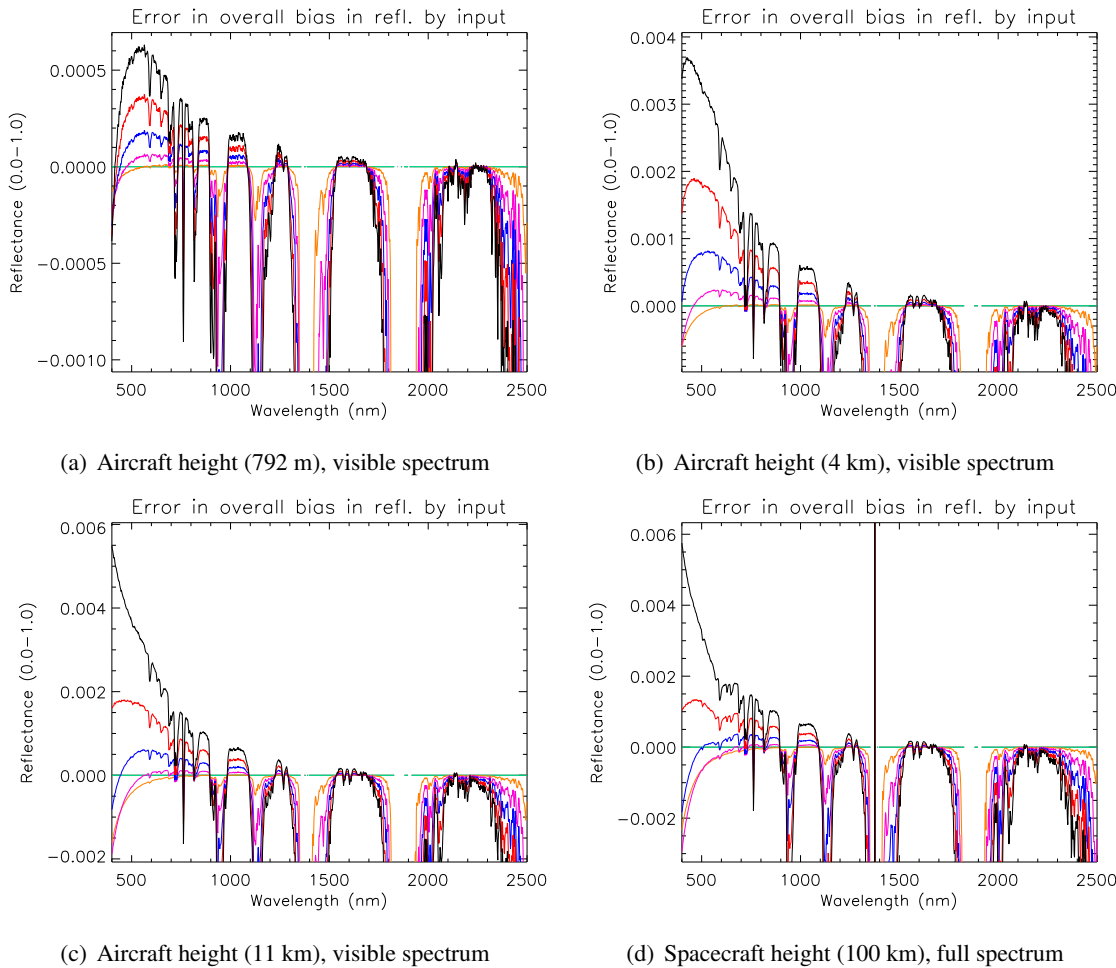


Figure E.2: Scenarios 6-8, bias error for a 20% reflector caused by off-nadir pointing effects
Nadir angles are 0° , 3° , 6° , 9° , 12° , and 15°

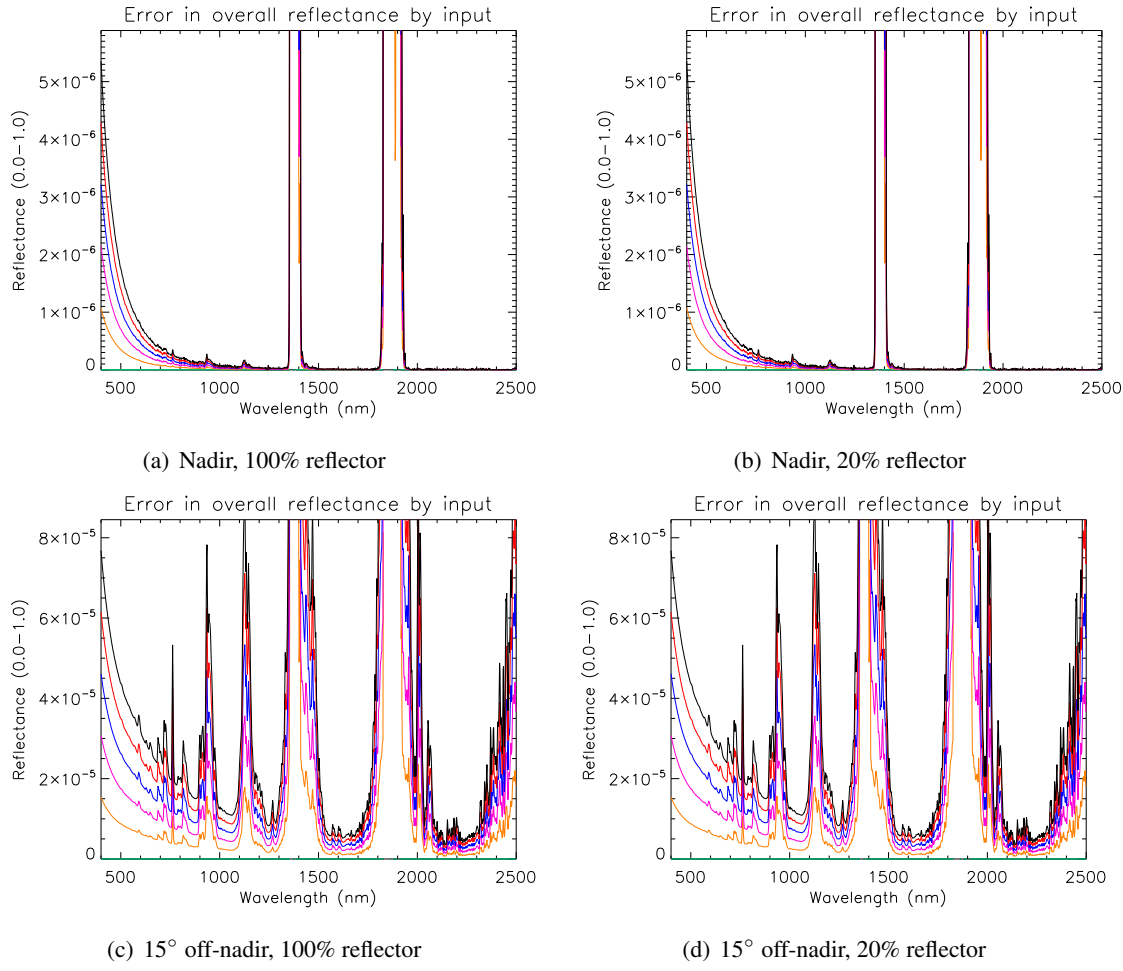


Figure E.3: Scenarios 9-10, random error caused by pointing angle uncertainty.

Note that off-nadir bias error is not shown, but it is consistent with figure E.1.

Pointing uncertainty is 0° , 0.2° , 0.4° , 0.6° , 0.8° , and 1.0°

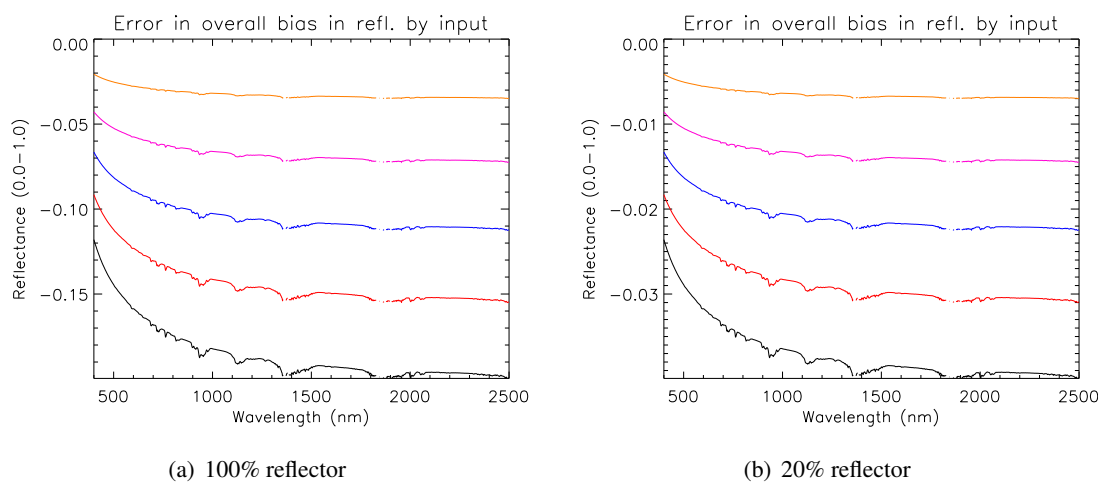


Figure E.4: Scenario 11, bias error caused by ground tilt
Ground tilt (angle from normal) is $0^\circ, 3^\circ, 6^\circ, 9^\circ, 12^\circ$, and 15°

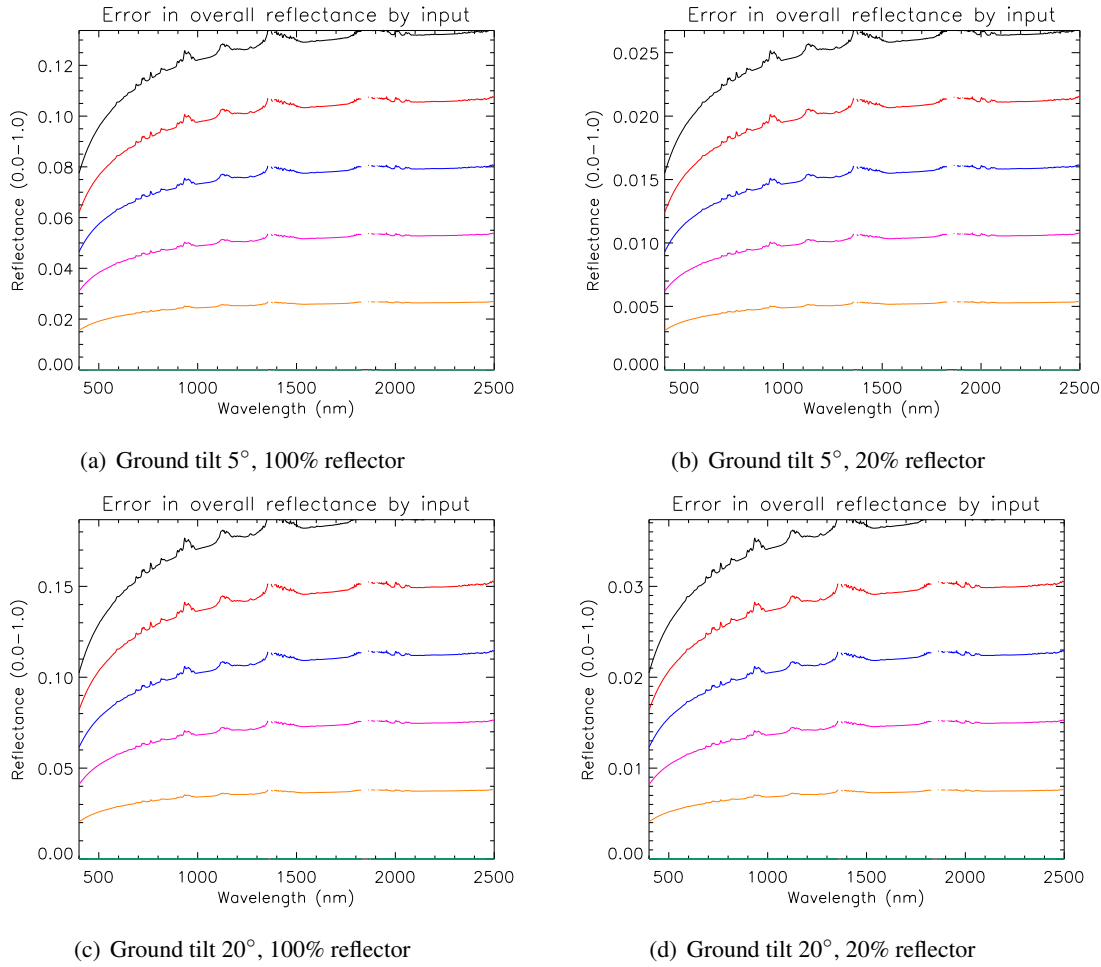


Figure E.5: Scenarios 12-13, random error caused by ground tilt angle uncertainty. Note that bias error is not shown, but it is consistent with figure E.4. Ground tilt knowledge uncertainty is 0° , 2° , 4° , 6° , 8° , and 10°

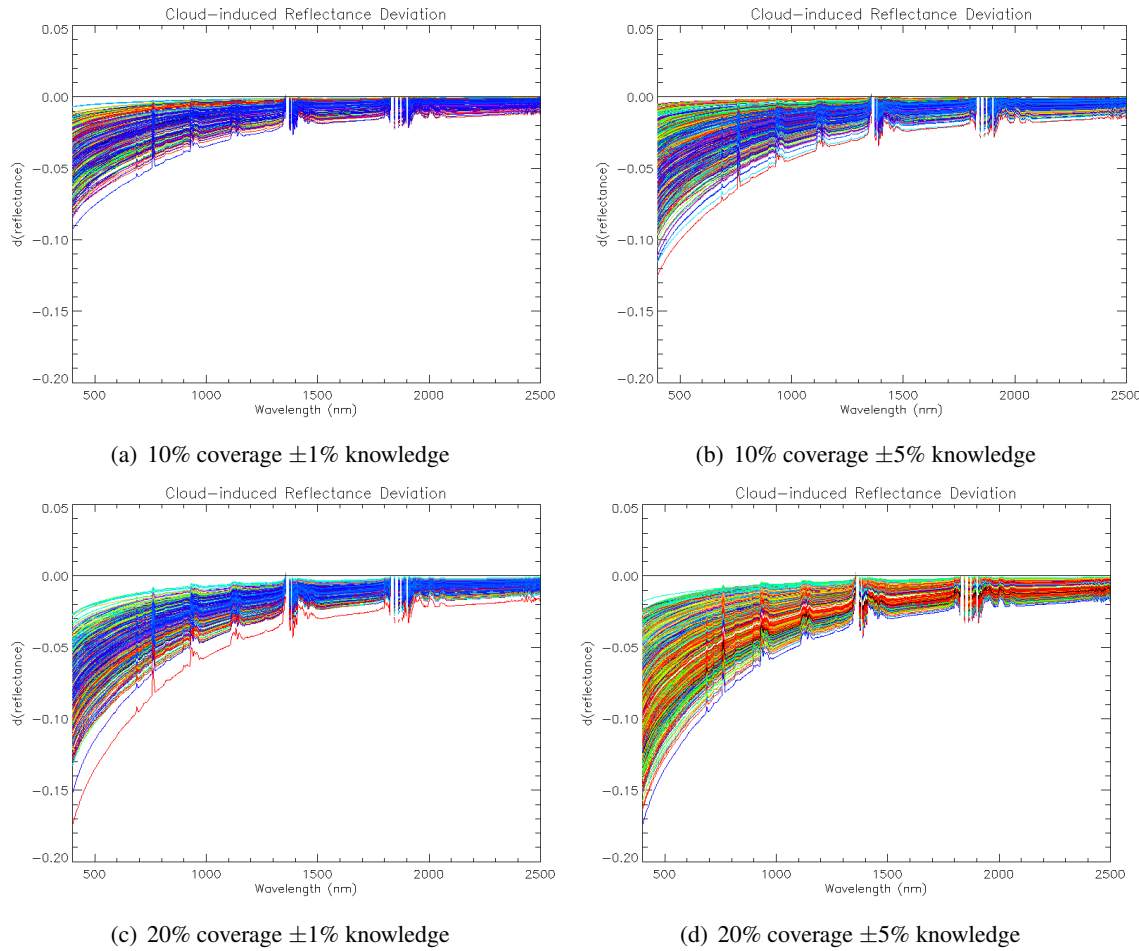


Figure E.6: Scenarios 14-15, cloud object bias error, for a 100% reflector. The spread reflects reflectance bias due to the range of possible cumulus cloud configurations. These results show bias errors for 10% and 20% cloud cover, $\pm 1\%$ and $\pm 5\%$, over a spectrally flat ground target with 100% reflectance

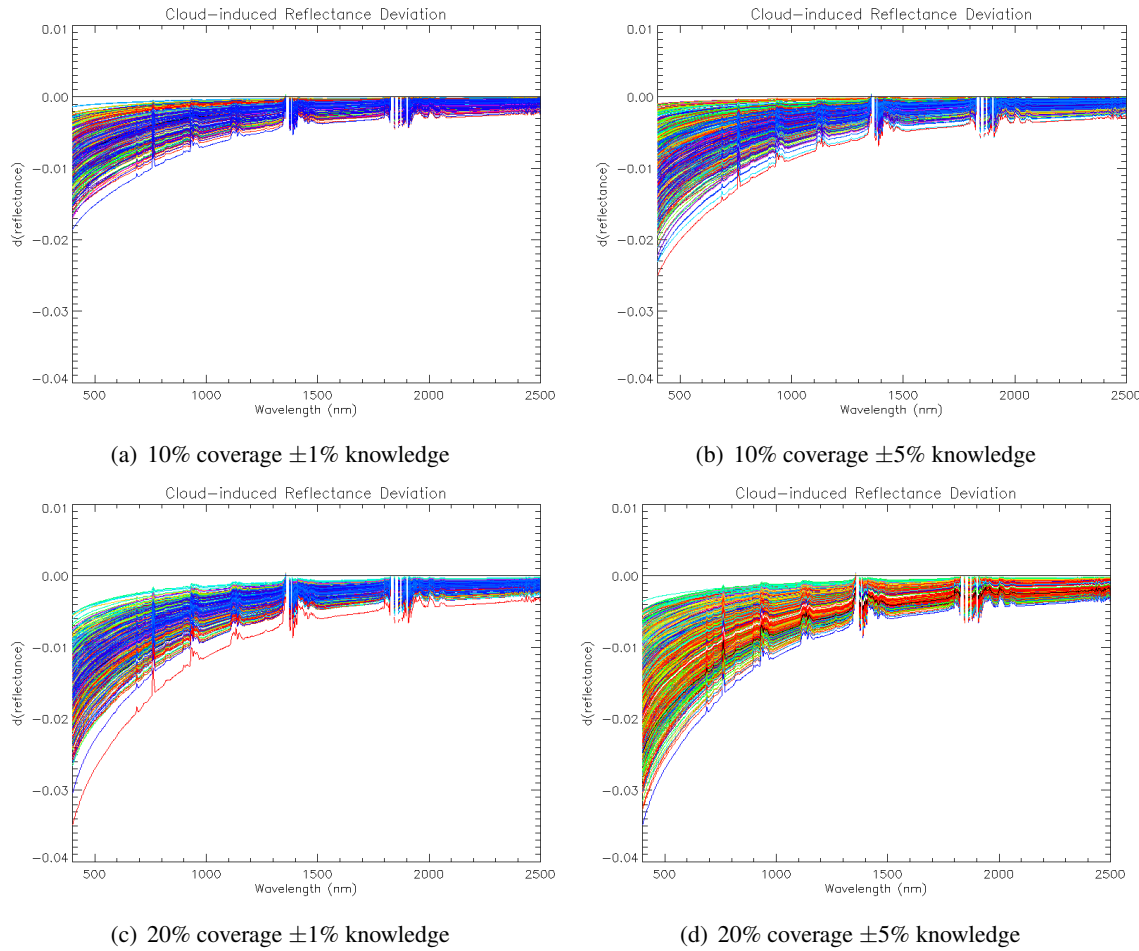


Figure E.7: Scenarios 14-15, cloud object bias error, for a 20% reflector. The spread reflects reflectance bias due to the range of possible cumulus cloud configurations. These results show bias errors for 10% and 20% cloud cover, $\pm 1\%$ and $\pm 5\%$, over a spectrally flat ground target with 20% reflectance

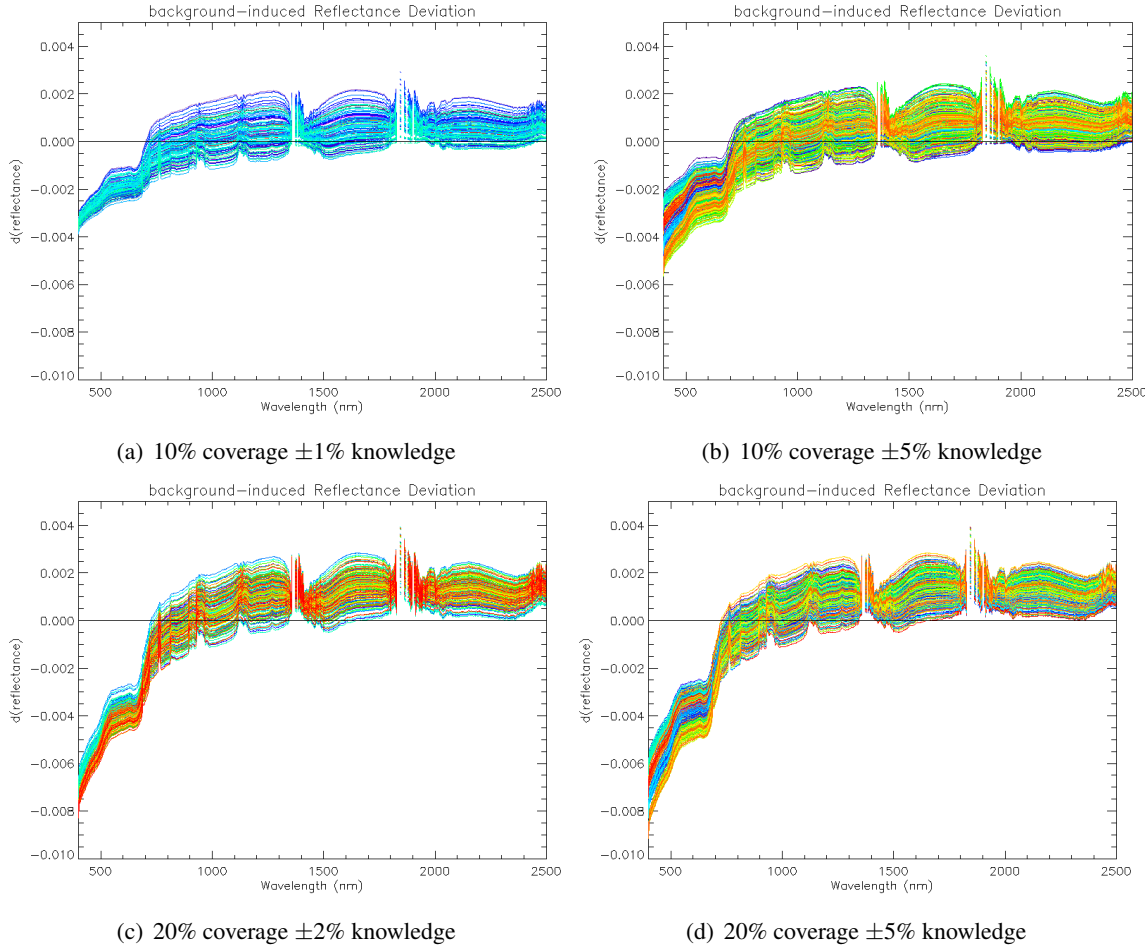


Figure E.8: Scenarios 16-17, background object bias error, for a 100% reflector. The spread reflects reflectance bias due to the range of possible low-elevation background object configurations. These results show bias errors for 10% and 20% terrain masking, $\pm 1\%-2\%$ and $\pm 5\%$, over a spectrally flat ground target with 100% reflectance

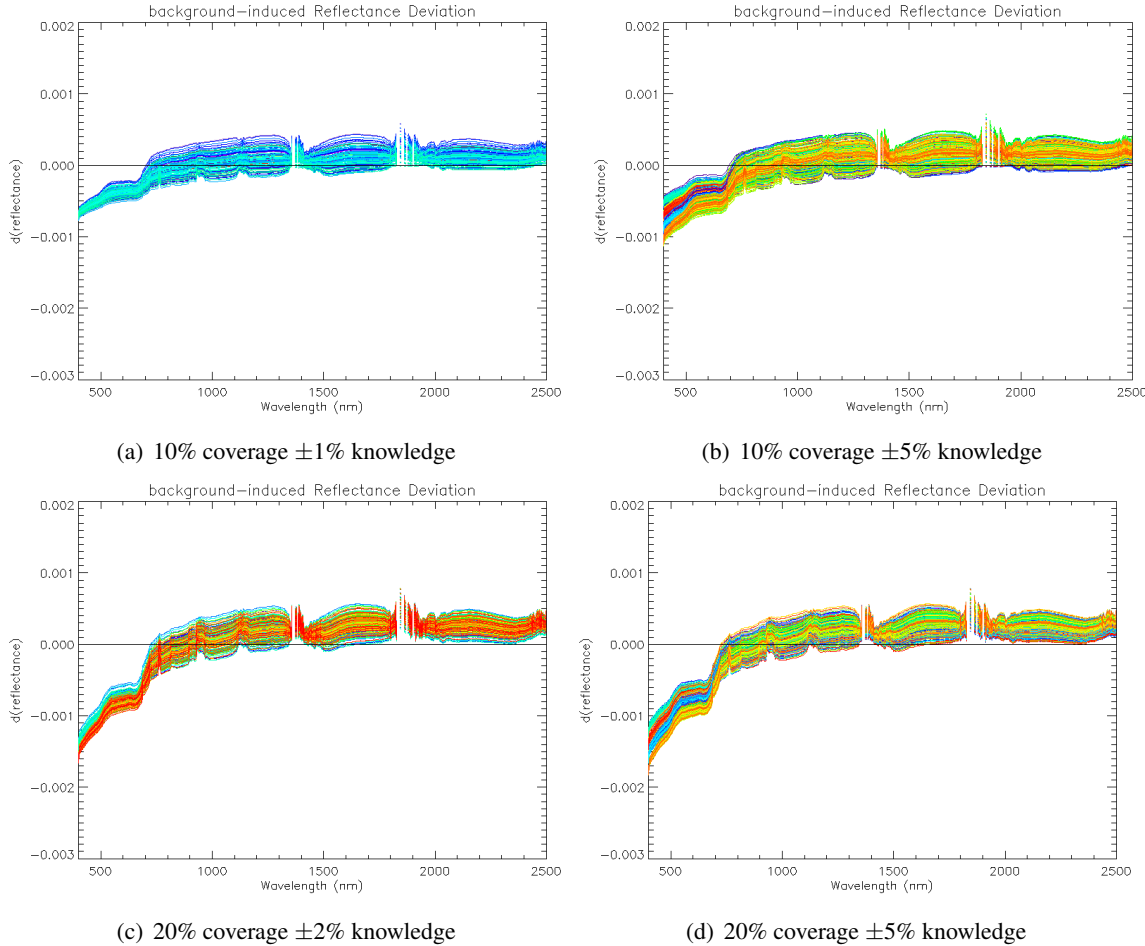


Figure E.9: Scenarios 16-17, background object bias error, for a 20% reflector. The spread reflects reflectance bias due to the range of possible low-elevation background object configurations. These results show bias errors for 10% and 20% terrain masking, $\pm 1\%-2\%$ and $\pm 5\%$, over a spectrally flat ground target with 20% reflectance

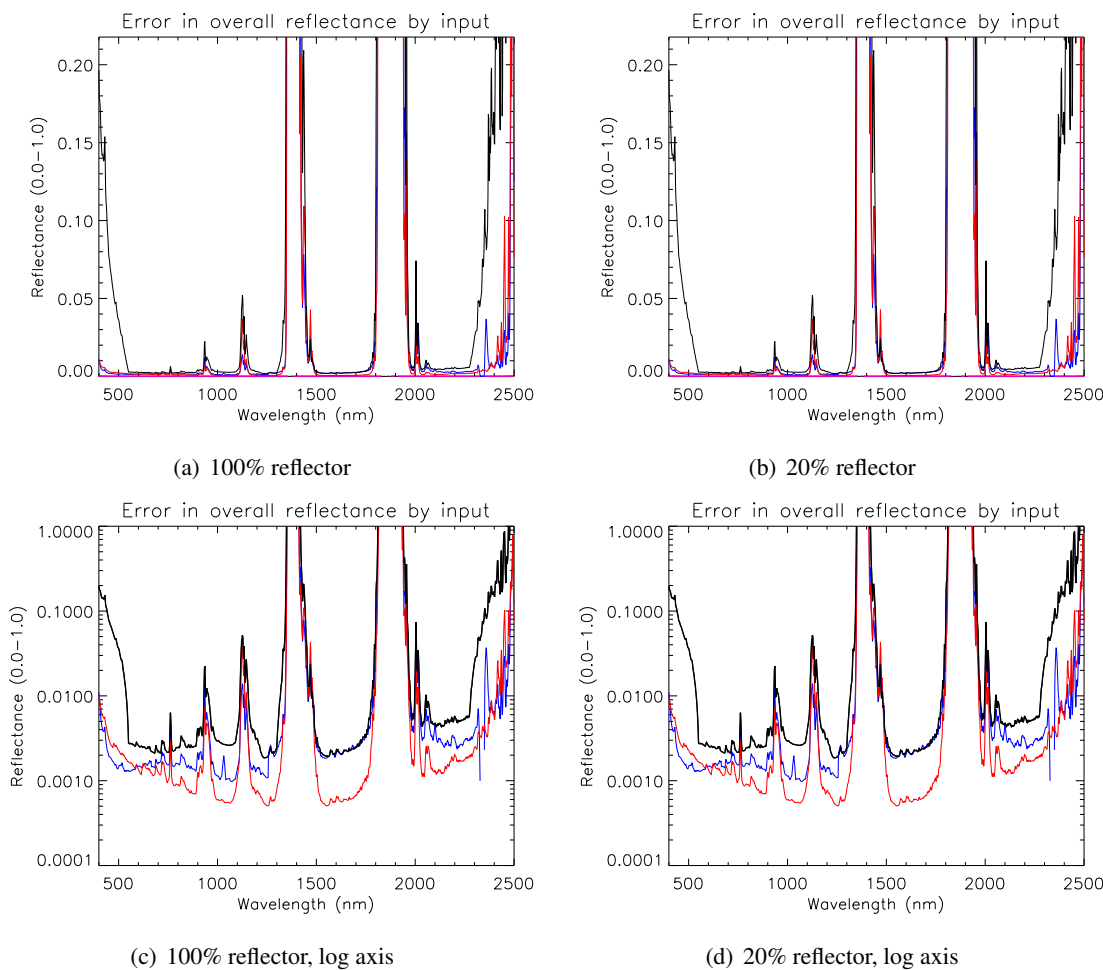


Figure E.10: Scenario 18, sensor noise random error
AVIRIS (red), HYDICE (blue), and Hyperion (black) are shown here

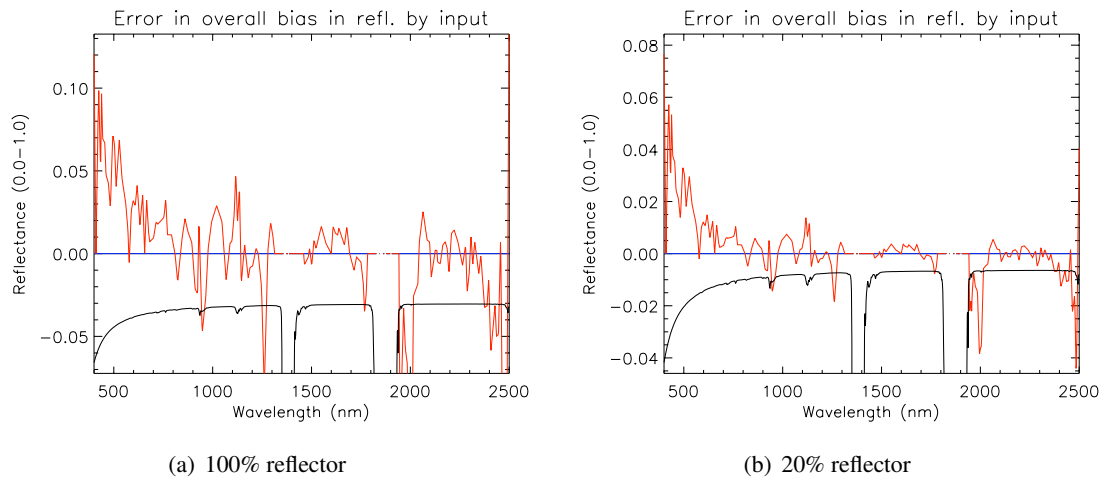
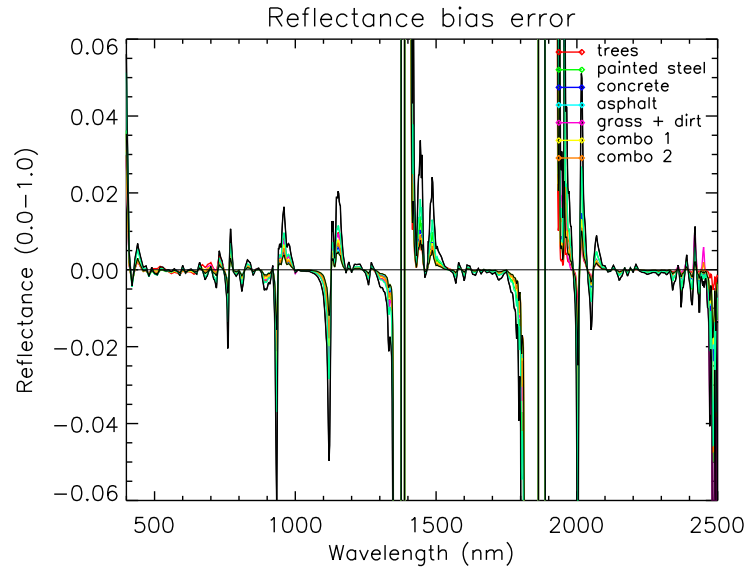
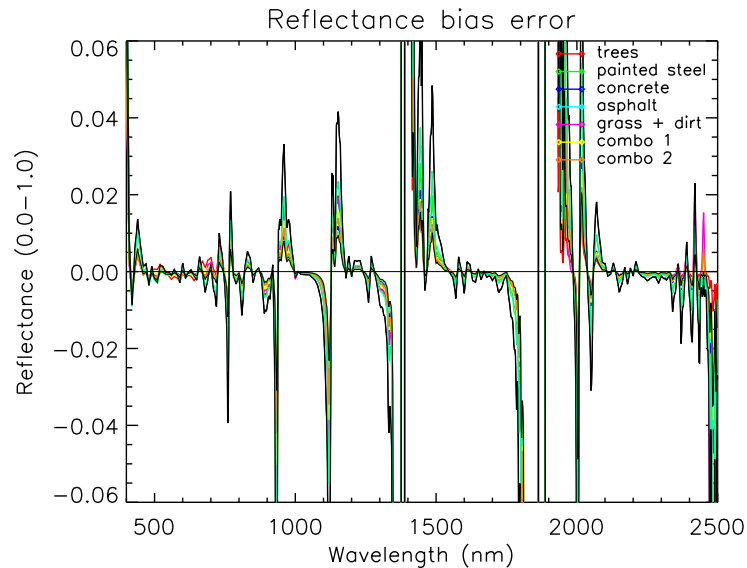


Figure E.11: Scenario 19, sensor radiometric calibration bias error. Bias estimation results from the 2002 AVIRIS study (red) and a straight -3% bias based on Hyperion validation study (black) are shown here.



(a) 0.25 nm misregistration



(b) 0.5 nm misregistration

Figure E.12: Scenario 20, retrieved reflectance bias error due to spectral misregistration

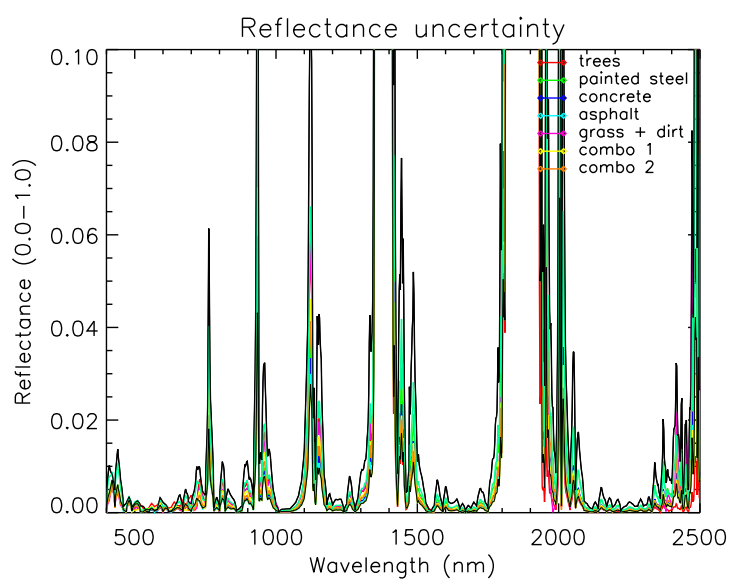


Figure E.13: Scenario 21, uncertainty in retrieved reflectance due to 0.5 nm spectral jitter

Appendix F

Validation Results

This appendix contains results for the validation scenarios listed in table 4.5. Each curve shows the standard deviation of total reflectance uncertainty as calculated from results generated using randomly perturbed input variables, as described in section 4.15.

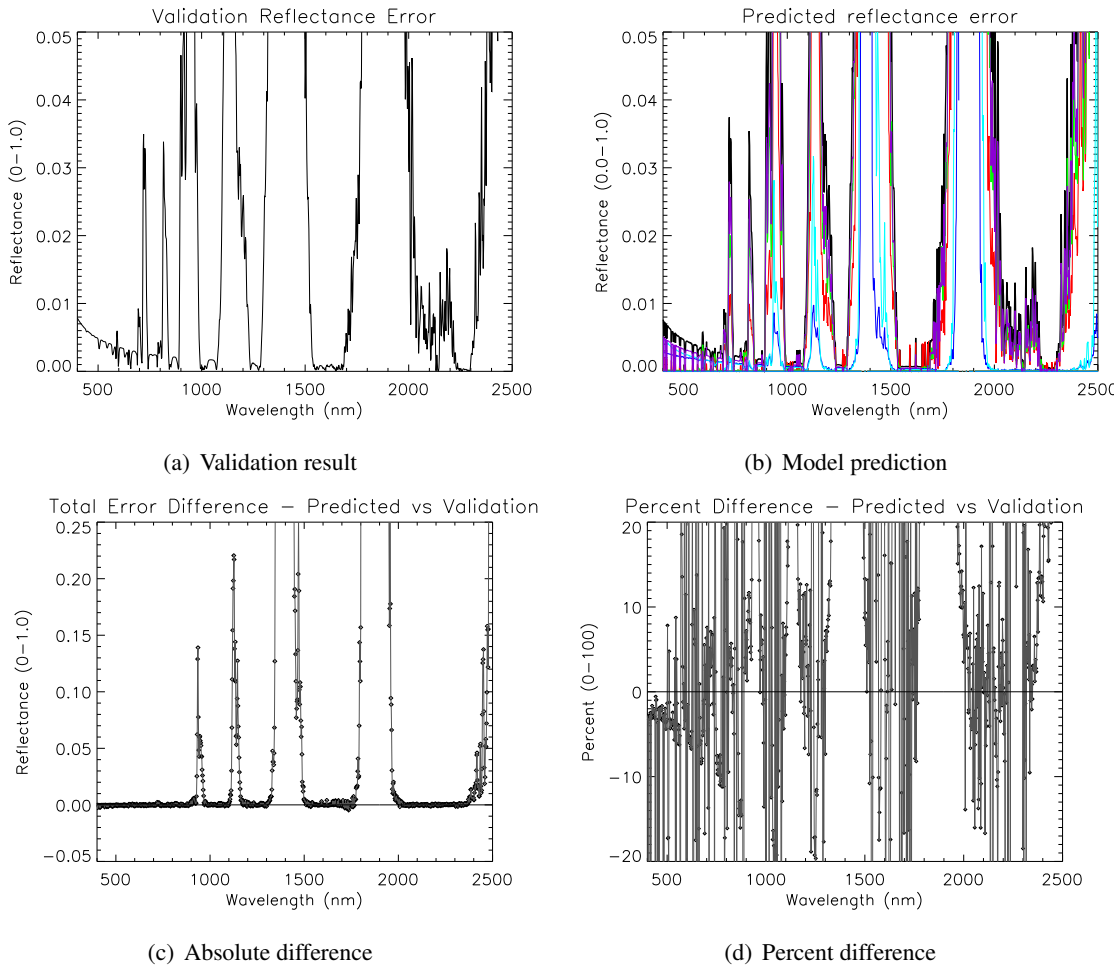


Figure F.1: Validation scenario 1 – 100% reflector. Target water vapor uncertainty was 0.2. Actual uncertainty was 0.199. The error propagation model input was adjusted to match the actual uncertainty.

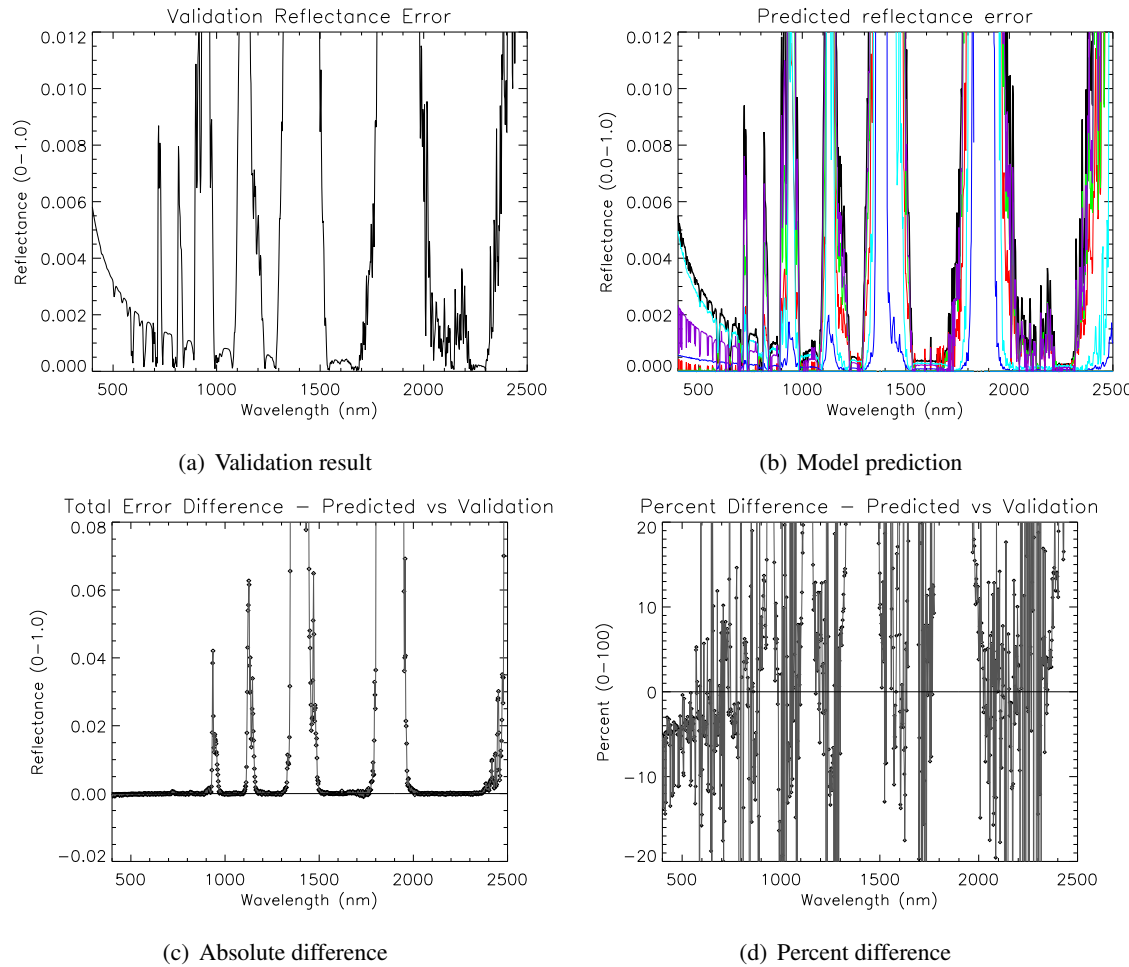


Figure F.2: Validation scenario 1 – 20% reflector. Target water vapor uncertainty was 0.2 cm. Actual uncertainty was 0.202 cm. The error propagation model input was adjusted to match the actual uncertainty.

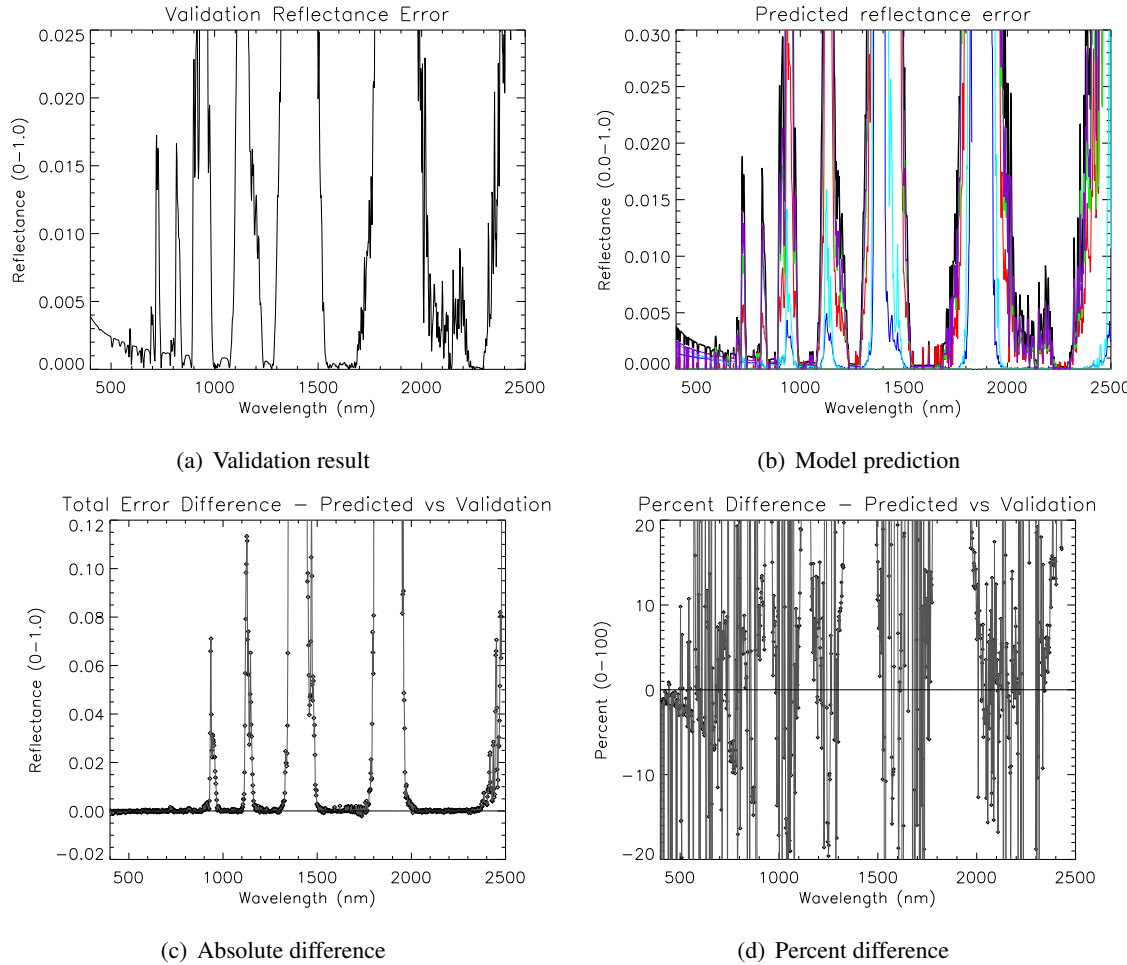


Figure F.3: Validation scenario 2 – 100% reflector. Target water vapor uncertainty was 0.1 cm. Actual uncertainty was 0.1 cm. The error propagation model input was adjusted to match the actual uncertainty.

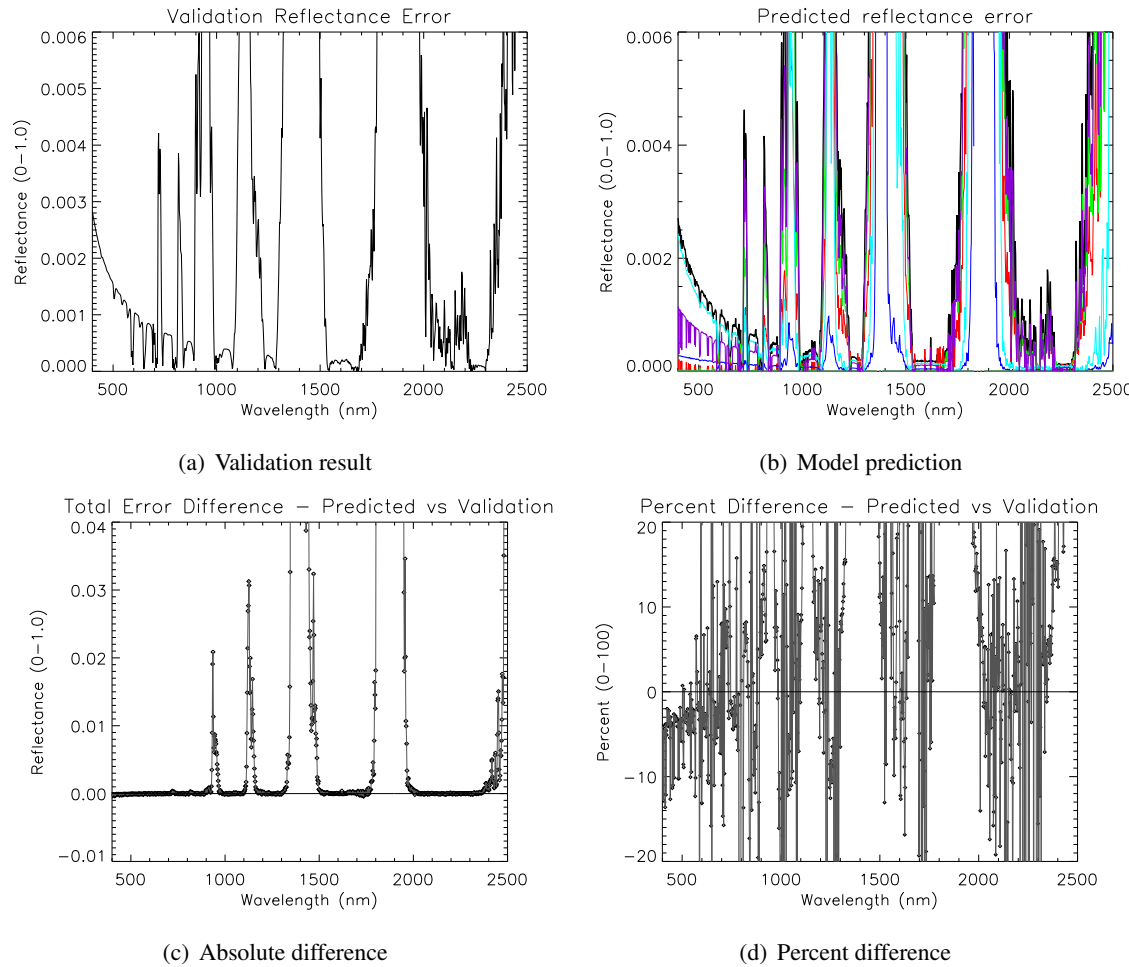


Figure F.4: Validation scenario 2 – 20% reflector. Target water vapor uncertainty was 0.1 cm. Actual uncertainty was 0.099 cm. The error propagation model input was adjusted to match the actual uncertainty.

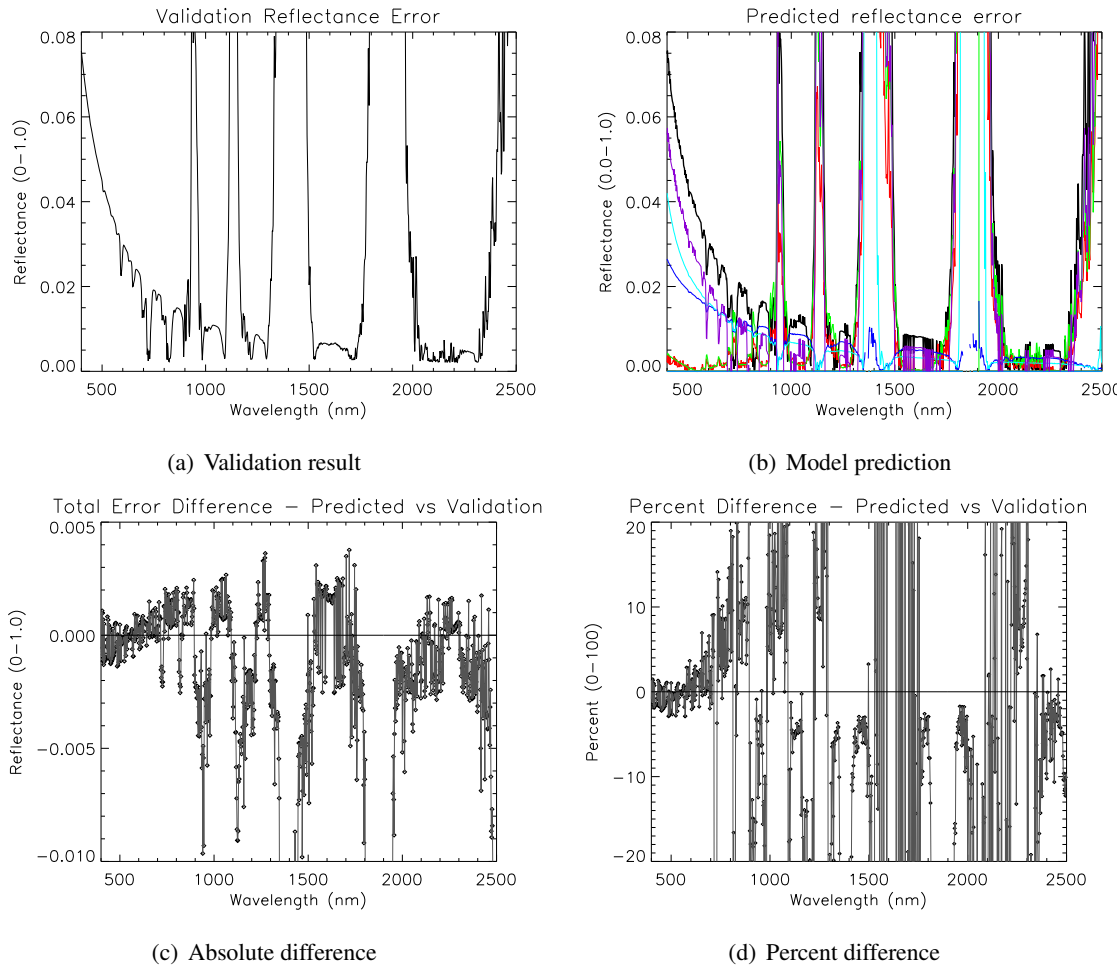


Figure F.5: Validation scenario 3 – 100% reflector. Target water vapor uncertainty was 0.2 cm. Actual uncertainty was 0.19 cm. The error propagation model input was adjusted to match the actual uncertainty.

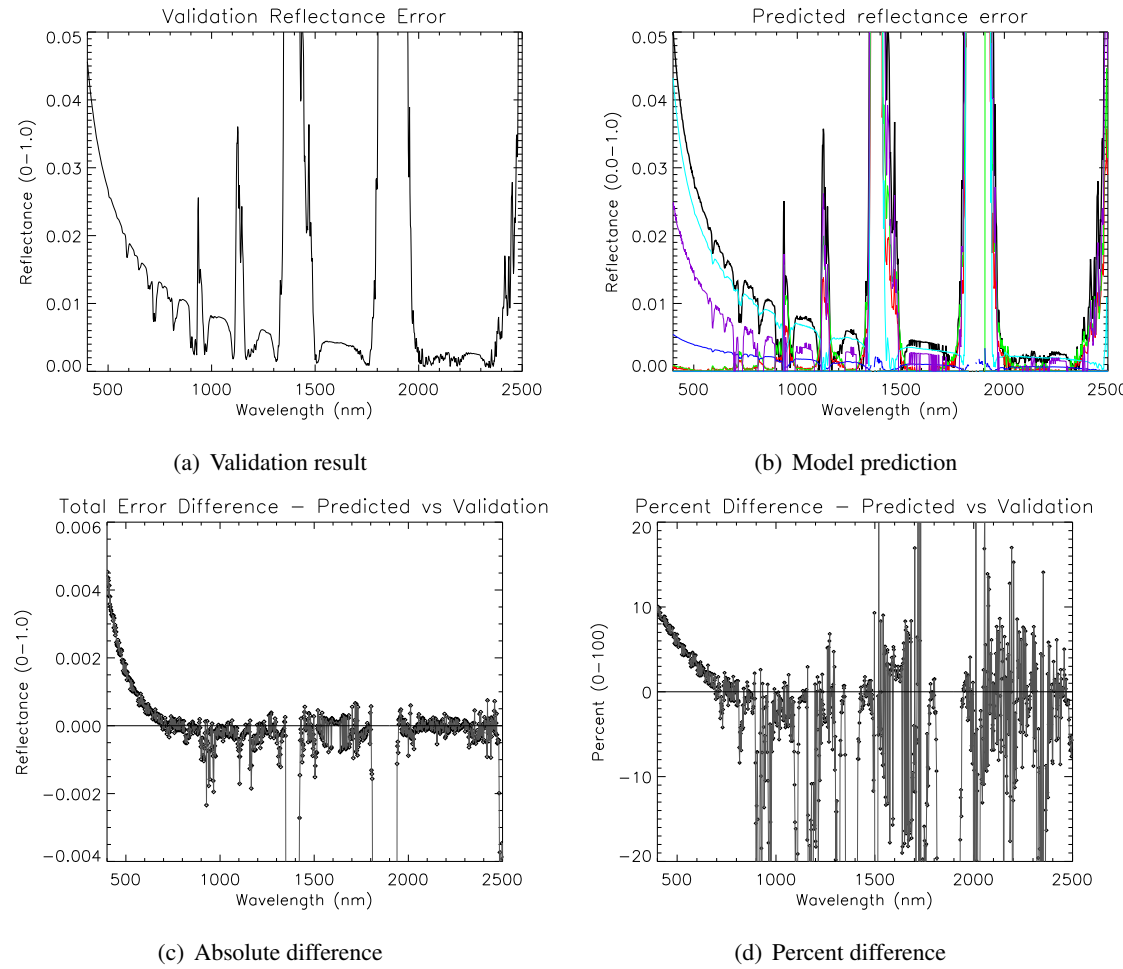


Figure F.6: Validation scenario 3 – 20% reflector. Target water vapor uncertainty was 0.2 cm. Actual uncertainty was 0.196 cm. The error propagation model input was adjusted to match the actual uncertainty.

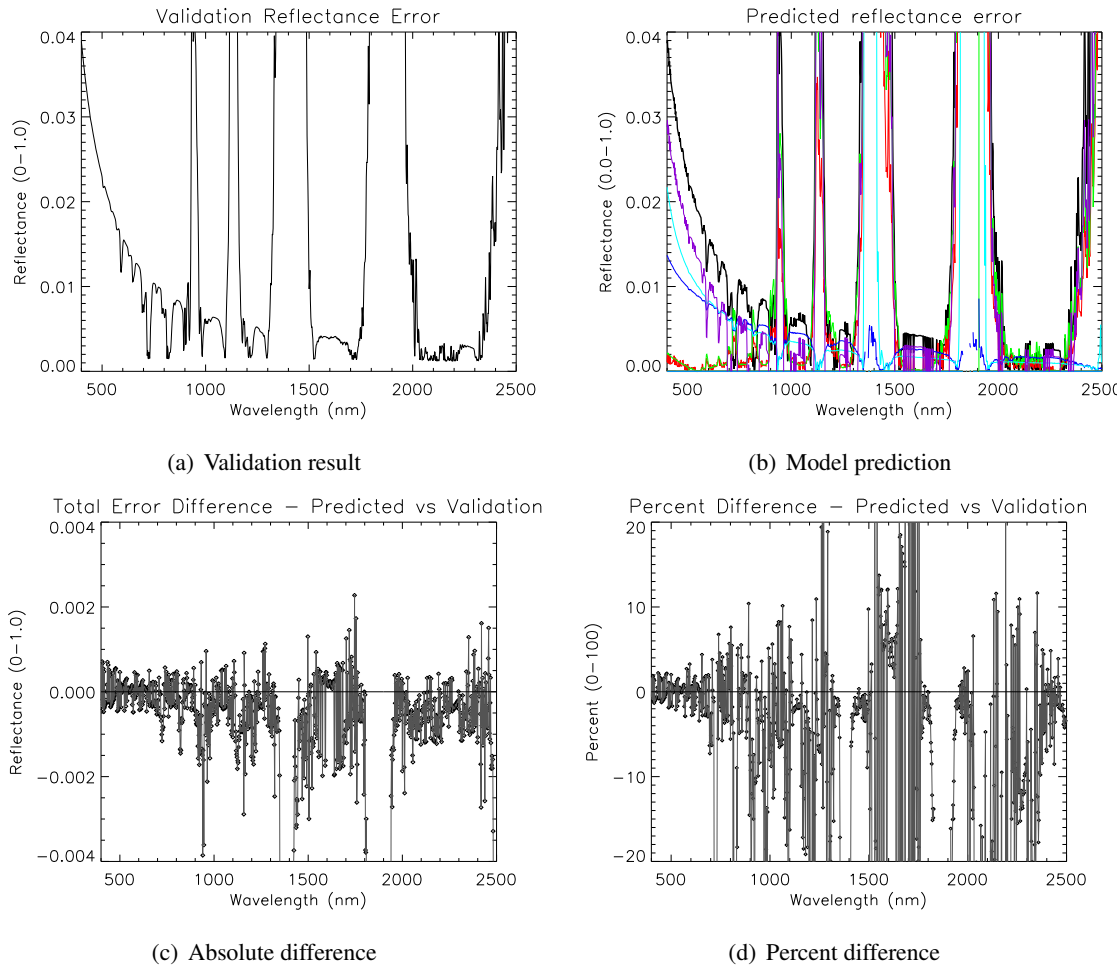


Figure F.7: Validation scenario 4 – 100% reflector. Target water vapor uncertainty was 0.1 cm. Actual uncertainty was 0.098 cm. The error propagation model input was adjusted to match the actual uncertainty.

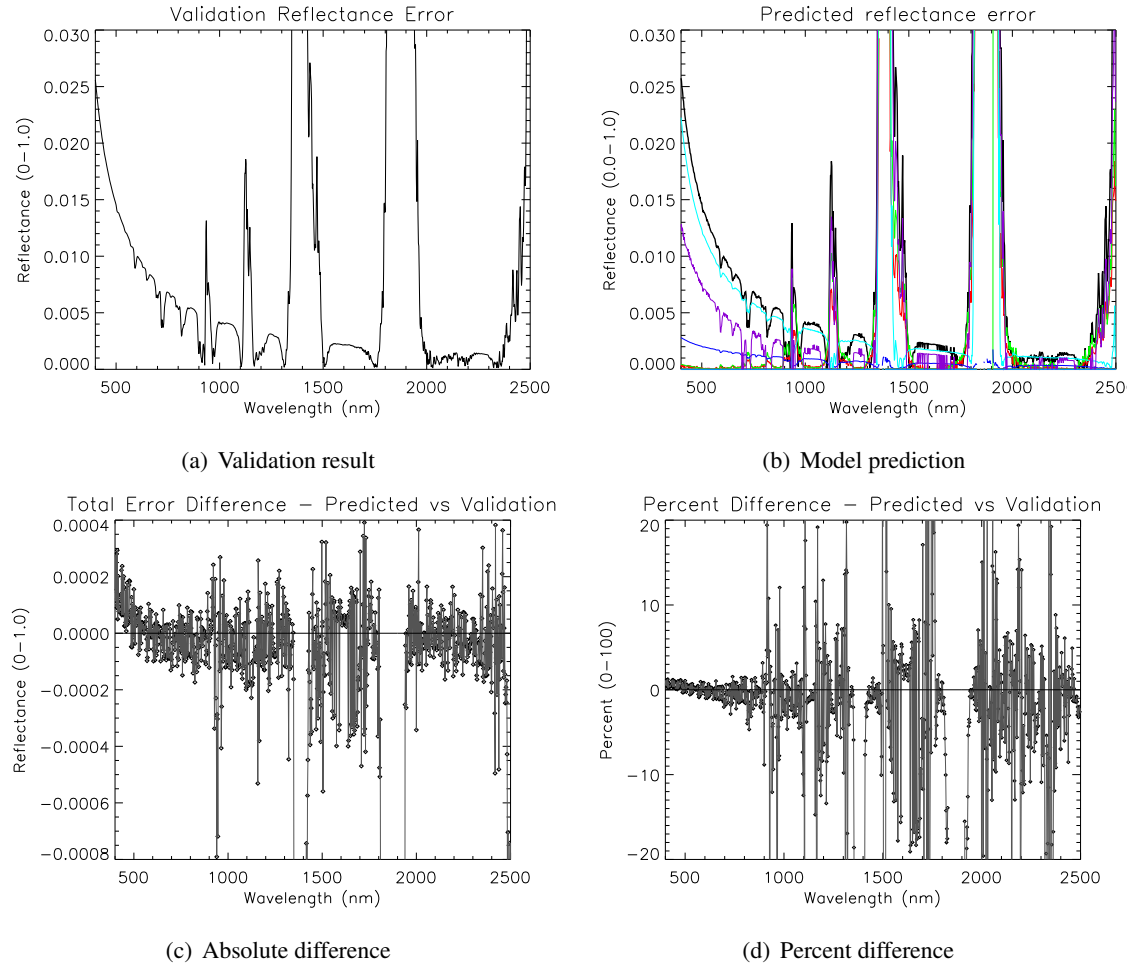


Figure F.8: Validation scenario 4 – 20% reflector. Target water vapor uncertainty was 0.1 cm. Actual uncertainty was 0.1001 cm. The error propagation model input was adjusted to match the actual uncertainty.

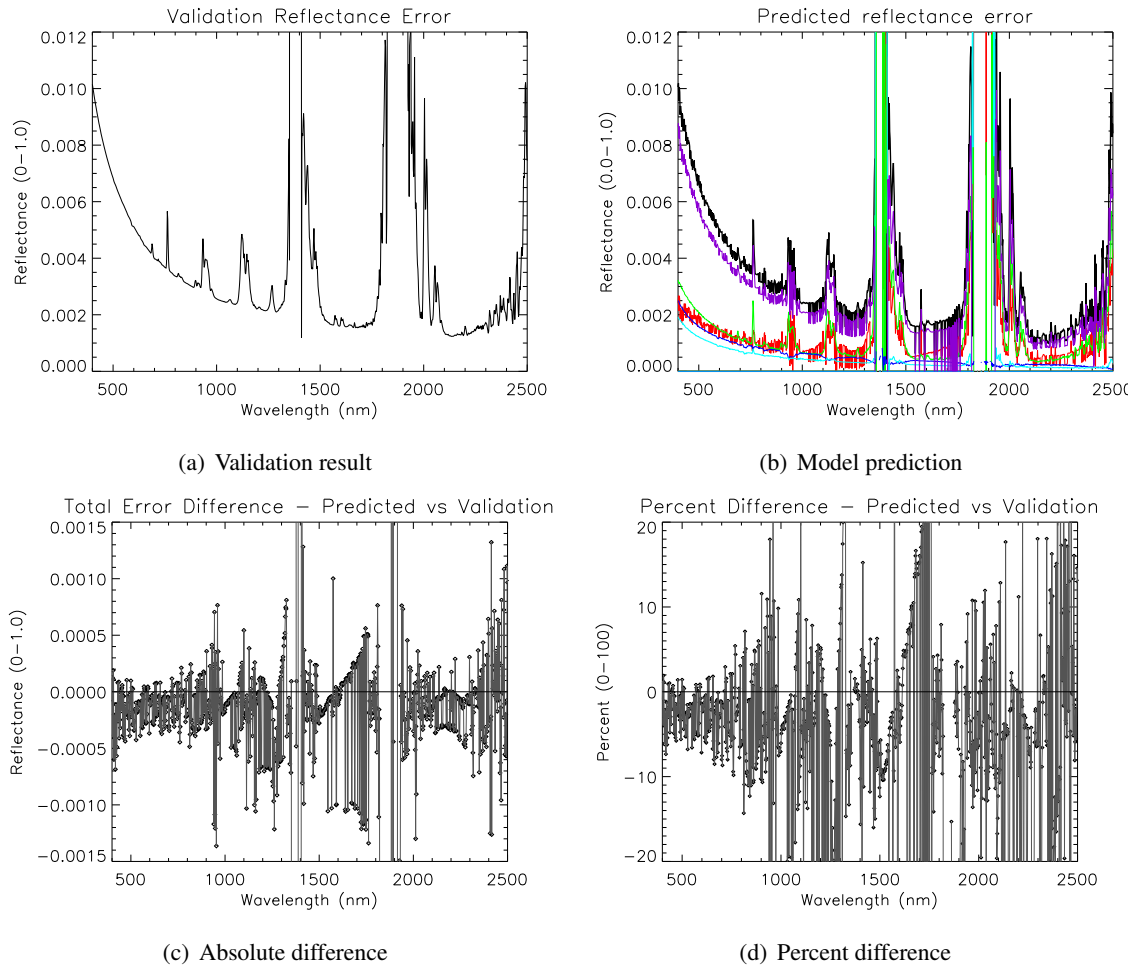


Figure F.9: Validation scenario 5 – 100% reflector. Target density altitude uncertainty was 0.02 km. Actual uncertainty was 0.02 km. The error propagation model input was adjusted to match the actual uncertainty.

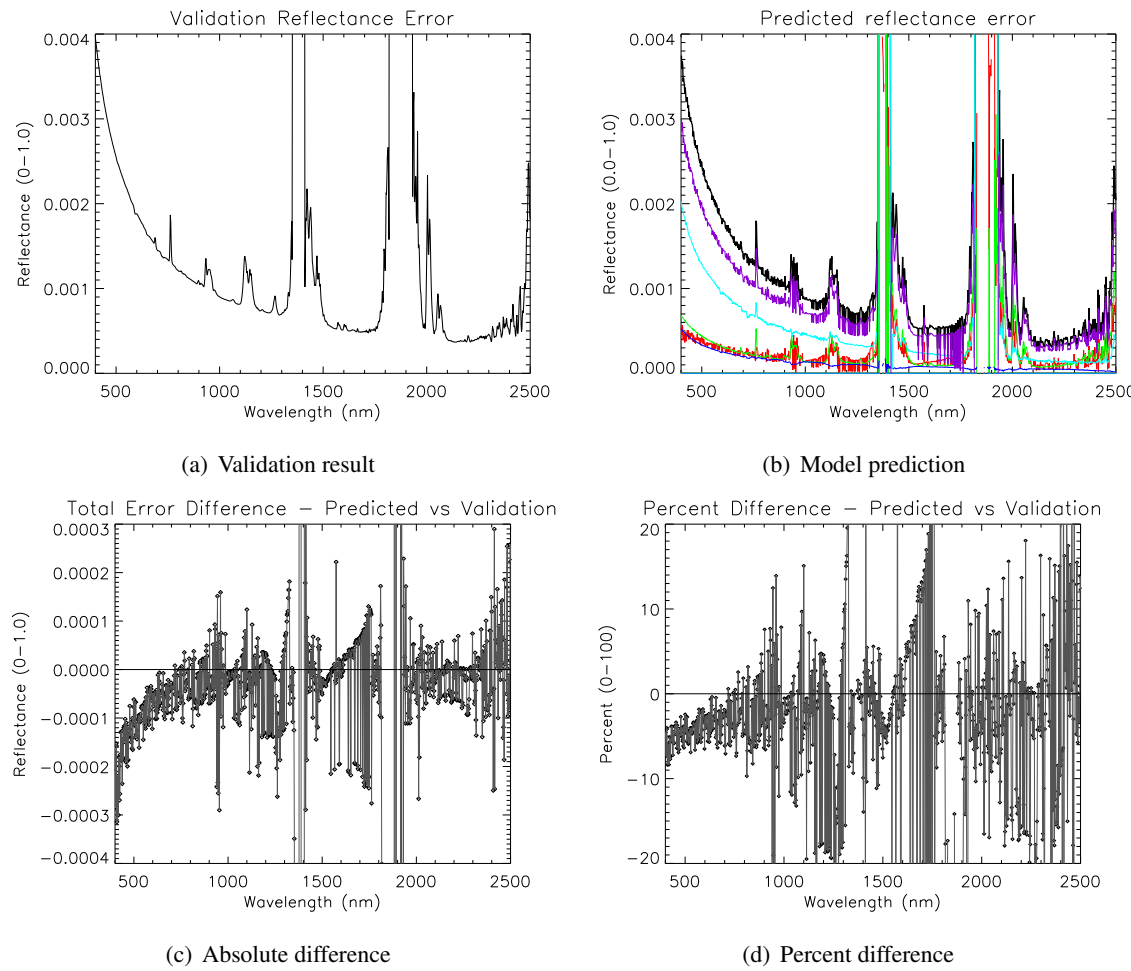


Figure F.10: Validation scenario 5 – 20% reflector. Target density altitude uncertainty was 0.02 km. Actual uncertainty was 0.0214 km. The error propagation model input was adjusted to match the actual uncertainty.

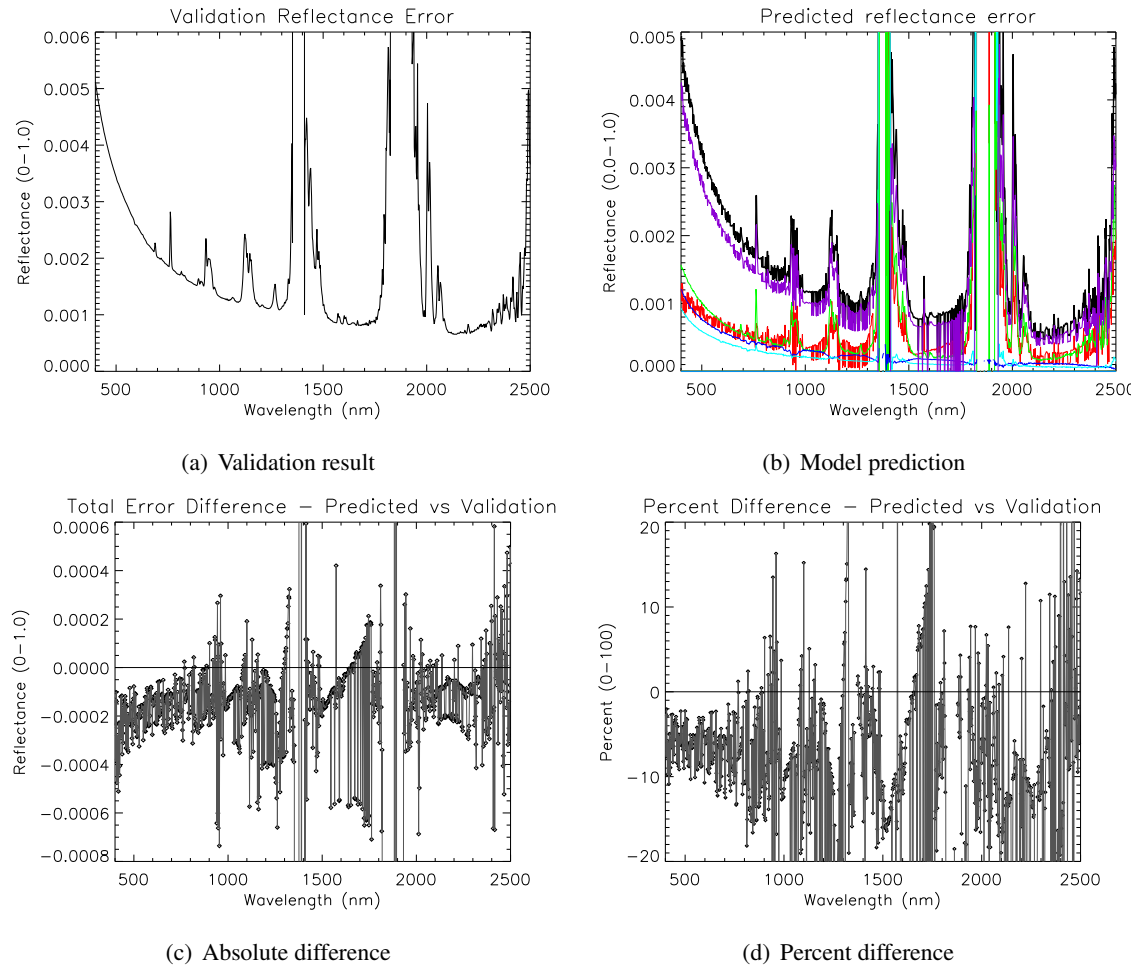


Figure F.11: Validation scenario 6 – 100% reflector. Target density altitude uncertainty was 0.01 km. Actual uncertainty was 0.0098 km. The error propagation model input was adjusted to match the actual uncertainty.

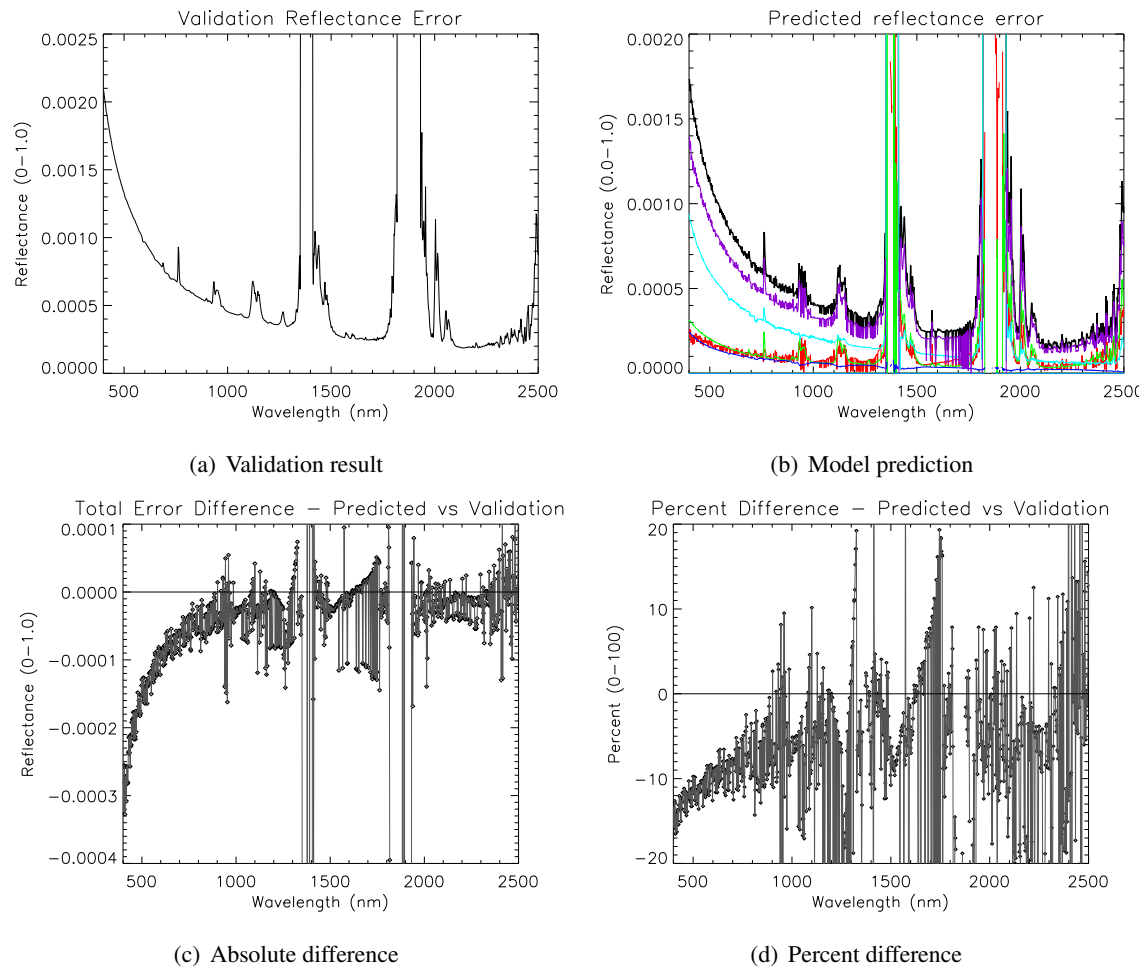


Figure F.12: Validation scenario 6 – 20% reflector. Target density altitude uncertainty was 0.01 km. Actual uncertainty was 0.0099 km. The error propagation model input was adjusted to match the actual uncertainty.

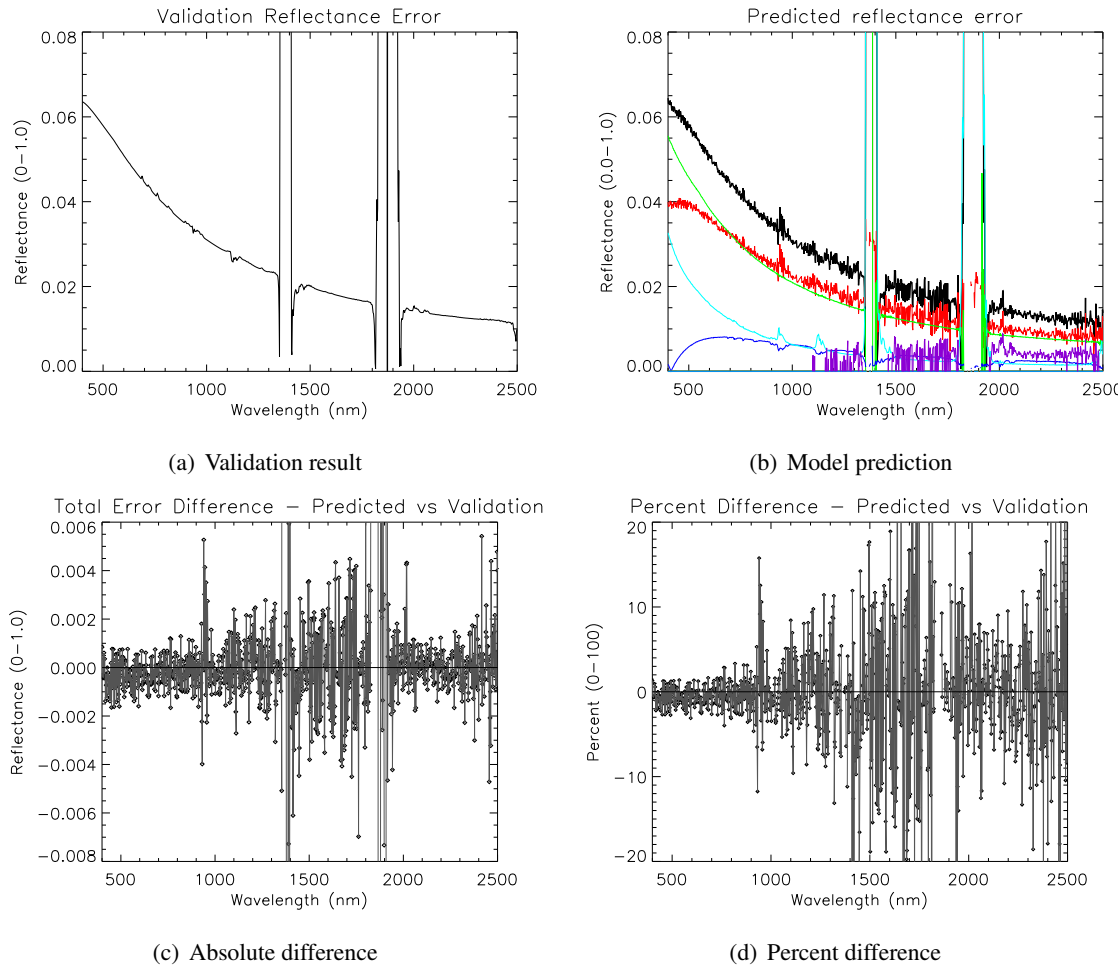


Figure F.13: Validation scenario 7 – 100% reflector. Target aerosol optical depth uncertainty was 0.04. Actual uncertainty was 0.04218. The error propagation model input was adjusted to match the actual uncertainty.

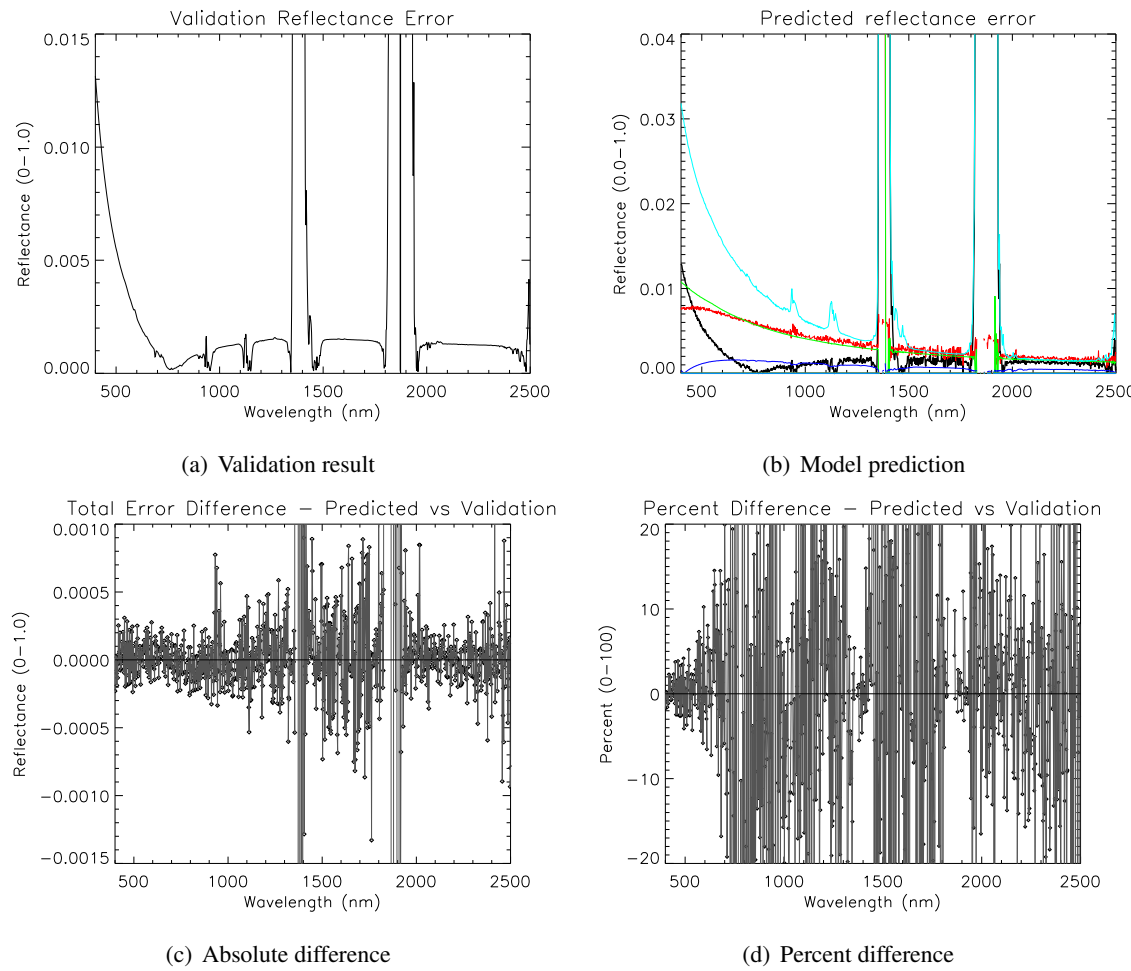


Figure F.14: Validation scenario 7 – 20% reflector. Target aerosol optical depth uncertainty was 0.04. Actual uncertainty was 0.0411. The error propagation model input was adjusted to match the actual uncertainty.

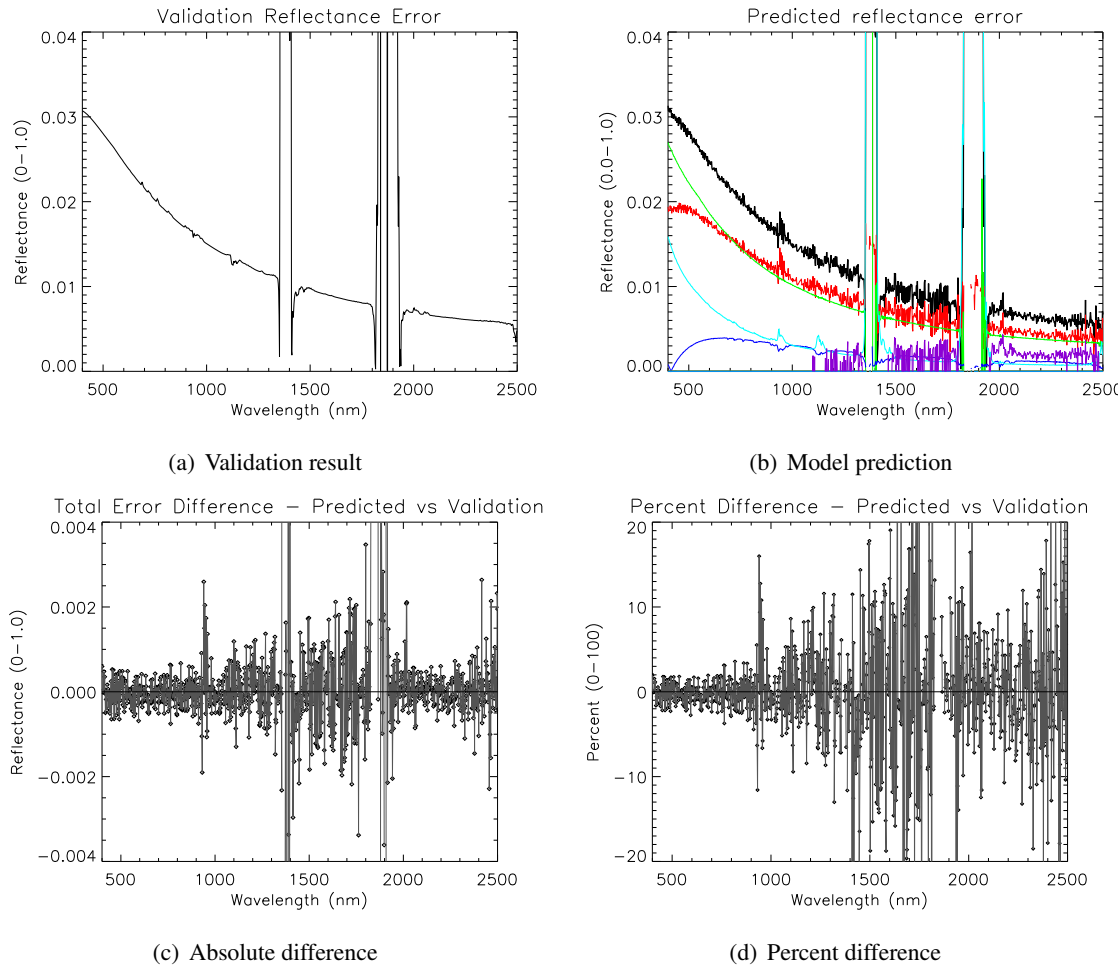


Figure F.15: Validation scenario 8 – 100% reflector. Target aerosol optical depth uncertainty was 0.02. Actual uncertainty was 0.0205. The error propagation model input was adjusted to match the actual uncertainty.

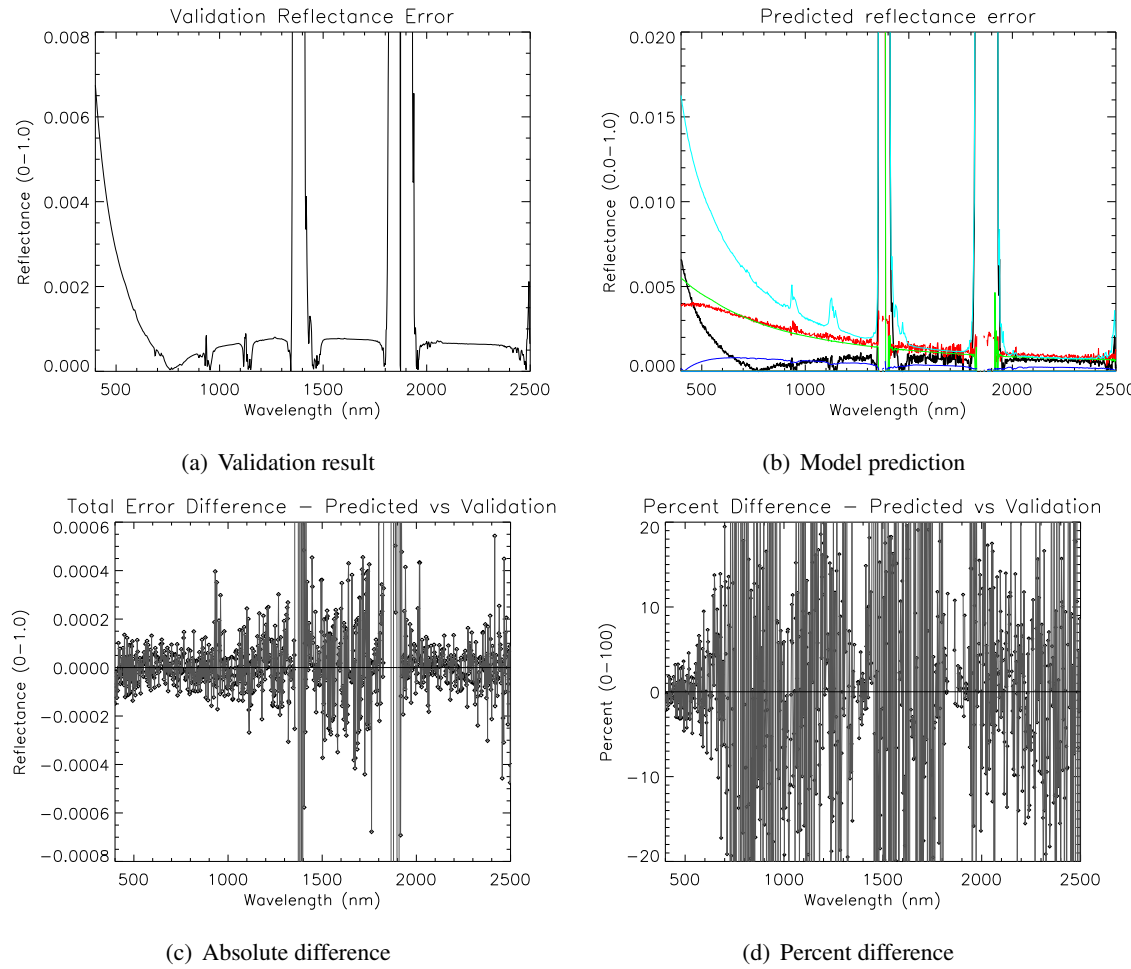


Figure F.16: Validation scenario 8 – 20% reflector. Target aerosol optical depth uncertainty was 0.02. Actual uncertainty was 0.021. The error propagation model input was adjusted to match the actual uncertainty.

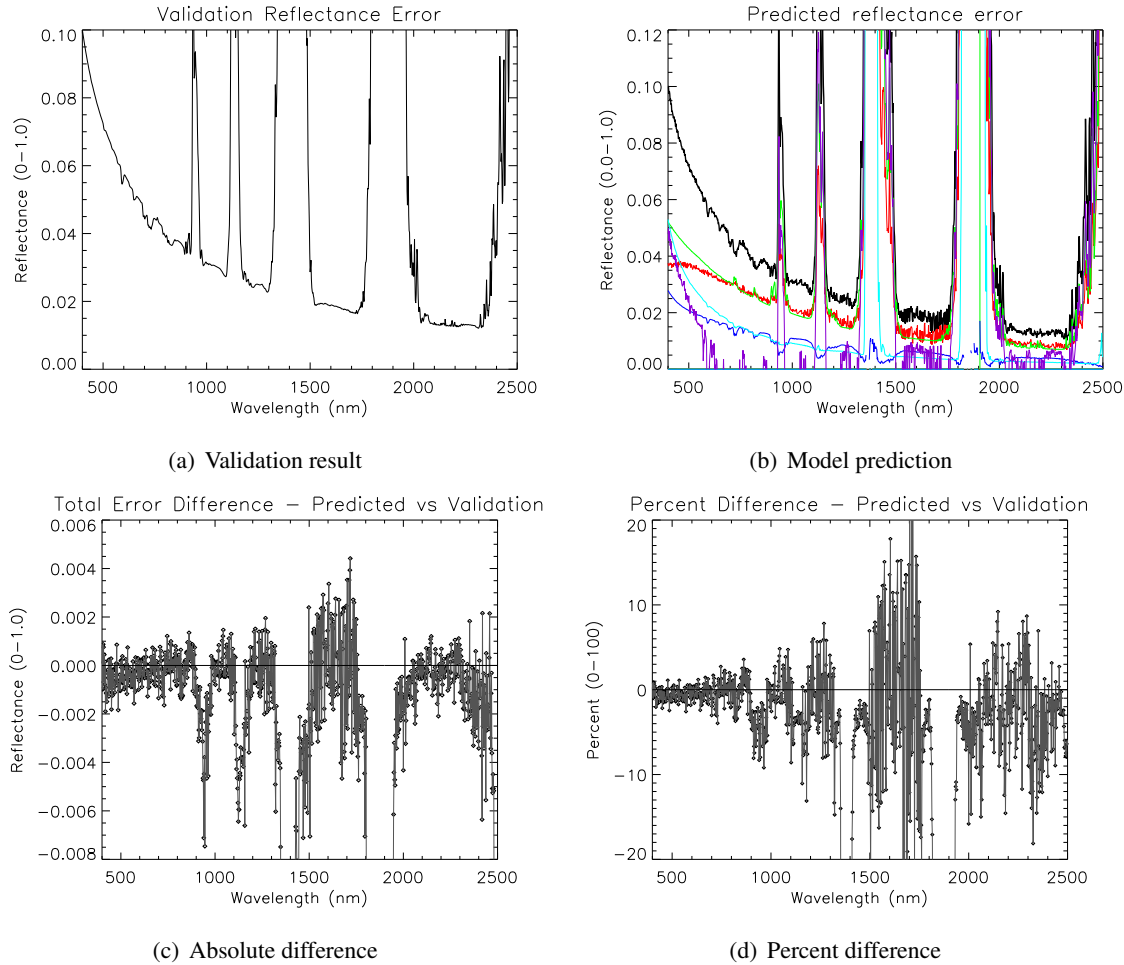


Figure F.17: Validation scenario 9 – 100% reflector. Target parameter uncertainties were 0.2 cm, 0.045 km, and 0.04. Actual uncertainty was 0.196 cm, 0.039 km, and 0.0452. The error propagation model inputs were adjusted to match the actual uncertainties.

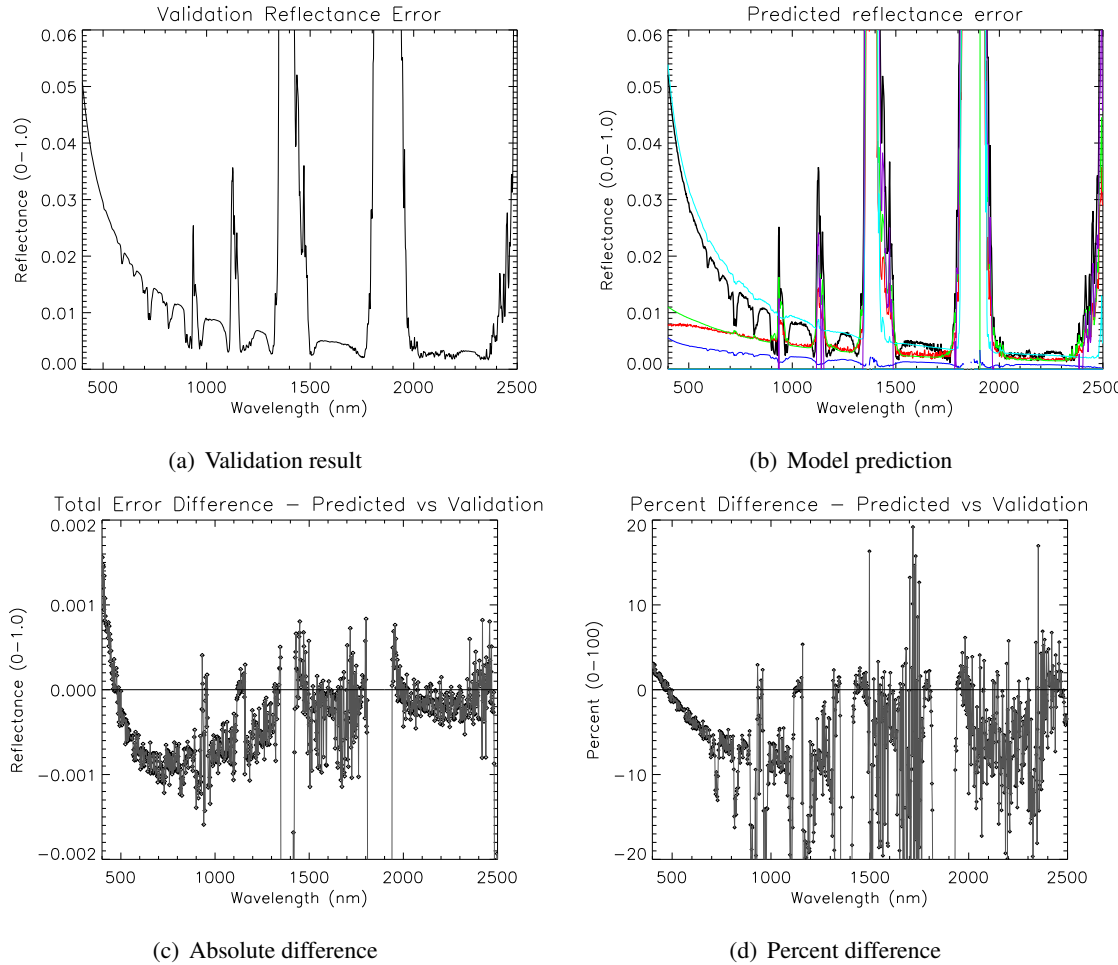


Figure F.18: Validation scenario 9 – 20% reflector. Target parameter uncertainties were 0.2 cm, 0.045 km, and 0.04. Actual uncertainty was 0.2 cm, 0.045 km, and 0.04. The error propagation model inputs were adjusted to match the actual uncertainties.

Appendix G

Error Improvement Sensitivity Results

This appendix shows the results of an error sensitivity study conducted to directly trace the error contributions of each atmospheric constituent. Figure G.1 shows the color significance for the following plots. The fourth item on the legend is not part of the constituent study, rather it shows the effect of adding a sky radiometer with 3% broadband precision (Michalsky, 2001) to a truth-assisted inversion network.

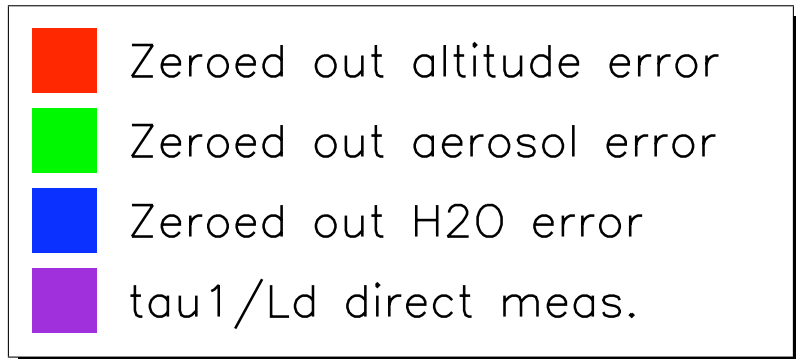


Figure G.1: Legend for error sensitivity results

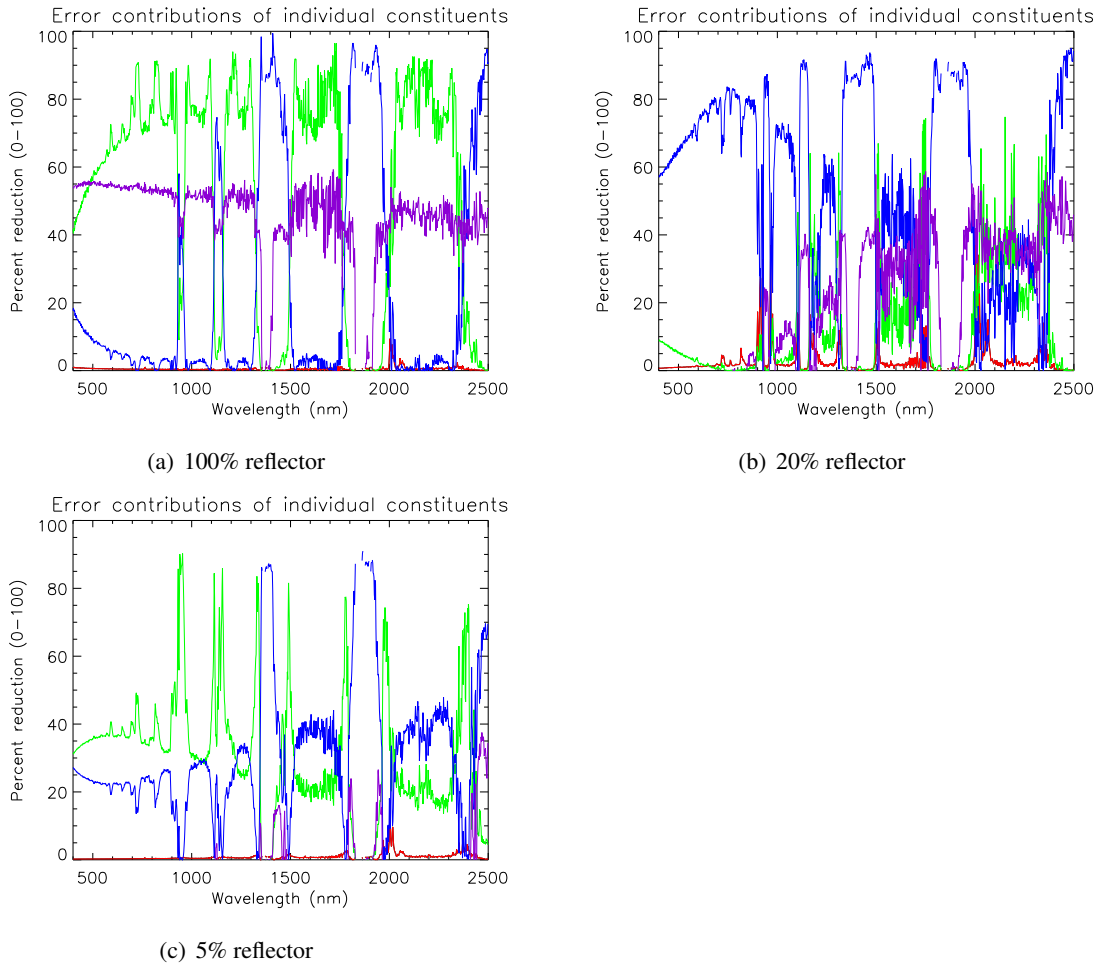


Figure G.2: Scenario 1 – *a priori* knowledge climatology inputs. Each curve is the percent reduction in uncertainty when a constituent is set to zero. In other words, the strength of each constituent's error contribution is judged by the improvement gained when it is perfectly known. Red = altitude, green = aerosols, and blue = water vapor. Magenta shows the improvement resulting from the direct ground measurement of τ_1 and L_d . Also see figure G.1.

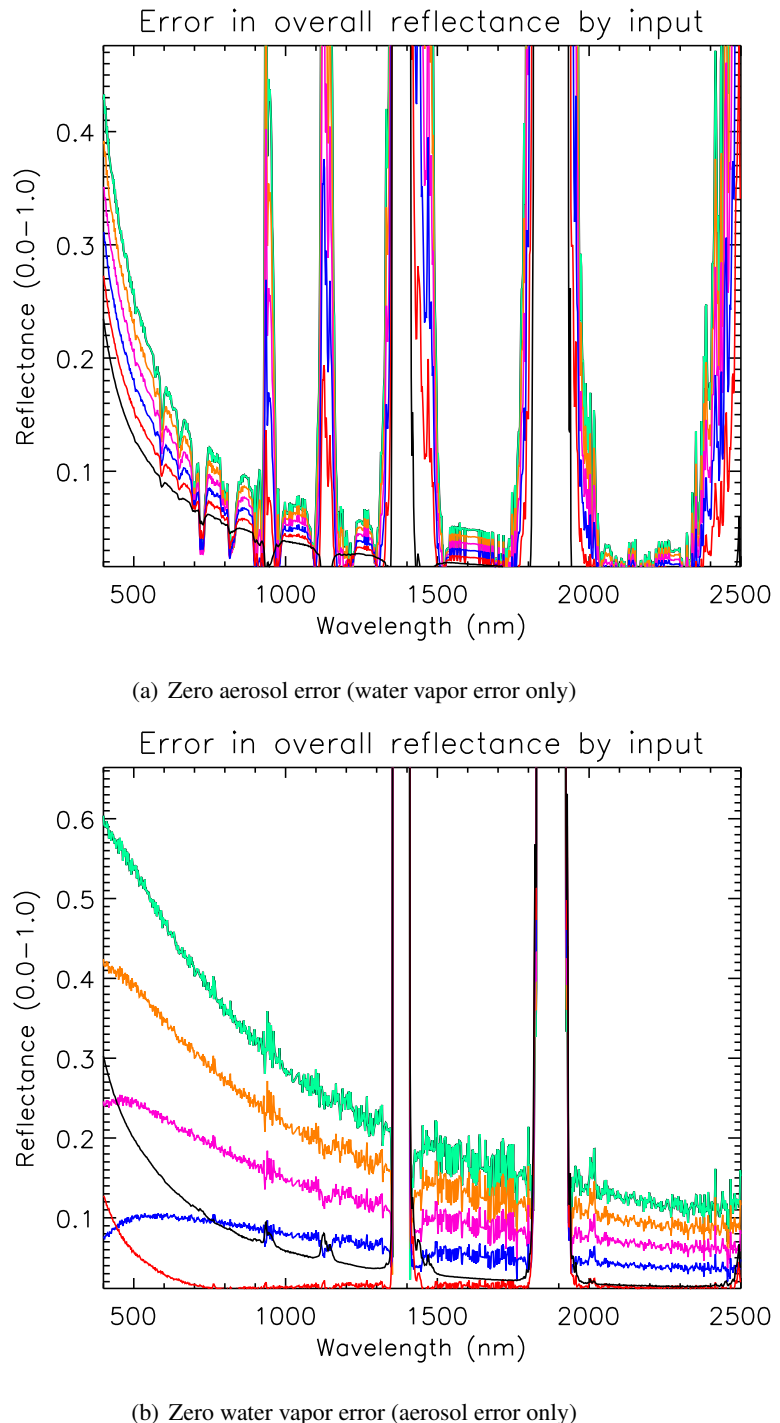


Figure G.3: Scenario 1 – multiple reflectance comparison. Each curve represents a different surface reflectance, ranging from 0% (black) to 20% (red), 40% (blue), 60% (magenta), 80% (orange), and 100% (sea green) in 20% increments.

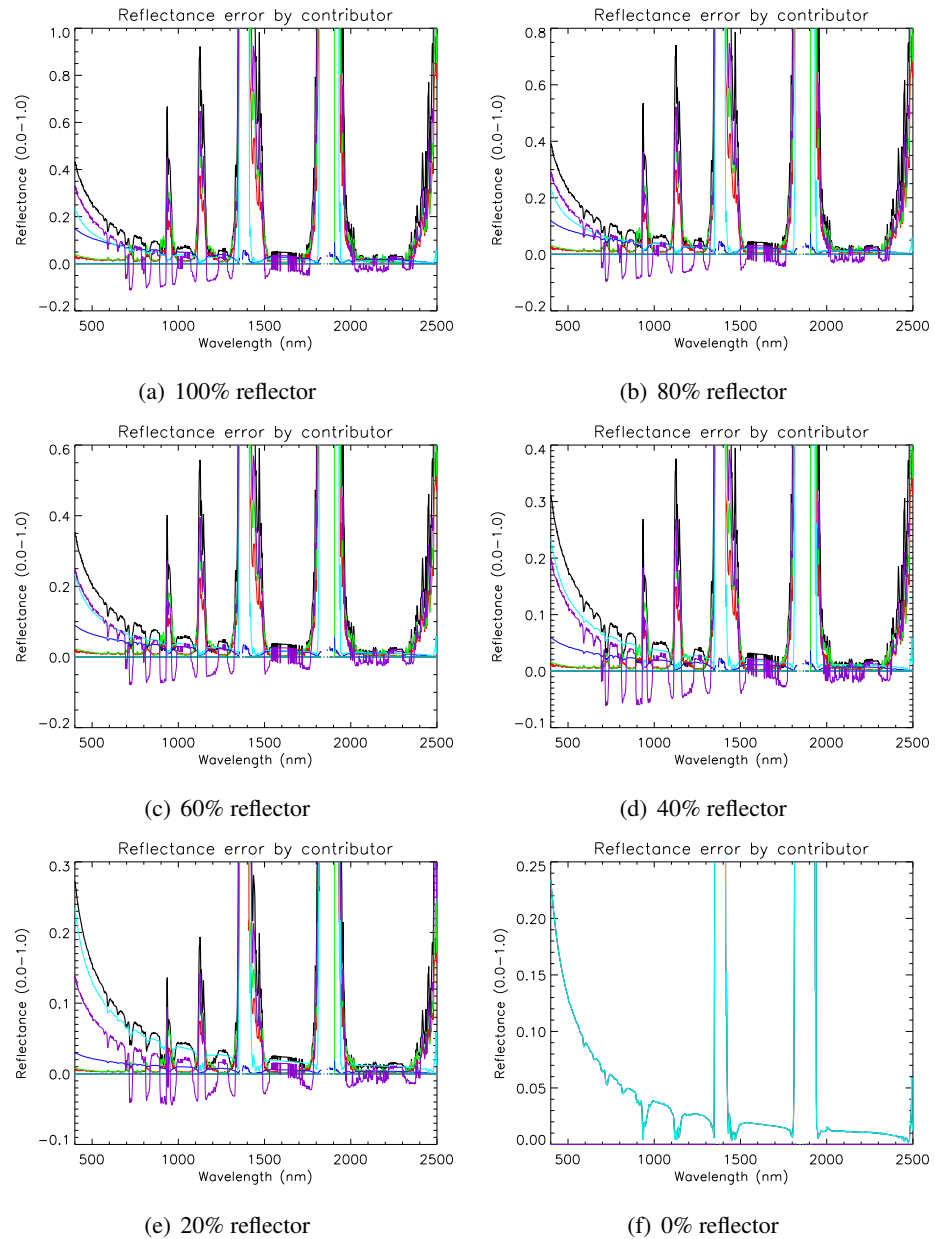


Figure G.4: Scenario 1 – individual results for zero aerosol error (water vapor error only). These plots use the legend in figure D.1. Color coding for contributors: red = τ_1 , green = τ_2 , blue = L_d , cyan = L_u , and violet = sum of all correlation terms.

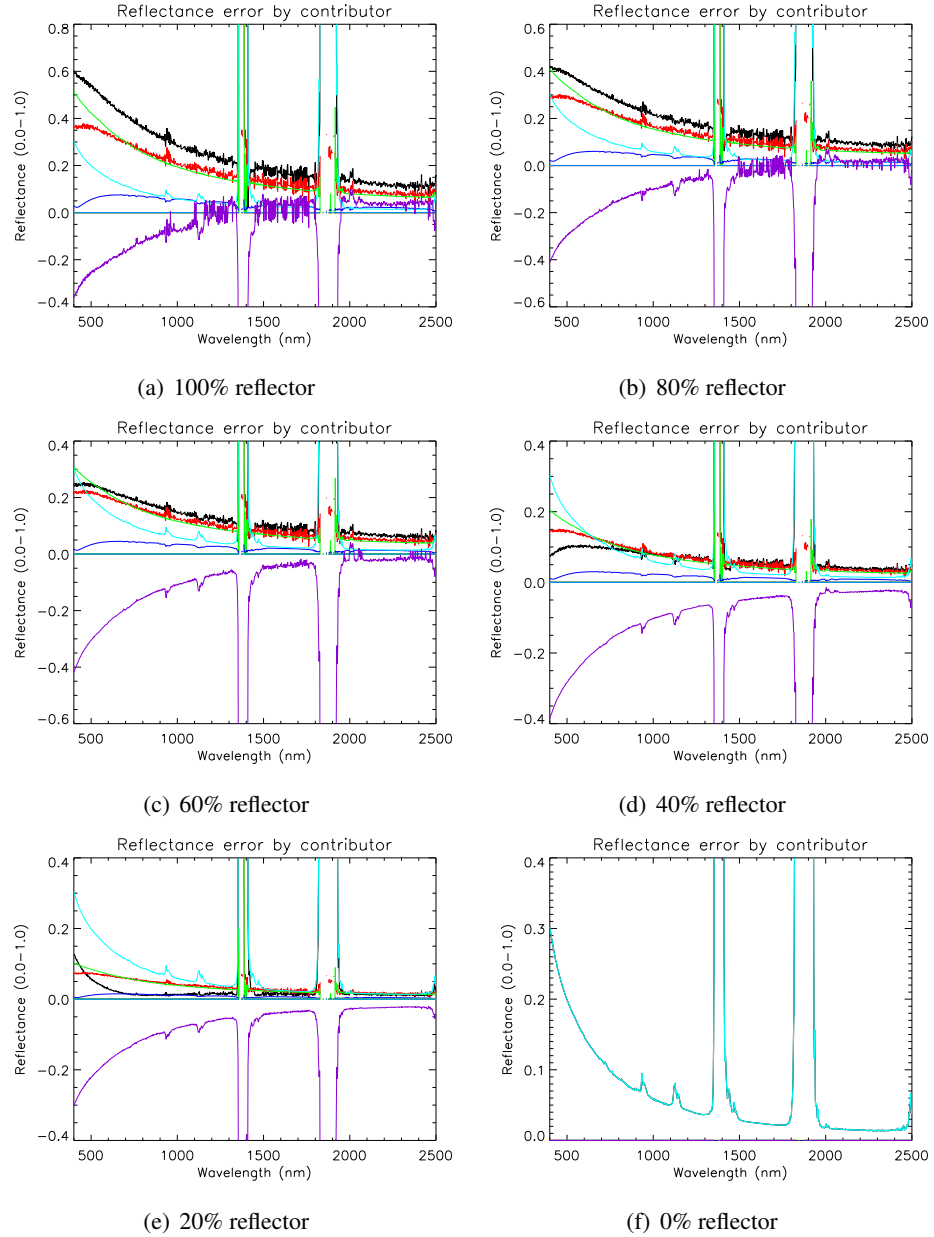


Figure G.5: Scenario 1 – individual results for zero water vapor error (aerosol error only). These plots use the legend in figure D.1. Color coding for contributors: red = τ_1 , green = τ_2 , blue = L_d , cyan = L_u , and violet = sum of all correlation terms.

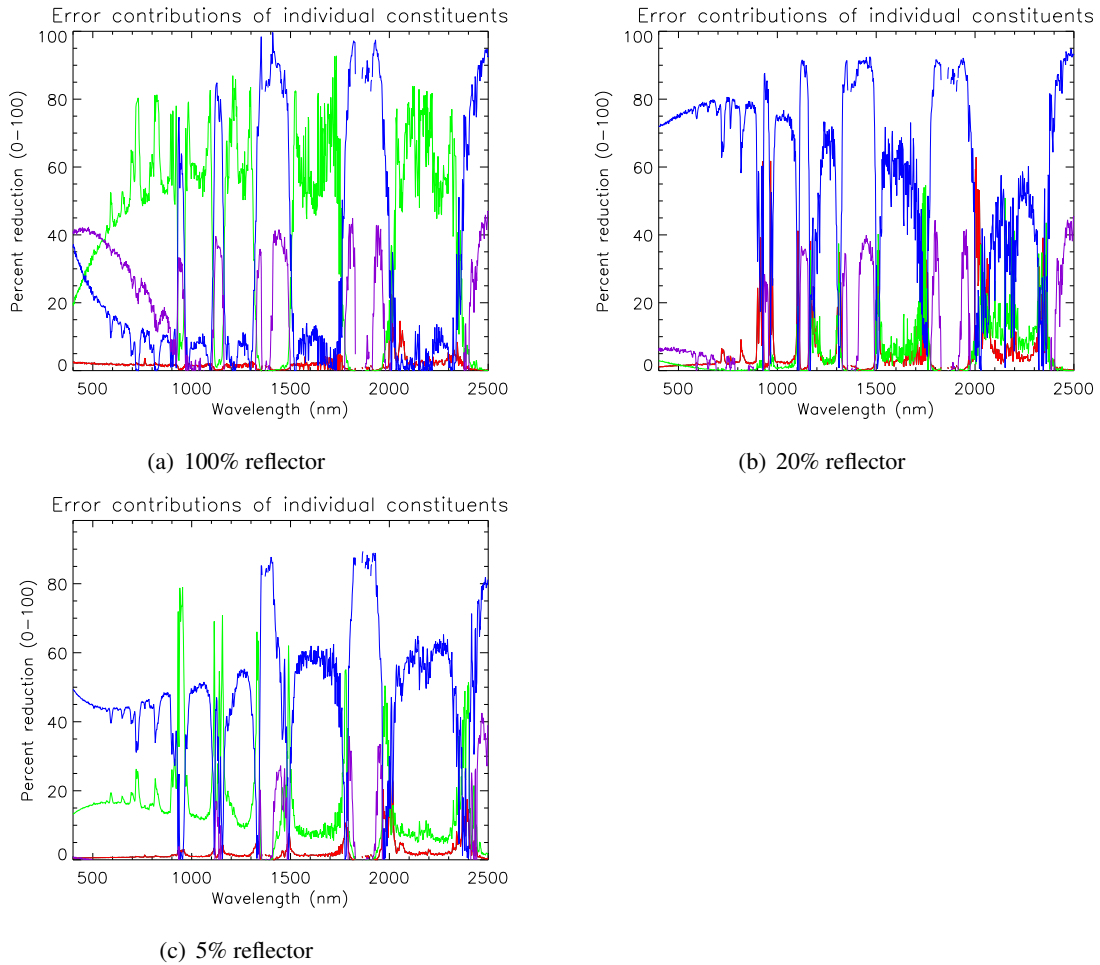
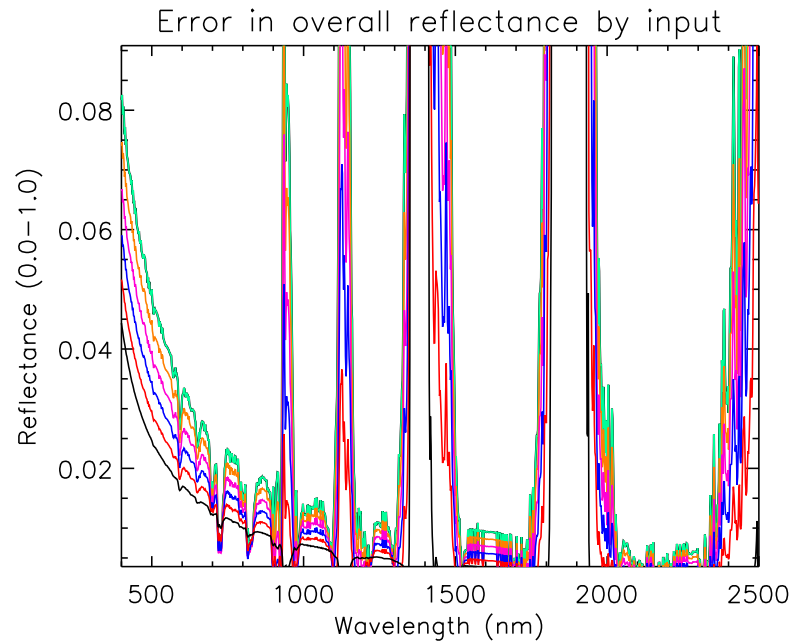
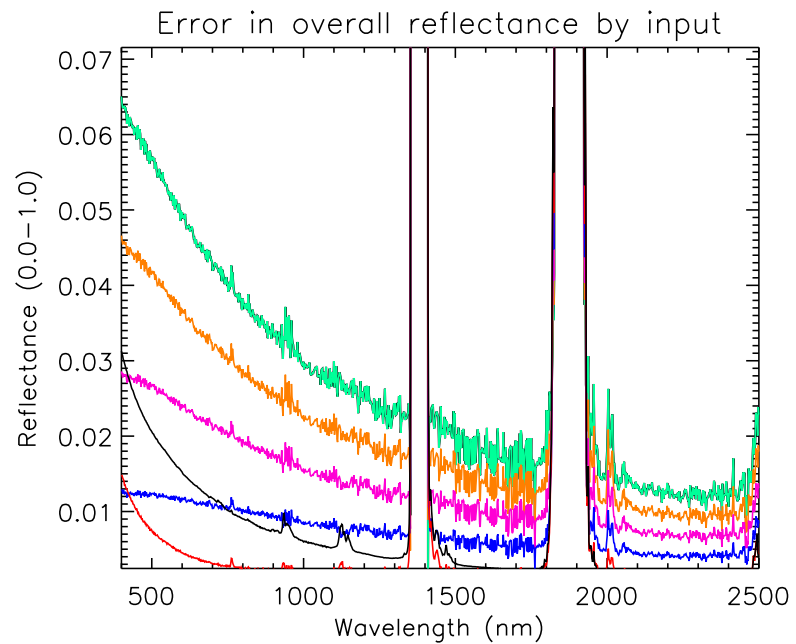


Figure G.6: Scenario 2 – inputs from commercial quality instrumentation. Each curve is the percent reduction in uncertainty when a constituent is set to zero. In other words, the strength of each constituent's error contribution is judged by the improvement gained when it is perfectly known. Red = altitude, green = aerosols, and blue = water vapor. Magenta shows the improvement resulting from the direct ground measurement of τ_1 and L_d . Also see figure G.1.



(a) Zero aerosol error (water vapor error only)



(b) Zero water vapor error (aerosol error only)

Figure G.7: Scenario 2 – multiple reflectance comparison. Each curve represents a different surface reflectance, ranging from 0% (black) to 20% (red), 40% (blue), 60% (magenta), 80% (orange), and 100% (sea green) in 20% increments.

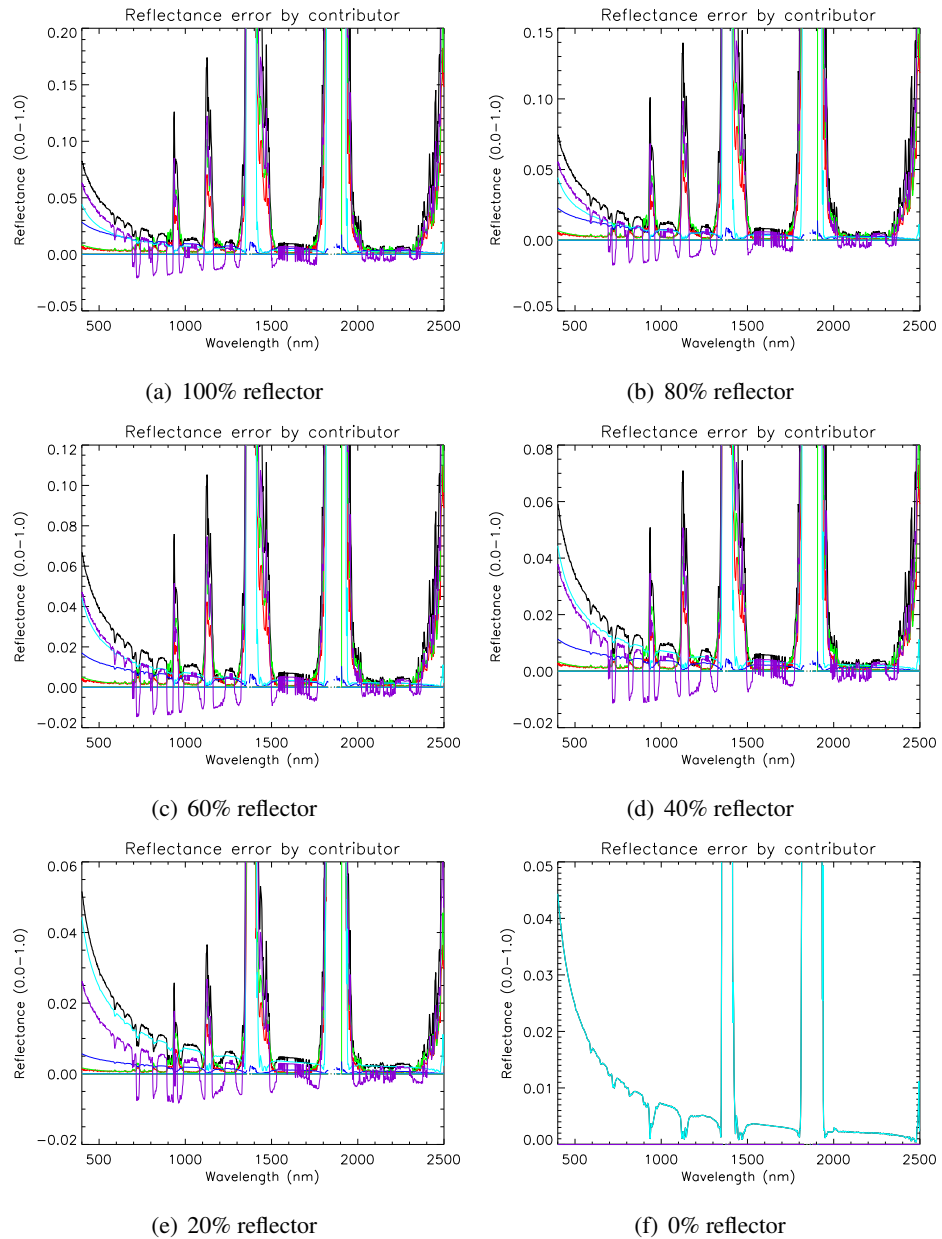


Figure G.8: Scenario 2 – individual results for zero aerosol error (water vapor error only). These plots use the legend in figure D.1. Color coding for contributors: red = τ_1 , green = τ_2 , blue = L_d , cyan = L_u , and violet = sum of all correlation terms.

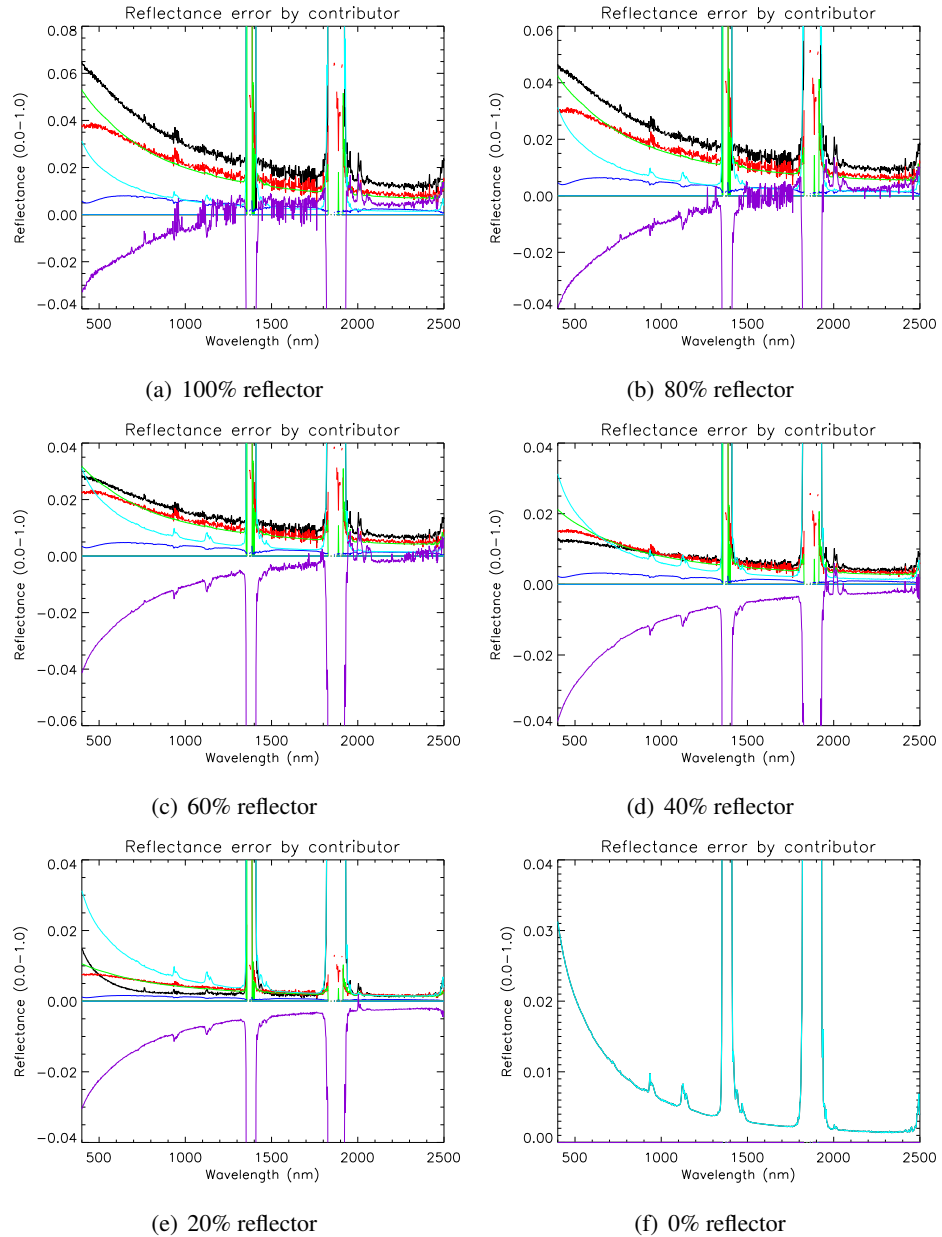


Figure G.9: Scenario 2 – individual results for zero water vapor error (aerosol error only). These plots use the legend in figure D.1. Color coding for contributors: red = τ_1 , green = τ_2 , blue = L_d , cyan = L_u , and violet = sum of all correlation terms.

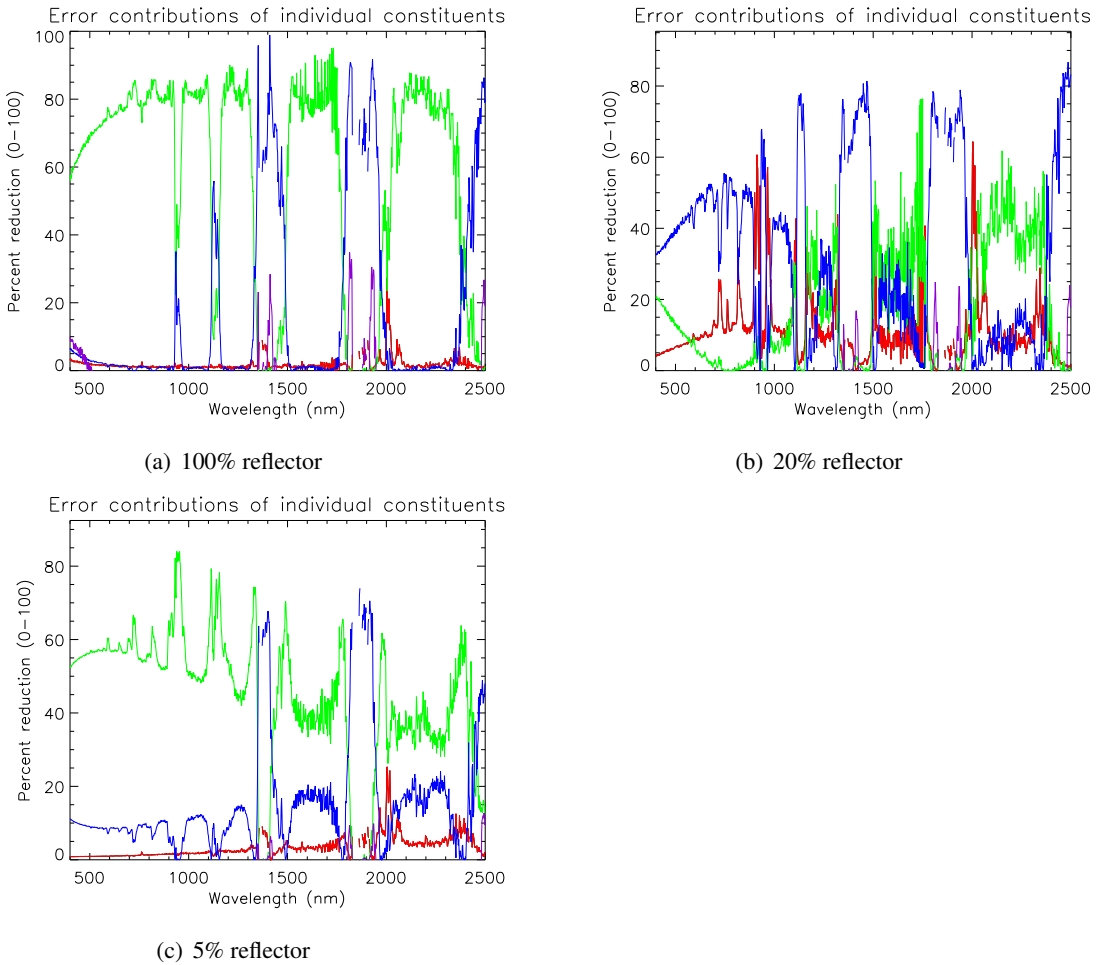
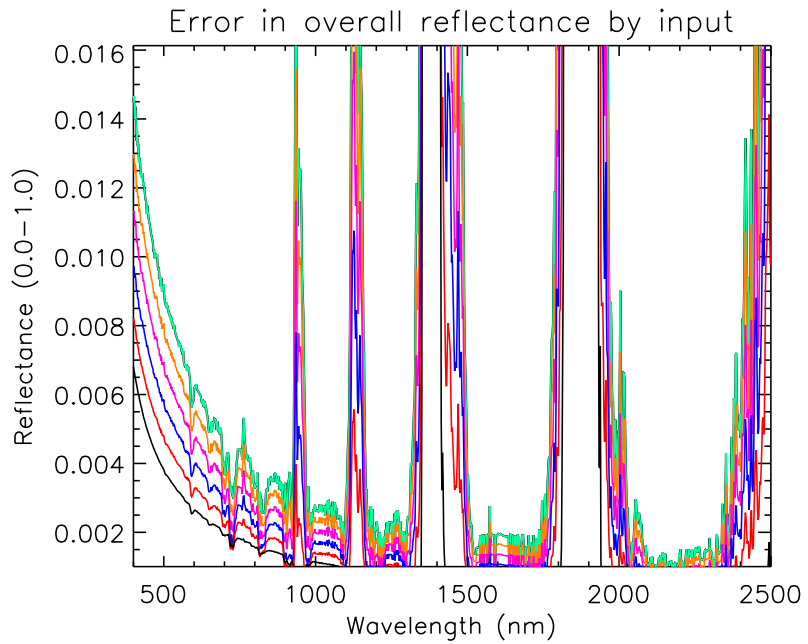
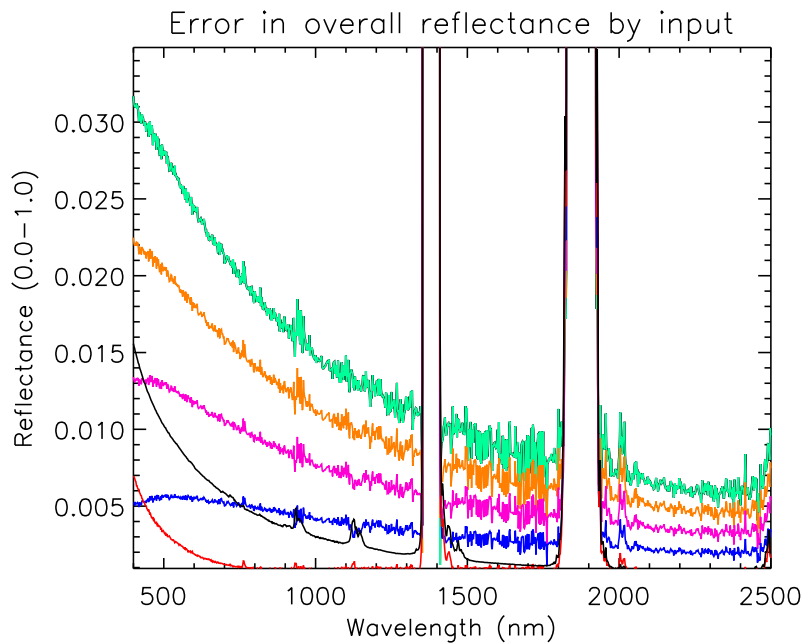


Figure G.10: Scenario 3 – inputs from ARM-grade instrumentation. Each curve is the percent reduction in uncertainty when a constituent is set to zero. In other words, the strength of each constituent's error contribution is judged by the improvement gained when it is perfectly known. Red = altitude, green = aerosols, and blue = water vapor. Magenta shows the improvement resulting from the direct ground measurement of τ_1 and L_d . Also see figure G.1.



(a) Zero aerosol error (water vapor error only)



(b) Zero water vapor error (aerosol error only)

Figure G.11: Scenario 3 – multiple reflectance comparison. Each curve represents a different surface reflectance, ranging from 0% (black) to 20% (red), 40% (blue), 60% (magenta), 80% (orange), and 100% (sea green) in 20% increments.

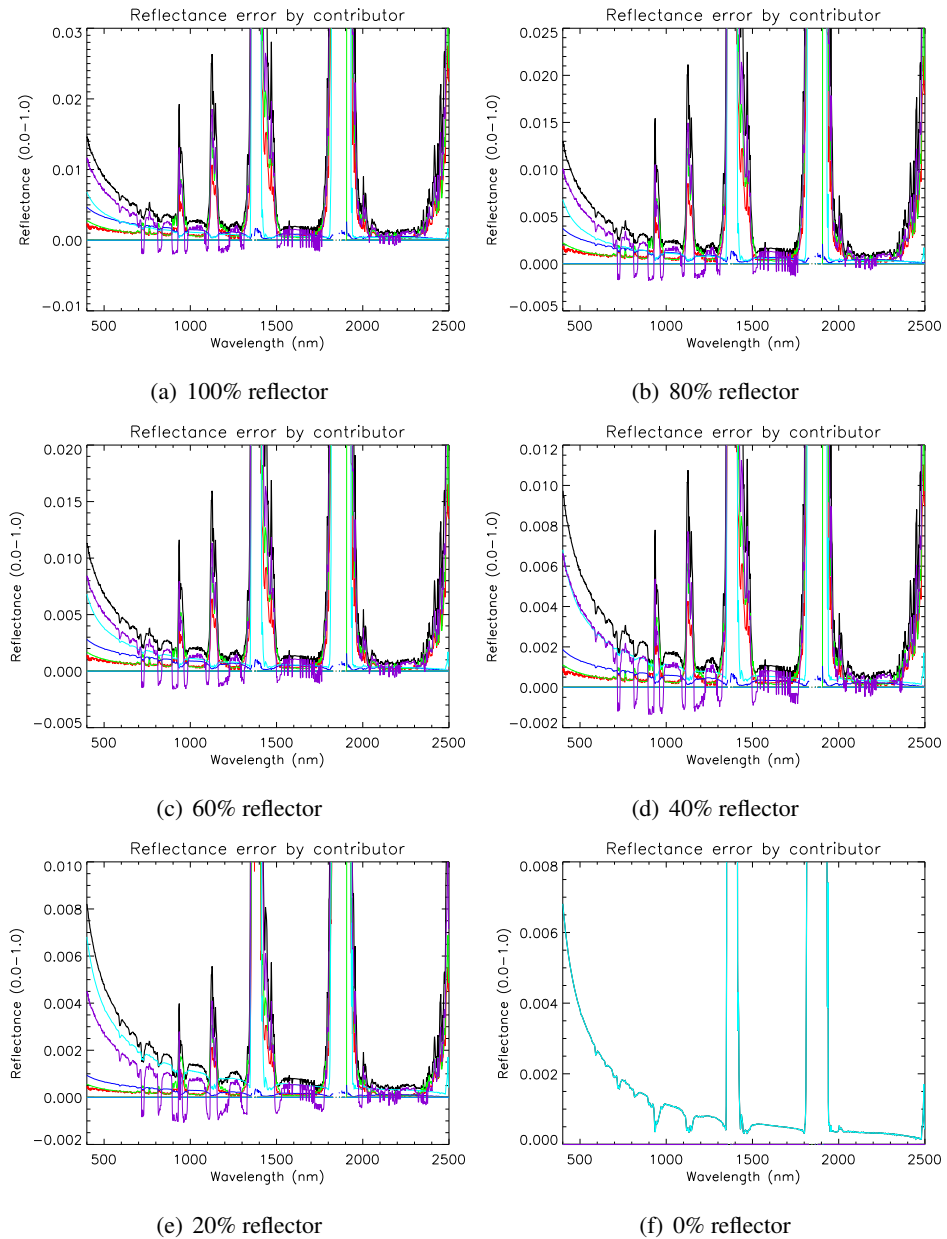


Figure G.12: Scenario 3 – individual results for zero aerosol error (water vapor error only). These plots use the legend in figure D.1. Color coding for contributors: red = τ_1 , green = τ_2 , blue = L_d , cyan = L_u , and violet = sum of all correlation terms.

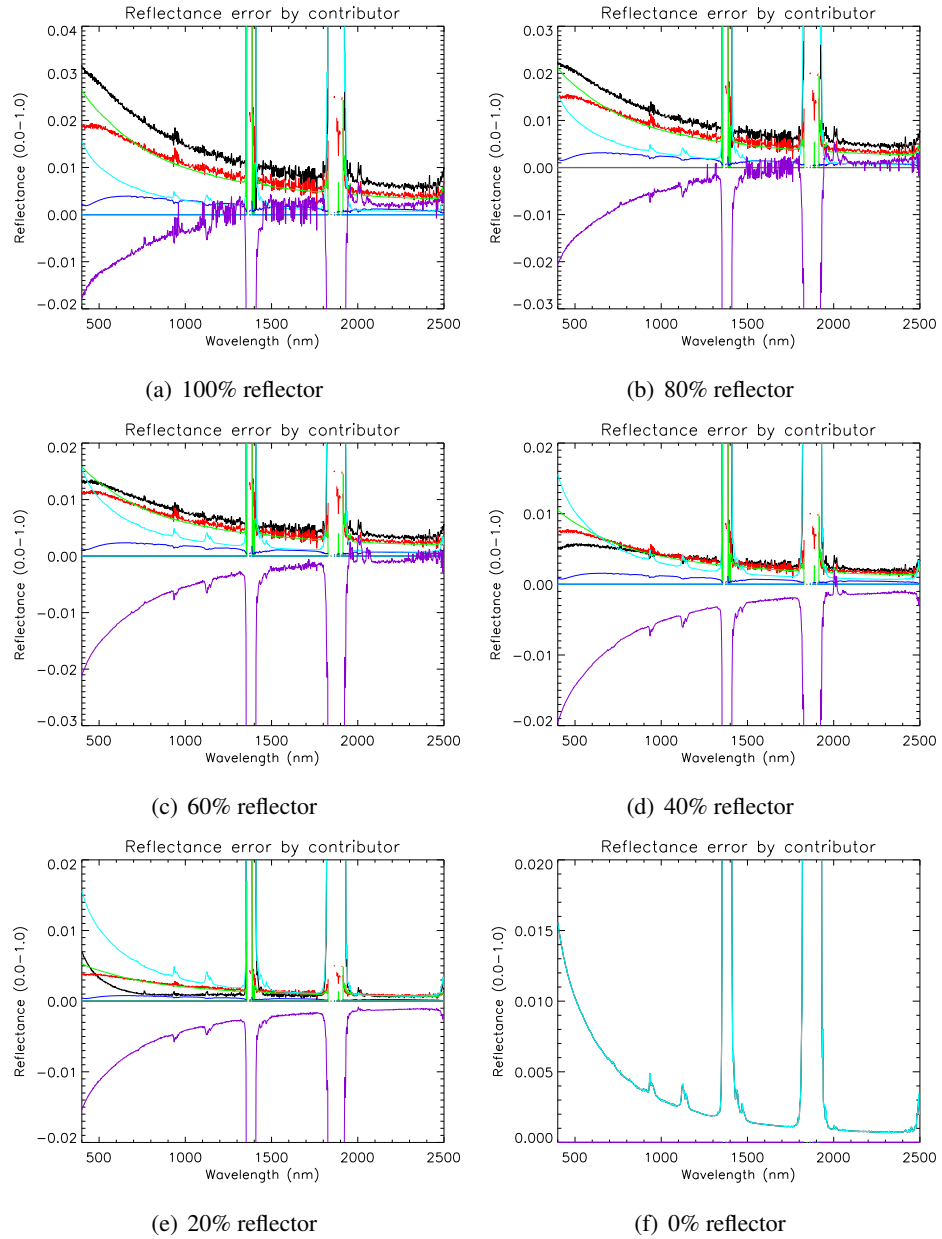


Figure G.13: Scenario 3 – individual results for zero water vapor error (aerosol error only). These plots use the legend in figure D.1. Color coding for contributors: red = τ_1 , green = τ_2 , blue = L_d , cyan = L_u , and violet = sum of all correlation terms.

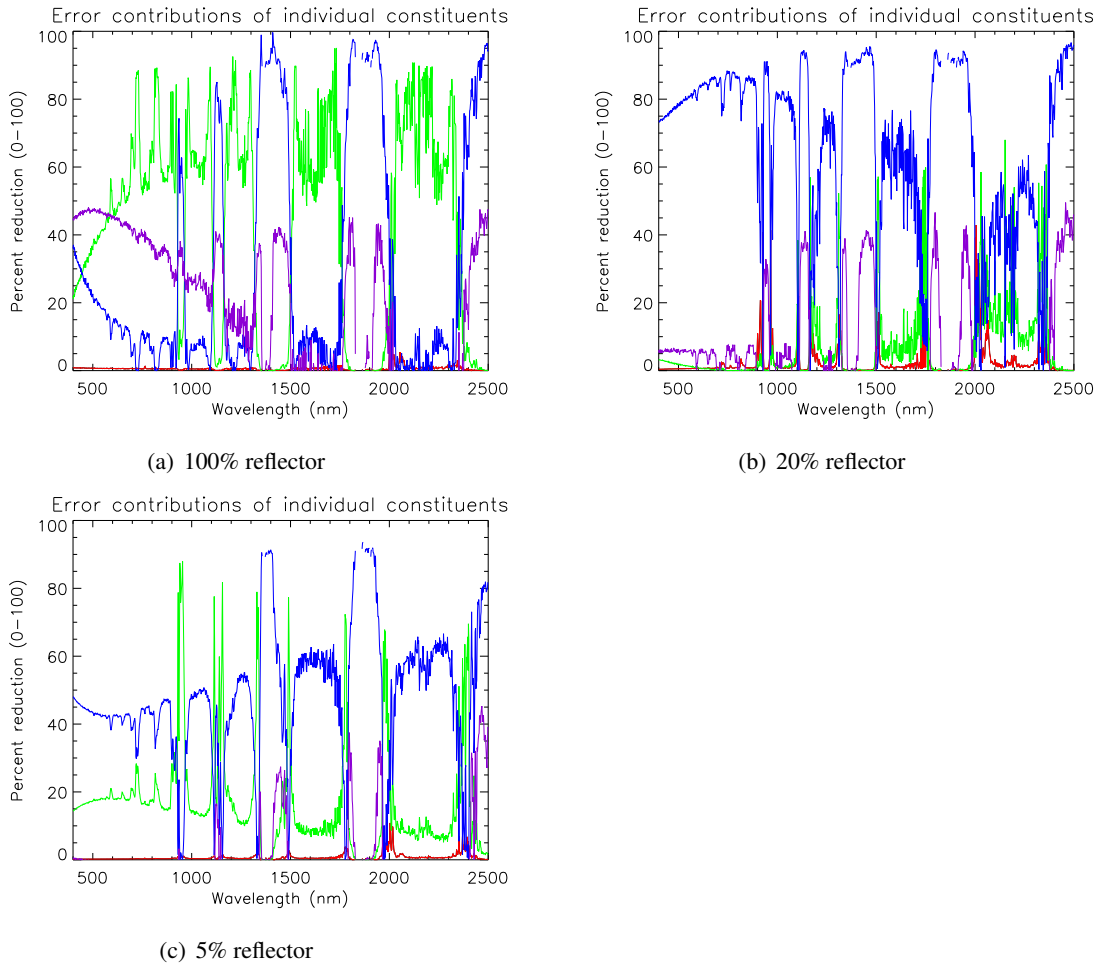
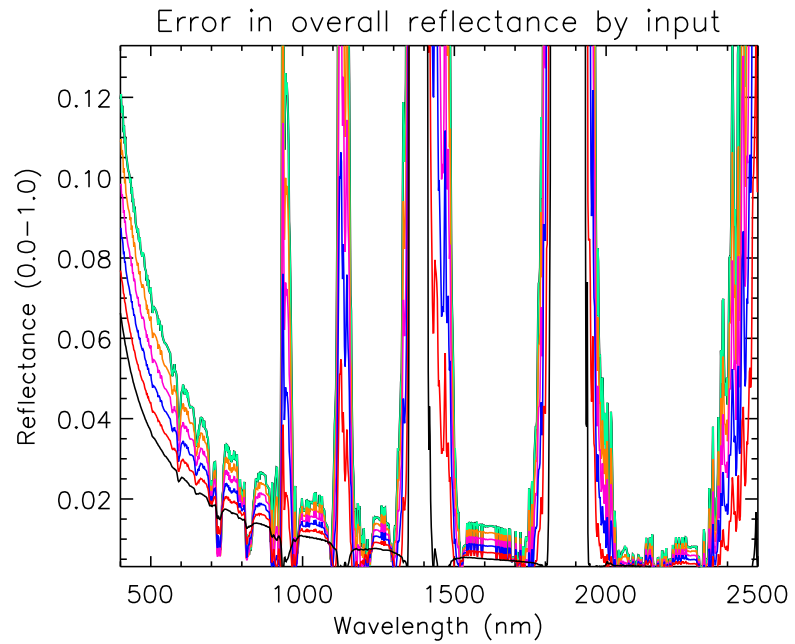
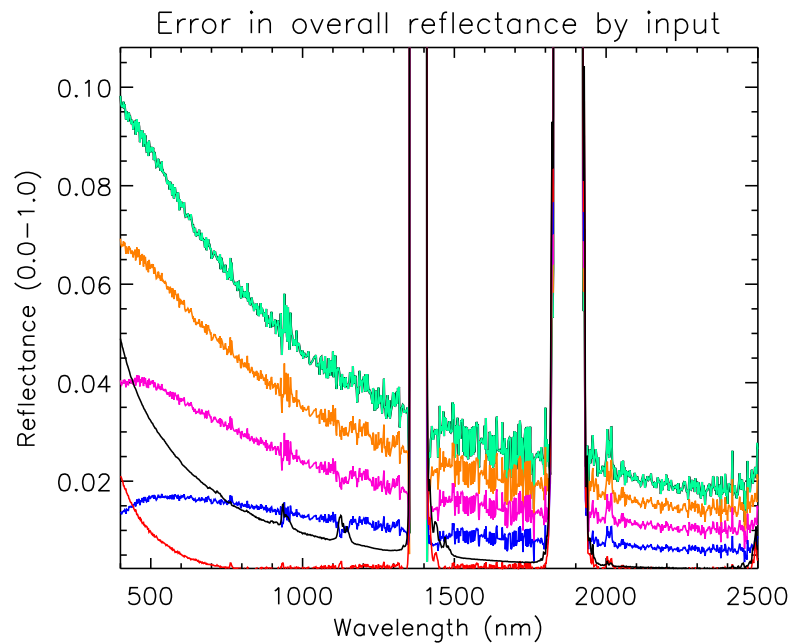


Figure G.14: Scenario 4 – *a priori* knowledge climatology inputs. Each curve is the percent reduction in uncertainty when a constituent is set to zero. In other words, the strength of each constituent's error contribution is judged by the improvement gained when it is perfectly known. Red = altitude, green = aerosols, and blue = water vapor. Magenta shows the improvement resulting from the direct ground measurement of τ_1 and L_d . Also see figure G.1.



(a) Zero aerosol error (water vapor error only)



(b) Zero water vapor error (aerosol error only)

Figure G.15: Scenario 4 – multiple reflectance comparison. Each curve represents a different surface reflectance, ranging from 0% (black) to 20% (red), 40% (blue), 60% (magenta), 80% (orange), and 100% (sea green) in 20% increments.

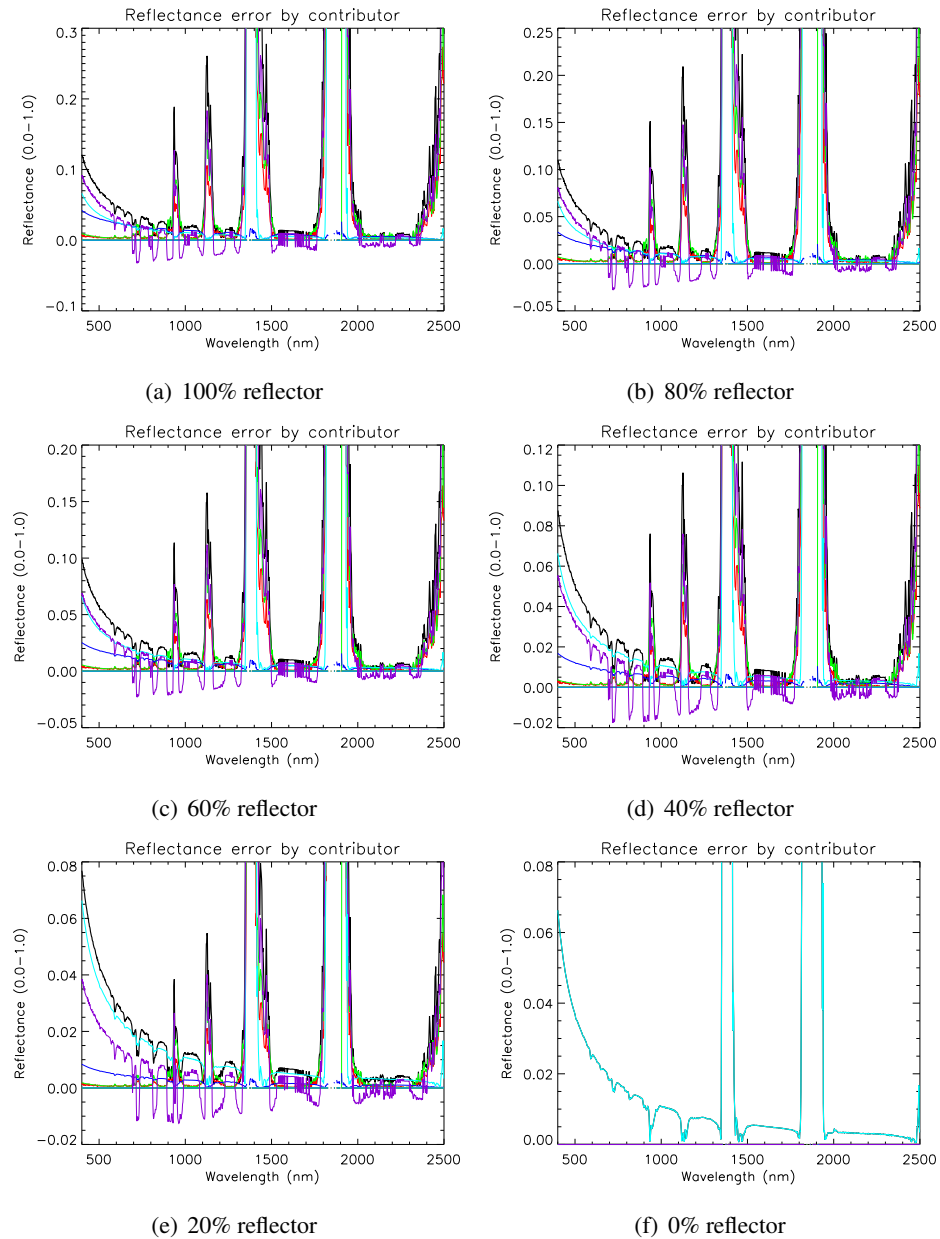


Figure G.16: Scenario 4 – individual results for zero aerosol error (water vapor error only). These plots use the legend in figure D.1. Color coding for contributors: red = τ_1 , green = τ_2 , blue = L_d , cyan = L_u , and violet = sum of all correlation terms.

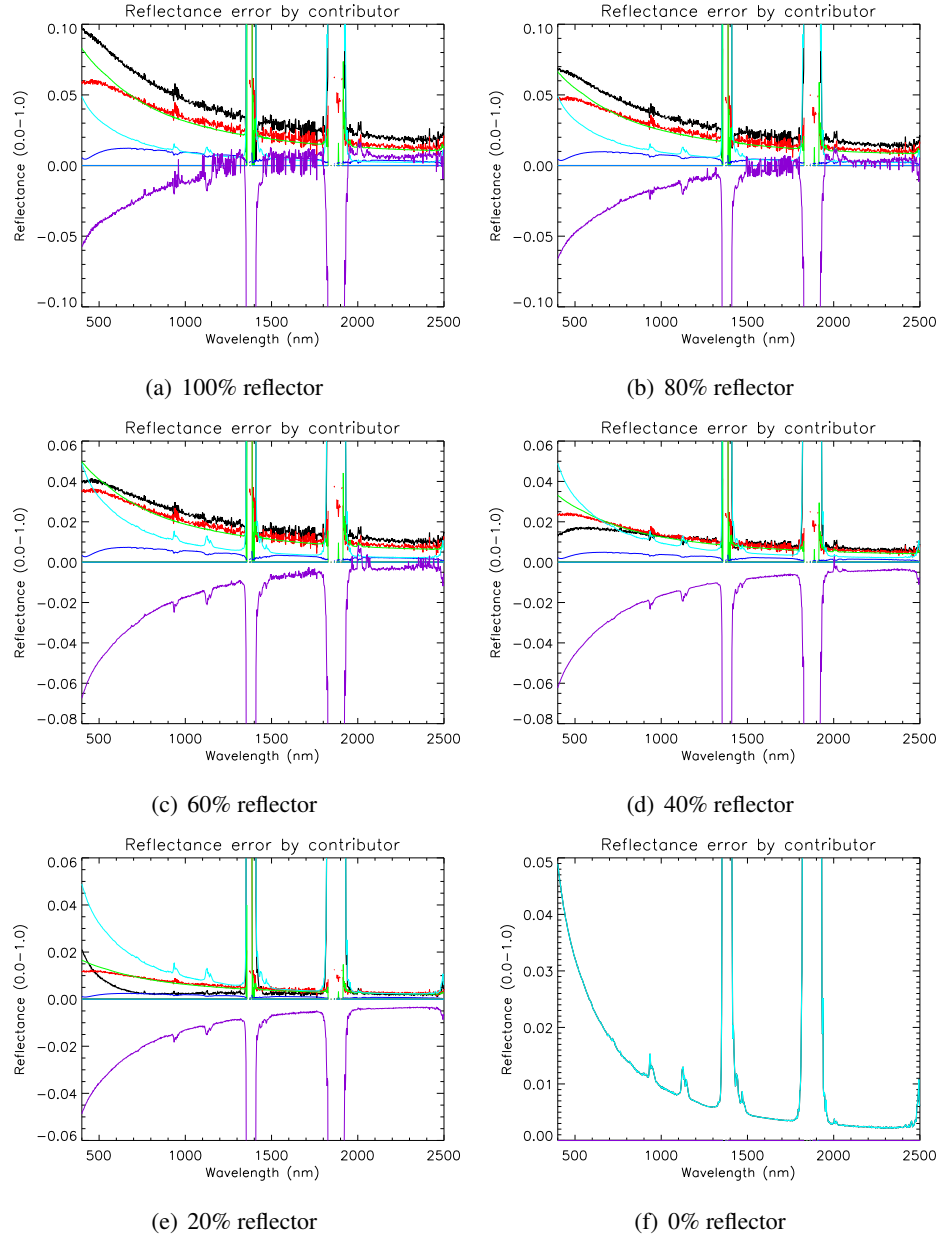


Figure G.17: Scenario 4 – individual results for zero water vapor error (aerosol error only). These plots use the legend in figure D.1. Color coding for contributors: red = τ_1 , green = τ_2 , blue = L_d , cyan = L_u , and violet = sum of all correlation terms.

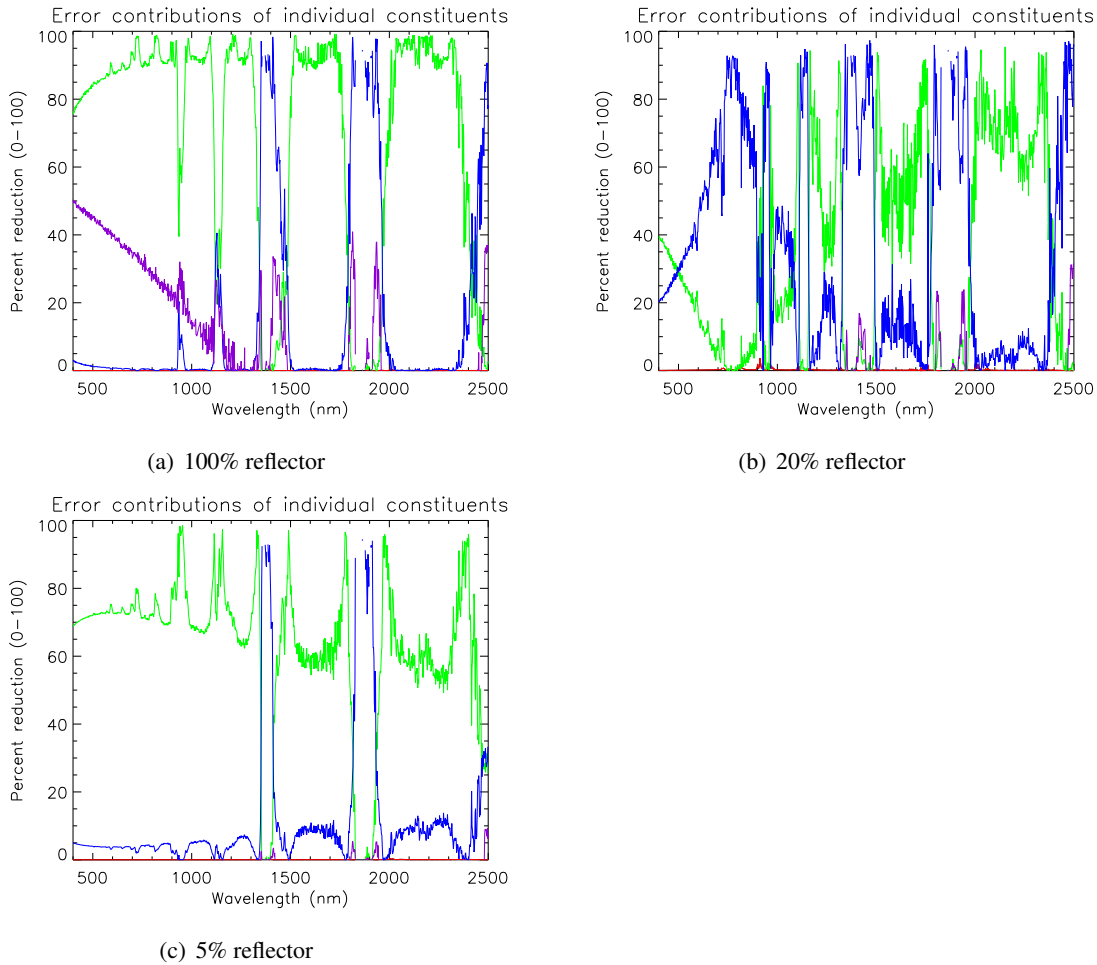
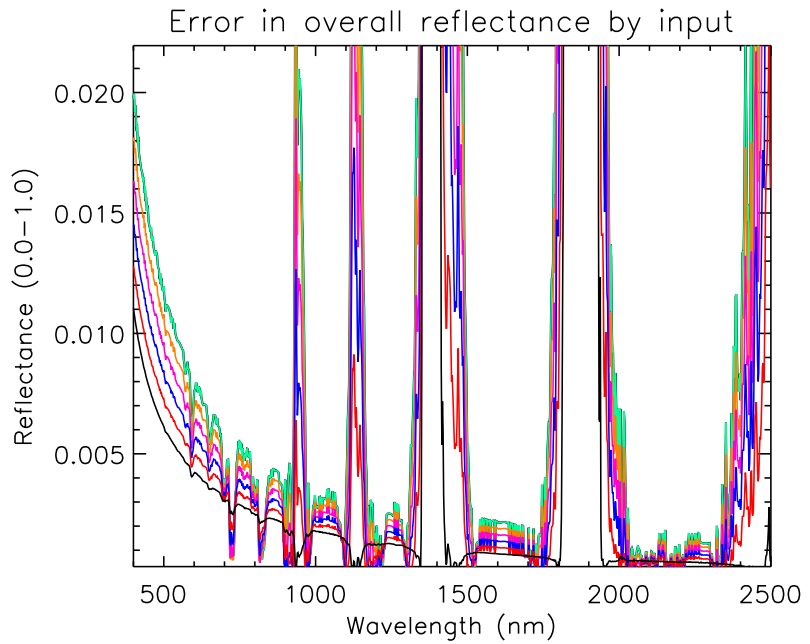
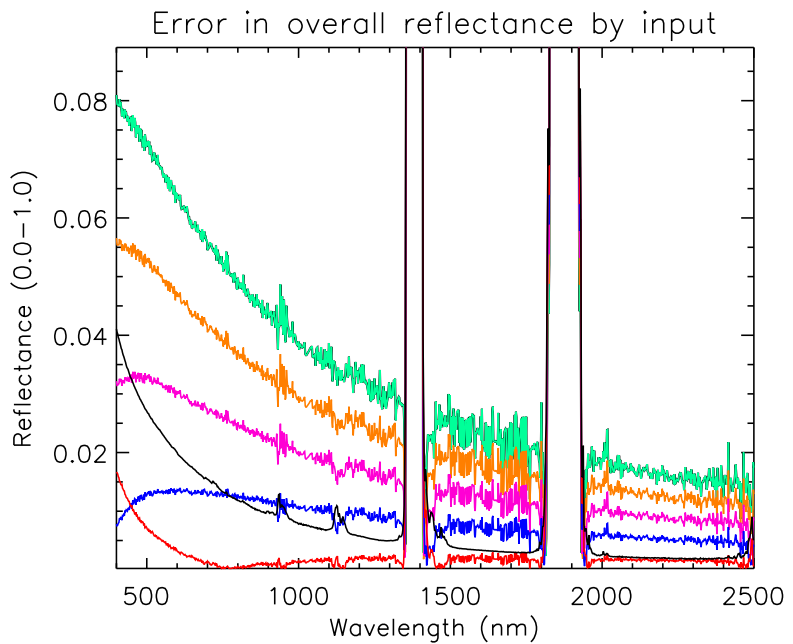


Figure G.18: Scenario 5 – *a priori* knowledge climatology inputs. Each curve is the percent reduction in uncertainty when a constituent is set to zero. In other words, the strength of each constituent's error contribution is judged by the improvement gained when it is perfectly known. Red = altitude, green = aerosols, and blue = water vapor. Magenta shows the improvement resulting from the direct ground measurement of τ_1 and L_d . Also see figure G.1.



(a) Zero aerosol error (water vapor error only)



(b) Zero water vapor error (aerosol error only)

Figure G.19: Scenario 5 – multiple reflectance comparison. Each curve represents a different surface reflectance, ranging from 0% (black) to 20% (red), 40% (blue), 60% (magenta), 80% (orange), and 100% (sea green) in 20% increments.

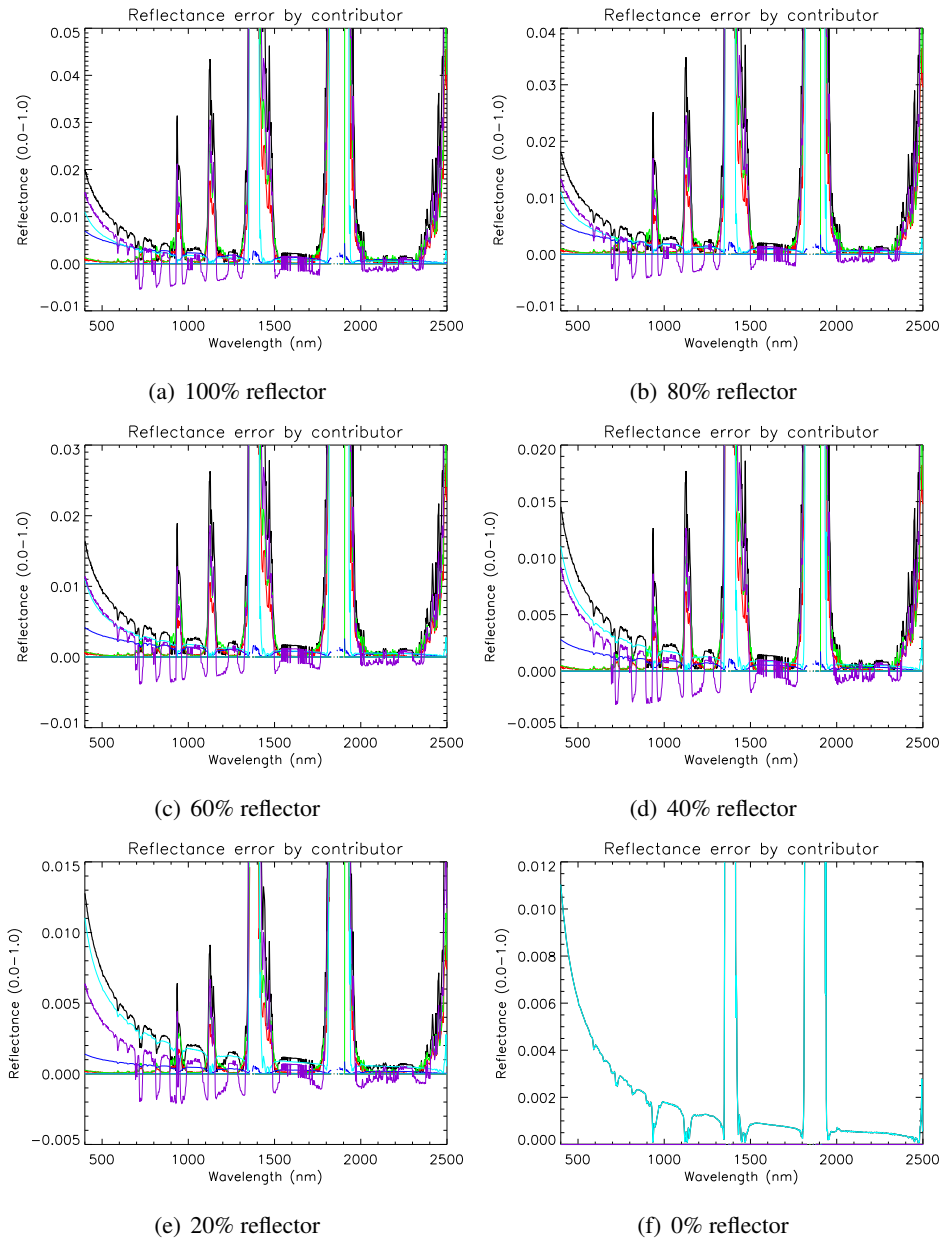


Figure G.20: Scenario 5 – individual results for zero aerosol error (water vapor error only). These plots use the legend in figure D.1. Color coding for contributors: red = τ_1 , green = τ_2 , blue = L_d , cyan = L_u , and violet = sum of all correlation terms.

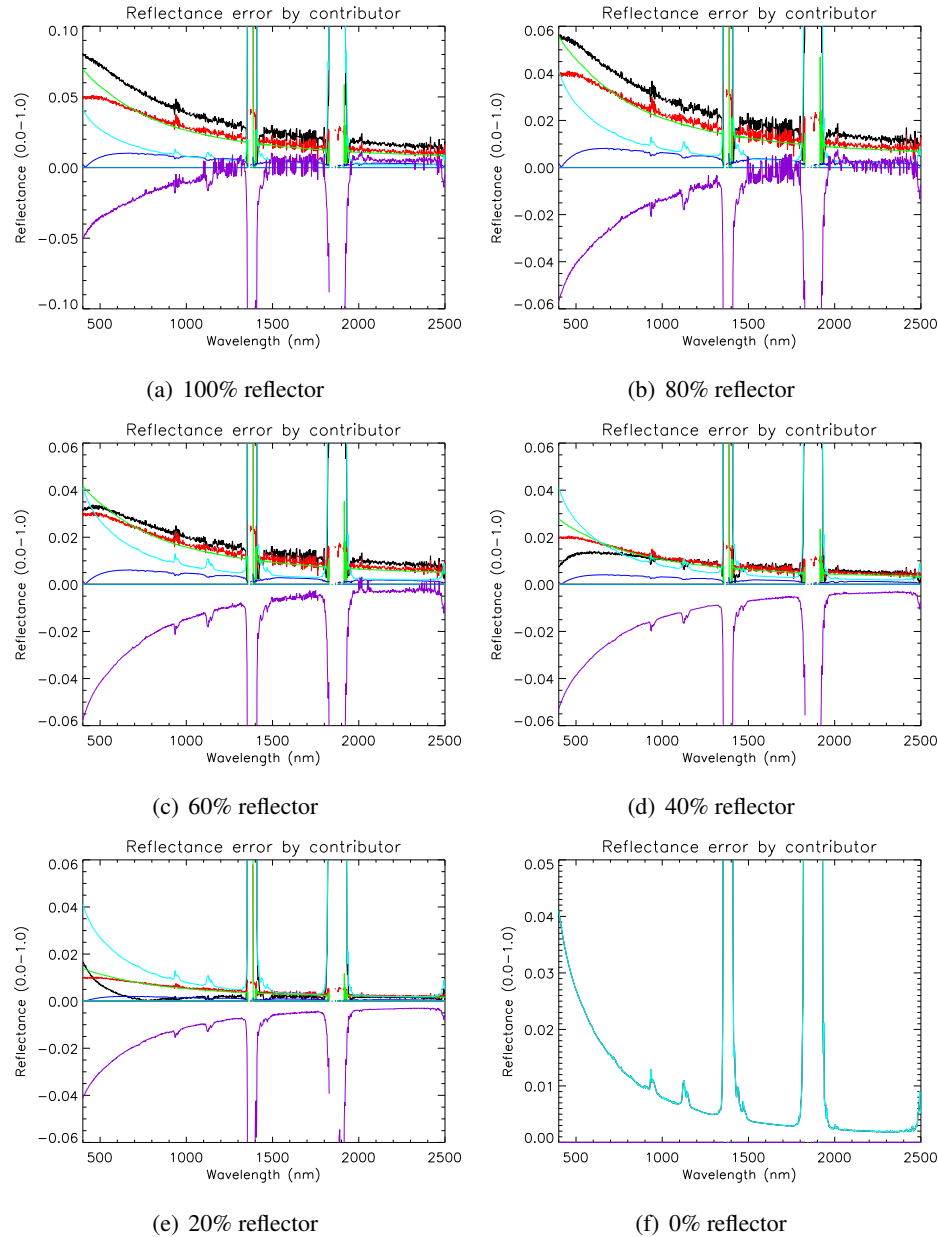
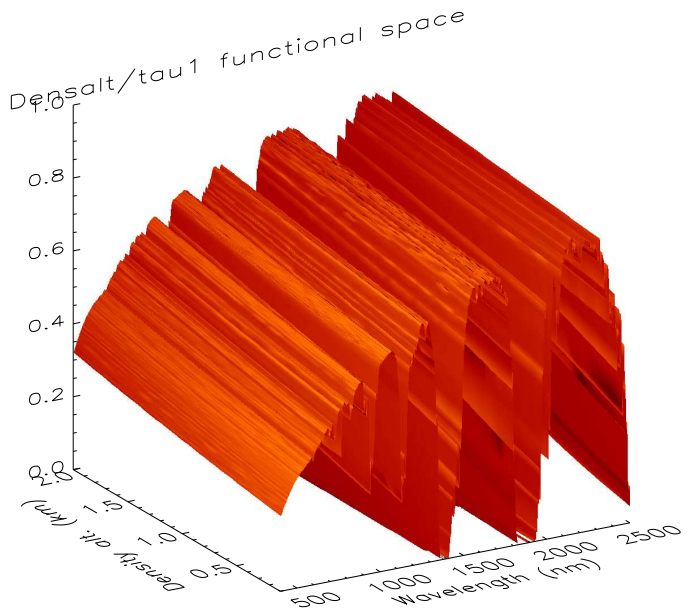
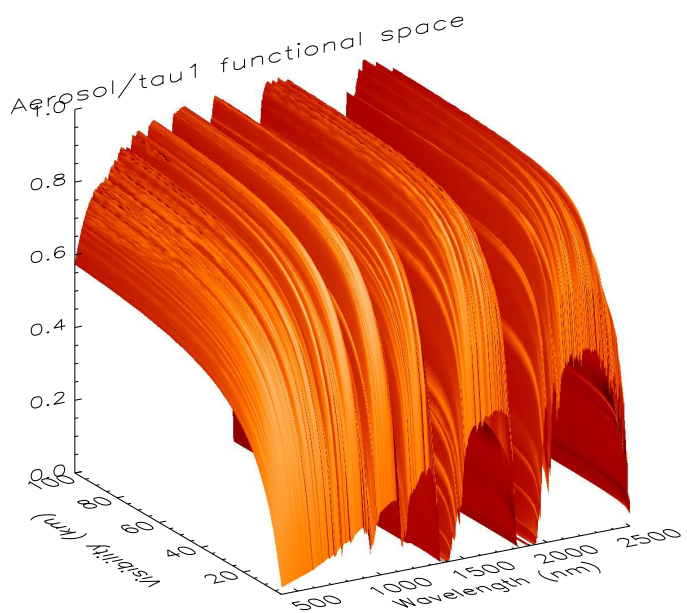


Figure G.21: Scenario 5 – individual results for zero water vapor error (aerosol error only). These plots use the legend in figure D.1. Color coding for contributors: red = τ_1 , green = τ_2 , blue = L_d , cyan = L_u , and violet = sum of all correlation terms.

Appendix H

Atmospheric Derivative Functional Spaces

Figure H.1: Derivative $\partial\tau_1/\partial alt$ Figure H.2: Derivative $\partial\tau_1/\partial vis$

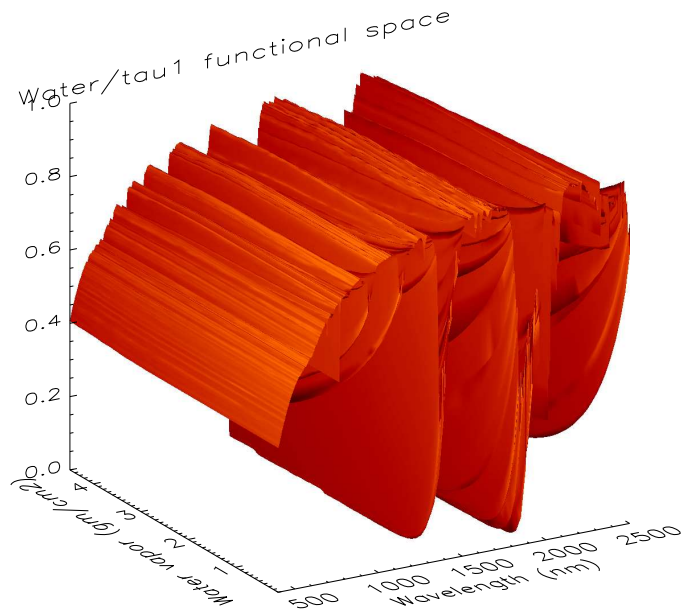


Figure H.3: Derivative $\partial\tau_1/\partial H_2O$

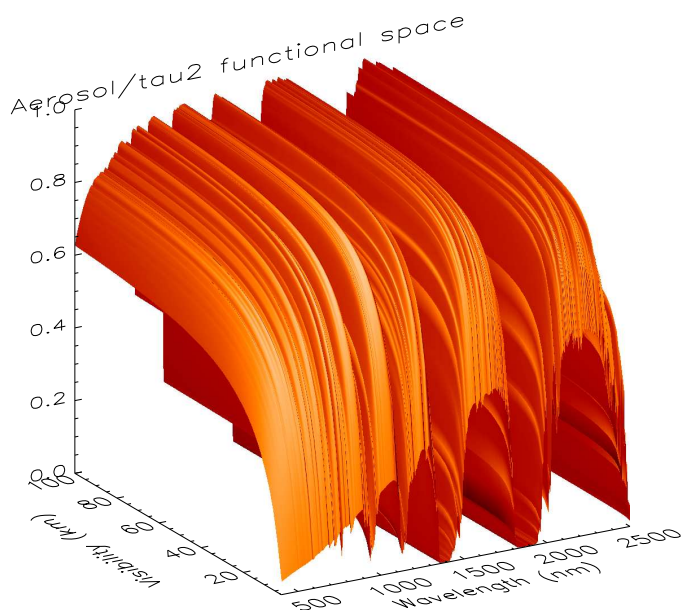
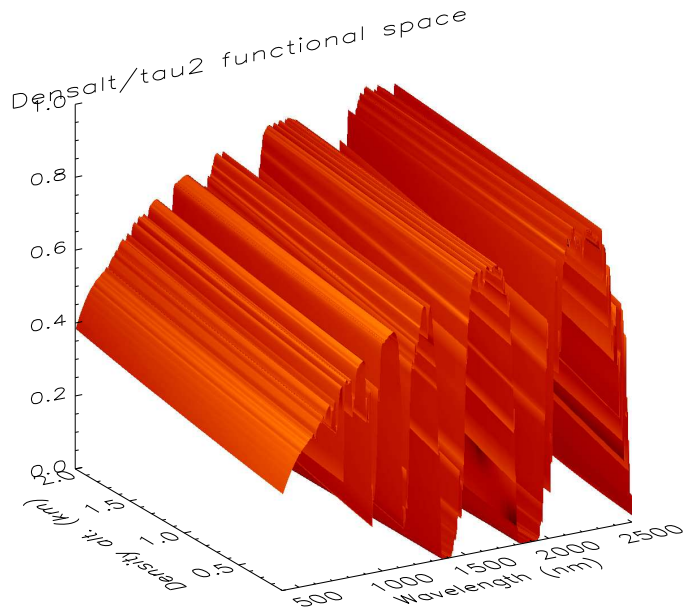
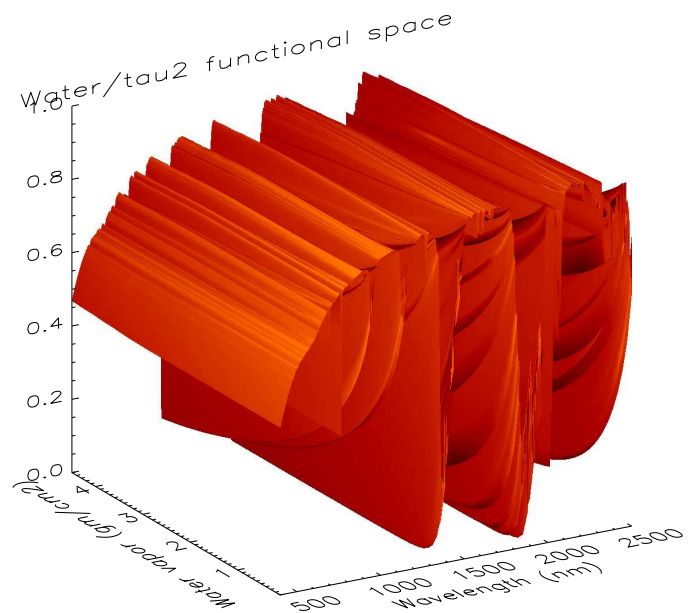


Figure H.4: Derivative $\partial\tau_2/\partial vis$

Figure H.5: Derivative $\partial\tau_2/\partial a_{lt}$ Figure H.6: Derivative $\partial\tau_2/\partial H_2O$

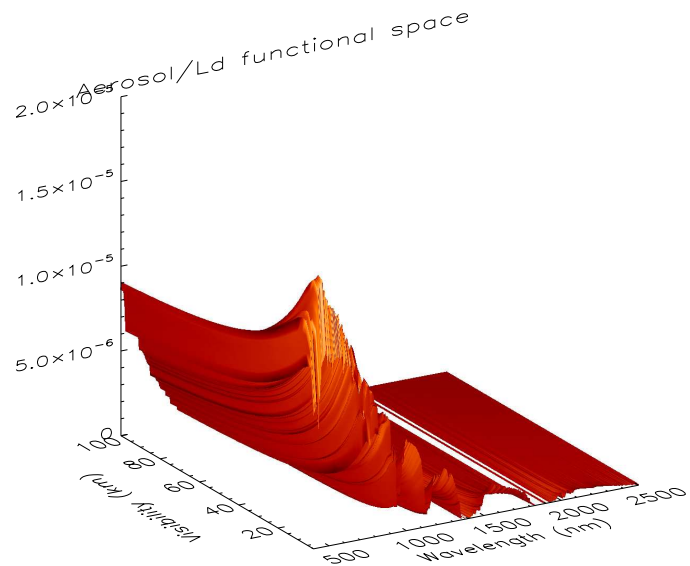


Figure H.7: Derivative $\partial L_d / \partial v_{\text{vis}}$

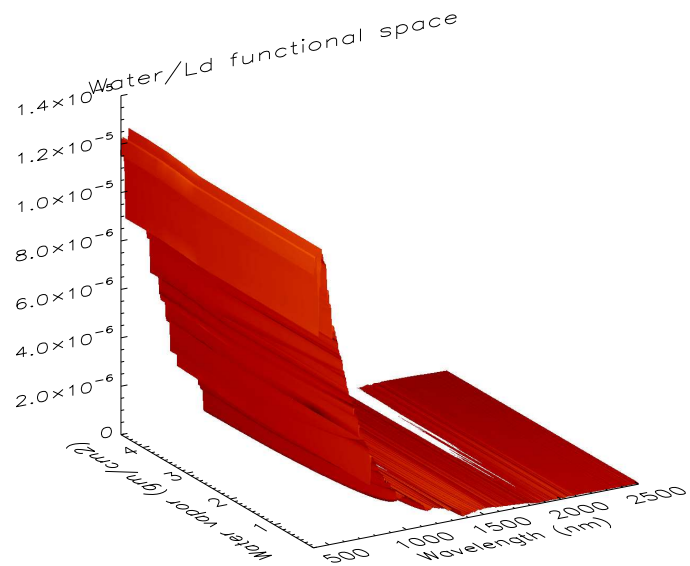
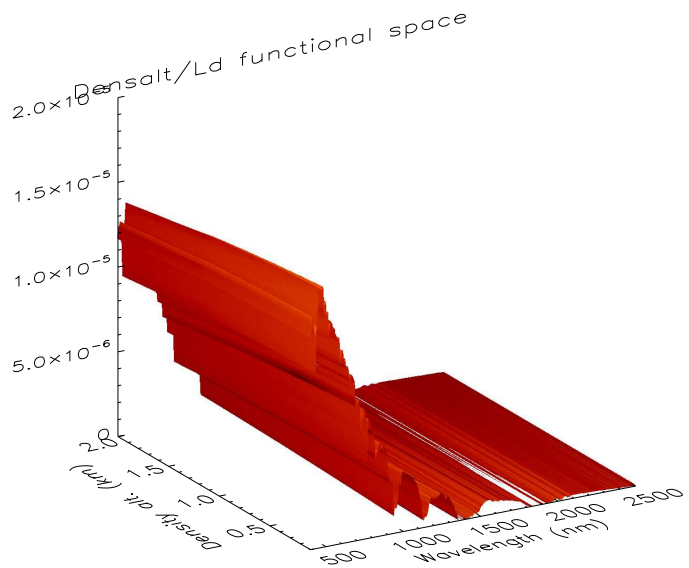
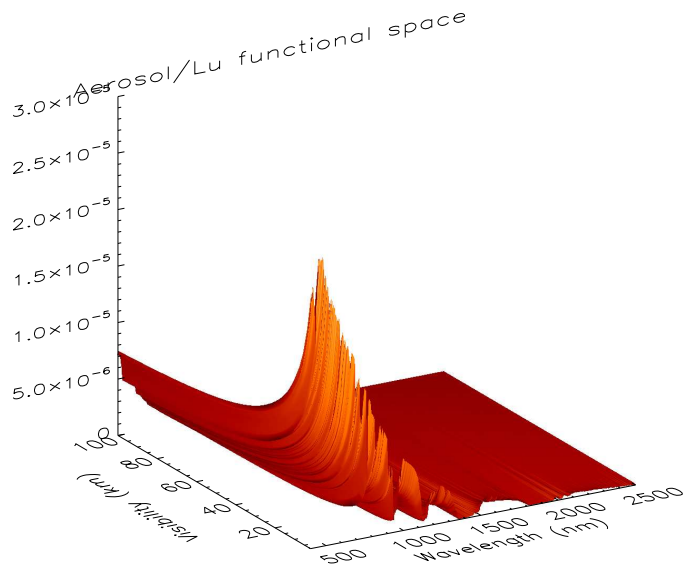


Figure H.8: Derivative $\partial L_d / \partial H_2O$

Figure H.9: Derivative $\partial L_d / \partial alt$ Figure H.10: Derivative $\partial L_u / \partial vis$

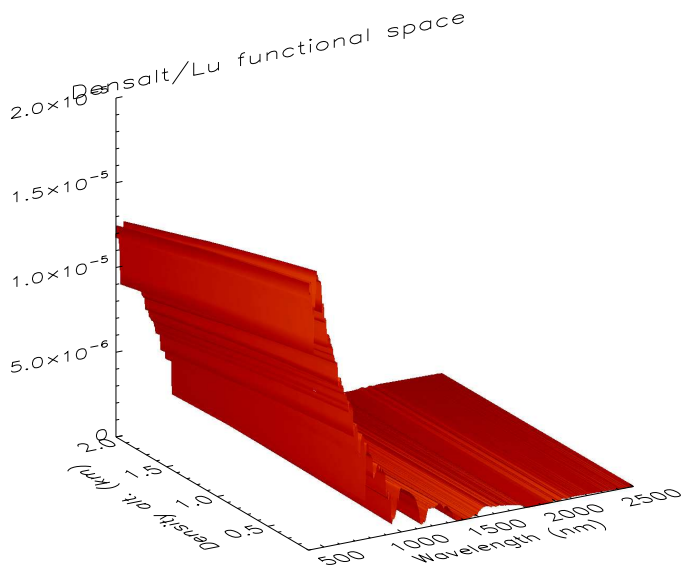


Figure H.11: Derivative $\partial L_u / \partial alt$

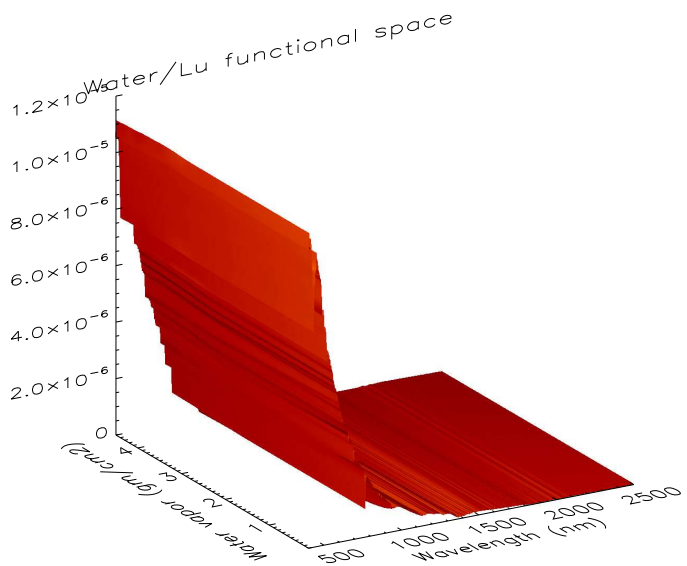


Figure H.12: Derivative $\partial L_u / \partial H_2O$

Appendix I

Explanation of Water Vapor Units

MODTRAN allows the use of several different methods for specifying water vapor. The units for each method of specification are obscure to someone not specializing in atmospheric research, or at least to someone more familiar with imaging science. This short section describes the differences between the units and presents methods of conversion and computation.

The basic principle behind specifying an amount of gas is to isolate it in a column defined by a given spatial area on the ground and stating how much of the gas exists in that column from earth to space. The amount can be given as number of molecules, a volume, a mass, or a linear dimension.

One primary unit of gas measurement is called the Dobson unit, named for G.M.B. Dobson (1889-1976), a pioneer in ozone research and inventor of the “Dobson Spectrometer,” which incidentally employs a type of band ratio method to determine atmospheric ozone content (Total Ozone Mapping Spectrometer Ozone Processing Team, 2007). The Dobson unit is a linear dimension based on a compressed column of gas (assuming no horizontal variation across the column). If all of the gas molecules in a vertical column were brought to standard temperature and pressure (STP, 0° C at 1 atmosphere), that gas would occupy a certain volume slab. The horizontal dimensions are constrained by the column size, say a square meter or square centimeter, and the vertical dimension of the volume is given by the Dobson unit (DU), where 1 DU equals 0.01 mm of vertical thickness (equation I.1). Given the assumption of horizontal invariance, the column area is not actually relevant as it does not affect the vertical dimension.

$$1 \text{ DU} = 0.01 \text{ mm} @ \text{STP} \quad (\text{I.1})$$

A similar unit is called the atmosphere-meter, meter-atmosphere, or atmometer, described as the depth, in meters, a layer of gas would have if brought to STP (Rowlett). This definition is nearly identical to that for Dobson units (equation I.2). Additionally, Rowlett adds that this is equivalent to $2.686\ 99 \times 10^{25}$ molecules of gas per square meter of horizontal area. MODTRAN uses a related unit, the atm-cm for gaseous quantities (equation I.3).

$$1 \text{ atm-cm} = 1000 \text{ DU} = 10 \text{ mm} @ \text{STP} \quad (\text{I.2})$$

$$\begin{aligned} 1 \text{ atm-cm} &= 0.01 \text{ atm-m} = 2.687 \times 10^{23} \text{ molecules/m}^2 \\ &= 2.687 \times 10^{19} \text{ molecules/cm}^2 \end{aligned} \quad (\text{I.3})$$

The other main unit used by MODTRAN is grams per square centimeter, or the mass of water vapor contained in a column with a horizontal area of a square centimeter. The introduction of mass now requires a way to relate molar volume to mass. This is accomplished using the molecular mass for the gas under study. Molecular masses for most gases, including water vapor and air, and can be found in standard chemical reference sources (Lide, 2003). Equation I.4 shows this conversion, where N_a is Avogadro's number (6.02×10^{23} molecules per mole) and W_{H_2O} is the molecular weight of water, 18.015 34 g/mol. Substituting equation I.3 into I.4 and combining terms produces a constant conversion factor for each gas. For water, this conversion factor is 8.038×10^{-4} .

$$\begin{aligned} 1 \text{ g/cm}^2 &= 1 \text{ atm-cm} \left(\frac{2.687 \times 10^{19} \cdot W_{H_2O}}{N_a} \right) \\ &= 8.038 \times 10^{-4} \text{ atm-cm} \end{aligned} \quad (\text{I.4})$$

Mass per unit area is a particularly useful unit for water vapor because it directly relates to the final water vapor unit to be addressed, total or integrated precipitable water (TPW or IPW). If all of the water vapor in a specified column were to be condensed, the height of the resulting volume of liquid (with the area constrained to match the column footprint) is the IPW. Because liquid water has unit density, 1 cm³ of liquid water is equal to 1 g/cm² (equation I.5).

$$1 \text{ g/cm}^2 = 1 \text{ cm IPW} \quad (\text{I.5})$$

Bibliography

- N. C. Barford. *Experimental Measurements: Precision, Error and Truth*. Addison-Wesley Publishing Company, Great Britain, 1967.
- Brent Bartlett. Personal communication, 2006.
- Y. Beers. *Introduction to the Theory of Errors*. Addison-Wesley, Reading, MA, 1957.
- A. Berk, L.S. Bernstein, and D.C. Robertson. MODTRAN: A Moderate Resolution Model for LOWTRAN 7. Technical Report GL-TR-89-0122, Air Force Geophysics Laboratory, Hanscom AFB, MA, 1989.
- A. Berk, S. M. Adler-Golden, A. J. Ratkowski, G. W. Felde, G. P. Anderson, M. L. Hoke, T. Cooley, J. H. Chetwynd, J. A. Gardner, M. W. Matthew, L. S. Bernstein, P. K. Acharya, D. Miller, and P. Lewis. Exploiting MODTRAN radiation transport for atmospheric correction: The FLAASH algorithm. In *Information Fusion, 2002. Proceedings of the Fifth International Conference on*, volume 2, pages 798–803, 2002.
- Alexander Berk, Gail P. Anderson, Lawrence S. Bernstein, Prabhat K. Acharya, H. Dothe, Michael W. Matthew, Steven M. Adler-Golden, Jr. James H. Chetwynd, Steven C. Richtsmeier, Brian Pukall, Clark L. Allred, Laila S. Jeong, and Michael L. Hoke. MODTRAN4 radiative transfer modeling for atmospheric correction. volume 3756, pages 348–353. SPIE, 1999.
- Daniel Birkenheuer and Seth Gutman. A Comparison of GOES Moisture-Derived Product and GPS-IPW Data during IHOP-2002. *Journal of Atmospheric and Oceanic Technology*, 22(11):1838–1845, 2005.
- Joseph W. Boardman. Inversion of high spectral resolution data. In Gregg Vane, editor, *Proceedings of SPIE Conference on Imaging Spectrometry of the Terrestrial Environment*, volume 1298, pages 222–233, Orlando, FL, 1990.

- Joseph W. Boardman. Post-ATREM polishing of AVIRIS apparent reflectance data using EFFORT: a lesson in accuracy versus precision. In *Summaries of the Seventh JPL Airborne Earth Science Workshop*, volume 1, page 53, 1998.
- Bill Browne. New millennium program EO-1 pre-ship review. URL <http://eo1.gsfc.nasa.gov/overview/Docs-PSR.html>. Slide presentation, Dec 15-17 1999.
- Carol J. Bruegge, James E. Conel, Jack S. Margolis, Robert O. Green, Geoffrey C. Toon, Veronique Carrere, Ronald G. Holm, and Gordon Hoover. In-situ atmospheric water-vapor retrieval in support of aviris validation. volume 1298, pages 150–163. SPIE, 1990.
- James B. Campbell. *Introduction to Remote Sensing*. The Guilford Press, New York, 1987.
- V. Carrere and J.E. Conel. Recovery of atmospheric water vapor total column abundance from imaging spectrometer data around 940 nm - sensitivity analysis and application to airborne visible/infrared imaging spectrometer (AVIRIS) data. *Remote Sensing of the Environment*, 43(2-3):179–204, May 1993.
- Domenico Cimini, Ed Westwater, Yong Han, and Stephen Keihm. Accuracy of ground-based microwave radiometer and balloon-borne measurements during the WVOP2000 field experiment. *IEEE Transactions of the Geosciences Remote Sensing*, 41:2605–2615, 2003.
- Roger N. Clark, Gregg A. Swayze, Kathleen B. Heidebrecht, Robert O. Green, and Alexander F. H. Goetz. Calibration to surface reflectance of terrestrial imaging spectrometry data: Comparison of methods. In *Summaries of the Fifth Annual JPL Airborne Earth Science Workshop*, pages 41–42, Pasadena, CA, 1995. Jet Propulsion Laboratory.
- Roger N. Clark, K. Eric Livo, and Raymond F. Kokaly. Geometric correction of aviris imagery using on-board navigation and engineering data. In Robert O. Green, editor, *Summaries of the 7th Annual JPL Airborne Earth Science Workshop*, volume JPL Publication 97-21, pages 57–65, Jan 12-14 1998.
- T. Cooley, G.P. Anderson, G.W. Felde, M.L. Hoke, A.J. Ratkowski, J.H. Chetwynd, J.A. Gardner, S.M. Adler-Golden, M.W. Matthew, A. Berk, L.S. Bernstein, P.K. Acharya, D. Miller, and P. Lewis. FLAASH, a MODTRAN4-based atmospheric correction algorithm, its application and validation. In *IEEE International Geoscience and Remote Sensing Symposium*, volume 3, pages 1414–1418, 2002.

- R. E. Crippen. The regression intersection method of adjusting image data for band rationing. *International Journal of Remote Sensing*, 8(2):137–155, 1986.
- D. Crommelynck, A. Fichot, R. B. Lee III, and J. Romero. First realisation of the space absolute radiometric reference (sarr) during the atlas 2 flight period. *Advances in Space Research*, 16(8):817–823, 1995.
- Davis Instruments. Cabled Vantage Pro2TM & Vantage Pro2 PlusTM Stations. Manufacturer Specification Sheet, November 2004.
- Davis Instruments. NIST Traceable Sensors. Weather Resource Manual, January 2005.
- Godelieve Deblonde, Stephen Macpherson, Yves Mireault, and Pierre Héroux. Evaluation of gps precipitable water over canada and the igs network. *Journal of Applied Meteorology*, 44(1):153–166, 2005.
- John E. Dennis and Robert B. Schnabel. *Numerical Methods for Unconstrained Optimization and Nonlinear Equations*. Number 16 in Classics in Applied Mathematics. Society for Industrial and Applied Mathematics (SIAM), Philadelphia, PA, 1996.
- Ronald R. Fairbanks. *A characterization of the impact of clouds on remotely sensed water quality*. PhD thesis, Rochester Institute of Technology, July 1999.
- Federal Aviation Administration. *PILOT'S HANDBOOK of Aeronautical Knowledge*. U.S. Government Printing Office, Washington, D.C., 2003.
- Gerald W. Felde, Gail P. Anderson, James A. Gardner, Steven M. Adler-Golden, Michael W. Matthew, and Alexander Berk. Water vapor retrieval using the FLAASH atmospheric correction algorithm. In Sylvia S. Shen and Paul E. Lewis, editors, *Algorithms and Technologies for Multispectral, Hyperspectral, and Ultraspectral Imagery X*, volume 5425 of *Proceedings of the SPIE*, pages 357–367. SPIE, 2004.
- Derek D. Feng and Benjamin M. Herman. Remotely Sensing the Earth's Atmosphere Using the Global Positioning System (GPS) – The GPS/MET Data Analysis. *Journal of Atmospheric and Oceanic Technology*, 16(8):989–1002, 1999.
- Bo-Cai Gao and Alexander F. H. Goetz. Determination of total column water vapor in the atmosphere at high spatial resolution from aviris data using spectral curve fitting and band ratioing techniques. volume 1298, pages 138–149. SPIE, 1990a.

- Bo-Cai Gao and Alexander F. H. Goetz. Column atmospheric water vapor and vegetation liquid water retrievals from airborne imaging spectrometer data. *Journal of Geophysical Research*, 95:3549–3564, March 1990b.
- Bo-Cai Gao and Alexander F. H. Goetz. Derivation of equivalent water thickness and an index of biochemical component abundance in vegetation from aviris data. In Gregg Vane, editor, *Proceedings of SPIE Conference on Imaging Spectrometry of the Terrestrial Environment*, volume 1937, pages 12–22. SPIE, 1993.
- Bo-Cai Gao, K. B. Heidebrecht, and A. F. H. Goetz. Derivation of scaled surface reflectances from aviris data. *Remote Sensing of Environment*, 44(2-3):165–178, 1993.
- J.D. Giorgini, D.K. Yeomans, A.B. Chamberlin, P.W. Chodas, R.A. Jacobson, M.S. Keesey, J.H. Lieske, S.J. Ostro, E.M. Standish, and R.N. Wimberly. Jpl's on-line solar system data service. *Bulletin of the American Astronomical Society*, 28(3): 1158, 1996.
- A. F. H. Goetz, B.C. Kindel, M. Ferri, and Qu Zheng. HATCH: results from simulated radiances, AVIRIS and Hyperion. *Geoscience and Remote Sensing, IEEE Transactions on*, 41(6):1215–1222, June 2003.
- Robert O. Green. Retrieval of reflectance from aviris-measured radiance using a radiative transfer code. In *JPL Publication 91-28*, Third Annual AVIRIS Workshop, pages 200–210, 1991.
- Robert O. Green. An improved spectral calibration requirement for aviris. In *Summaries of the Fifth Annual JPL Airborne Earth Science Workshop*, volume 1, pages 75–78, 1995.
- Robert O. Green. AVIRIS Lunar Lake. URL <http://aviris.jpl.nasa.gov/html/aviris.freedata.html>. Data set, 1997.
- Robert O. Green and Betina Pavri. Aviris in-flight calibration experiment, sensitivity analysis, and intraflight stability. In *AVIRIS Workshop 2000*, Pasadena, CA, 2000.
- Robert O. Green and Betina Pavri. Inflight Calibration Experiment Results for AVIRIS on May 6, 2002 at Rogers Dry Lake, California. In *Proceedings of the 12th Airborne Earth Science Workshop, JPL Pub. 04-6*, pages 109–120, Pasadena, California, 2003. Jet Propulsion Laboratory.

- Robert O. Green, James E. Conel, and Dar A. Roberts. Estimation of aerosol optical depth, pressure elevation, water vapor, and calculation of apparent surface reflectance from radiance measured by the airborne visible/infrared imaging spectrometer (aviris) using a radiative transfer code. volume 1937, pages 2–11, Orlando, FL, USA, 1993. SPIE.
- Robert O. Green, Betina Pavri, and Thomas G. Chrien. On-orbit radiometric and spectral calibration characteristics of EO-1 Hyperion derived with an underflight of AVIRIS and in situ measurements at Salar de Arizaro, Argentina. *Geoscience and Remote Sensing, IEEE Transactions on*, 41(6):1194–1203, June 2003.
- Michael K. Griffin and Hsiao-hua K. Burke. Compensation of hyperspectral data for atmospheric effects. *Lincoln Laboratory Journal*, 14(1):29–54, 2003.
- R. N. Halthore, S. E. Schwartz, Y. Liu, P. Daum, B. Holben, and J. J. Michalsky. Sun and sky radiometric measurements at the CART ARM SGP site. In *9th Annual ARM Meeting*, San Antonio, Texas, March 1999.
- Hewlett-Packard Components Group. *Noise Sources in CMOS Image Sensors*. Imaging Products Operations, Jan 4 1998. URL http://www.stw.tu-ilmenau.de/~ff/beruf_cc/cmos/cmos_noise.pdf.
- Karen L. Hirsch, Lee K. Balick, Christoph C. Borel, and Peter M. McLachlan. Comparison of four methods for determining precipitable water vapor content from multispectral data. volume 4381, pages 417–428. SPIE, 2001.
- E. J. Ientilucci and S. D. Brown. Advances in wide-area hyperspectral image simulation. In W. R. Watkins, D. Clement, and W. R. Reynolds, editors, *Targets and Backgrounds IX: Characterization and Representation*, volume 5075 of *Proceedings of the SPIE*, pages 110–121. SPIE, September 2003.
- E. Karpouzli and T. Malthus. The empirical line method for the atmospheric correction of IKONOS imagery. *International Journal of Remote Sensing*, 24(5):1143–1150, 2003.
- Y. J. Kaufman, D. Tanré, L. A. Remer, E. F. Vermote, A. Chu, and B. N. Holben. Operational remote sensing of tropospheric aerosol over land from eos moderate resolution imaging spectroradiometer. *Journal of geophysical research*, 102(D14):17051–17067, July 1997.
- Yoram J. Kaufman and Bo-Cai Gao. Remote sensing of water vapor in the near IR from EOS/MODIS. *Geoscience and Remote Sensing, IEEE Transactions on*, 30(5):871–884, Sep 1992.

- J.P. Kerekes. Error analysis of spectral reflectance derived from imaging spectrometer data. *Geoscience and Remote Sensing Symposium Proceedings, 1998. IGARSS '98. 1998 IEEE International*, 5:2697–2701 vol.5, Jul 1998.
- Scott L. Klempner, Brent Bartlett, and John R. Schott. Ground truth-based variability analysis of atmospheric inversion in the presence of clouds. *Atmospheric and Environmental Remote Sensing Data Processing and Utilization II: Perspective on Calibration/Validation Initiatives and Strategies*, 6301(1):630109, 2006.
- R. Kremens, J. Faulring, A. Gallagher, A. Seema, and A. Vodacek. Autonomous field-deployable wildland fire sensors. *International Journal of Wildland Fire*, 12(2):237–244, 2003.
- R. Kremens, A. Bova, M. Dickinson, J. Faulring, and S. McNamara. Mapping heat production from wildland fires using time-sequenced airborne imaging. In Doug Fox, John Qu, Al Riebau, and Ruixin Yang, editors, *EastFIRE Conference Proceedings*. George Mason University, May 2005.
- Frank A. Kruse. Atmospheric Corrections using Low-Altitude AVIRIS Data of Boulder, Colorado. In *13th JPL Airborne Geoscience Workshop*, Pasadena, CA, March-April 2004. Jet Propulsion Laboratory.
- David R. Lide, editor. *CRC Handbook of Chemistry and Physics*. CRC Press, 83rd edition, 2003.
- J.C. Liljegren and B.M. Lesht. Measurements of integrated water vapor and cloud liquid water from microwave radiometers at the DOE ARM Cloud and Radiation Testbed in the U.S. Southern Great Plains. In *Remote Sensing for a Sustainable Future*, volume 3 of *Proceedings of the International Geoscience and Remote Sensing Symposium*, pages 1675–1677. IEEE, 1996.
- V. Mattioli, E.R. Westwater, S.I. Gutman, and V.R. Morris. Forward model studies of water vapor using scanning microwave radiometers, global positioning system, and radiosondes during the cloudiness intercomparison experiment. *Geoscience and Remote Sensing, IEEE Transactions on*, 43(5):1012–1021, May 2005.
- Robert McIntyre. Personal communication, 2004.
- J. J. Michalsky. Accuracy of Broadband Shortwave Irradiance Measurements Using the Open Silicon Channel of the MFRSR. In *Eleventh ARM Science Team Meeting Proceedings*, Atlanta, Georgia, March 2001.

- Peter A. Mitchell. Hyperspectral digital imagery collection experiment (HYDICE). In Joan B. Lurie, James J. Pearson, and Eugenio Zilioli, editors, *Geographic Information Systems, Photogrammetry, and Geological/Geophysical Remote Sensing*, volume 2587, pages 70–95. SPIE, 1995.
- Douglas C. Montgomery and George C. Runger. *Applied Statistics and Probability for Engineers*. John Wiley & Sons, New York, NY, 2nd edition, November 1998.
- M. L. Nischan, J. P. Kerekes, J. E. Baum, and R. W. Basedow. Analysis of HYDICE noise characteristics and their impact on subpixel object detection. In *Proc. SPIE Vol. 3753, p. 112-123, Imaging Spectrometry V, Michael R. Descour; Sylvia S. Shen; Eds.*, pages 112–123, October 1999.
- Gregory S. Okin, Dar A. Roberts, Bruce Murray, and William J. Okin. Practical limits on hyperspectral vegetation discrimination in arid and semiarid environments. *Remote Sensing of the Environment*, 77:212–225, 2001.
- Peyton Z. Peebles. *Probability, Random Variables, and Random Signal Principles*. McGraw Hill, 4th edition, 2001.
- William H. Press, Saul L A. Teukolsky, Brian N P. Flannery, and William M T. Vetterling. *Numerical Recipes: FORTRAN*. Cambridge University Press, New York, NY, USA, 1990. ISBN 0521383307.
- Zheng Qu, Bruce C. Kindel, and Alexander F. H. Goetz. The high accuracy atmospheric correction for hyperspectral data (hatch) model. *IEEE TRANSACTIONS ON GEOSCIENCE AND REMOTE SENSING*, 41(6):1223–1231, June 2003.
- M. Rainwater and L. Gregory. Cimel Sunphotometer (CSPHOT) Handbook. Technical Report ARM TR-056, U.S. Department of Energy Atmospheric Radiation Measurement Program, January 2005.
- N. G. Raqueno, L. E. Smith, D. W. Messinger, C. Salvaggio, R. V. Raqueno, and J. R. Schott. Megacollect 2004: hyperspectral collection experiment of terrestrial targets and backgrounds of the rit megascene and surrounding area (rochester, new york). volume 5806, pages 554–565. SPIE, 2005.
- H. E. Revercomb, D. D. Turner, D. C. Tobin, R. O. Knuteson, W. F. Feltz, J. Barnard, J. Bösenberg, S. Clough, D. Cook, R. Ferrare, J. Goldsmith, S. Gutman, R. Halthore, B. Lesht, J. Liljegren, H. Linné, J. Michalsky, V. Morris, W. Porch, S. Richardson, B. Schmid, M. Splitt, T. Van Hove, E. Westwater, and

- D. Whiteman. The ARM Program's Water Vapor Intensive Observation Periods. *Bulletin of the American Meteorological Society*, 84(2):217–236, 2003.
- CJF Ridders. Technical note: Accurate computation of $f'(x)$ and $f''(x)$. *Advances in Engineering Software*, 4(2):75–76, 1982.
- P. A. Rochford, P. K. Acharya, S. M. Adler-Golden, A. Berk, L. S. Bernstein, M. W. Matthew, S. C. Richtsmeier, Jr. Gulick, S., and J. Slusser. Validation and refinement of hyperspectral/multispectral atmospheric compensation using shadowband radiometers. *IEEE Transactions on Geoscience and Remote Sensing*, 43(12):2898–2907, December 2005.
- E. Rodriguez, C.S. Morris, J.E. Belz, E.C. Chapin, J.M. Martin, W. Daffer, and S. Hensley. An Assessment of the SRTM Topographic Products. Technical Report JPL D-31639, Jet Propulsion Laboratory, Pasadena, California, 2005.
- Russ Rowlett. How Many? A Dictionary of Units of Measurement. URL <http://www.unc.edu/~rowlett/units/dictA.html>.
- Kevin C. Ruffner, editor. *Corona : America's first satellite program*. History Staff, Center for the Study of Intelligence, Central Intelligence Agency, Washington, D.C., 1995.
- P. Santos, K. Carey, W. M. MacKenzie, J. Zhang, R. Ferraro, and J. G. Yoe. Global positioning system (gps) meteorology integrated precipitable water (ipw). *Submitted to the Electronic Journal of the Nat. Wea. Assoc.*, 2007.
- Daniel Schläpfer and Jens Nieke. Using the MODO / MODTRAN4 environment. In *4th EARSeL Workshop on Imaging Spectroscopy*, Warsaw, 2005.
- John R. Schott. *Remote Sensing The Image Chain Approach*. Oxford University Press, New York, 1997.
- Geoffrey M. Smith and Edward J. Milton. The use of the empirical line method to calibrate remotely sensed data to reflectance. *International Journal of Remote Sensing*, 20(13):2653–2662, September 1999.
- Lon Smith. Personal communication, 2004.
- Sami K. Solanki and Natalie A. Krivova. Solar irradiance variations: From current measurements to long-term estimates. *Solar Physics*, 224(1):197–208, Oct 2004.

- Sami K. Solanki, Natalie A. Krivova, and T. Wenzler. Irradiance models. *Advances in Space Research*, 35(3):376–383, 2005.
- Jim Soukup. Personal communication, 2008.
- K. Staenz. Radiative transfer codes applied to hyperspectral data for the retrieval of surface reflectance. *International Journal of Photogrammetry and Remote Sensing*, 57:194–203, December 2002.
- James Stewart. *Calculus*. Brooks/Cole Publishing Company, 3rd edition, 1995.
- Total Ozone Mapping Spectrometer Ozone Processing Team. What is a Dobson Unit?, 2007. URL <http://toms.gsfc.nasa.gov/teacher/basics/dobson.html>.
- U.S. Department of Energy. ARM climate research facility management plan, June 2004.
- Vaisala. Vaisala Radiosonde RS92-SGP. Manufacturer Specification Sheet, 2006.
- Vaisala. Vaisala PTU300. Manufacturer Specification Sheet, 2008.
- Gregg Vane. Airborne Visible/Infrared Imaging Spectrometer (AVIRIS). A description of the sensor, ground data processing facility, laboratory calibration, and first results. Technical report, JPL Publication 87-38, Pasadena, CA, 1987.
- E. F. Vermote, D. Tanre, J.L. Deuze, M. Herman, and J.J. Morcrette. *Second Simulation of the Satellite Signal in the Solar Spectrum (6S), 6S User Guide Version 6.0*. NASA-GSFC, Greenbelt, MD, 1994.
- E.F. Vermote, D. Tanre, J.L. Deuze, M. Herman, and J.-J. Morcette. Second Simulation of the Satellite Signal in the Solar Spectrum, 6S: an overview. *Geoscience and Remote Sensing, IEEE Transactions on*, 35(3):675–686, May 1997.
- E. Webber, R.V. Raqueño, and J.R. Schott. Sensitivity analysis of atmospheric compensation algorithms for multispectral systems configuration. Technical Report Report 00/01-76-161, Rochester Institute of Technology Digital Imaging and Remote Sensing Laboratory, Jan 2001.
- D. P. Wylie and W. P. Menzel. Two Years of Cloud Cover Statistics Using VAS. *Journal of Climate*, 2(4):380–392, 1989.